

NATIONAL AERONAUTICS AND SPACE ADMINISTRATION

*Technical Report 32-1526*

*Volume XIX*

*The Deep Space Network*

*Progress Report*

*For November and December 1973*

(NASA-CR-136730) THE DEEP SPACE NETWORK,  
VOLUME 19 Progress Report, Nov. - Dec.  
1973 (Jet Propulsion Lab.) 241 p  
HC \$14.25

N74-15846

CSCI 17I

Unclas  
G3/07 29034

JET PROPULSION LABORATORY  
CALIFORNIA INSTITUTE OF TECHNOLOGY  
PASADENA, CALIFORNIA

February 15, 1974

NATIONAL AERONAUTICS AND SPACE ADMINISTRATION

*Technical Report 32-1526*

*Volume XIX*

*The Deep Space Network*

*Progress Report*

*For November and December 1973*

JET PROPULSION LABORATORY  
CALIFORNIA INSTITUTE OF TECHNOLOGY  
PASADENA, CALIFORNIA

February 15, 1974



## **Preface**

This report presents DSN progress in flight project support, TDA research and technology, network engineering, hardware and software implementation, and operations. Each issue presents material in some, but not all, of the following categories in the order indicated:

### **Description of the DSN**

#### **Mission Support**

- Interplanetary Flight Projects
- Planetary Flight Projects
- Manned Space Flight Projects
- Advanced Flight Projects

#### **Radio Science**

#### **Supporting Research and Technology**

- Tracking and Ground-Based Navigation
- Communications, Spacecraft/Ground
- Station Control and Operations Technology
- Network Control and Data Processing

#### **Network Engineering and Implementation**

- Network Control System
- Ground Communications
- Deep Space Stations

#### **Operations and Facilities**

- Network Operations
- Network Control System Operations
- Ground Communications
- Deep Space Stations
- Facility Engineering

In each issue, the part entitled "Description of the DSN" describes the functions and facilities of the DSN and may report the current configuration of one of the five DSN systems (Tracking, Telemetry, Command, Monitor and Control, and Test and Training).

The work described in this report series is either performed or managed by the Tracking and Data Acquisition organization of JPL for NASA.

**PRECEDING PAGE BLANK NOT FILMED**





## **Contents**

### **DESCRIPTION OF THE DSN**

<b>DSN Functions and Facilities</b> . . . . .	<b>1</b>
N. A. Renzetti	
<b>DSN Command System Mark III-74</b> . . . . .	<b>5</b>
W. G. Stinnett	
NASA Code 311-03-42-94	

### **MISSION SUPPORT**

#### **Planetary Flight Projects**

<b>Viking Mission Support</b> . . . . .	<b>10</b>
D. J. Mudgway and D. W. Johnston	
NASA Code 311-03-21-70	
<b>Pioneer 10 and 11 Mission Support</b> . . . . .	<b>23</b>
R. B. Miller	
NASA Code 311-03-21-20	
<b>Summary Report on the Mariner Venus/Mercury 1973 Spacecraft/ Deep Space Network Test Program</b> . . . . .	<b>25</b>
A. I. Bryan	
NASA Code 311-03-22-10	

### **SUPPORTING RESEARCH AND TECHNOLOGY**

#### **Tracking and Ground-Based Navigation**

<b>The Mariner Quasar Experiment: Part I</b> . . . . .	<b>31</b>
M. A. Slade, P. F. MacDoran, I. I. Shapiro, D. J. Spitzmesser, J. Gubbay, A. Legg, D. S. Robertson, and L. Skjerve	
NASA Code 310-10-60-56	
<b>Radio Interferometry Measurements of a 16-km Baseline With 4-cm Precision</b> . . . . .	<b>36</b>
J. B. Thomas, J. L. Fanelow, P. F. MacDoran, D. J. Spitzmesser, and L. Skjerve	
NASA Code 310-10-60-50	
<b>Improved Dichroic Reflector Design for the 64-m Antenna S- and X-Band Feed Systems</b> . . . . .	<b>55</b>
P. D. Potter	
NASA Code 310-10-61-04	
<b>Range Measurements to Pioneer 10 Using the Digitally Controlled Oscillator</b> . . . . .	<b>63</b>
A. S. Liu	
NASA Code 310-10-60-50	

## Contents (cont'd)

<b>S/X Open-Loop Receiver</b>	71
H. G. Nishimura	
NASA Code 310-10-64-03	
<b>X-Band Radar System</b>	77
R. L. Leu	
NASA Code 310-10-64-01	

### Communications, Spacecraft/Ground

<b>An Algorithm for the Computation of Linear Forms</b>	82
J. E. Savage	
NASA Code 310-20-67-08	
<b>Radio Metric Applications of the New Broadband Square Law Detector</b>	89
R. A. Gardner, C. T. Steizried, and M. S. Reid	
NASA Code 310-20-66-06	
<b>Low-Noise Receivers: Microwave Maser Development</b>	93
R. Clauss and E. Wiebe	
NASA Code 310-20-66-01	
<b>System Noise Temperature Calibrations of the Research and Development Systems at DSS 14</b>	100
M. S. Reid and R. A. Gardner	
NASA Code 310-20-66-06	
<b>The Design and Performance of a Programmed Controller</b>	105
O. B. Parham	
NASA Code 310-20-66-06	
<b>Radio Frequency Performance of DSS 14 64-m Antenna at 3.56- and 1.96-cm Wavelengths</b>	110
A. J. Freiley	
NASA Code 310-20-65-03	
<b>Optimal Station Location for Two-Station Tracking</b>	116
E. R. Rodemich	
NASA Code 310-20-78-08	

### Station Control and Operations Technology

<b>Bandwidth Selection for Block VI SDA</b>	122
R. B. Crow	
NASA Code 310-30-68-10	
<b>Frame Synchronization Performance Analysis for MVM'73 Uncoded Telemetry Modes</b>	126
B. K. Levitt	
NASA Code 310-30-63-01	

## Contents (contd)

<b>DSN Research and Technology Support . . . . .</b>	<b>137</b>
E. B. Jackson	
NASA Code 310-30-69-02	

<b>Design of a High-Speed Reference Selector Switch Module for the Coherent Reference Generator Assembly . . . . .</b>	<b>141</b>
T. K. Tucker	
NASA Code 310-30-68-10	

### Network Control and Data Processing

<b>A Scaled-Time Telemetry Test Capability for Sequential Decoding . . . . .</b>	<b>144</b>
S. Butman, J. Layland, J. MacConnell, R. Chernoff, N. Ham, and J. Wilcher	
NASA Code 310-40-72-02	

## NETWORK ENGINEERING AND IMPLEMENTATION

### Network Control System

<b>NCS Standard Computer Interface Hardware, Its Timing and Timing Control Logic . . . . .</b>	<b>152</b>
T. O. Anderson	
NASA Code 311-03-41-11	

### Ground Communications

<b>High-Speed Data Outage Distribution . . . . .</b>	<b>161</b>
J. P. McClure	
NASA Code 311-06-04-00	

### Deep Space Stations

<b>Planetary Ranging . . . . .</b>	<b>165</b>
R. W. Tappan	
NASA Code 311-03-42-52	
<b>Adjustable Tuner for S-Band High-Power Waveguide . . . . .</b>	<b>169</b>
J. R. Loreman	
NASA Code 311-03-14-21	
<b>X-Band Antenna Feed Horn Assembly . . . . .</b>	<b>173</b>
R. W. Hartop	
NASA Code 311-03-42-48	
<b>Variable S-Band High-Power Tuner . . . . .</b>	<b>176</b>
H. R. Buchanan	
NASA Code 311-03-14-21	

## Contents (contd)

<b>A No-Load RF Calorimeter .</b>	<b>. 179</b>
R. C. Chernoff	
NASA Code 311-03-14-52	

<b>Dual-Carrier Preparations for Viking . . .</b>	<b>. 186</b>
D. A. Bathker and D. W. Brown	
NASA Code 311-03-14-52	

## Network Operations

<b>Computer Program Copy-Verify and Load Check System .</b>	<b>. 193</b>
R. Billings	
NASA Code 311-03-14-42	

<b>Network Telemetry System Performance Tests in Support of the MVM'73 Project . . . . .</b>	<b>. 196</b>
R. D. Rey and E. T. Lobdell	
NASA Code 311-03-14-52	

## Deep Space Stations

<b>Analysis of Staffing and Training Policies for a DSN Tracking Station . . .</b>	<b>. 207</b>
A. Bahadur and P. Gottlieb	
NASA Code 311-03-13-30	

<b>The DSN Hydromechanical Service Program—A Second Look . . . . .</b>	<b>. 221</b>
R. Smith and O. Sumner	
NASA Code 311-03-14-64	

<b>Network Command System Performance Test Report for Mariner Venus/Mercury 1973 . . . . .</b>	<b>. 224</b>
B. Falin	
NASA Code 311-03-14-52	

<b>Bibliography . . . . .</b>	<b>. 227</b>
-------------------------------	--------------

# DSN Functions and Facilities

N. A. Renzetti  
Mission Support Office

*The objectives, functions, and organization of the Deep Space Network are summarized. The Deep Space Instrumentation Facility, the Ground Communications Facility, and the Network Control System are described.*

The Deep Space Network (DSN), established by the National Aeronautics and Space Administration (NASA) Office of Tracking and Data Acquisition under the system management and technical direction of the Jet Propulsion Laboratory (JPL), is designed for two-way communications with unmanned spacecraft traveling approximately 16,000 km (10,000 mi) from Earth to planetary distances. It supports or has supported, the following NASA deep space exploration projects: Ranger, Surveyor, Mariner Venus 1962, Mariner Mars 1964, Mariner Venus 67, Mariner Mars 1969, Mariner Mars 1971, Mariner Venus-Mercury 1973 (JPL); Lunar Orbiter and Viking (Langley Research Center); Pioneer (Ames Research Center); Helios (West Germany); and Apollo (Manned Spacecraft Center), to supplement the Spaceflight Tracking and Data Network (STDN).

The Deep Space Network is one of two NASA networks. The other, STDN, is under the system management and technical direction of the Goddard Space Flight Center. Its function is to support manned and unmanned Earth-orbiting and lunar scientific and communications satellites. Although the DSN was concerned with unmanned lunar spacecraft in its early years, its primary objective now and into the future is to continue its support of planetary and interplanetary flight projects.

A development objective has been to keep the network capability at the state of the art of telecommunications and data handling and to support as many flight projects as possible with a minimum of mission-dependent hardware and software. The DSN provides direct support of each flight project through that project's tracking and

data system. This management element is responsible for the design and operation of the hardware and software in the DSN which are required for the conduct of flight operations.

Beginning in FY 1973 a modified DSN interface has been established with the flight projects. In lieu of the SFOF, a multimission Mission Control and Computing Center (MCCC) has been activated as a separate functional and management element within JPL. This function, as negotiated with each flight project, will provide all computing and mission operations support for missions controlled from JPL. DSN computing support will be provided separately by the DSN. Radio metric, telemetry, and command data interfaces with the DSN are a joint DSN, MCCC, and flight project responsibility. The organization and procedures necessary to carry out these new activities will be reported in this document in the near future.

The DSN function, in supporting a flight project by tracking the spacecraft, is characterized by five network systems:

- (1) DSN Tracking System. Generates radio metric data; i.e., angles, one- and two-way doppler and range, and transmits raw data to mission control.
- (2) DSN Telemetry System. Receives, decodes, records, and retransmits engineering and scientific data generated in the spacecraft to Mission Control.
- (3) DSN Command System. Accepts coded signals from mission control via the GCF and transmits them to the spacecraft in order to initiate spacecraft functions in flight.
- (4) DSN Monitor and Control System. Instruments, transmits, records, and displays those parameters of the DSN necessary to verify configuration and validate the network. Provides operational direction and configuration control of the network and primary interface with flight project Mission Control personnel.
- (5) DSN Test and Training System. Generates and controls simulated data to support development, test, training and fault isolation within the DSN. Participates in mission simulation with flight projects.

The facilities needed to carry out these functions have evolved in three technical areas: (1) the Deep Space Stations (DSSs) and the telecommunications interface

through the RF link with the spacecraft is known as the Deep Space Instrumentation Facility (DSIF); (2) the Earth-based point-to-point voice and data communications from the stations to Mission Control is known as the Ground Communications Facility (GCF); (3) the network monitor and control function is known as the Network Control System (NCS).

## I. Deep Space Instrumentation Facility

### A. Tracking and Data Acquisition Facilities

A world-wide set of Deep Space Stations with large antennas, low-noise phase-lock receiving systems, and high-power transmitters provide radio communications with spacecraft. The DSSs and the deep space communications complexes (DSCCs) they comprise are given in Table 1.

Radio contact with a spacecraft usually begins when the spacecraft is on the launch vehicle at Cape Kennedy, and it is maintained throughout the mission. The early part of the trajectory is covered by selected network stations of the Air Force Eastern Test Range (AFETR) and the STDN of the Goddard Space Flight Center.<sup>1</sup> Normally, two-way communications are established between the spacecraft and the DSN within 30 min after the spacecraft has been injected into lunar, planetary, or interplanetary flight. A compatibility test station at Cape Kennedy (discussed later) tests and monitors the spacecraft continuously during the launch checkout phase. The deep space phase begins with acquisition by 26-m DSSs. These and the remaining DSSs listed in Table 1 provide radio communications until the end of the mission.

To enable continuous radio contact with spacecraft, the DSSs are located approximately 120 deg apart in longitude; thus a spacecraft in deep space flight is always within the field-of-view of at least one DSS, and for several hours each day may be seen by two DSSs. Furthermore, since most spacecraft on deep space missions travel within 30 deg of the equatorial plane, the DSSs are located within latitudes of 45 deg north and south of the equator. All DSSs operate at S-band frequencies: 2110-2120 MHz for Earth-to-spacecraft transmission and 2290-2300 MHz for spacecraft-to-Earth transmission. An X-band capability is being readied for future missions beginning in 1973.

<sup>1</sup>The 9-m (30-ft) diam antenna station established by the DSN on Ascension Island during 1965 to act in conjunction with the STDN orbital support 9-m (30-ft) diam antenna station was transferred to the STDN in July 1968.

To provide sufficient tracking capability to enable returns of useful data from around the planets and from the edge of the solar system, a 64-m (210-ft) diam antenna subnet will be required. Two additional 64-m (210-ft) diam antenna DSSs are under construction at Madrid and Canberra and will operate in conjunction with DSS 14 to provide this capability. These stations are scheduled to be operational by the middle of 1973.

## **B. Compatibility Test Facilities**

In 1959, a mobile L-band compatibility test station was established at Cape Kennedy to verify flight-spacecraft/DSN compatibility prior to the launch of the Ranger and Mariner Venus 1962 spacecraft. Experience revealed the need for a permanent facility at Cape Kennedy for this function. An S-band compatibility test station with a 1.2-m (4-ft) diameter antenna became operational in 1965. In addition to supporting the preflight compatibility tests, this station monitors the spacecraft continuously during the launch phase until it passes over the local horizon.

Spacecraft telecommunications compatibility in the design and prototype development phases was formerly verified by tests at the Goldstone DSCC. To provide a more economical means for conducting such work and because of the increasing use of multiple-mission telemetry and command equipment by the DSN, a Compatibility Test Area (CTA) was established at JPL in 1968. In all essential characteristics, the configuration of this facility is identical to that of the 26-m (85-ft) and 64-m (210-ft) diameter antenna stations.

The JPL CTA is used during spacecraft system tests to establish the compatibility with the DSN of the proof test model and development models of spacecraft, and the Cape Kennedy compatibility test station is used for final flight spacecraft compatibility validation testing prior to launch.

## **II. Ground Communications Facility**

The GCF provides voice, high-speed data, wideband data, and teletype communications between the Mission Operations Center and the DSSs. In providing these capabilities, the GCF uses the facilities of the worldwide NASA Communications Network (NASCOM)<sup>2</sup> for all long

<sup>2</sup>Managed and directed by the Goddard Space Flight Center.

distance circuits, except those between the Mission Operations Center and the Goldstone DSCC. Communications between the Goldstone DSCC and the Mission Operations Center are provided by a microwave link directly leased by the DSN from a common carrier.

Early missions were supported by voice and teletype circuits only, but increased data rates necessitated the use of high-speed and wideband circuits for DSSs. Data are transmitted to flight projects via the GCF using standard GCF/NASCOM formats. The DSN also supports remote mission operations centers using the GCF/NASCOM interface.

## **III. Network Control System**

The DSN Network Control System is comprised of hardware, software, and operations personnel to provide centralized, real-time control of the DSN and to monitor and validate the network performance. These functions are provided during all phases of DSN support to flight projects. The Network Operations Control Area is located in JPL Building 230, adjacent to the local Mission Operations Center. The NCS, in accomplishing the monitor and control function does not alter, delay, or serially process any inbound or outbound data between the flight project and tracking stations. Hence NCS outages do not have a direct impact on flight project support. Voice communications are maintained for operations control and coordination between the DSN and flight projects, and for minimization of the response time in locating and correcting system failures.

The NCS function will ultimately be performed in data processing equipment separate from flight project data processing and specifically dedicated to the NCS function. During FY 1973, however, DSN operations control and monitor data will be processed in the JPL 360/75 and in the 1108. In FY 1974 the NCS data processing function will be partly phased over to an interim NCS processor, and finally, in FY 1975, the dedicated NCS data processing capability will be operational. The final Network Data Processing Area will be located remote from the Network Operations Control Area so as to provide a contingency operating location to minimize single point of failure effects on the network control function. A preliminary description of the NCS appears elsewhere in this document.



**Table 1. Tracking and data acquisition stations of the DSN**

DSCC	Location	DSS	DSS serial designation	Antenna		Year of initial operation
				Diameter, m (ft)	Type of mounting	
Goldstone	California	Pioneer	11	26(85)	Polar	1958
		Echo	12	26(85)	Polar	1962
		(Venus) <sup>a</sup>	13	26(85)	Az-El	1962
		Mars	14	64(210)	Az-El	1966
Tidbinbilla	Australia	Weemala (formerly Tidbinbilla)	42	26(85)	Polar	1965
		Ballima (formerly Booroomba)	43	64(210)	Az-El	1973
—	Australia	Honeysuckle Creek <sup>b</sup>	44	26(85)	X-Y	1973
—	South Africa	Hartebeesthoek	51	26(85)	Polar	1961
Madrid	Spain	Robledo	61	26(85)	Polar	1965
		Cebreros	62	26(85)	Polar	1967
		Robledo	63	64(210)	Az-El	1973

<sup>a</sup>A maintenance facility. Besides the 26-m (85-ft) diam. Az-El mounted antenna, DSS 13 has a 9-m (30-ft) diam Az-El mounted antenna that is used for interstation time correlation using lunar reflection techniques, for testing the design of new equipment, and for support of ground-based radio science.

<sup>b</sup>To be shared with STDN until January 1974.

# DSN Command System Mark III-74

W. G. Stinnett  
DSN Systems Engineering Office

*A general description is presented of the DSN Command System software changes that are being implemented to support the Helios and Viking missions. Comparisons are made between the present system (Mark III-71) and the new system (Mark III-74). Included are the reasons for the changes, and the DSN plans to phase all mission support over to the Mark III-74 system.*

## I. Introduction

The DSN Multiple Mission Command (MMC) System has successfully supported the Mariner Mars 1971 (MM71) mission and the Pioneer 10 mission to Jupiter. The system is now supporting the ongoing Pioneer 10 mission, the Pioneer 11 mission to Jupiter, and the Mariner Venus/Mercury 1973 (MVM73) mission. All of these missions have been supported with the same DSN hardware.

The command software provided by the DSN in the Deep Space Stations' (DSSs) telemetry and command processors (TCPs) has been basically the same from mission to mission. The command requirements for each mission have been similar, and thus the software has remained basically the same as that designed for the MM71 mission (hereafter referred to as the DSN Mark III-71 Command System).

The DSS TCP is an XDS 920 computer. The DSN implemented the DSS telemetry and command functions into this computer for all the missions. One of the primary problems in implementing the command portion of the software was timing. These timing problems had to be overcome in the software used during the Mark III-71 era. All the missions supported during this era required the same transmission rate (1 bit/s); thus, the software timing considerations were similar.

The DSN is presently implementing significant changes in the DSN MMC System (the DSN Mark III-74 Command System). The Helios and Viking mission command transmission rates are 8 symbols per second (SPS) and 4 bits/s, respectively. The software timing considerations are significantly increased over those missions supported during the Mark III-71 era. For this reason, the Command System is undergoing extensive software changes.

## **II. Mark III-74—Command System Changes**

### **A. Transfer of System Functions**

The increased command transmission rates from the Mark III-71 to the Mark III-74 era have made it necessary to transfer some command functions from the DSS TCP to the Mission Operations Center (MOC). Figure 1 shows a simplified block diagram comparison of the Mark III-71 and the Mark III-74 Command Systems. One of the prime time-consuming functions provided by the TCP in the Mark III-71 System was command stack manipulation. The TCP sorted, arranged, and searched the command stack frequently for the Mark III-71 System. The Mark III-74 System has transferred these functions to the MOC.

### **B. MOC Software Changes**

In the Mark III-71 Command System, the MOC software basically provided a remote terminal capability to the TCP. Under operator control, the MOC software generates high speed data (HSD) blocks of command data. The data are transmitted to a DSS TCP, where they are placed in the TCP command stack. A verification block is returned, and the MOC performs a bit-by-bit comparison with what was transmitted. Failure to verify results in automatic retransmission of the command block. An enable block is generated, either automatically after successful verification or under operator control, and transmitted to the DSS TCP. Again a verification block is returned, and the MOC software performs a bit-by-bit verification on the enable block. After successful transmission of the command from the DSS to the spacecraft, the TCP constructs a command confirmation HSD message and sends it to the MOC. The MOC software displays the command confirmation to the operator.

In the Mark III-74 Command System, the MOC software provides direct control of the contents of the TCP command stack. The operator controls the contents of the command queue in the MOC. The MOC software then can, via HSD messages, force the TCP stack contents to be consistent with the command queue in the MOC. Under operator control, commands are entered into the command queue. When the operator enables commands in the queue, the commands are "eligible" for transmission to the DSS TCP. The commands are sent to the DSS TCP and placed in the TCP per direction in the HSD message. An acknowledge message is constructed at the TCP and sent to the MOC. The data are compared against the contents of the queue. Failure to compare results in automatic retransmission to the TCP. After successful transmission of a command from the DSS to the spacecraft, a message

is sent from the TCP to the MOC. The MOC compares this message with the contents of the queue. The command is then marked "successfully confirmed" and displayed to the operator.

The basic changes to the MOC software are the command queue concept and the ability to directly control the contents of the TCP command stack.

### **C. TCP Software Changes**

In the Mark III-71 Command System, the TCP sorts, arranges, and searches the commands in the command stack. Upon receipt of commands from the MOC, the TCP software sorts priority and timed commands into basically two stacks. When enable messages are received from the MOC, the TCP software is required to search the complete stack to ensure proper command enabling. When interrupts (every bit time) are received that tell the software that the hardware is ready to transmit the next command, the complete stack is searched in an attempt to find a command that is eligible (enabled and/or timed) for transmission.

In the Mark III-74 Command System, the TCP software is no longer required to arrange and search the TCP command stack. The MOC software is required to keep the stack in logical order such that the TCP only has to "look" at the top command in the stack. The TCP stack is arranged into four modules and an active register. The stack is loaded by module via HSD block from the MOC. The MOC software is required to keep the stack modules updated consistent with the command queue in the MOC. The only command eligible for transmission to the spacecraft is the top command in the number one module. Note that an enable message is no longer required from the MOC. There are two types of commands in the Mark III-74 System: (1) timed commands, and (2) nontimed commands. A nontimed command will be transmitted immediately when it occupies the top command in the number one stack module. A timed command will be transmitted when the GMT reaches the command transmit time and the command occupies the top command in the number one stack module. The command is transmitted to the spacecraft by "moving" it to the active register. Upon successful transmission of the command from the DSS to the spacecraft a HSD message is constructed by the TCP and sent to the MOC for notification of confirmation.

The primary change to the TCP software for the Mark III-74 System is the deletion of stack arranging and searching. This has allowed the capability for the

software to perform more important functions at the higher command bit rates. The same types of hardware checks provided at 1 bit/s for the Mark III-71 System can be provided for the Helios command rate of 8 SPS.

### **III. Mark III-74 Command System— Mission Support Plans**

It is desirable from an operational and sustaining engineering viewpoint that all missions supported by the DSN be supported by the same DSN Command System. An

operational consideration is that two-system operation can lead to confusion when different characteristics exist. Another operational consideration is that personnel training is simplified when one system is used. The sustaining engineering consideration is, of course, less cost. For these reasons, the DSN plans to phase all mission support over to the Mark III-74 Command System. The present plans for phase-over of all support is shown in Table 1. All missions will be phased over after critical events are complete. The Helios and Viking test periods and flight operations will be supported entirely by the Mark III-74 Command System.

**Table 1. Mission support phase-over plans to the  
Mark III-74 command system**

Mission	Test period	Flight operations
MVM73	May-June 1974	July 1974
Pioneer 10	January-August 1974	September 1974
Pioneer 11	Same as Pioneer 10	January 1975

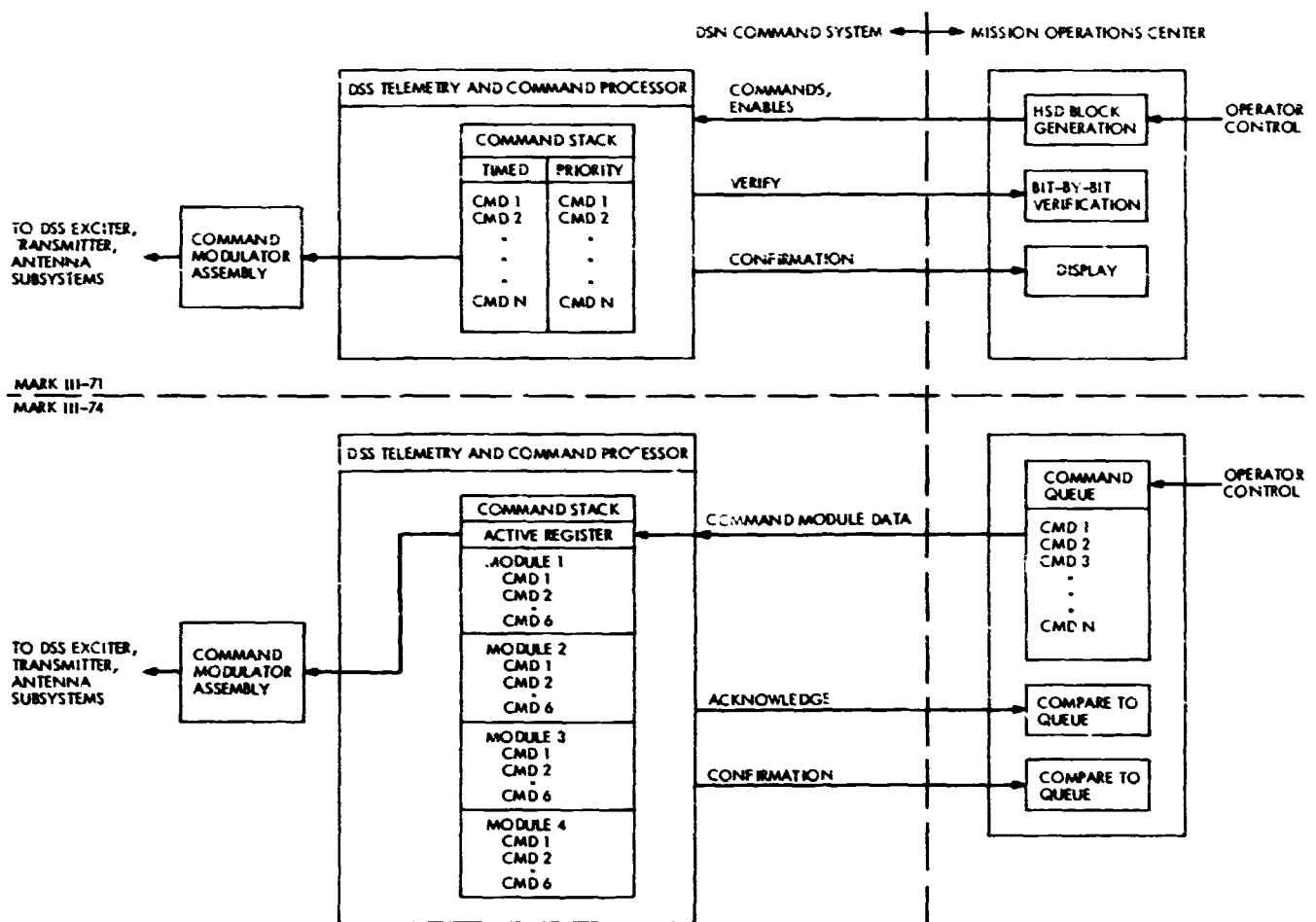


Fig. 1. Comparison of Mark III-71 and Mark III-74 command systems

# Viking Mission Support

D. J. Mudgway

DSN Systems Engineering Office

D. W. Johnston

Network Operations Office

*This article describes the Network Operations Plan for Viking 1975 and includes some DSN support requirements unique to Viking which have resulted in unusual attention to Deep Space Station hardware failure mode configurations. Also discussed are samples of the single point failure strategies incorporated in the Viking 1975 Deep Space Station telemetry hardware configurations. The rationale for the implementation of 100-kW transmitter capability at DSSs 43 and 63 is also given.*

## I. Network Operations Plan for Viking

The publication of the Network Operations Plan for Viking 1975 (Ref. 1) constitutes a further milestone marking the initial point at which the DSN operations personnel in general became directly involved with the Viking Project. This document interprets all the Project requirements levied on the Deep Space Network to support the Viking 1975 mission. It specifies the required human and technical interfaces and the manner in which the DSN capabilities, described in the DSN Preparation Plan for Viking 1975 Project (Ref. 2), will be employed by Network Operations to support Viking pre-launch and flight operations activities. Finally, this constitutes the prime reference regarding the Viking DSN training, testing, configurations, procedures, and operations, for all personnel in the DSN Operations Office.

## II. Unique Viking Requirements

In previous missions, during the limited critical and/or extremely high-activity periods, the requirement for hardware failure backup has been met at the Deep Space Stations by scheduling a second station in parallel and/or the use of complete parallel strings of equipment readied in a "standby" state.

The Viking 1975 mission is unique in this respect in that: (1) the critical/high-activity periods will extend for up to 5 months continuously, (2) three DSSs at each location will be required for 2 months, 7 days per week (no backup stations) (see Fig. 1), and (3) the 5-month period requires the simultaneous use of six telemetry hardware strings out of a total station complement of six strings (no backup strings) at each 64-m-antenna DSS.

Another unique characteristic of the Viking mission is that, during the planetary operations phase, four spacecraft will be within the beamwidth of a single DSS antenna, and the 64-m subnet will be required to track up to three spacecraft simultaneously and to provide one uplink and process six telemetry subcarriers. As practically all of the Deep Space Station equipment will be in use during three-spacecraft operations, the configurations defined in the Network Operations Plan have been designed to include new extensive "cross-switching" capabilities. These greatly increase the flexibility over current configurations and provide optimum use of the equipment for data processing in the case of an equipment failure. Also, the conjoint 26-m-antenna stations provide uplink and backup telemetry hardware, accessible from their conjoint 64-m-antenna stations. (DSSs 11 and 14 have the same capability, using a microwave link.)

### III. Deep Space Station Telemetry Requirements for Viking

The 64-m-antenna DSS Viking 1975 telemetry configurations are required to be capable of processing the types of data shown in Tables 1 and 2 from two Orbiters and one Lander simultaneously.

### IV. Configuration Rationale

Because of the difference in capabilities between the 26-m co-located, 26-m conjoint, and 64-m DSSs and also the difference between the hardware strings inside the DSSs, some configuration rules or guidelines became evident when the Viking configurations were formulated. Examples of some basic rules are:

- (1) *Rule:* The 64-m-antenna DSS should be regarded as prime telemetry receiver for all three spacecraft.  
*Reason:* Greater antenna gain of 64-m DSS.
- (2) *Rule:* The 64-m-antenna DSS should be configured to provide the prime Orbiter uplink and receive that spacecraft telemetry on the Block IV receiver/exciter.  
*Reason:* The Block III and Block IV receiver/exciter subsystems are separate subsystems with no coherent, common reference, and the X-band receiver (Block IV only) must be coherent with the S-band uplink, which is being multiplied in the spacecraft to provide the S-band and X-band downlinks.
- (3) *Rule:* Only one Orbiter should be scheduled to provide X-band ranging, for a complete station pass.

*Reason:* To switch from one Orbiter to the other would involve a double station uplink transfer of the two Orbiters between the 26-m, Block III and 64-m Block IV exciters, causing approximately 60 min loss of command, metric, and ranging data on each transfer.

As these rules emerged with the development of the detailed configurations, it became apparent that certain spacecraft/ground receiver configurations had logically evolved. These will vary with the single Orbiter, Orbiter and Lander, Orbiter and Orbiter, or Orbiter, Lander, and Orbiter situations encountered during the mission. The Network Operations Plan for Viking contains a total capabilities configuration, standard configurations for each of the spacecraft combinations, plus approximately 50 alternate backup configurations to cover specific failures. Each configuration is designated by a code number. The samples used here to illustrate the concept are for the Orbiter/Lander/Orbiter situation.

### V. 64-m-Antenna Telemetry Configurations for Viking

The DSS 14 Viking 1975 hardware capabilities are shown in Fig. 2. The Orbiter/Lander/Orbiter standard configuration is presented in Fig. 3.

### VI. Failure Strategy and Configurations

The single point failure recovery is presented in the Network Operations Plan for Viking in the form of tables, listing the reconfiguration to be applied in the case of failure of each receiver, subcarrier demodulator assembly (SDA), symbol synchronizer assembly (SSA), block decoder assembly (BDA), data decoder assembly (DDA), and telemetry and command processor (TCP).

Experience has shown that an assembly failure rarely occurs during real-time tracking, but quite often is discovered during the pre-track calibrations. The tables referred to have a column labeled "Resultant Constraint," which indicates what data, if any, are changed (e.g., lower bit rate) or lost (e.g., X-band doppler and ranging deleted) when the reconfiguration is complete. There is no listing of amount of data lost during the reconfiguration resulting from real-time re-initialization or reloading of the software. The example shown in Fig. 4 would be applicable in the event of failure of Receiver No. 1, which is listed under Code 31. In this case, the receiver is replaced by Receiver No. 4, which is normally receiving the X-band



signal, so that the X-band data are "given up" in favor of the S-band telemetry.

The second example, as shown in Fig. 5, would be applicable in the event of failure of SDA 3, which is listed under Code 36. In this case, SDA 3 is replaced by SDA 7 (in the 26-m conjoint DSS). During planetary operations, the conjoint 26-m DSS (or DSS 11 at Goldstone) would normally be scheduled to support in parallel to supply the second uplink. At DSSs 43 and 63, the receiver output (subcarrier plus data) is hardwired to the SDA at DSS 42 or 61, and the SDA output is hardwired back to the 64-m SSA. At DSS 14/11, these functions are carried out via a microwave link.

## VII. Rationale for Implementation of 100-kW Transmitter Capability at DSSs 43 and 63

The DSN response to the Viking requirement for 100-kW transmit capability at the overseas DSSs (Ref. 3, p. 2300.2) is given in the NASA Support Plan (Ref. 4, p. 430.1) as follows: "... at DSSs 43 and 63, 100 kw transmitter will provide dual links at 10 kw each." At the time this was written, the requirement and its response were principally oriented toward the need for simultaneous commanding from a single station to two spacecraft (Orbiter/Orbiter or Orbiter/Lander).

Early in 1973, the Tracking and Data System met with the Project and indicated that the dual-carrier, single-transmitter mode of operation presented technical problems which were not fully understood and recommended that the "dual-carrier" mode be considered as a "mission enhancement" feature only in all future mission planning. The prime mission mode was to be based on the use of two subnets, with the simultaneous command requirement being met with two stations, i.e., a 64-m and a 26-m DSS at each longitude. This decision is reported in Ref. 5.

In preparing the FY74/75 budget, it was proposed that the "mission enhancement" feature of Viking support be dropped by deferring the 100-kW transmitters to a post-Viking era.

Evaluation of the consequent impact on the Viking mission planning and flight support showed that, irrespective of the dual-carrier requirement, there remained a need for a 100-kW transmit capability at DSSs 43 and 63, as well as the 400-kW transmit capability at DSS 14, to avoid unacceptable risks and/or constraints to Viking Lander operations (Mission B particularly) due to any of the following causes:

- (1) Worst-case telecommunications performance
- (2) Adverse landing slopes (20 deg)
- (3) Random Lander orientation
- (4) High-gain antenna or computer malfunction
- (5) Southerly landing sites (30° S)
- (6) Need for real-time retargeting of landing site
- (7) Late launch in the secondary mission

The dominant factor influencing all of the foregoing effects is the most recent Lander low-gain antenna patterns measured on a 3-scale model. These patterns show severe distortion due to adjacent hardware on the Lander structure, which results in large negative gain over substantial portions of the antenna field of view. Most of the conditions described above could result in Earth look vectors which lie in these negative gain areas, and hence require a high-power transmit capability to compensate for the antenna gain deficiencies.

Typical low-gain antenna radiation patterns discussed above were analyzed at gain levels of -3 and -10 dB. These are the levels required to support the command link for 20- and 100-kW transmitters. This analysis is summarized in Fig. 6, which shows the Lander cone and clock angle regions where the low-gain antenna coverage is adequate to support the command link.

The history of the look vector to Earth as seen from the Lander for a 30°S latitude landing site is also shown in Fig. 6. The dashed line represents the nominal Earth track as seen from the Lander early in the mission. Time ticks are located on the nominal track to provide a relative time reference. The envelope about the nominal track considers a  $\pm 20$ -deg adverse surface slope, +20 deg uncertainty in the landed azimuth of Lander leg 1, and the worst case relative Earth/Mars geometry over the 90-day landed mission.

The shaded areas within the Earth track envelope represent those areas where the Lander antenna gain is not sufficient to support the command link with a 100-kW transmitter. The area which lies between the shaded contour and the upper contour line is that Lander cone/clock angle region where command capability exists with a 100-kW transmitter but not with 20 kW. Command capability exists with a 20-kW transmitter for the Lander cone/clock angle region above the second contour.

Obviously, the opportunity to command the Lander over the low-gain antenna is severely limited for the 30°S latitude landing site. Only one half of the total daily Earth view period is available for Lander command with a 20-kW transmitter.

The command link performance for this same set of conditions (30°S latitude) is given in Fig. 7 for no-slope conditions and in Fig. 8 for 20-deg slope conditions.

In Fig. 7, the performance is shown for the time of day when Earth has risen to a 15-deg elevation angle above the local horizon. No adverse slope is considered. At this time of day, the Lander cone angle of the look vector to Earth is 105 deg, or conversely, the aspect angle of Earth as seen from the Lander antenna boresight is 75 deg.

The curve labeled "nominal" was generated from the free space Lander gain pattern at an aspect angle of 75 deg. This curve shows a margin of approximately 3 dB above that required with 20 kW of transmitter power. The best and worst curves were developed from the installed 3-scale model antenna pattern data as follows: The curve labeled "best" was derived from the highest Lander gain found on the installed patterns at an aspect angle of 75 deg. Because of the uncertainty in the landed Lander azimuth orientation and the desire to place no further constraint on the time of day at which a command session can occur, the entire Lander clock angle region (0-360 deg) was considered.

The curve labeled "worst" was derived as explained above, except that the lowest Lander gain at an aspect angle of 75 deg over the total clock angle region was considered.

Figure 8 reflects the same conditions as defined for Fig. 7, except that a 20-deg adverse surface slope was considered. The nominal, best, and worst curves consider Lander antenna gain at an aspect angle of 95 deg.

The curves shown in Figs. 7 and 8 indicate that the 20-kW capability is inadequate to meet the required command link margins under the worst-case conditions considered.

These data were presented in overview by the Martin Marietta Corporation (MMC) at the Viking Lander Critical Design Review in Denver on September 18-20 and in detail to the Viking Telecommunications Working Group at MMC in Denver on September 21. Both these organizations, as well as the Viking Project Manager, agreed that the 100-kW transmit capability at the overseas stations was a necessary element in the DSN support planned for the Viking mission. Accordingly, the current revision to the Viking Support Instrumentation Requirements Document, dated September 17, 1973, deletes the dual-carrier requirement, but restates the requirements for the 100-kW capability at DSSs 43 and 63 for the purposes described above. Implementation of this capability has since been reinstated and is proceeding toward an operational date of January 1, 1976.

## References

1. Network Operations Plan for Viking 75 Project, JPL Document 614-21, Nov. 1, 1973 (JPL internal document).
2. Deep Space Network, Preparation Plan for Viking 75 Project, JPL Document 614-20, Rev. A, Nov. 15, 1973 (JPL internal document).
3. Support Instrumentation Requirements Document (SIRD) for Viking, July 1, 1971 (JPL internal document).
4. NASA Support Plan (NSP) for Viking, Rev. 0, May 1, 1972 (JPL internal document).
5. Mudgway, D. J., and Johnston, D., "Viking Mission Support," in *The Deep Space Network Progress Report*, Technical Report 32-1526, Vol. XVII, p. 9, Jet Propulsion Laboratory, Pasadena, Calif., Oct. 15, 1973.

**Table 1. Viking Orbiter (VO) channel assignments**

TLM channel	Designator	Description	Bit rate	Subcarrier frequency, kHz
Low	B	Uncoded engineering data	8 $\frac{1}{3}$ or 33 $\frac{1}{3}$ bits/s	24.0
High	C	Coded (32, 6) science data	1, 2, 4, 8, or 16 kbits/s	240.0
	A	Uncoded science data	1, 2, or 4 kbits/s	240.0

**Table 2. Viking Lander (VL) channel assignments (for VL/DSN S-band direct link)<sup>a</sup>**

TLM channel	Designator	Description	Bit rate, bits/s	Subcarrier frequency, kHz
Low	B	Uncoded engineering data	8 $\frac{1}{3}$	12.0
High	A	Coded (32, 6) science data	250, 500, and 1000	72.0

<sup>a</sup>The VL/VO UHF link at 4 or 16 kbits/s will not be received by the DSSs.

Relay "feedthrough" data (VL to VO) during preseparation and landing will be received at the DSSs via the VO subcarrier and are regarded as VO data by the DSN.

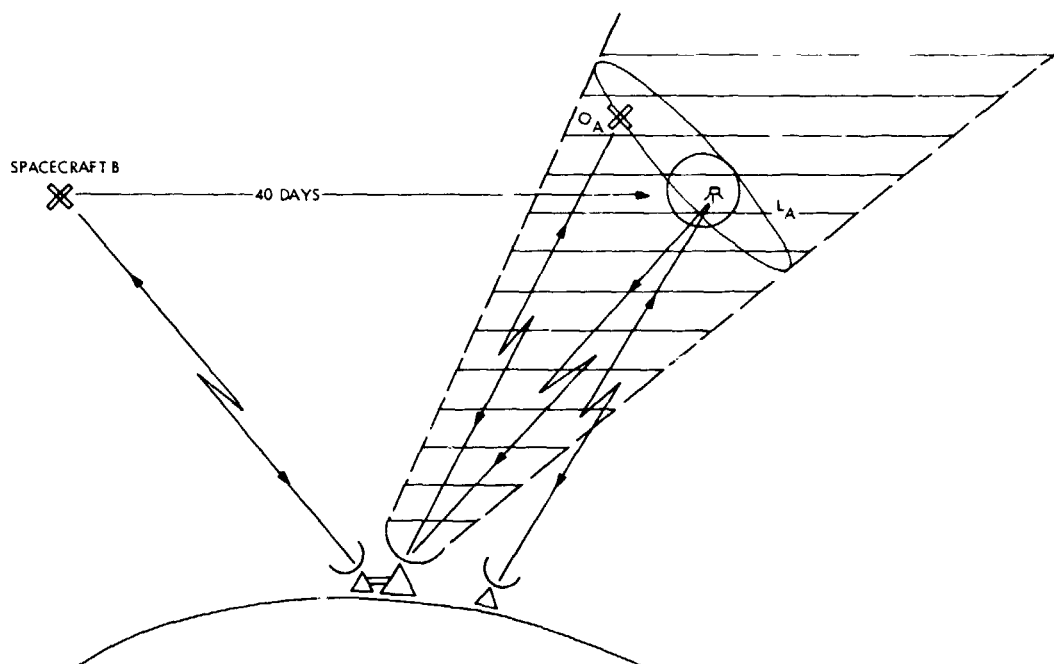
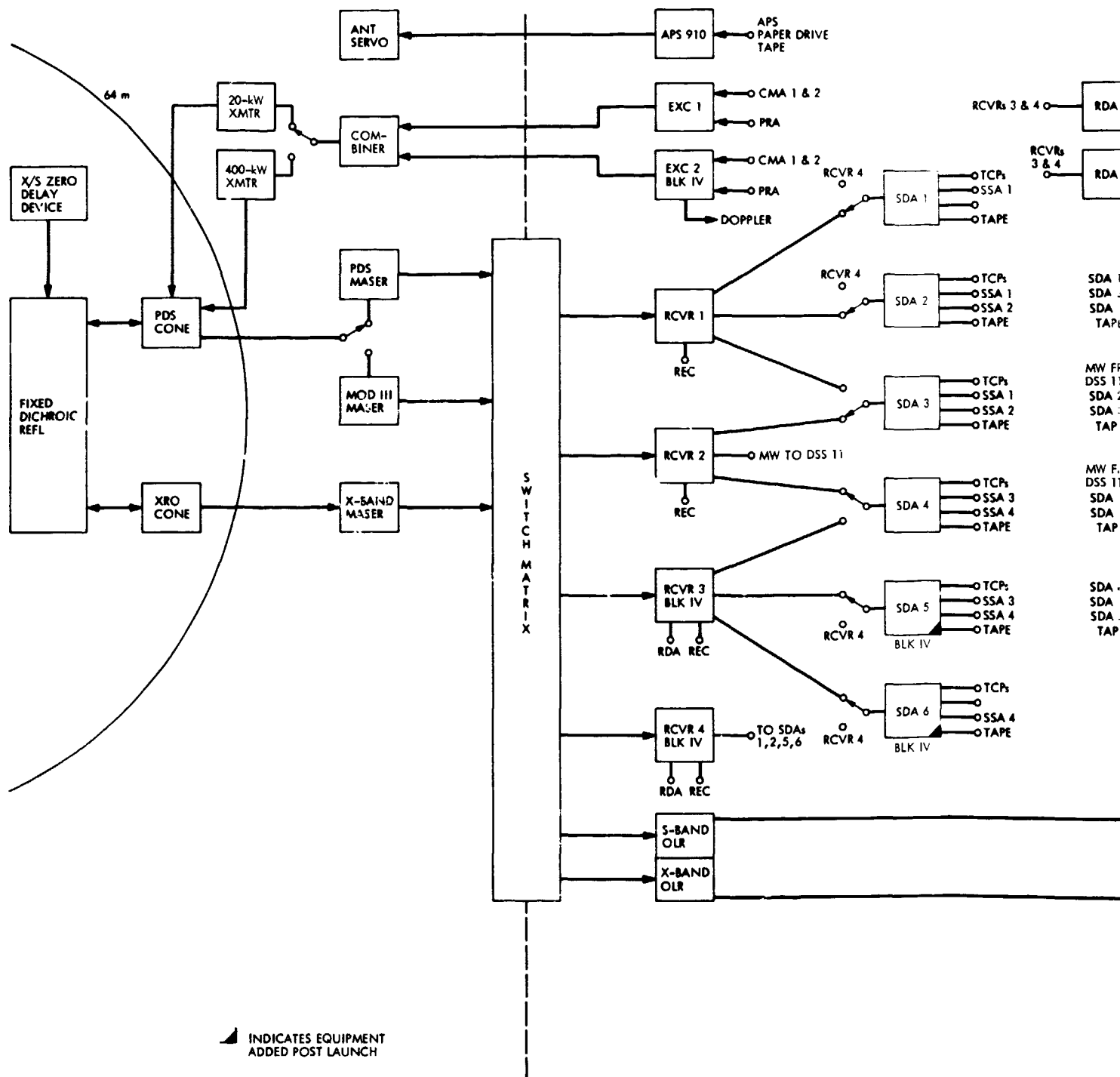


Fig. 1. Three-station requirement





PRECEDING PAGE BLANK NOT FILMED

JPL TECHNICAL REPORT 32-1526, VOL. XIX

WOLFOUT FRAME

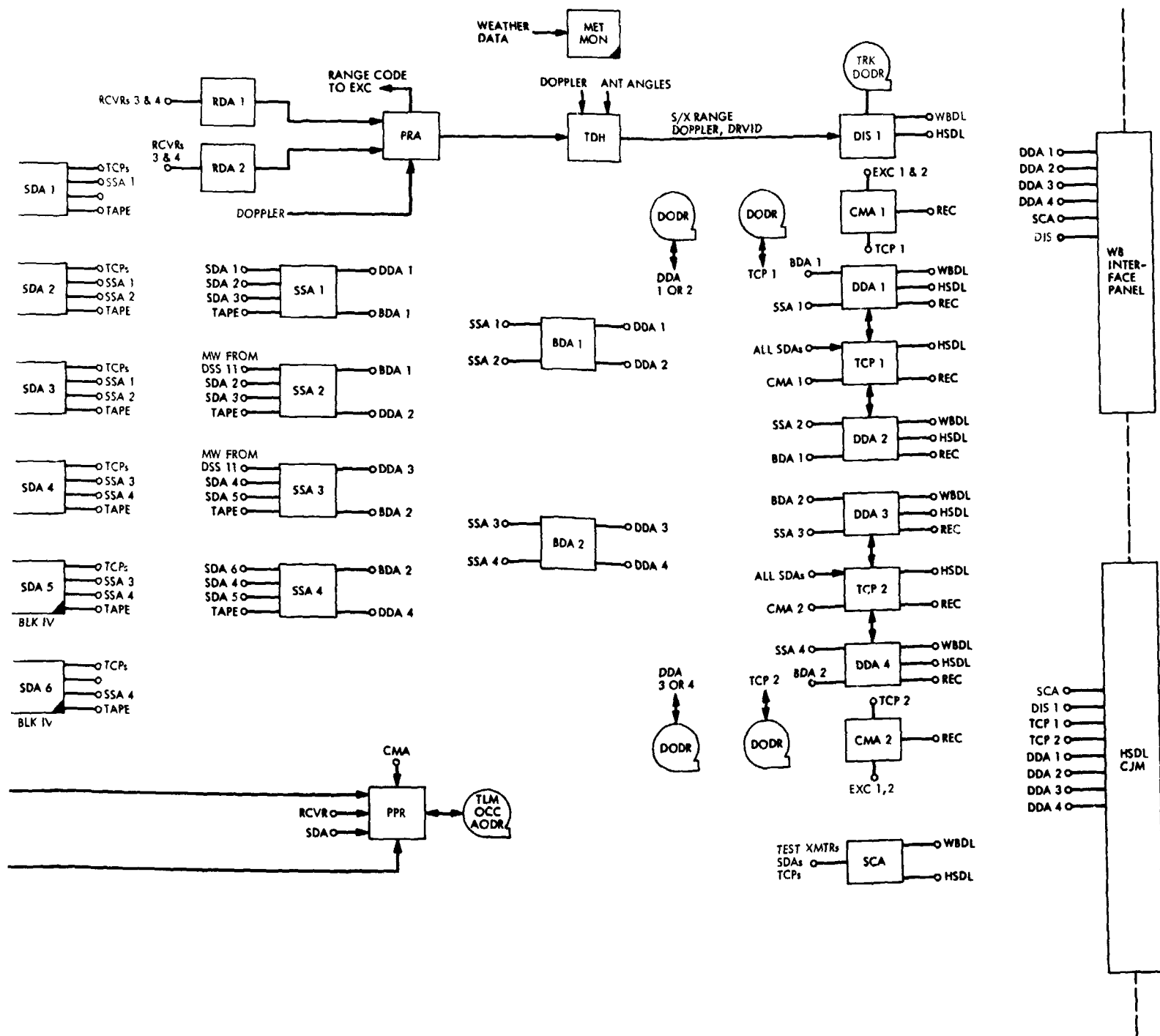
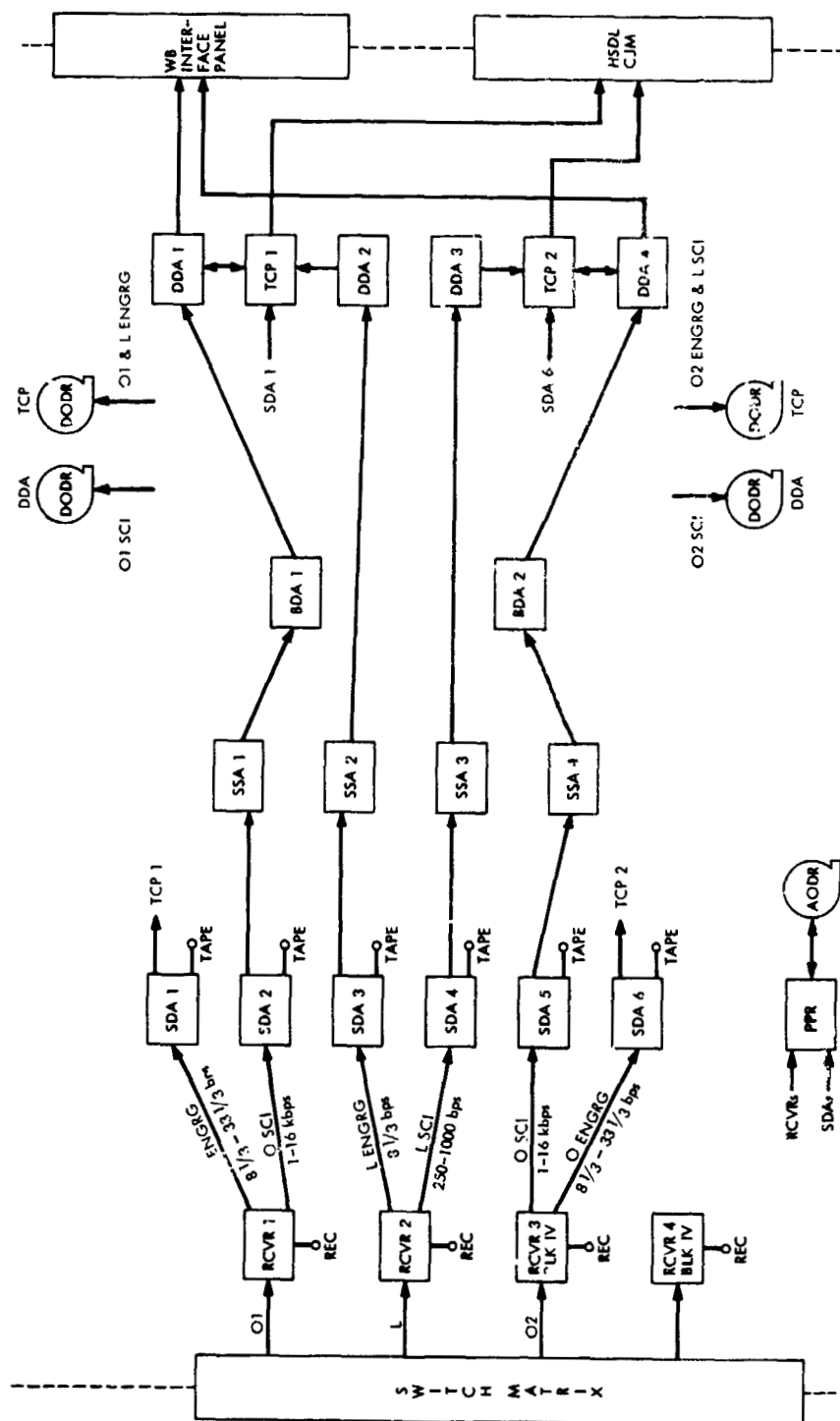


Fig. 2. DSS 14 Viking hardware capabilities







CODE	SPACECRAFT	RECEIVER	DATA TYPE	SDA	SSA	SDA	SSA	SDA	SSA	SDA	SSA	TCP
30	ORBITER 1	1	ENGINEERING	1	0	0	0	0	0	0	0	1
			SCIENCE	2	1	1	1	1	1	1	1	
	LANDER	2	ENGINEERING	3	2	0	2	0	2	0	2	2
			SCIENCE	4	3	0	3	0	3	0	3	
	ORBITER 2	3	SCIENCE	5	4	2	4	2	4	2	4	2
			ENGINEERING	6	0	0	0	0	0	0	0	

Fig. 3. Standard planetary configuration, Orbiter/Lander/Orbiter, Code 30

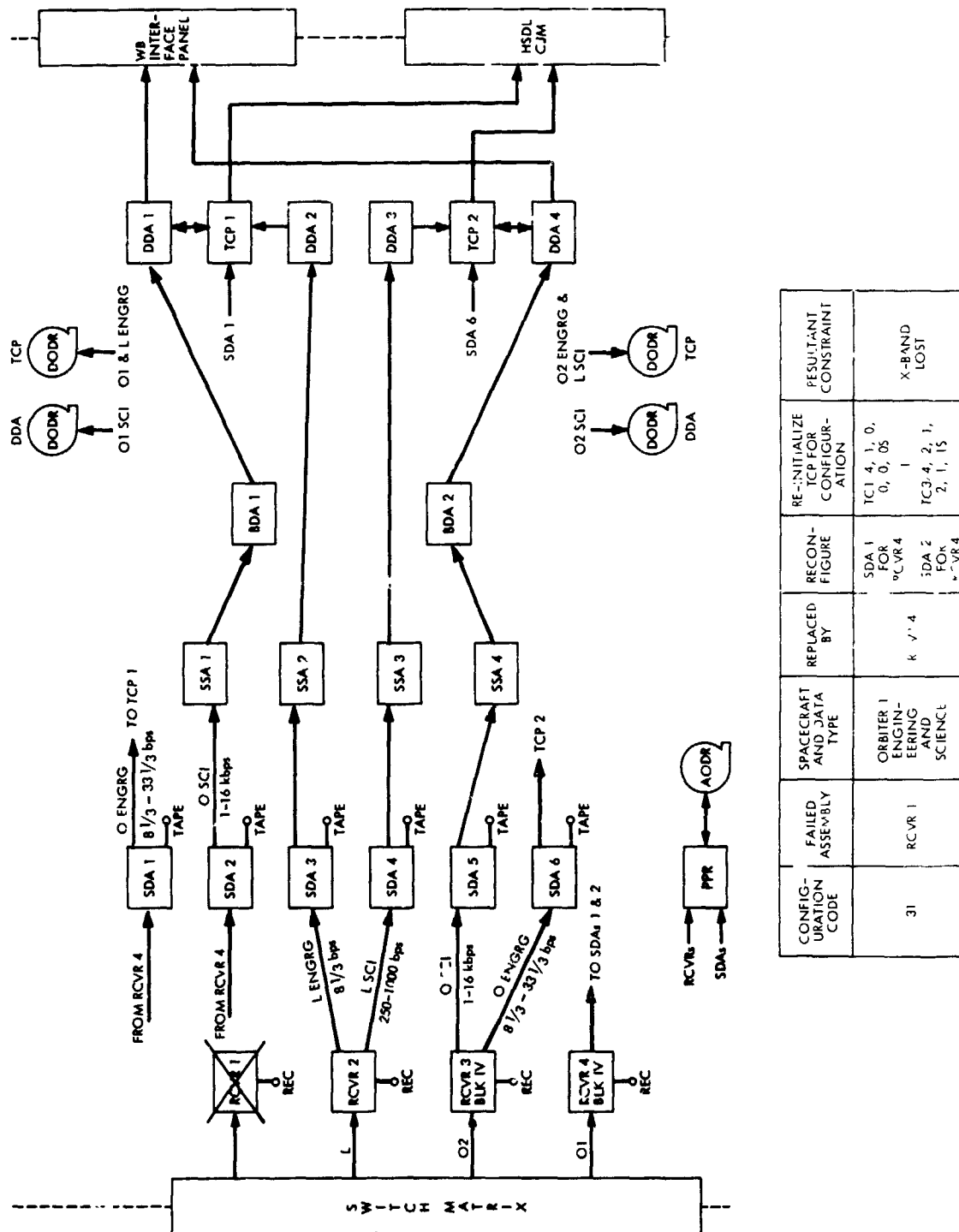
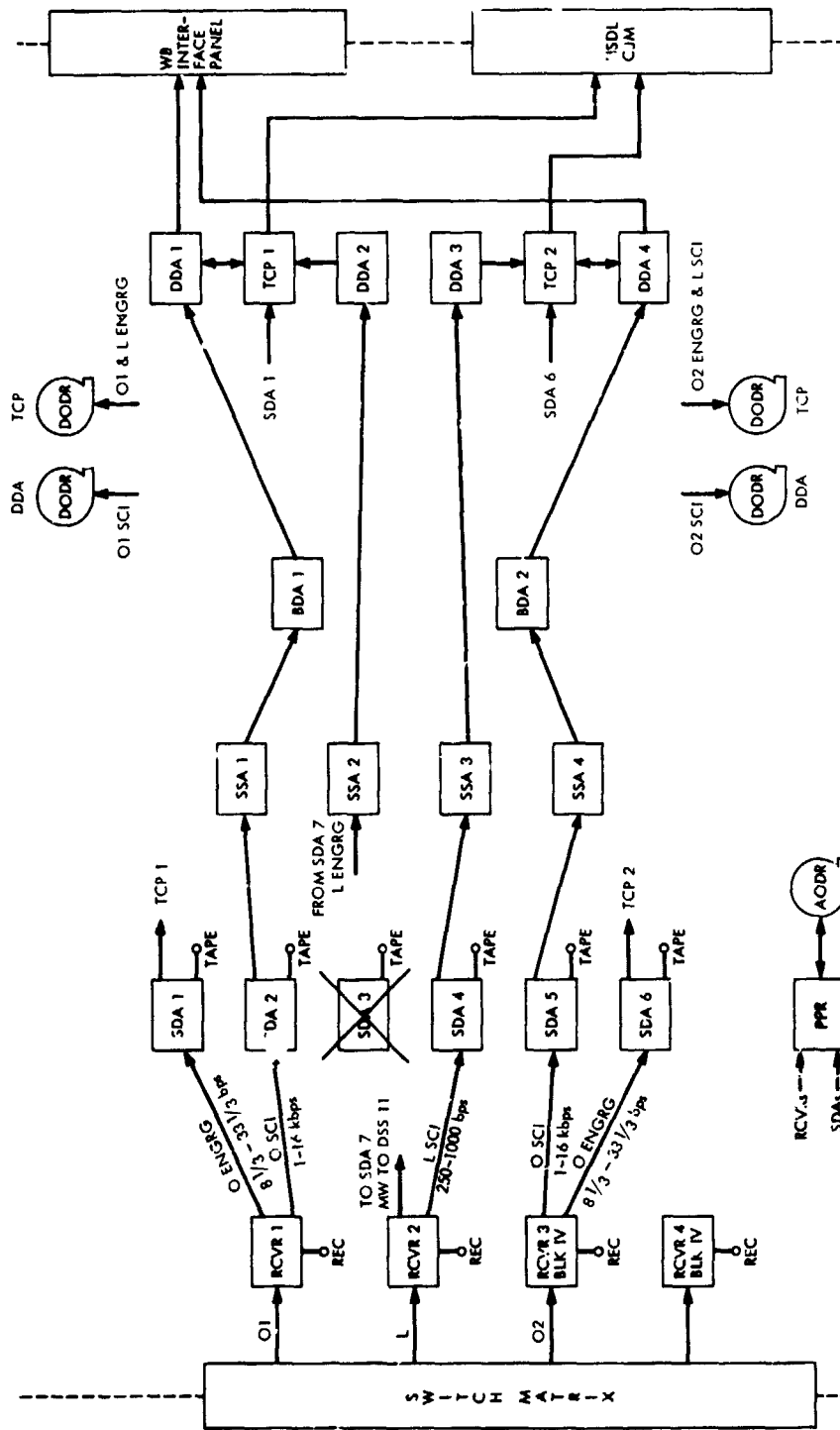


Fig. 4. Failure strategy configuration, Orbiter/Lander/Orbiter, Code 31



CONFIGURATION CODE	FAILED ASSEMBLY	SPACECRAFT AND DATA TYPE	REPLACED BY	RECON-FIGURE	RE-INITIALIZE TCP FOR CONFIGURATION	RESULTANT CONSTRAINT
36	SDA 3	LANDER ENGINEERING	SDA 7	SDA 7 FOR RCVR 2	TC2/2, 7, 2, 1, 0, 25	24 m DSS LOSES ONE SDA
	NOTE SDA 7 AND 8 ARE LOCATED AT CONJOINT 26-m STATIONS FOR DSS 43/63 AND AT A DSS 11 FOR DSS 14.					

Fig. 5. Failure strategy configuration, Orbiter/Lander/Orbiter, Code 36

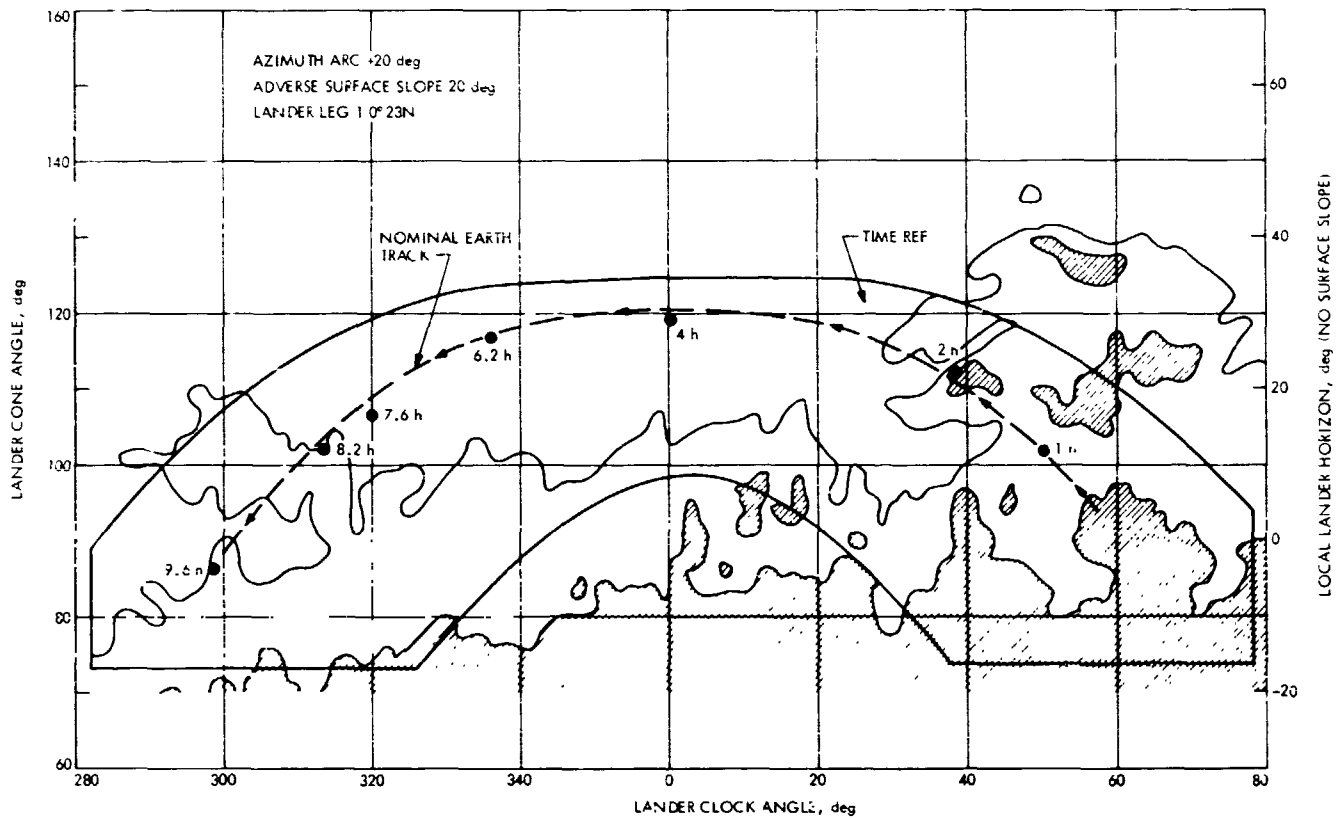


Fig. 6. Earth track envelope (30°S latitude)

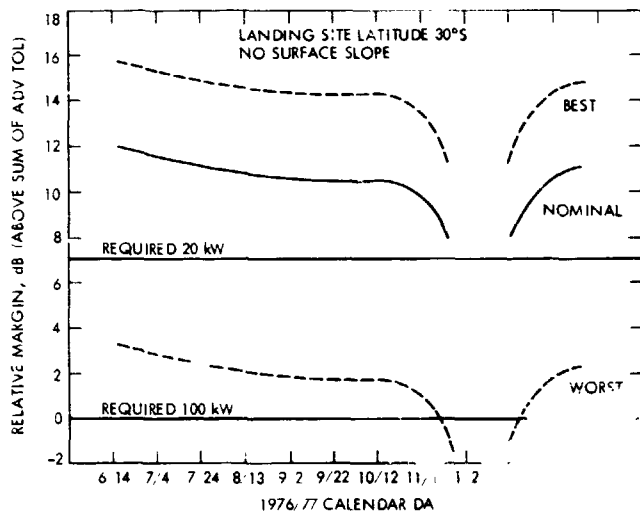


Fig. 7. Viking Lander command margin (Earth elevation = 15 deg, cone angle = 105 deg)

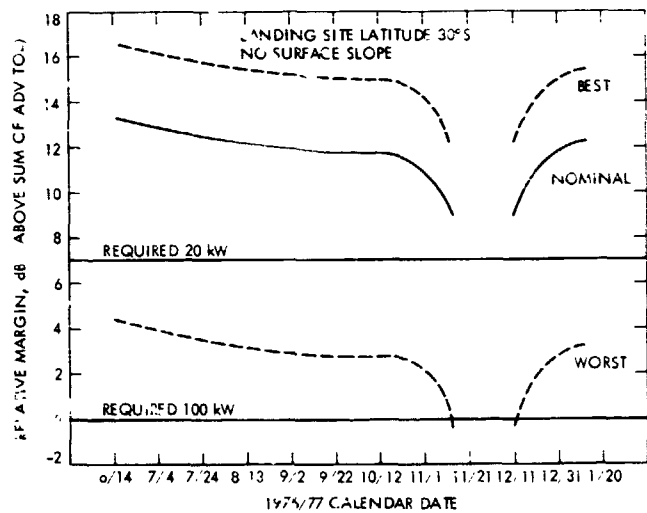


Fig. 8. Viking Lander command margin (Earth elevation = 25 deg, cone angle = 115 deg)

# Pioneer 10 and 11 Mission Support

R. B. Miller

DSN Systems Engineering Office

*This article describes significant aspects of the successful Pioneer 10 encounter of the planet Jupiter.*

## I. Encounter Summary

At the time of writing, Pioneer 10 had completed all but 1 week of the 60-day encounter of the planet Jupiter. The Jupiter environment was found to be much more complex and interesting than had been anticipated. The field and particle environment is not simply a dipole field with trapped particles interacting with the solar wind in a semi-static fashion. Tremendous fluctuations in the extent of the bow shock were observed, apparently related to the changes in intensity of the solar wind. Complex structure was observed inside of the bow shock, and a radiation intensity 1000 times higher than is considered lethal to a human being, although the actual magnetic field strength measured was at the lower end of the preflight range of estimates.

Closest approach to Jupiter was reached at 02 25:19 Greenwich mean time on December 4, 1973, at a range of 2.86 Jupiter radii, 203,250 km from the center of the planet (the radius of the visible disk is about 71,000 km), or 132,250 km from the visible surface. The spacecraft appears to have experienced nearly the maximum radiation dose it could take without catastrophic damage to equipment and instruments. Temporary (reversible)

damage was experienced in some areas such as in the ultraviolet spectrometry, and mild effects on the radio subsystem were apparent as shifts in the on-board oscillator frequency and receiver rest frequency. The asteroid/meteoroid detector appears to have suffered permanent damage in its optics. There was no loss of primary science data due to the radiation effects.

The occultation experiment was successful; an ionosphere was detected on the moon Io, and all data were obtained during the entry and exit phases of the Jupiter occultation. The occultation experiment seeks to determine atmospheric characteristics by ground-based measurement of the effects on the S-band radio link as it transmits through the atmosphere. The Jupiter atmosphere is apparently very complex, and much analysis by the experimenter will be necessary to model the observed effects.

The imaging photopolarimeter returned many intriguing pictures of the planet. The radiation measurements by other instruments peaked at something like 400 million 30-MeV electrons and 4 million 3-MeV protons per square centimeter per second. The temperature measurements showed that the planet radiates about

2½ times the thermal energy it receives from the Sun and that there is no significant difference between daytime and nighttime temperatures.

## II. Ground System Performance

Besides being the first spacecraft to fly by the planet Jupiter, and the first to utilize nuclear power, the Pioneer mission had another unique aspect which reflected heavily on the ground system: the flying of a complex planetary encounter at a tremendous distance from Earth, and therefore a long round-trip light time, without an on-board flight sequencer. Virtually the entire encounter sequence had to be controlled by ground commands, with a 92-m round-trip light time before the effects of transmitted commands could be observed. Between November 4, the start of Jupiter encounter, and December 14, over 13,000 commands were sent to the Pioneer 10 spacecraft. By DSN count, 1,712 commands were sent on the day of periapsis passage alone, which corresponds to a 44% service rate for the command system, considering that each command is 22 s long and that there are 56,400 s in a day. This means that commands were radiating the day of periapsis about 4 min out of every 9, or a command was transmitted an average of every 50 s the entire day.

The high level of command loading and the potentially serious effect of interruptions in command capability on the encounter sequence were recognized, and the primary activity in preparing the ground system for this encounter was to seek means to improve total command reliability. Improvement of the command system reliability involved making very minor changes in DSN software, but there were no hardware changes. Improvement in reliability came principally from changes in procedures, heavy training activity, and providing maxi-

mum redundancy available from the existing implementation. The most important two factors in achieving a significant increase in command reliability were first, getting the Project personnel to use the existing command capabilities in a consistent and optimized mode—i.e., switching from priority commands to timed commands and using command file capabilities in the Mission Control and Computing Center (MCCC) 360/75; and, second and most important, ensuring that all personnel in each element of the Ground Data System understood the importance of command reliability to the success of the mission.

The fruits of the preparation efforts were exceptional ground system reliability during the 60 days of encounter. Prior to the encounter, there had been an interruption to commanding an average of about one every 30 h of heavy command activity. From November 4 to December 20, with the large volume of commanding described, there were only six such interruptions caused by DSN hardware, software, or procedural problems, and, fortunately, none of these failures caused a loss of science data.

A further aspect of the spacecraft design that reflected on ground system reliability was the lack of an on-board data recording system to allow for data playback. The data received in real time at the DSS were the only data acquired. In this regard, the telemetry system reliability performance was also excellent, with only a few minutes of data lost on a single day during encounter (November 9), when several antenna stoppages were experienced.

Therefore, with a statistical sample of one, the capability of having a highly successful planetary encounter using a low-cost spacecraft with limited automatic operation and heavy reliance on ground system reliability was demonstrated.

# Summary Report on the Mariner Venus/Mercury 1973 Spacecraft/Deep Space Network Test Program

A. I. Bryan  
DSN Systems Engineering Office

*The Mariner Venus Mercury 1973 (MVM'73) Spacecraft/Deep Space Network (DSN) compatibility test program consisted of three phases of testing. Subsystem design, system design, and system verification tests were performed at JPL and Cape Canaveral. Preliminary design tests, initiated in late 1971, preceded the formal compatibility test program that culminated in final verification of DSN/MVM'73 Spacecraft compatibility on October 23, 1973. This report describes the tests and test results that provided the basis for establishment and continuous verification of DSN MVM'73 Spacecraft compatibility.*

## I. Introduction

The initial efforts to establish DSN/MVM'73 Spacecraft compatibility consisted of an intensive series of tests to determine the Telemetry and Command Data Handling (TCD) Subsystem performance for MVM'73 telemetry modes. The tests were performed in late 1971 at the Compatibility Test Station (DSS 71), the Compatibility Test Area (CTA 21), and the Telemetry Development Laboratory (TDL) utilizing telemetry simulators and test software.

Preliminary design tests utilizing MVM'73 Spacecraft components were performed at CTA 21 and TDL during the early part of 1972. These tests were accomplished with TCD software that consisted of modified Mariner Mars 1971 (MM'71) operational software and revised TCD test software.

Phase I of a three-phase test program to establish DSN/MVM'73 Spacecraft compatibility was performed with CTA 21 and TDL starting in September, 1972. This phase

of testing continued through April 1973, and demonstrated design compatibility between the spacecraft telecommunications subsystems and the DSN.

Phase II of the test program was performed with CTA 21 in July 1973. The objective of this series of tests was to establish system design compatibility between the flight spacecraft and the DSN. Operational TCD software was utilized by CTA 21, and the spacecraft was located in the thermal-vacuum facility at JPL.

Phase III compatibility tests were performed at Cape Canaveral between DSS 71 and both of the MVM73 flight Spacecraft located in the Assembly and Checkout Facility (Building AO), the Explosive Safe Facility (ESF), and Launch Complex 36. The objective of these tests was to verify continued interface integrity and maintenance of compatibility during prelaunch preparations.

## II. Test Report

Initial tests to determine the TCD performance for MVM73 telemetry modes were performed at DSS 71 in September 1971. These tests indicated losses that were higher than predicted for the high-rate modes, and minor operational difficulties with the low-rate modes. These test results prompted an intensive series of tests at TDL and CTA 21 in an effort to better understand the TCD performance for MVM73 telemetry. These tests utilized simulated MVM73 telemetry, MM71 hardware, and software that consisted of modified MM71 operational software combined with revised TCD test software. Details concerning test configuration and measured test results are contained in Division 33 correspondence and reports.

Preliminary design tests with spacecraft components were performed at CTA 21 and TDL during the period April through August 1972. This series of tests could not demonstrate subsystem design compatibility because TCD operational software was not available and the spacecraft components consisted of breadboards. The primary objective of these tests was to provide insight into spacecraft and DSN performance capabilities and to enhance analysis and conclusions derived from compatibility testing.

In September 1972, the three-phase test program to establish DSN MVM73 Spacecraft compatibility was initiated. Each phase of testing was divided into segments as shown in Fig. 1; the individual tests performed in each phase and segment are shown in Table 1. Test descriptions for all test phases are contained in Ref. 1. Details concerning spacecraft modes, test criteria, and

measured test results are contained in DSN test procedures prepared in response to PD 615-115 and in Office 420 100 test reports.

### A. Phase I Tests

The objective of tests in this phase was to demonstrate design compatibility between the MVM73 spacecraft telecommunications subsystems and the DSN.

**1. Flight No. 1 tests.** These tests were conducted at CTA 21 on September 29, 1972, utilizing Flight No. 1 spacecraft components and TCD test software. Although S-band RF interface testing was emphasized, preliminary telemetry and command tests were performed. The use of TCD test software did not ensure subsystem design compatibility, but did provide a functional test of the DSN and spacecraft hardware.

**2. Flight No. 2 tests.** Tests were performed in December 1972, and January 1973, with CTA 21 and the MVM73 Flight II radio frequency subsystem (RFS) and modulation demodulation subsystem (MDS). Emphasis was placed on the RF and command interfaces. A total of eighteen tests were successfully completed with no anomalies observed. All telemetry tests were performed as functional tests since operational software had not yet been developed.

**3. Command and telemetry tests.** Formal compatibility testing was changed to informal software checkout and development testing status. This action was the result of delays in acceptance testing of the operational software, and was performed over the time period April through July 1973. Several problems with the software were discovered. Most of these problems were related to the inability to acquire  $8\frac{1}{2}$  bits/s at high signal conditions. Of lesser significance was loss of TCD program control when selecting a redundant Subcarrier Demodulator Assembly (SDA) or initialization of 490 bits/s.

Hardware problems uncovered were a possible alignment problem with the SDA and an interference problem using the discrete spectrum from the Planetary Ranging Assembly (PRA). With the former problem, one of the two SDAs at CTA 21 would not acquire at the project-specified Mercury encounter telemetry threshold  $ST_b N_0$  (0.63 dB).

A special alignment of the SDA was considered to be a resolution to the problem. With the latter problem, the telemetry signal-to-noise ratio (SNR) estimators in both telemetry channels (22.05/2.45 kilobits/s) indicated an increase in SNR with the PRA discrete spectrum ranging as opposed to the Mark 1-A continuous ranging.



4. **Block IV exciter tests.** Block IV exciter (S-band) command capability was established during tests on August 3, 1973, utilizing a flight radio (S. N 006) and the prototype command unit. The S X-band receiver tests were not accomplished because of the nonavailability of Block IV receiver equipment.

## **B. Phase II Tests: Flight No. 2 Spacecraft/ CTA 21 Testing**

This testing was performed during the month of July 1973 with the spacecraft located in the Thermal Vacuum Chamber. Testing was conducted at various sun levels to simulate: (1) 1.0 Sun, (2) 2.0 Sun, (3) 4.8 Sun, and (4) Ambient. Several problem areas were uncovered and are listed below:

- (1) The SDA lock indicator would not indicate in-lock at threshold,  $5 \times 10^{-2}$  data bit error rate (BER), for 22 kilobits/s, block coded data.
- (2) For some SDA Symbol Synchronizer Assembly (SSA) combinations, insufficient SDA correlation voltage was achieved for 22 kilobits/s block coded data to achieve SSA lock.
- (3) The Mission and Test Computer (MTC) experienced difficulty in achieving frame sync at threshold for 22 kilobits/s, block coded data.
- (4) The operational software (DSN Program Library Software No. (DOI-5050-OP) would not achieve reliable bit sync lock for  $8\frac{1}{2}$  bits/s at high signal level conditions.

These problems were not resolved during the July 1973 testing at CTA 21, but were given high priority for continued investigation during the Flight No. 1 testing to be conducted at DSS 71. All other objectives of the test plan for Flight No. 2 spacecraft were successfully completed during this phase.

## **C. Phase III Tests**

1. **Flight No. 1 compatibility verification tests.** This testing was performed at Cape Canaveral on August 26, 1973. The spacecraft was located in Building AO and an RF link was established to DSS 71; however, Revision A of the operational TCD software was not available. Special emphasis was placed on problems uncovered at CTA 21 during Flight No. 2 testing. A summary of the testing and results is as follows:

- (1) Command: the DSN Spacecraft command system design was declared compatible. There were no outstanding problems remaining upon completion of this testing.

- (2) Telemetry: the SDA and SSA lock problems discussed under Phase II testing were tested extensively during this period. A standard alignment of the SDAs was performed followed by a series of acquisition tests at an  $ST_R/N_a$  of 0.63 for 22 kilobits/s coded data.

The SDA/SSA combination acquired and performed without any difficulty. A decision was made to abandon further tests. Although the telecommunications system was designed to operate at a point below SDA/SSA design threshold, there appeared to be no problem in meeting project requirements at Mercury encounter.

- (3) Ranging: an interference problem in the telemetry signal-to-noise estimator occurred when the PRA discrete code was applied to the up-link. This problem was manifested by higher-than-normal SNR printouts. An operational resolution of this compatibility problem was to operate the uplink RF signal at or below  $-100$ -dB signal levels.
- (4) RF tests: all RF tests were successfully completed and compatibility was declared satisfactory.

2. **Flight No. 2 compatibility verification tests.** This test was performed on September 22 and October 23, 1973 at Cape Canaveral. The spacecraft was located in Building AO for the September 22 test, and Launch Complex 36 for the October 23 test. All testing was performed via an RF link and the launch version (Revision A) of the TCD operational software was utilized successfully.

Tests performed on September 22, 1973 cleared an outstanding compatibility problem. For the first time, a video picture was sent from the spacecraft to MTC and fully reconstructed. Data rate for this event was 22 kilobits/s, block coded. The M26X software module was also successfully exercised during this test. All other objectives of testing on this date were successfully completed.

Following completion of these tests, an operational readiness review was held on September 26, 1973 with a report of compatibility status as follows:

- (1) Command design compatibility established.
- (2) Telemetry design compatibility established with additional testing of DOI-5050-OP-A scheduled for October 23, 1973.
- (3) RF design compatibility established.

- (4) Ranging design compatibility established with additional operational testing scheduled for October 23, 1973.

On October 23, 1973, final compatibility testing was conducted with the Flight No. 2 spacecraft encapsulated in its launch configuration and located at Launch Complex 36. All compatibility deficiencies encountered during the September 22, 1973 testing were resolved. Therefore, complete compatibility was established for all elements of the Spacecraft DSN interface.

### III. Conclusions

The successful conclusion of the formal DSN/MVM73 compatibility program enabled the establishment of telecommunications compatibility as evidenced by the successful launch of the MVM73 spacecraft on November 3, 1973.

The importance of the performance of a formal compatibility test program is clearly demonstrated by the problem areas uncovered, verified, and resolved during the DSN MVM73 testing.

### Reference

1. *Mariner Venus/Mercury 1973 DSN-Spacecraft Compatibility Test Plan*, Project Document (PD) 615-115. Jet Propulsion Laboratory, Pasadena, Calif., Feb. 12, 1973. (JPL internal document.)

Table 1. DSN/MVM'73 compatibility test matrix

System tests	Phase											
	I						II <sup>a</sup>			III		
	Segment											
	1	2	3	4	5	6	7a	7b	7c	8	9	10
S-Band RF												
Downlink, one-way	X		X									
Uplink threshold two-way	X		X					X	X	X	X	
Two-way	X		X									
Spacecraft receiver pull-in range	X		X							X	X	
Spacecraft receiver tracking rate and range	X		X							X	X	
Carrier residual 0 jitter	X		X							X	X	
Uplink spectrum analysis	X		X									
Downlink spectrum analysis	X		X							X	X	
Simulated dynamic condition	X	X	X									
Spacecraft receiver best-lock frequency	X		X					X		X	X	
Auxiliary oscillator frequency	X		X							X	X	
Dynamic acquisition							X					
X-Band RF												
Carrier residual 0 jitter												
Tracking range and rate					X							
Downlink threshold					X							
Command												
Polarity verification		X	X				X					
Acquisition		X	X				X	X	X	X	X	
Capability under doppler		X	X									
Capability with ranging		X										
Operational capability		X					X	X	X			
Dynamic acquisition							X					
Telemetry												
Functional (strong signal)			X	X						X	X	
Mode 1		X	X	X			X	X				
Mode 2			X	X					X			
Mode 3			X	X								
Mode 4			X	X			X					
Mode 5			X	X				X				
Mode 6		X	X	X			X					
Mode 7			X	X								
Threshold				X								
Mode 1		X		X			X	X	X			
Mode 2				X				X	X			
Mode 3				X					X			
Mode 4				X			X	X	X			
Mode 5				X					X			
Mode 6		X		X			X	X	X			
Mode 7				X				X	X			
S-band ranging												
Acquisition	X		X		X					X	X	
Polarity verification	X		X		X							
Channel delay	X		X		X							
Under doppler conditions	X				X							
X-band ranging												
Acquisition					X							
Polarity verification					X							
Channel delay					X							

<sup>a</sup>Tests 7a, b, and c are Sun levels 1, 2, and 4.8, respectively.

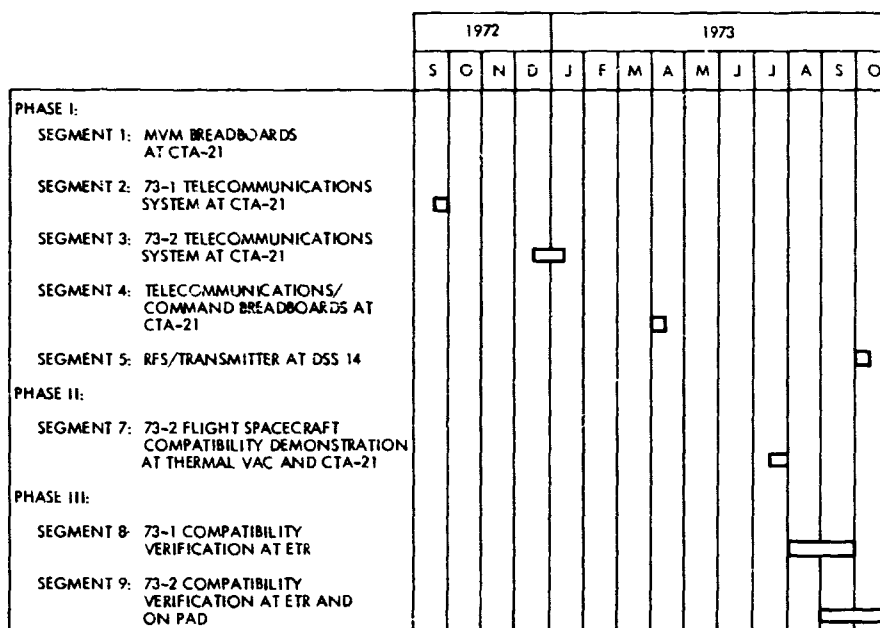


Fig. 1. DSN/MVM'73 compatibility test schedule

# The Mariner 9 Quasar Experiment: Part I

M. A. Slade and P. F. MacDoran  
Tracking and Orbit Determination Section

I. I. Shapiro  
Massachusetts Institute of Technology

D. J. Spitzmesser  
Network Operations Section

J. Gubbay, A. Legg, and D. S. Robertson  
Weapons Research Establishment, Australia

L. Skjerve  
Philco-Ford Corporation

*Differential very long baseline interferometry (VLBI) experiments were conducted in 1972 between Mariner 9 and various quasars. The objective of these experiments was to determine the position of Mars in the VLBI reference frame. This first of two articles gives background and describes experimental procedures. A subsequent article will describe the analysis of the data and the result obtained for the differential position.*

## I. Introduction

The technique of very long baseline interferometry, presently under rapid development, holds promise of making important contributions to spacecraft navigation. Through VLBI observations of extragalactic radio sources, many of them quasars, it will be possible to determine Earth's orientation (UT1 and polar motion) accurately with respect to the inertial frame formed by these sources. Our expectation is that within the next 5 years VLBI will be able to provide, for example, measurements of UT1 routinely with uncertainty below the 1-ms level, which

projects to a position error of about 10 km at a geocentric distance of 1 AU (still by no means the theoretical limit of the technology). In order to utilize this accuracy for interplanetary spacecraft navigation, we must know the orientation of the planetary system with respect to the same inertial frame. Since the planets are not themselves suitable targets for VLBI observations, an indirect approach is necessary. It was therefore suggested by one of us (I.I.S.) that a spacecraft in orbit about another planet would be an appropriate target.

In brief, the procedure proposed was to utilize two of the DSN antennas to observe alternately, but in synchronism, the spacecraft and an extragalactic radio source that lies nearby in the sky. With sufficiently stable frequency standards and adequate signal-to-noise ratios, it is possible to switch back and forth between observations of the spacecraft and the natural radio source so as to be able to determine the time development of the fringe phase for each target without the introduction of any  $2\pi$  ambiguities other than the initial one that affects all such observations. The differences in the fringe phases for the two targets represent extremely accurate observables since they are freed, through cancellation, from most instrumental effects. Because the two sources, by design, subtend a very small angle at Earth, the propagation-medium effects tend to cancel as well. This technique of differential VLBI ( $\Delta$ VLBI) appears capable, when developed, of the determination of relative positions with an uncertainty at the milliarcsecond level. (Also see Ref. 1.)

The first opportunity to apply this technique arose with the Mariner 9 spacecraft in January 1972. During this primary portion of the mission, several sets of observations were conducted. Other observations were carried out during the extended mission. Unfortunately, the required first local oscillator (LO) signal could not be derived from the station frequency standards by integer multiplication because of the lack of appropriate instrumentation. Therefore, the first LO chain was driven by a synthesizer signal and, as a consequence, sufficient frequency stability with the interferometer was not obtained to allow the fringe phase to be "connected" between observations of either of the two targets without the introduction of  $2\pi$  ambiguities.<sup>1</sup> Therefore, only the fringe rates, which are inherently unambiguous although less accurate, were available for the determination of relative position. A detailed description of these experiments is given in the following sections; the results will be discussed in the final article of this two-part series.

## II. Experiment Description

Initially, three sets of observations were taken on January 17, 20, and 25, 1972, during mutual visibility between the 64-m Mars antenna (DSS 14) at Goldstone, California, and a 26-m antenna at Woomera, Australia (DSS 41). The natural source which was observed alternately

<sup>1</sup>Had four antennas been available (a pair at each end of the long baseline), observations of each target could have been carried out continuously, and this lack of frequency stability would have been of no consequence (provided the same local oscillator signal was used at each antenna pair).

with Mariner 9 was the quasar P0106 - 01. Later in the year, another set of observations was made during the extended mission on October 13 and 17. On a third day (October 27), observations could not be carried out because of the final loss of altitude control gas by Mariner 9. This later series of observations was carried out between the 26-m Echo antenna at Goldstone (DSS 12) and DSS 41, with the natural sources observed being the quasars 3C273 and 3C279.

Unfortunately, no observations after January 20 were successful. The cause of these failures is believed to be in the frequency system of one or both stations. The observations of 3C273 yielded intermittent, weak fringes; no other signals were detected.

On each of the 2 days when useful data were obtained, three kinds of tracking were performed. Table 1 summarizes these tracking modes. During the first 2 h, the spacecraft was completing its high-bit-rate science playback to DSS 14. This signal was simultaneously recorded to be processed in a VLBI mode using the 24-kHz system (Ref. 2). Three-way doppler data were also obtained during this same interval. The next 2 h, until Mariner 9 set at DSS 14, were used for the actual switching experiment. Finally, 4 h of observations on various natural radio sources were taken at the same frequency as the switching experiment to give sensitivity to baseline and clock parameters.<sup>2</sup> On January 20, runs 9-13 of the switching experiment were lost due to an unanticipated, although mission-planned, termination of the high-rate science sub-carrier signal which served as the interferometer illuminator.

## III. Data Reduction

The accuracy of the data, as explained above, did not approach the level possible for this type of experiment. However, these data did allow the development and checkout of software to be used in later experiments. Therefore, the exercise of processing these data was carried through.

The cross-correlation of the magnetic tapes was accomplished using a modification of software developed for Earth physics and UT1 observations (Ref. 3). The model for the spacecraft motion used in fringe stopping was taken from probe ephemeris tapes (PETs). The ephemeris for Mars was the JPL ephemeris designated DE69 (Ref. 4).

<sup>2</sup>The differential position measurement, however, has virtually no dependence on these parameters.

Figure 1 shows typical residual sine fringes for Mariner 9 over a small portion of one VLBI tape pair on January 17. The best-fitting sine wave over this interval is also shown.

The fringes which resulted from the cross-correlation were then analyzed to extract the information about the time development of the fringe phase (Ref. 3). Differencing the relative fringe phase at different times for a given source then yielded average fringe rates over these intervals. The results from one such analysis are shown in Fig. 2 for a tape taken on January 20. The residual phase after a constant fringe rate was removed is plotted as a function of time from the beginning of the tape. The figure also illustrates the antenna switching sequence followed in all

the switched observations. The spacecraft phase points are more finely spaced because the higher signal-to-noise ratio for Mariner 9 allowed a shorter averaging time (12.8 s compared to 57.6 s). Note that the scale of the abscissa is  $\sim 1/3$  cycle of S-band phase ( $\sim 4$  cm light-time equivalent).

The final step in the processing of the raw observations was the removal of the phase models used in fringe stopping for the two sources. The resulting "total" fringe rates were then analyzed using programs with more sophisticated modeling of the theoretical expression for the motion of Earth and the spacecraft. The result of this analysis is to be the subject of the final article of this two-part sequence.

## Acknowledgments

The authors wish to acknowledge the contribution of J. Gunckle of the JPL staff, and the personnel of DSS 14, 12, and 41, particularly the servo, digital, and microwave subsystems. The PET ephemeris for Mariner 9 was kindly supplied by R. K. Hylkema. We also thank H. Peters of Goddard Space Flight Center for the loan of a hydrogen maser at the Woomera station.

## References

1. Couselman, C. C., Hinteregger, H. F., and Shapiro, I. I., "Astronomical Applications of Differential Interferometry," *Science*, Vol. 179, p. 607, 1972.
2. Fanselow, J. L., MacDoran, P. F., Thomas, J. B., Williams, J. G., Finnie, C. J., Sato, T., Skjerve, L., and Spitzmesser, D. J., "The Goldstone Interferometer for Earth Physics," in *The Deep Space Network Progress Report*, Technical Report 32-1526, Vol. V, pp. 45-57, Jet Propulsion Laboratory, Pasadena, Calif., Oct. 15, 1971.
3. Thomas, J. B., "An Analysis of Long Baseline Interferometry, Part III," in *The Deep Space Network Progress Report*, Technical Report 32-1526, Vol. XVI, pp. 47-64, Jet Propulsion Laboratory, Pasadena, Calif., Aug. 15, 1973.
4. O'Handley, D. A., Holdridge, D. B., Melbourne, W. G., Mulholland, J. E., *JPL Development Ephemeris Number 69*, Technical Report 32-1465, Jet Propulsion Laboratory, Pasadena, Calif., Dec. 15, 1969.

**Table 1. Tracking mode summary**

Run Nos.	Time (U.T.)	Mode
1-8	0220-0420	Mariner 9 only
9-19	0427-0647	$\Delta$ VLBI
20-35	0649-1041	Natural sources only



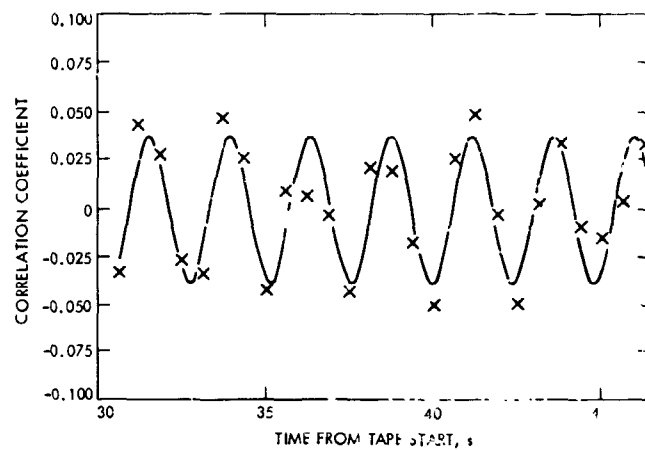


Fig. 1. Typical residual sine fringes for Mariner 9

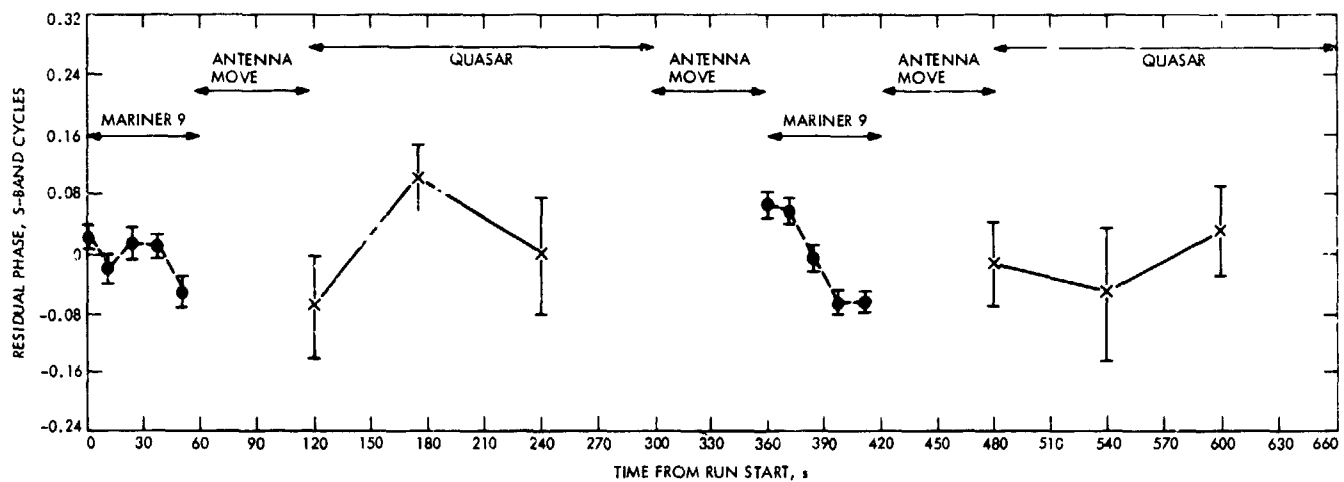


Fig. 2. Results of fringe phase analysis

# Radio Interferometry Measurements of a 16-km Baseline With 4-cm Precision

J. B. Thomas, J. L. Fanselow, and P. F. MacDoran  
Tracking and Orbit Determination Section

D. J. Spitzmesser  
Network Operations Office

L. Skjerve  
Philco-Ford Corporation  
Barstow, California

*In order to demonstrate the feasibility of eventually using radio interferometry techniques to measure tectonic motion, a series of interferometry experiments has been conducted between two antennas at the Goldstone Deep Space Communications Complex. The primary objective of these experiments was to develop independent-station instrumentation capable of making three-dimensional baseline measurements with an accuracy of a few centimeters. To meet this objective, phase-stable instrumentation was developed to precisely measure the time delay by means of two-channel bandwidth synthesis. Delay measurements produced by this instrumentation lead to three-dimensional baseline measurements with a precision of 2-5 cm for the components of a 16-km baseline.*

## I. Introduction

In the last few years, there has been increasing interest in developing a system capable of accurately measuring the relative motion of points separated by distances ranging from 100 km up to intercontinental distances on the Earth's crust. Information concerning this far-field motion is of critical importance in the development of theoretical models of crustal dynamics. Since crustal motion is about 3-10 cm/year, the measurement accuracy should be about 1-3 cm with about 1 week of data. Radio interferometry is one technique that holds great promise for fulfilling this accuracy requirement.

In order to begin development of a radio system with few-centimeter accuracy, a series of interferometry experiments has been conducted between two antennas at the Goldstone Deep Space Communications Complex. The primary objective of these experiments was to develop independent-station instrumentation capable of making three-dimensional baseline measurements with an accuracy of a few centimeters. A short Goldstone baseline (16 km between DSS 12 and DSS 14) was selected so that transmission media uncertainties and astronomical parameters would be relatively unimportant compared with

radio system limitations. These experiments led to the refinement of a two-channel approach to bandwidth synthesis, a technique for measuring time delay that was originally developed by A. E. E. Rogers (Ref. 1). In this report, the instrumentation, analysis, and results of these Goldstone experiments are presented.

## II. Radio Interferometer Technique

In the radio interferometry measurements described in this report, two antennas simultaneously receive the radio noise generated by an extragalactic radio source, as shown in Fig. 1. Because of a difference in ray paths, a given wave front will reach the two antennas at different times. This difference in arrival times is called the time delay  $\tau$ . In this section, the technique for the measurement of this delay is described, while a mathematical model for this quantity is discussed in Section IV.

Since the radio interferometry method has been analyzed in detail in other papers (Refs. 1-6), it will be described only briefly in this report. Single-channel interferometry will be reviewed first, followed by an outline of two-channel bandwidth synthesis.

In single-channel measurements, each antenna system records on magnetic tape radio noise centered at frequency  $\omega_a$  with bandwidth  $W_B$ . The tapes are then carried to a central site for digital processing. In this reduction, the two data streams are processed to obtain the stopped fringes (Ref. 5), which, for channel  $a$ , are given by

$$U_a(t, \tau_m) = A_B \frac{\sin(\pi W_B \Delta \tau_r)}{\pi W_B \Delta \tau_r} \cos \phi_s \quad (1)$$

where the stopped phase is given by

$$\phi_s = \epsilon t + \omega_a(\tau_g + \tau_t + \tau_l + \tau_c - \tau_m) + \psi_a + C_a + R_a$$

In addition,

$$\Delta \tau_r = \tau_g + \tau_t + \tau_l + \tau_c - \tau_m \quad (2)$$

In these expressions,

$W_B$  = single-channel bandwidth

$\omega_a$  = effective interferometer bandpass center

$\psi_a$  = instrumental phase drifts

$C_a$  = differential charged-particle phase shift

$R_a$  = brightness transform phase

$\tau_g$  = geometric delay

$\tau_t$  = differential tropospheric delay

$\tau_c$  = differential ionospheric delay

$\tau_l$  = instrumental delays plus clock synchronization error

$\tau_m$  = model delay

$\epsilon$  = analytical frequency offset

$A_B$  = peak amplitude

Thus the stopped fringes are a product of an amplitude factor  $A_B$ , a delay curve,  $\sin(\pi W_B \Delta \tau_r)$ , and a sinusoidal function,  $\cos \phi_s$ . The amplitude factor depends on the brightness transform in addition to signal and system noise temperatures. The delay curve is a measure of bit stream alignment in the time domain, including all group delay effects. This particular form for the delay curve assumes that the system bandpass is rectangular with a linear phase-versus-frequency response, an approximation of negligible error for the purposes of this experiment. Finally,  $\phi_s$  describes the phase behavior of the system. In this phase is buried the geometric delay  $\tau_g$ , the observable of primary interest in these measurements. Note that, since the ionosphere is a dispersive medium, the ionosphere effect has been expressed as a phase shift in the fringe phase and as a delay in the total group delay.

The next step in the data reduction is to determine the fringe phase  $\phi_s$  by a process known as phase tracking (Ref. 5), a technique that fits a least-squares sinusoid to the stopped fringes  $U_a$ . After  $\phi_s(t)$  is extracted as a function of time, the analytical offset  $\epsilon t$  is removed in a manner that gives the correct sign (Ref. 5) to the resulting residual phase. The theoretical behavior of this measured residual phase  $\Delta \phi_a$  is given by

$$\Delta \phi_a = \omega_a(\tau_g + \tau_t + \tau_l - \tau_m) + \psi_a + C_a + R_a \quad (3)$$

The adjective "residual" denotes the fact that, in effect, the data reduction process subtracts a model delay ( $\tau_m$ ) from the fringe phase. This "phase stopping" procedure removes most of the time-varying components of the total delay.

Because fringe phase can be determined only to within a constant ( $2n\pi$ ), narrow-band, single-channel interferometry can essentially measure only phase changes. Therefore, if residual phase is measured over a short time interval, it is essentially a measure of residual fringe frequency given by

$$\Delta \nu_a \equiv \dot{\Delta \phi}_a = \omega_a(\dot{\tau}_g + \dot{\tau}_t + \dot{\tau}_l - \dot{\tau}_m) + \dot{\psi}_a + \dot{C}_a + \dot{R}_a \quad (4)$$

where  $\Delta\dot{\phi}_a$  is the time derivative of the phase extracted from the fringes. This time derivative is insensitive to the  $z$ -component of the baseline, since that particular projection does not change appreciably as the Earth rotates. Consequently, a measurement of delay is essential if three-dimensional baseline measurements are to be made. This requirement for delay measurements lead to the development of two-channel bandwidth synthesis.

In two-channel bandwidth synthesis, the output of each antenna system is alternately switched between two narrow-band channels. For example, during even seconds, both systems would record a bandpass centered at  $\omega_a$ , while during odd seconds, both would record at  $\omega_b$ . For channel  $a$ , the stopped fringes and fringe phase expressions would be identical to Eq. (1) and Eq. (2), except that the subscript  $a$  is replaced by  $b$ . An example of two-channel stopped fringes (Eq. 1) with one-second switching is shown in Fig. 2. On this Goldstone baseline, this radio source, 3C 454.3, has a correlated flux strength of about 10 flux units (one flux unit =  $10^{-26}$  W m<sup>2</sup> Hz). The amplitude noise on the fringes comes primarily from system noise (receiver, source, and background noise). This plot, which exhibits the first 30 s from a 600-s tape-pair, displays fringe points containing 0.5 s of data recorded at a 48-kilobit/s rate. Alternate seconds in the plot switch between fringes from two channels centered at 2270 MHz and 2310 MHz. The stopped fringe frequency is about 0.1 Hz in both channels and is due primarily to an analytical rate offset  $\epsilon$  in the phase model used in fringe stopping. This offset allows a determination of the sign (Ref. 5) of the residual fringe frequency  $\Delta\omega_a$  and  $\Delta\omega_b$  (Eq. 4).

Fringe phase plots obtained from these fringes are shown in Fig. 3. Each phase point contains 50 s of data (100 fringe points of the type in Fig. 2), while the entire plot covers a complete tape-pair (600 s). In the plot, the error bars on the phase points represent the phase error produced by the actual amplitude noise on the fringes. The slope of each of these phase plots is a measurement of residual fringe frequency represented analytically in Eq. (4). Since an accurate model delay was used in the data reduction, the phase slopes are relatively constant over one tape. The small nonlinear trends ( $\approx 0.03$  cycle = 0.4 cm) that are present could be due to ionospheric effects. (Nonlinear trends due to large *a priori* delay errors would be quadratic in appearance over this short time interval.) Fringe frequency values obtained from the phase slopes are important interferometer observables and are utilized as shown in Section V.

In addition to the frequency observable, the measured delay values can be obtained by combining the phase out-

put of the two channels as follows:

$$\Delta\tau = \frac{\Delta\phi_a - \Delta\phi_b}{\omega_a - \omega_b} \quad (5)$$

This computed value will be referred to as the *a priori* residual delay. The use of the term "residual" means that a model delay has in effect been subtracted from the total delay, leaving a much smaller value. In combining the two phase outputs, care must be taken to avoid  $2\pi$  ambiguities (Ref. 5). When computing  $\Delta\tau$ , one can assume that the channel separation  $\omega_a - \omega_b$  is essentially exactly known, since frequency calibration is accurate to parts in  $10^{12}$ .

An example of a delay calculation is shown in Fig. 4, where the phase values have been combined from Fig. 3. Note how the systematic phase trends in Fig. 3 have disappeared in the difference, which in effect has scaled phase variations at S-band down to much lower levels at 40 MHz, the synthesized bandwidth. A covariance analysis indicates that the observed noise on these delay values comes almost entirely from the amplitude noise on the fringes. Over one tape, the residual delay  $\Delta\tau$  is essentially constant due to an accurate delay model  $\tau_m$ . Therefore, these delay values are averaged to produce one delay measurement for each tape-pair. After averaging, the resulting delay values, one for each tape-pair, become the primary observables of the interferometer system.

Note that, if the phase error in  $\Delta\phi_a$  and  $\Delta\phi_b$  is independent of frequency, the delay precision improves as the channel separation,  $\omega_a - \omega_b$ , increases. For this reason, the observing frequencies are generally separated as far as possible. As discussed in Section III, the maximum channel separation is determined by the bandpass limits of the antenna system.

The theoretical behavior of the measured delay is given by the expression (Ref. 5)

$$\Delta\tau = \Delta\tau_r + \frac{\psi_a - \psi_b}{\omega_a - \omega_b} = \tau_g + \tau_f + \tau_t + \tau_c - \tau_m + \frac{\psi_a - \psi_b}{\omega_a - \omega_b} \quad (6)$$

In the present measurements, the instrumental phase difference  $\psi_a - \psi_b$  introduces a long-term linear drift in the measured delays. This drift is due primarily to a frequency offset between the frequency standards at the two stations. This term, as well as the other components of the measured delay, will be modeled in Section IV.

In summary, the data on each tape-pair are reduced to two observable values—time delay and fringe frequency.

Before proceeding to a discussion of the mathematical model for delay and the fitting procedure, the experiments and their instrumentation will be described.

### III. Experiment Description

Over the last two years, five separate radio interferometry experiments, which are summarized in Table 1, have been conducted between DSS 12 and DSS 14 at the Goldstone Deep Space Communications Complex. All experiments involved S-band observations, JPL H-maser frequency standards, and a 24-kHz bandwidth digital recording system developed by D. S. Robertson and A. H. Legg of the Weapons Research Establishment, Australia. As indicated in Table 1, the various experiments were between 7 and 14 hours in duration and involved 13 to 18 radio sources. The sources used in the last four experiments are described in Table 2.

In the first Goldstone experiment (Ref. 2), one narrow-band (24-kHz bandwidth) channel of radio noise was recorded, so that only the fringe frequency observable was precisely obtained. An analysis of the resulting frequency observables revealed frequency instability at the 1-mHz level ( $\Delta f/f \approx 5 \times 10^{-13}$ ) over several hours. As indicated in Ref. 2, the HP5100 synthesizers associated with the first local oscillator (LO) signal were the most likely source of this instability. Consequently, in subsequent experiments, the synthesizers were replaced by more stable X7 multipliers, which will be described below.

After this first experiment, instrumentation was also developed to measure time delay in addition to fringe frequency. The technique adopted for delay measurements required the measurement of more than one channel of radio noise. This technique, commonly called bandwidth synthesis (Refs. 1 and 5), combines, either directly or indirectly, the fringe phase information of band-limited channels recorded at frequencies whose separations are large compared to that of the single-channel bandwidth.

In the original application of the bandwidth synthesis technique (Ref. 1), six channels were recorded in a time-shared mode. However, because of signal-to-noise ratio (SNR) improvement and simplification of instrumentation, we employed instrumentation that recorded only two channels. The only disadvantage of the two-channel system is that sufficiently precise *a priori* delay information is required to avoid  $2\pi$  ambiguities (Ref. 5). Since delay measurement precision improves as channel separation increases, the goal of the instrumental design was to obtain maximum channel separation within the restric-

tions of the DSN antenna systems. In the final system, the maximum separation was defined by the limits of the traveling wave maser (TWM) receiver bandpass.

For the second experiment, a relatively simple instrumental configuration was devised to demonstrate the feasibility of the two-channel approach to bandwidth synthesis. In this intermediate system, which will not be described here in detail, two channels separated by 10 MHz at S-band were heterodyned to intermediate frequency (IF) and added. This combined signal was then heterodyned to baseband and continuously sampled at a 48-kilobits rate. While this system pays a price in SNR, it avoids the complications of simultaneous recorder channel switching at the two stations. This intermediate instrumentation demonstrated the feasibility of the two-channel approach and helped perfect the final instrumentation described below.

The final configuration used for bandwidth synthesis is shown in Fig. 5. In this system, a 10-MHz signal from the H-maser is converted to a 2240-MHz first LO signal by using only multipliers—the standard X4X8 multipliers of the DSN system and a new X7 multiplier. This X7 multiplier, which was constructed<sup>1</sup> to avoid the use of a synthesizer, converts the input sinusoid to a square wave, then filters and amplifies the seventh harmonic.

In order to achieve maximum channel separation and better delay precision, the S-band traveling wave maser receiver bandpass was broadened by retuning the trim coil currents. In this retuned state, the receiver exhibited ample amplification over a 40-MHz interval (2270 to 2310 MHz) while maintaining an operating system noise temperature less than 30 K. Therefore, after mixing with the first LO signal at 2240 MHz, the edges of the receiver passband were placed at 30 MHz and 70 MHz. However, this frequency spread exceeded the bandpass of the standard first mixer preamplifier, which possesses adequate gain only over 45 to 55 MHz. Consequently, the standard mixer preamplifier was replaced by a similar module with a bandpass between 10 and 160 MHz, thereby making the system TWM-limited. This IF passband was then filtered into two channels—one centered at 30 MHz and the other at 70 MHz. Each channel was mixed with a 20-MHz signal derived from the H-maser and each mixer response was appropriately filtered to place both channels at 50 MHz. At this point, each channel was transferred on alternate seconds to the video converter. The video converter mixed the input IF signal to baseband with a 50-MHz signal derived from the H-maser. The resulting time-shared

<sup>1</sup>R. L. Sydnor, Telecommunication Research Section, JPL.

baseband signal was then passed through a 24-kHz band-pass filter before digital sampling and recording at a 48-kilobit/s rate.

#### IV. Time Delay Model

The residual delay  $\Delta\tau$  observed in radio interferometry measurements is a sum of geometric, instrumental, and transmission media delays, as indicated in Eq. (6). This section outlines the model adopted for these terms in the observed delay, starting with the largest and most important term, the geometric delay.

As indicated in Fig. 1, a given wave front will reach the two antennas of the interferometer at different times. It is readily shown that the geometric delay is given by the expression (Ref. 3)

$$\tau_g = -\frac{\mathbf{B} \cdot \hat{\mathbf{S}}}{c} \left( 1 + \frac{\mathbf{V}_2 \cdot \hat{\mathbf{S}}}{c} \right) \quad (7)$$

where  $\mathbf{B}$  is the baseline vector between the two antennas,  $\mathbf{S}$  is the apparent source direction,  $\mathbf{V}_2$  is the velocity of antenna 2, and  $c$  is the speed of light. Note that the geometric delay is essentially the instantaneous geometric path difference multiplied by a small correction that accounts for the motion of antenna 2 during the wave transit.

In the present analysis, true equatorial coordinates of date (TECD) are chosen as the coordinate frame for geometric delay calculations. In this Earth-centered right-handed frame, the  $z$ -axis is along the instantaneous spin axis of Earth while the  $x$ -axis is along the true equinox of date. The source vector  $\mathbf{B}$  and the baseline vector  $\hat{\mathbf{S}}$  can be expressed in terms of these coordinates as follows.

In TECD, the source vector  $\mathbf{S}$  is usually characterized by two angles—apparent declinations  $\delta_s$  and apparent right ascension  $\alpha_s$ . These angles lead to the usual expression for the source vector:

$$\hat{\mathbf{S}} = (\cos \delta_s \cos \alpha_s, \cos \delta_s \sin \alpha_s, \sin \delta_s) \quad (8)$$

The term “apparent” indicates the presence of a correction to the source direction that accounts for aberration due to the Earth’s orbital motion (Refs. 3 and 7). In addition, precession and nutation of the Earth’s spin axis (Refs. 7 and 8) are included to rotate to TECD from mean equatorial coordinates of 1950.0 since the 1950.0 frame is conventionally used to catalogue source positions. In the present short-baseline measurements, these corrections are easily made with adequate accuracy.

The baseline vector  $\mathbf{B}$  must include two general features: an Earth-fixed definition and Earth orientation factors. The Earth-fixed vector,  $\mathbf{B}_{03}$ , is defined in terms of a right-handed coordinate frame with a  $z$ -axis toward the Conventional International Origin (CIO) pole and  $X$ -axis along the Greenwich meridian. It will be represented in Cartesian coordinates as follows:

$$\mathbf{B}_{03} = (x_b, y_b, z_b) \quad (9)$$

where  $x_b, y_b$  are the equatorial components and  $z_b$  is the  $z$ -component, as schematically indicated in Fig. 1.

At this point in the discussion of the baseline vector, a definition of antenna location is desirable. The effective location of an antenna depends on antenna structure. Most directional antennas have two primary axes of rotation that allow antenna orientation. For DSS 14, an azimuth/elevation antenna, the rotation axes intersect. By geometrical considerations, one can show that this point of intersection is the effective antenna location.

On the other hand, DSS 12 is a polar mount, for which the rotation axes are nonintersecting. In this case, the effective location is the point at which the hour-angle axis orthogonally intersects a plane containing the declination axis. Therefore, for this polar mount, one must include the correction factor  $b \cos \delta$ , in delay calculations, where  $b$  is the shortest distance between the two axes. This correction factor accounts for the fact that this type of antenna “stretches toward” low-declination objects. For DSS 12, the axis separation  $b$  is 6.706 m and is easily accounted for with adequate precision.

The baseline vector  $\mathbf{B}$  rotates in space as a result of polar motion and Earth spin. To account for those motions, the Earth-fixed baseline vector is rotated to its instantaneous orientation in TECD as follows:

$$\mathbf{B}(t) = \mathbf{R}_e \mathbf{R}_p \mathbf{B}_{03} \quad (10)$$

where the Earth spin matrix is given by the expression

$$\mathbf{R}_e = \begin{pmatrix} \cos \alpha_e & -\sin \alpha_e & 0 \\ \sin \alpha_e & \cos \alpha_e & 0 \\ 0 & 0 & 1 \end{pmatrix} \quad (11)$$

and the polar motion matrix is given by

$$\mathbf{R}_p = \begin{pmatrix} 1 & 0 & -X_p/a \\ 0 & 1 & Y_p/a \\ X_p/a & -Y_p/a & 1 \end{pmatrix} \quad (12)$$

In these expressions, the angle  $\alpha_G$  is the hour angle of the equinox at the time of interest and is easily obtained from universal time (UT1). Parameters  $X_p$  and  $Y_p$  are the polar displacements relative to the CIO pole, while  $a$  is the polar radius. See Ref. 3 for more detail concerning these Earth orientation factors.

The expressions above for  $B$  and  $\hat{S}$  are easily combined to calculate the geometric delay for a given source. It should be noted that the model for the geometric delay outlined above neglects general relativistic effects which, for longer baselines, may be significant.

In these experiments, no corrections were made for ionospheric effects. In all the measurements reported here, radio sources were observed at night when ionospheric delays, inhomogeneities, and turbulence were at a minimum. At S-band, the nighttime ionosphere causes about a 1-m delay along a single ray path at a typical elevation angle ( $\approx 30$  deg). However, the *difference* in ionospheric delays along the two interferometer ray paths is the important quantity in delay measurements. Since nighttime observations involve a relatively homogeneous ionosphere, this difference for a 16-km baseline will be a small fraction of a single ray-path delay. As we shall see, the delay residuals in the present experiments strongly indicate that differential ionosphere delays were less than 6 cm. Below the 6-cm level, differential ionosphere corrections, even if they were available, would be of marginal value in the present delay measurements. However, as discussed in Section VI, the frequency residuals contain an unmodeled noise term at the 0.1-mHz level that could possibly be an ionospheric effect.

The total troposphere delay for a single ray path is about 4 m for a typical elevation angle. In the present work, small corrections are made to the delay observables to remove small known differences ( $\leq 15$  cm) in tropospheric delays along the two ray paths. These differences are a consequence of Earth curvature as well as a slight altitude difference (40 m) between the two antennas. The altitude difference produces a 1-cm difference in the "dry" component of the zenith tropospheric delay. The Earth's curvature leads to elevation angle differences that cause differential troposphere corrections as large as 10 cm. It is believed that, with these corrections, the differential "dry" troposphere delay becomes a negligible source of error. The total "wet" troposphere delay for one ray path at Goldstone is only 10–20 centimeters at typical elevation angles. For a 16-km baseline with only small changes in altitude, the difference in the wet troposphere between ray paths should be only a small fraction ( $< 10\%$ ) of the

single ray path delay. It is estimated that, with the listed corrections, the total troposphere effect in the delay observable becomes a negligible source of error ( $\leq 3$  cm).

Finally, with regard to the present instrumentation, the instrumental terms ( $\tau_i, \psi_a - \psi_b$ ) in the measured delay (Eq. 6) can be adequately modeled as a constant plus a linear drift, where the constant and slope are used as solve-for parameters.

## V. Fitting Procedure

As outlined in Section II, the reduction of each tape-pair gives the residual delay  $\Delta\tau$  and fringe frequency  $\Delta\nu$  for a particular radio source observed for a 12-min interval. In order to extract the baseline vector, the delay and frequency values from many tape-pairs recorded for many radio sources must be simultaneously fit by a least-squares technique using a model for the delay. The construction of a mathematical model for the geometric delay was outlined in Section IV. This section outlines the weighted least-squares fitting procedure used to extract the Goldstone baseline.

In these short-baseline measurements, uncertainties in the geometric delay due to errors in source location and Earth orientation factors (polar motion, UT1, precession, nutation) are small compared with instrumental errors. That is, all of these factors have been measured with sufficient accuracy by other methods so that they may be treated as "known" quantities in delay calculations. For the radio sources in these experiments, source locations have been independently measured with an accuracy of 0.2–0.9 arc seconds, as indicated in Table 2. The position errors in this table represent approximate external accuracy, conservatively estimated in some cases by root-sum-squaring the quoted internal errors with 0.3 arc second. The adequacy of these measurements can be demonstrated by the following approximate calculation. A typical value for the sensitivity partials in the present experiments is approximately 0.1 ns/arc second. When this sensitivity is multiplied by a typical source location error of about 0.5 arc second, a delay error equal to 0.05 ns (1.5 cm) results. This delay error is small compared with a typical system noise error of about 7 cm. Similar detailed calculations for all sources in Table 2 indicate that these source positions are adequate for present delay model calculations. By similar arguments, one can show that polar motion and UT1, which are known with about 0.03 arc second accuracy (Ref. 9), also contribute negligible errors in delay calculations. The BIH values for UT1 – UTC and polar motion parameters are listed in Table 3. Finally,

known errors in the models for precession and nutation of the Earth's spin axis contribute errors less than 0.2 arc second (Ref. 8), and may be regarded as negligible. Therefore, only the three baseline parameters must be regarded as solve-for parameters in the geometric delay.

In addition to the geometric delay parameters, the observed delay contains unknown offset and linear drift terms which are equivalent in effect to a synchronization error and rate difference between clocks. The linear drift is due mainly to a small uncalibrated rate difference between the H-maser frequency standards. In the fringe frequency observable, the rate difference becomes a constant frequency offset. In principle, the frequency offset and the delay rate offset should be equal. However, as will be shown, the fringe frequency observable contains extra noise considerably above the expected system noise. In addition, the frequency observable contains elements of the frequency system that cancel in the delay observable. For these reasons, the two rate factors are varied independently in the fit so that the frequency offset can freely seek its own level without coupling in a corrupting fashion with the delay observable. However, comparison of the two rate offsets is one means of judging the quality of these measurements.

Under these assumptions, the complete models<sup>2</sup> for the residual delay and fringe frequency observables become

$$\Delta\tau_i = \left. \frac{\partial\tau_g}{\partial x_b} \right|_i \Delta x_b + \left. \frac{\partial\tau_g}{\partial y_b} \right|_i \Delta y_b + \left. \frac{\partial\tau_g}{\partial z_b} \right|_i \Delta z_b + \tau_s + \dot{\tau}_s t_i \quad (13)$$

$$\Delta\nu_i = \left. \frac{\partial\nu_g}{\partial x_b} \right|_i \Delta x_b + \left. \frac{\partial\nu_g}{\partial y_b} \right|_i \Delta y_b + \nu_s \quad i = 1, N_t \quad (14)$$

where  $\Delta\tau_i, \Delta\nu_i$  are the *a priori* residual delay and fringe frequency for the *i*th tape-pair recorded at time  $t_i$ , and  $N_t$  is the total number of tape-pairs.

The terms in Eqs. (13) and (14) have been accounted for as follows. The first terms with partials are the usual linear expansions of the residual geometric delay,  $\tau_g - \tau_m$ , where  $\Delta x_b, \Delta y_b$ , and  $\Delta z_b$  are the solve-for deviations from the three components of the *a priori* baseline used in  $\tau_m$ . The delay terms  $\tau_s$  and  $\dot{\tau}_s$  account for the instrumental phase effects entering in the difference  $\Delta\phi_a - \Delta\phi_b$ . The parameter  $\nu_s$  is the offset in the fringe frequency observable. As indicated in Section IV, transmission media de-

lays are assumed to be a negligible source of error after small tropospheric corrections. Thus, there are six solve-for parameters in the fitting procedure:  $\Delta x_b, \Delta y_b, \Delta z_b, \tau_s, \dot{\tau}_s, \nu_s$ .

Extra frequency noise, which is discussed in Section VI, reduced the strength of the fringe frequency observables. Normally, if only system noise is present, each channel contributes a statistically independent measure of fringe frequency. The extra frequency noise in the present experiment was almost perfectly correlated between channels. This correlation meant, in effect, that the two channels produced only one independent fringe frequency measurement for each tape-pair.

In order to simultaneously fit the delay and frequency observables, the fitting equations (Eq. 13 and 14) are more conveniently expressed in the following form:

$$u = Ap \quad (15)$$

where

$$u = \begin{pmatrix} \Delta\tau_1 \\ \Delta\tau_2 \\ \vdots \\ \Delta\tau_{N_t} \\ \Delta\nu_1 \\ \vdots \\ \Delta\nu_{N_t} \end{pmatrix} \quad p = \begin{pmatrix} \Delta x_b \\ \Delta y_b \\ \Delta z_b \\ \tau_s \\ \dot{\tau}_s \\ \nu_s \end{pmatrix} \quad (16)$$

and

$$A = \begin{pmatrix} \left. \frac{\partial\tau_g}{\partial x_b} \right|_1 & \left. \frac{\partial\tau_g}{\partial y_b} \right|_1 & \left. \frac{\partial\tau_g}{\partial z_b} \right|_1 & 1 & t_1 & 0 \\ \left. \frac{\partial\tau_g}{\partial x_b} \right|_2 & \left. \frac{\partial\tau_g}{\partial y_b} \right|_2 & \left. \frac{\partial\tau_g}{\partial z_b} \right|_2 & 1 & t_2 & 0 \\ \vdots & \vdots & \vdots & \vdots & \vdots & \vdots \\ \left. \frac{\partial\tau_g}{\partial x_b} \right|_{N_t} & \left. \frac{\partial\tau_g}{\partial y_b} \right|_{N_t} & \left. \frac{\partial\tau_g}{\partial z_b} \right|_{N_t} & 1 & t_{N_t} & 0 \\ \left. \frac{\partial\nu_g}{\partial x_b} \right|_1 & \left. \frac{\partial\nu_g}{\partial y_b} \right|_1 & 0 & 0 & 0 & 1 \\ \vdots & \vdots & \vdots & \vdots & \vdots & \vdots \\ \left. \frac{\partial\nu_g}{\partial x_b} \right|_{N_t} & \left. \frac{\partial\nu_g}{\partial y_b} \right|_{N_t} & 0 & 0 & 0 & 1 \end{pmatrix} \quad (17)$$

<sup>2</sup>The geometric fringe frequency is defined by  $\nu_g \equiv \omega \sigma \dot{\tau}_g$ .



The weighted least-squares solution for  $p$  is given by the standard matrix expression (Ref. 10)

$$\hat{p} = (A^T W A)^{-1} A^T W u \quad (18)$$

where the diagonal weighting matrix  $W$  is given by

$$W = \begin{pmatrix} \frac{1}{\sigma_{\tau_1}^2} & & & 0 \\ & \frac{1}{\sigma_{\tau_2}^2} & & \\ & & \ddots & \\ & & & \frac{1}{\sigma_{\tau_{N_t}}^2} \\ 0 & & & & \frac{1}{\sigma_{\nu_1}^2} \\ & & & & & \ddots \\ & & & & & & \frac{1}{\sigma_{\nu_{N_f}}^2} \end{pmatrix} \quad (19)$$

In the absence of *a priori* information concerning the model parameters, the vector  $\hat{p}$  is the best estimate of the solve-for parameters. In the weighting matrix  $W$ ,  $\sigma_{\tau_i}$  and  $\sigma_{\nu_i}$  are the *total* measurement error ( $1\sigma$ ) on each delay and frequency observable. In this solution, it is assumed that the noise on a given observable is uncorrelated with the noise on any other observable, so that the off-diagonal elements of  $W$  are zero. For the present experiments, this assumption can be partially justified as follows. Delay and frequency observables are uncorrelated since, as revealed by the fits, the dominant uncertainty in delay is system noise, while in the frequency observable, the dominant uncertainty is due to some unmodeled noise source, probably unpredictable ionospheric variations. The observables obtained from different tape-pairs are uncorrelated with regard to system noise. It is assumed that the unmodeled frequency noise is also uncorrelated between tape-pairs.

The *a priori* observable noise was assigned on the basis of instrumental factors: system noise temperature and frequency standard noise.

$$\sigma_{\tau_i}^2 = \sigma_{\tau_i}^2(s) + \sigma_{\tau_i}^2(f) \quad (20)$$

$$\sigma_{\nu_i}^2 = \sigma_{\nu_i}^2(s) + \sigma_{\nu_i}^2(f) \quad (21)$$

where  $s$  denotes system noise and  $f$  denotes frequency standard noise. The system noise contribution to each observable was calculated by a covariance analysis based on amplitude noise on the fringes. (The fringe signal-to-noise ratio in this experiment is determined primarily by the usual factors: system noise temperature, correlated flux, and bit count per fringe point.) The frequency standard noise terms were assigned the following values based on typical JPL hydrogen maser stability ( $\Delta f/f \approx 10^{-14}$ ). In the frequency domain, expected H-maser frequency noise is about 23  $\mu$ Hz at S-band for 700-s integration times. In the time domain, the effective delay (phase) noise introduced by the oscillators is estimated to be about 0.08 ns for 8 h of data. This delay noise estimate is considerably below the standard estimate ( $\Delta \tau_i \approx 10^{-14} \times 8 \text{ h} \approx 0.3 \text{ ns}$ ) because of the least-squares fitting procedure. That is, the delay offset and linear drift parameters contained in the fit absorb most of the delay excursions due to H-maser instability.

After a given fit, the best estimate of the fit function is given by

$$\hat{u} = A \hat{p} \quad (22)$$

The fit residuals for this process are given by the difference between the observables and the fit function:

$$\Delta u \equiv u - \hat{u} \quad (23)$$

Before the final simultaneous fit to both delay and frequency observables, preliminary fits were made *independently* to each observable type. These preliminary fits were used to establish the actual noise level in each observable type and to check for consistency in the resulting baseline (equatorial component) solutions. In the *first* independent fit to a given observable type, the weighting errors were assigned the *a priori* values based on instrumental factors in Eqs. (20) and (21). On the basis of this first fit using instrumental error estimates, fit residuals can be calculated for the data type under investigation. The noise exhibited by these residuals can be tested for conformity with the *a priori* error estimates by means of chi-square analysis. The fit chi-square is calculated according to the standard expression

$$\chi_h^2 = \frac{1}{N_f} \sum_{i=1}^{N_f} \frac{(h_i - \hat{h}_i)^2}{\sigma_{h_i}^2} \quad (24)$$

where  $h$  denotes either the delay or the frequency data type and  $\sigma_{a_i}$  is the *a priori* error in each observable. The quantity  $N_f$  is the number of degrees of freedom given by

$$N_f = N_t - N_p \quad (25)$$

where  $N_p$  is the number of solve-for parameters ( $N_p$  is 3 for frequency observables and 5 for delay). If the fitting assumptions are correct, it can be shown that the chi-square value will be given on the average by

$$\langle \chi^2 \rangle = 1.0 \pm \frac{1}{(2N_f)^{1/2}} \quad (26)$$

If the preliminary chi-square, based on instrumental noise, falls considerably above this range ( $> 2$ ), then either the observable model is inadequate or the observable noise is higher than expected.

In the present data reduction efforts, the preliminary chi-square for a given data-type did fall above the allowed range in certain cases. However, in those cases, the extra noise on the residuals appeared to be uniformly distributed with no trends or singularly bad points. Therefore, the total noise on that observable type was uniformly increased by adding an extra error term as follows:

$$\sigma_{\tau_i}^2 = \sigma_{\tau_i}^2(s) + \sigma_{\tau_i}^2(f) + N_{\tau}^2 \quad (27)$$

for delay observables and

$$\sigma_{\nu_i}^2 = \sigma_{\nu_i}^2(s) + \sigma_{\nu_i}^2(f) + N_{\nu}^2 \quad (28)$$

for frequency observables. The least-squares fit was then rerun for that data-type and the extra error term ( $N_{\tau}$  or  $N_{\nu}$ ) was adjusted to make chi-square equal to 1.0. Formally, this procedure assumes that the total observable noise contains, in addition to the expected instrumental noise, an extra noise source that affects all tape-pairs equally without correlations between tape-pairs. The principal argument in favor of this error adjustment procedure is that it is the simplest reasonable assumption that one can make when confronted with large, uniformly random residuals due to an unmodeled noise source. Furthermore, since large uniform residuals indicate degradation of the solution, this procedure, in a gross sense, accounts for this degradation in the fit and in the resulting covariance analysis for parameter errors.

After the observable noise was determined independently for each observable type by means of the chi-square analysis outlined above, the resulting observable

weighting errors were used in a *simultaneous* fit to the delay and frequency observables to determine the baseline. This procedure was repeated for each experiment in Table I, producing one baseline measurement per experiment.

After the final simultaneous fit, including error adjustments, the covariance error for the solve-for parameters was calculated by the standard expression (Ref. 10)

$$(\sigma_p)_k^2 = (A^T W A)^{-1}_{kk} \quad k = 1, N_p \quad (29)$$

where

$$\sigma_p = (\sigma_{x_b}, \sigma_{y_b}, \sigma_{z_b}, \sigma_{\tau_s}, \sigma_{\tau_r}, \sigma_{\nu_s})$$

These covariance error values will be referred to as the formal precision.

## VI. Results and Discussion

The Goldstone baseline has been measured in five separate experiments by means of radio interferometry. The first of these experiments, in January, 1971, involved only fringe frequency measurements. Since that experiment has been described in a previous report (Ref. 2), only the resulting baseline value will be included here. This section will outline the fitting results for the four subsequent bandwidth synthesis experiments. The fits to the delay observable will be discussed first, followed by the fringe frequency results.

The delays observed in the first bandwidth synthesis experiment are shown in Fig. 6. This set of observations covered about 14 h and involved 15 separate radio sources. Each data point represents the delay value obtained from one 12-min tape-pair. These delays were measured using two 24-kHz channels separated by 10 MHz at S-band with H-maser frequency standards at each station. Note the delay offset and the linear drift that has been introduced by the instrumentation. The scatter in these delay values is due to an intentional 4-m bias in the *a priori* baseline that maps into a delay error which changes as the antennas move from source to source. After a least-squares fit for the baseline vector, delay offset, and delay rate, the delay values in Fig. 6 produce the reduced residuals in Fig. 7. Note that these residuals exhibit a fairly uniform scatter and an RMS spread of 4.7 ns.

Delay values measured in the second experiment (8/16/72) are shown in Fig. 8. In this case, the two 24-kHz channels were separated by 40 MHz, as discussed in Section III. This set of observations covered about 8 h and

involved 15 separate radio sources. Again, the scatter in delay values is due to an intentional error in the *a priori* baseline. After the least-squares fit, this wide scatter is reduced to the small delay residuals in Fig. 9 with an RMS spread of 0.5 ns. By contrasting these residuals with the residuals of the 10-MHz system in Fig. 7, one readily sees the improved precision of the larger synthesized bandwidth (note the scale change).

For the 40-MHz system, delay noise due to system noise temperature was 0.1–1.0 ns for correlated source strengths between 1 and 10 flux units. H-maser flicker noise ( $\Delta f/f \approx 10^{-14}$ ) should contribute negligible delay noise ( $\approx 0.08$  ns) for 8-h fit intervals. In the fit to the delay observables in the first 40-MHz experiment (Fig. 9), an additional noise term  $N_r$  equal to 0.25 ns had to be included to bring the delay chi-square value down to its proper range (see Section V for a discussion of observable noise adjustment). Because of this extra noise, the instrumentation configuration was checked for possible noise sources. In that configuration, the upper channel was on the wing of the system bandpass, down 30 dB from the bandpass center. In order to eliminate the possibility of differential phase instability due to this situation, the system bandpass was broadened by removing the S-band preselector in the DSIF receiver and by adjusting the maser magnetic field for the last two experiments. When the delay data were analyzed for these two reconfigured experiments, no extra delay noise was required to place the delay chi-square in its proper range. This fitting result is readily ascertained graphically by noting that the delay residuals for the last two experiments, Figs. 10 and 11, are less noisy than the residuals in Fig. 9. An upper limit on possible unmodeled noise sources can be established by increasing the noise term  $N_r$  to the level that causes  $\chi^2_r$  to fall below 1.0 by  $2\sigma$ . For the last two experiments, the value of  $N_r$  required for such a  $\chi^2$  reduction is 6 cm. This result indicates that no unexpected (e.g., noninstrumental) noise sources greater than 6 cm were present in the delay observable.

The fact that the delay residuals were at the system noise limit places an upper bound on the differential ionosphere delays since the ionosphere effect should exhibit a fairly random sign and magnitude. That is, as the antennas move from source to source, the interferometer ray paths pierce areas of the ionosphere hundreds of kilometers apart. Since one would expect localized spatial inhomogeneities ( $\leq 16$  km) to be dissimilar over such a wide range, the differential ionosphere delays are probably fairly random and appear as delay noise. Therefore, because the delay residuals place a limit on additional noise, the differential ionosphere delays were evidently less than 6 cm.

In the fringe frequency fits, the residuals exhibited a random distribution with an rms spread of 0.1–0.2 mHz. An example of the frequency residuals is shown in Fig. 12. In all experiments the noise observed in the frequency residuals was considerably above the expected instrumental noise. For example, the expected instrumental frequency noise due to system noise temperature is 20–60  $\mu$ Hz for correlated source strengths between 3 and 10 flux units. In addition, H-maser flicker noise can contribute an uncertainty of about 25  $\mu$ Hz. However, for the last four experiments, the fitting procedure outlined in Section V required an additional noise term  $N_f$  equal to 0.1–0.2 MHz to bring the frequency chi square down to its proper range. The origin of this extra noise could easily be the ionosphere. For example, if the differential ionospheric delay changed by 1 cm in 700 s (one tape-pair), the frequency effect would be 0.15 mHz at S-band. Since the ionosphere delay for a single ray path is 1 m, differential delay changes of this magnitude (1%) seem reasonable.

The baseline components produced by all five experiments are shown in Table 4 and in Figs. 13 and 14. Note that as the frequency system stability improved and as bandwidth synthesis was introduced, the formal precision in the equatorial components steadily improved from 30 cm to about 3–5 cm. For the z-component, the improvement in measurement precision is even more dramatic. The first experiment (January, '72) did not determine the z-component, since only fringe frequency was measured. The second experiment (April, '72), with a 10-MHz synthesized bandwidth, measured the z-component with a formal precision of 45 cm. The last two experiments, utilizing a 40-MHz synthesized bandwidth, determined the z-component with a formal precision of about 3 cm. The three baseline components are easily combined to give the total length plotted in Fig. 14. Note that for all three components and the total length, all interferometry baseline measurements are in excellent agreement within the formal precision. This agreement indicates that the formal covariance errors described in Section V are accurate estimates of actual precision for the present system.

The baseline vector between DSS 12 and DSS 14 has also been determined by conventional survey techniques (Ref. 11) as indicated in Figs. 13 and 14 and in Table 4. Note that the *length* of the baseline vector obtained by geodetic traverse is in excellent agreement with the interferometry result. However, the results for the three components do not agree, particularly the z-component where the disagreement is about 60 cm ( $3\sigma$ ). Both the interferometry and survey techniques are being investigated to determine the source of this disagreement.

## VII. Summary and Conclusions

A series of Goldstone baseline (16-km) measurements have been conducted to demonstrate the feasibility of eventually using radio interferometry to monitor tectonic motion. In the course of these experiments, frequency- and phase-stable instrumentation was developed to allow delay measurements by means of two-channel bandwidth synthesis. The final system synthesized a 40-MHz bandwidth using a 24-kHz bandwidth digital recording system and H-maser frequency standards. The delay measurements produced by this system lead to precise three-dimensional baseline measurements. Because of instrumental improvements, the formal baseline precision improved from 30 cm to 4 cm with about 8 hours of data. In the last measurements, the delay residuals were found to lie at the system noise limit. This fact indicates that those delay observables were free of unmodeled noise

above the 6-cm level. In addition, the three most precise baseline measurements were in excellent agreement within the expected statistics, which indicated a formal precision of 2–5 cm for the various components. This agreement strongly indicates that formal baseline errors produced by covariance analysis were good estimates of the actual precision of the present system.

Since instrumental precision is independent of baseline length, these Goldstone measurements demonstrate the feasibility of measuring baseline vectors of several thousand kilometers with ultimate accuracies of 1–4 cm. However, attainment of this accuracy for longer baselines will require additional calibrations for transmission media effects and whole-Earth motions such as universal time (UT1), polar motion, precession, and nutation.

## Acknowledgments

The authors wish to acknowledge the contributions of C. J. Finnie, H. F. Fliegel, J. Gunckle, S. Petty, T. Sato, R. Sydnor, and J. G. Williams, of the JPL staff, and the personnel of the DSN Mars and Echo stations, particularly the servo, digital, and microwave subsystem operators.

## References

1. Rogers, A. E. E., "Very Long Baseline Interferometry with Large Effective Bandwidth for Phase-delay Measurements," *Radio Science*, Vol. 5, No. 10, p. 1239, Oct. 1970.
2. Fanelow, J. L., et al., *The Goldstone Interferometer for Earth Physics*, Technical Report 32-1526, Vol. V, p. 45, Jet Propulsion Laboratory, Pasadena, Calif., Oct. 15, 1971.
3. Thomas, J. B., "An Analysis of Long Baseline Radio Interferometry," in *The Deep Space Network Progress Report*, Technical Report 32-1526, Vol. VII, p. 37, Jet Propulsion Laboratory, Pasadena, Calif., Feb. 1972.
4. Thomas, J. B., "An Analysis of Long Baseline Radio Interferometry, Part II," in *The Deep Space Network Progress Report*, Technical Report 32-1526, Vol. VIII, p. 29, Jet Propulsion Laboratory, Pasadena, Calif., May 1972.

## References (contd)

5. Thomas, J. B., "An Analysis of Long Baseline Radio Interferometry, Part III," in *The Deep Space Network Progress Report*, Technical Report 32-1526, Vol. XVI, p. 47, Jet Propulsion Laboratory, Pasadena, Calif., Aug. 15, 1973.
6. Swenson, F. W., and Mathur, N. C., "The Interferometer in Radio Astronomy," *Proc. IEEE*, Vol. 56, p. 2114, 1968.
7. *Explanatory Supplement to the Ephemeris*, H. M. Stationery Office, London, 1961.
8. Melbourne, W. G., et al., *Constants and Related Information for Astrodynamic Calculations*, 1968, Technical Report 32-1306, Jet Propulsion Laboratory, Pasadena, Calif., July 1968.
9. *Notice to Users of Circular D*, Bureau International de l'Heure, Paris, March 2, 1971.
10. Solloway, C. B., *Elements of the Theory of Orbit Determination*, JPL Engineering Planning Document 255, Dec. 1964 (JPL internal document).
11. Meade, B. K., National Geodetic Survey, Rockville, Maryland, private communication for survey between Goldstone benchmarks at ECHO and MARS. W. Bollinger, JPL, private communication for surveys between DSS 12 and 13 and 14 and their respective ground level benchmarks.
12. Kristian, J., and Sandage, A., *Astrophys. J.* 162, p. 391-398, 1970.
13. Fanselow, J. L., JPL, private communication.
14. Argue, A. N., and Kenworthy, C. M., *Nature*, Vol. 228, p. 1076, 1970.
15. Hunstead, R. W., *Mon. Not. R. Astr. Soc.*, Vol. 152, p. 227-294, 1971.
16. Adgie, R. L., Crowther, J. H., and Gent, H., *Mon. Not. R. Astr. Soc.*, Vol. 159, p. 233-251, 1972.
17. Hazard, C., et al., *Nat. Phys. Sci.*, Vol. 233, p. 89, 1971.
18. Veron, M. P., *Astron. and Astrophys.*, Vol. 20, p. 471-473, 1972.

Table 1. Summary of Goldstone interferometry experiments

Experiment	Synthesized bandwidth, MHz	Observation Period, h	No. of Tape-pairs	No. of Sources	Observables
A (71/1/29)	—	11	37	14	Frequency
B (72/4/4)	10	14	37	15	Frequency, delay
C (72/8/16)	40	8	25	15	Frequency, delay
D (72/10/14)	40	7	24	18	Frequency, delay
E (72/10/18)	40	7	19	13	Frequency, delay

Table 2. Sources used in Experiments B-E\*

Source	Position (1950.0)		Approximate correlated flux (f.u.)	Observations <sup>a</sup> per experiment		Reference
	$\alpha_s$	$\delta_s$				
P 0106 + 01	1 6 4.48 $\pm$ 0.024	1 19 1.45 $\pm$ 0.3	1.7 - 2.5	B(1) D(1)	C(2) F(0)	12
DW 0224 + 67	2 24 41.14 $\pm$ 0.033	67 7 39.61 $\pm$ 0.5	1.1 - 1.7	B(0) D(2)	C(1) E(2)	13
P 0237 - 23	2 37 52.62 $\pm$ 0.033	-23 22 6.0 $\pm$ 0.32	4.5 - 5.5	B(0) D(3)	C(2) E(2)	12
3C 84	3 16 29.55 $\pm$ 0.02	41 19 52.2 $\pm$ 0.3	10 - 13	B(0) D(1)	C(1) E(2)	14
NRAO 190	4 40 5.27 $\pm$ 0.033	-0 23 20.0 $\pm$ 0.45	2.5 - 3	B(2) D(1)	C(0) E(2)	12
3C 138	5 18 16.525 $\pm$ 0.024	16 35 26.75 $\pm$ 0.36	5 - 6	B(0) D(1)	C(1) E(1)	12
P 0521 - 36	5 21 12.95 $\pm$ 0.028	-36 30 16.0 $\pm$ 0.68	2.5 - 3	B(0) D(1)	C(0) E(1)	15
P 0736 + 01	7 36 42.53 $\pm$ 0.028	1 43 59.9 $\pm$ 0.5	2	B(0) D(1)	C(0) E(0)	15
4C 55.16	8 31 4.38 $\pm$ 0.05	55 41 41.8 $\pm$ 0.4	8	B(3) D(1)	C(0) E(1)	16
P 0834 - 20	8 34 24.56 $\pm$ 0.04	-20 6 29.7 $\pm$ 0.45	2	B(3) D(1)	C(0) E(1)	12
P 1127 - 14	11 27 35.61 $\pm$ 0.033	-14 32 54.0 $\pm$ 0.15	3 - 5	B(4) D(0)	C(0) E(0)	12
3C 273	12 26 33.239 $\pm$ 0.013	2 19 43.28 $\pm$ 0.2	15 - 2	B(6) D(0)	C(0) E(0)	17
3C 309.1	14 58 56.70 $\pm$ 0.06	71 52 10.6 $\pm$ 0.32	3 - 3.5	B(4) D(0)	C(1) E(0)	12
3C 345	16 41 17.56 $\pm$ 0.033	39 54 10.7 $\pm$ 0.36	7 - 8	B(4) D(1)	C(2) E(0)	12
NRAO 530	17 30 13.43 $\pm$ 0.04	-10 2 46.2 $\pm$ 0.54	2.5 - 3	B(0) D(1)	C(1) E(0)	12
P 1741 - 038	17 41 20.61 $\pm$ 0.033	-3 48 49.2 $\pm$ 0.5	2.5 - 3	B(1) D(1)	C(1) E(0)	13
3C 371	18 7 18.49 $\pm$ 0.04	69 48 57.55 $\pm$ 0.36	1.5 - 2	B(2) D(1)	C(2) E(1)	12
P 2134 + 004	21 34 5.28 $\pm$ 0.033	0 28 25.9 $\pm$ 0.5	5.5 - 7	B(2) D(2)	C(1) E(1)	18
VRO 42.22.01	22 0 39.31 $\pm$ 0.04	42 2 9.0 $\pm$ 0.4	5.5 - 7	B(2) D(2)	C(3) E(3)	16
P 2203 - 16	22 3 25.675 $\pm$ 0.028	-16 50 16.8 $\pm$ 0.28	3.5 - 5	B(1) D(2)	C(4) E(1)	12
3C 454.3	22 51 20 485 $\pm$ 0.033	15 52 54.45 $\pm$ 0.45	10 - 11	B(1) D(1)	C(2) E(1)	12
P 2345 - 16	23 45 27.70 $\pm$ 0.028	16 47 52.7 $\pm$ 0.42	2.5	B(1) D(0)	C(1) E(0)	15

\*See Table 1.

Table 3. Time and polar motion parameters used in Experiments B-E

Experiment	UT1 - UTC, s	$X_p/a$ arc second	$Y_p/a$ arc second
B 4/4/72	-0.356	-0.192	+0.185
C 8/16/72	+0.244	+0.102	+0.433
D 10/14/72	+0.068	+0.164	+0.315
E 10/18/72	+0.055	+0.167	+0.306

Table 4. Goldstone baseline\* measurements

Experiment	X-component, m	Y-component, m	Z-component, m	Total length, m
A (1/29/71)	-3178.40 $\pm$ 0.20	10636.9 $\pm$ 0.30	Not measured	-
B (4/4/72)	-3178.57 $\pm$ 0.11	10637.08 $\pm$ 0.08	11423.34 $\pm$ 0.45	15929.33 $\pm$ 0.33
C (8/16/72)	-3178.515 $\pm$ 0.047	10637.111 $\pm$ 0.073	11423.103 $\pm$ 0.055	15929.167 $\pm$ 0.042
D (10/14/72)	-3178.548 $\pm$ 0.025	10637.041 $\pm$ 0.045	11423.154 $\pm$ 0.034	15929.164 $\pm$ 0.021
E (10/18/72)	-3178.568 $\pm$ 0.026	10637.132 $\pm$ 0.046	11423.115 $\pm$ 0.033	15929.196 $\pm$ 0.031
Survey 1963-66	-3178.73 $\pm$ 0.20	10636.64 $\pm$ 0.20	11423.67 $\pm$ 0.2	15929.30 $\pm$ 0.2
*DSS 14-DSS 12.				



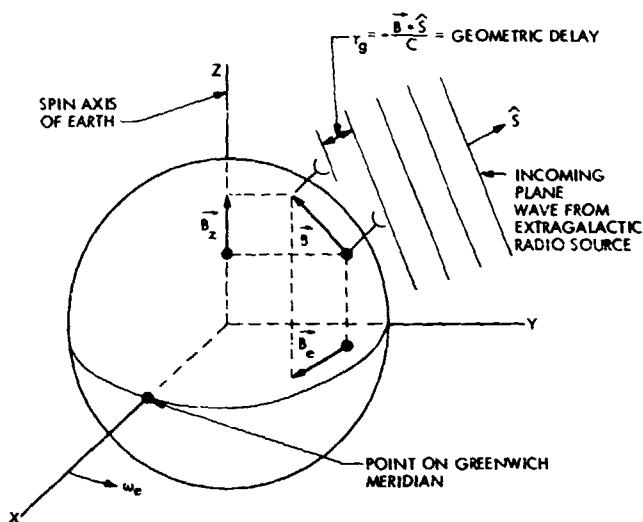


Fig. 1. Geometry of radio interferometry experiments

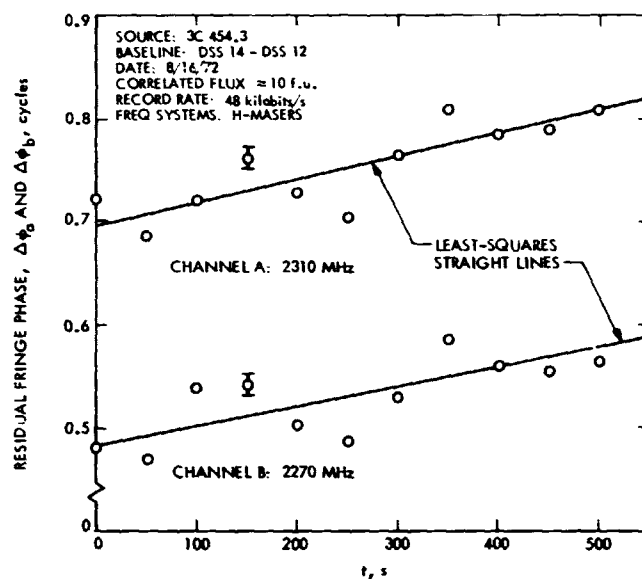


Fig. 3. Fringe phase values for two-channel bandwidth synthesis

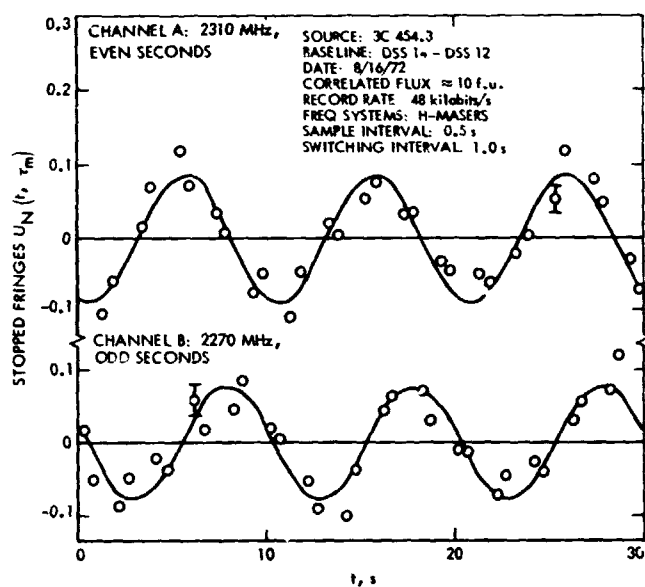


Fig. 2. Stopped fringes for two-channel bandwidth synthesis

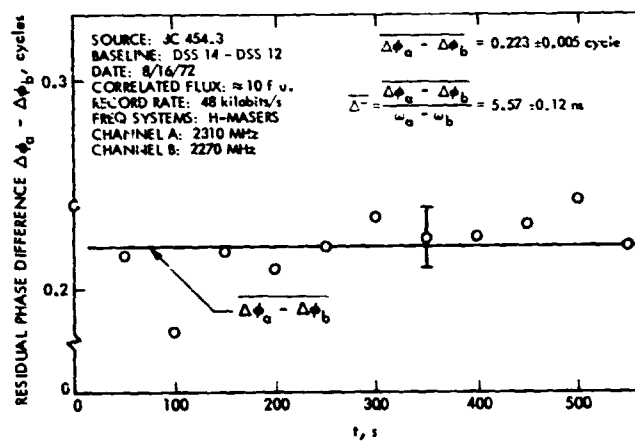


Fig. 4. An example of a delay calculation with two-channel bandwidth synthesis

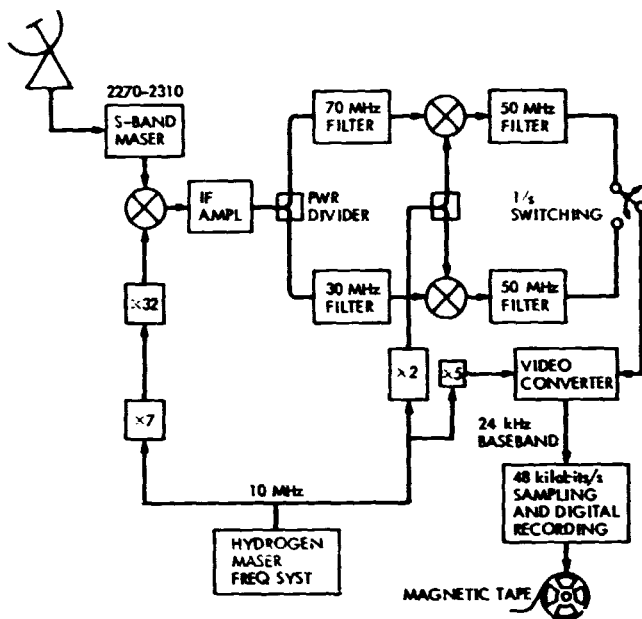


Fig. 5. Deep Space Station configuration for 40-MHz bandwidth synthesis

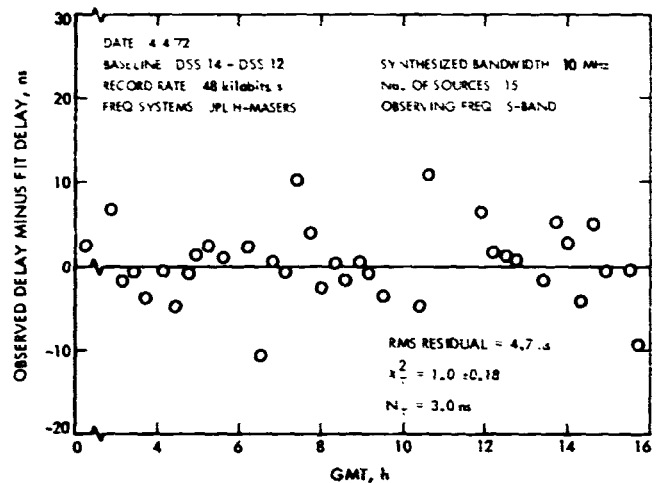


Fig. 7. Fit delay residuals for Experiment B

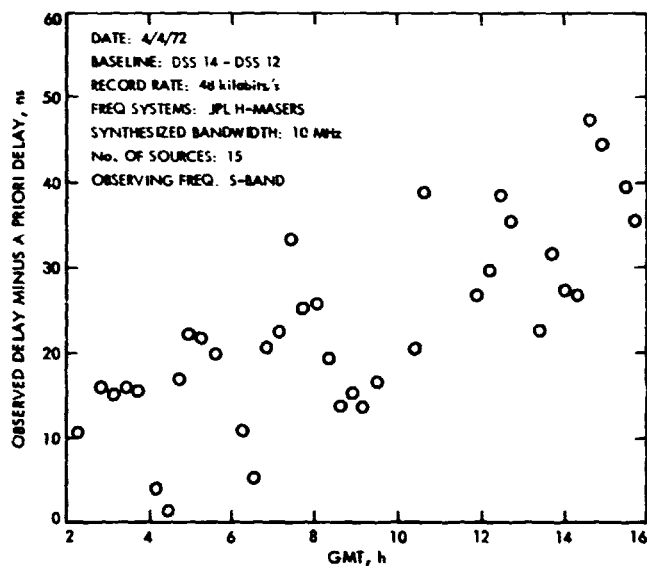


Fig. 6. A priori delay residuals for Experiment B

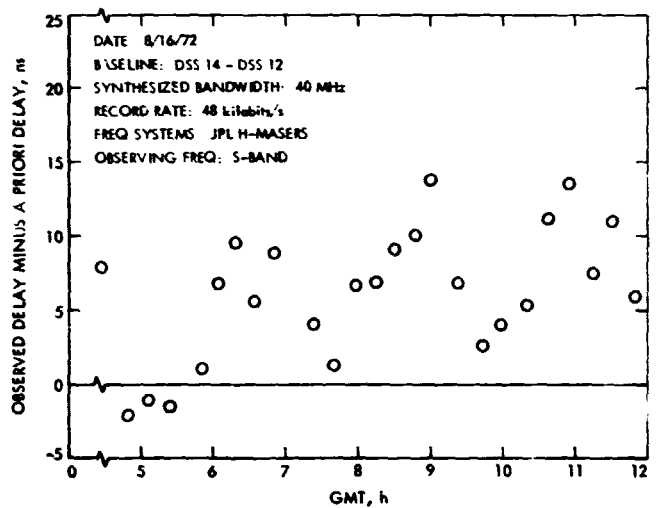


Fig. 8. A priori delay residuals for Experiment C

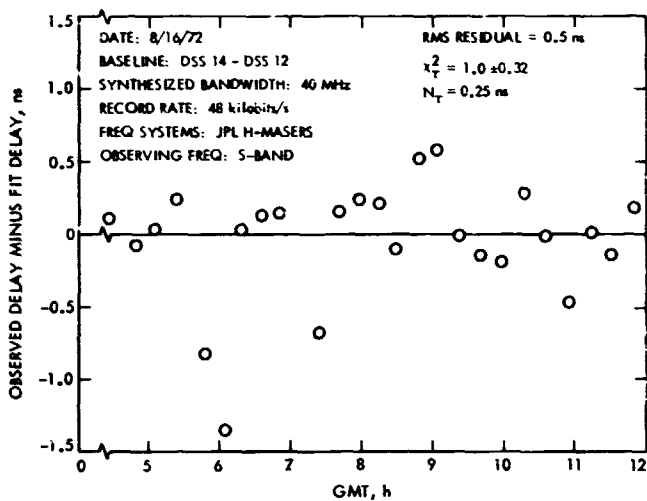


Fig. 9. Fit delay residuals for Experiment C

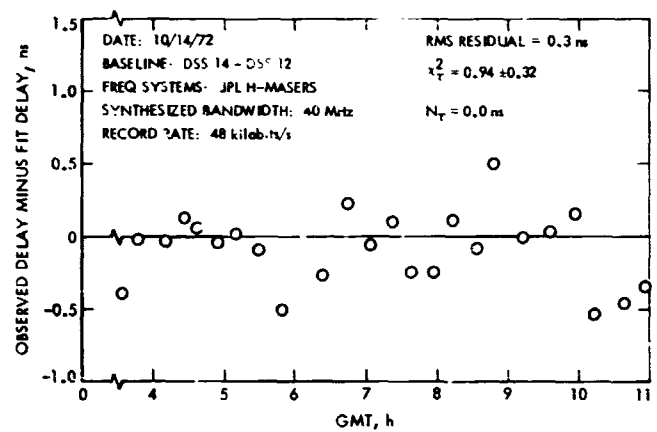


Fig. 10. Fit delay residuals for Experiment D

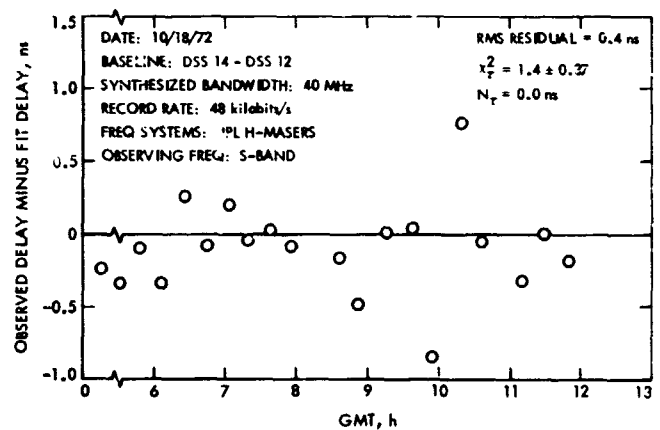


Fig. 11. Fit delay residuals for Experiment E

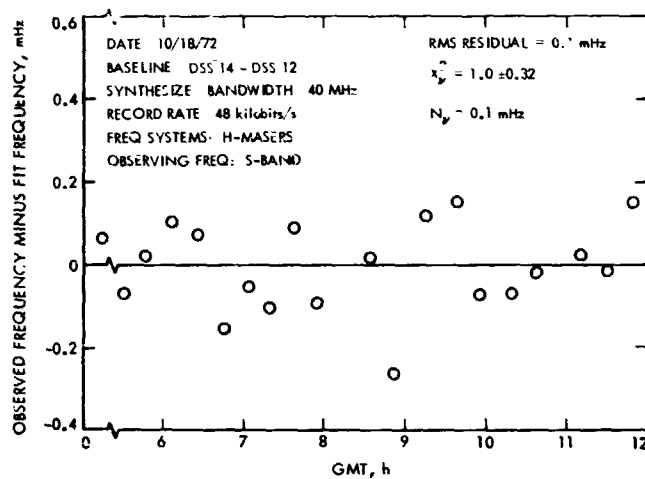


Fig. 12. Fringe frequency residuals for Experiment E

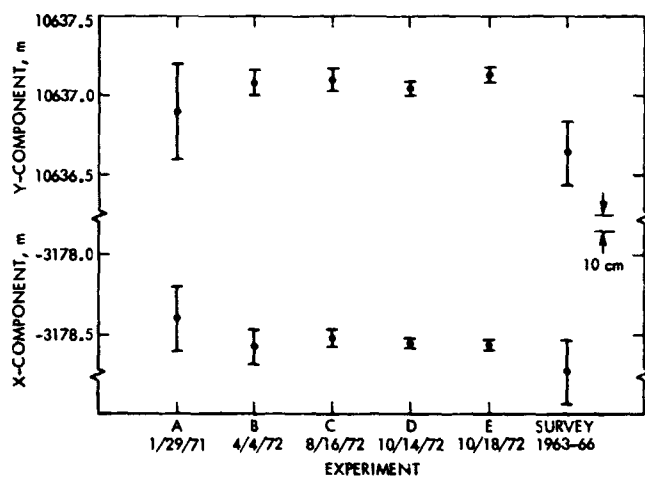


Fig. 13. Goldstone baseline measurements—  
equatorial projection

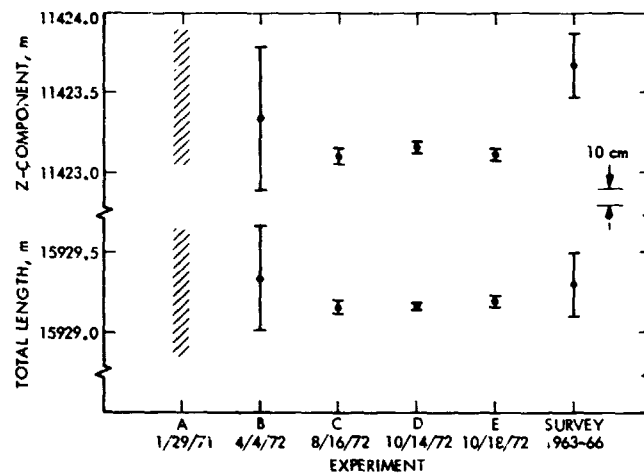


Fig. 14. Goldstone baseline measurements—  
z component and length

# Improved Dichroic Reflector Design for the 64-m Antenna S- and X-Band Feed Systems

P. D. Potter

Communications Elements Research Section

*In support of the Mariner Venus/Mercury 1973 (MVM'73) X-band experiment and planned future Mariner missions, the 64-m antenna network is being supplied with S- and X-band reflex feed systems. The initial installation, for MVM'73, was implemented at DSS 14 and provides satisfactory performance for that mission. The X-band performance of the dichroic reflector is, however, not acceptable for planned future missions which have more stringent X-band performance requirements. A new dichroic reflector which grossly reduces the X-band ellipticity and noise temperature degradation has been designed. In this reporting, the theory and experimental performance of this new design is reported.*

## I. Theory of Operation

The design and performance of the existing DSS 14 reflex feed dichroic reflector (plate) was described in Ref. 1 and is shown in Fig. 1. The plate is 3.576 cm thick, with an array of hexagonally packed 2.273-cm-diameter holes drilled normal to the plate surfaces. The center-to-center hole spacing is 2.388 cm, and the required frequency of operation is 8.415 GHz.

As described in Ref. 1, the E- and H-plane plate resonant frequencies (frequencies of complete transparency) are displaced because of a difference in the E- and

H-plane free-space-to-circular waveguide transition discontinuity at the (tilted) plate surfaces. Since the plate is used with circular polarization, this resonant frequency difference causes a differential phase shift between the E- and H-plane, resulting in depolarization of the circularly polarized incident wave. Additionally, because the plate is not reflectionless for all polarizations (at a fixed frequency), a serious (approximately 2-K) noise temperature contribution results from ground radiation. Actual calculations using the Chen Holey Plate Computer Program (Ref. 2) show that the plate E- and H-plane resonant frequencies (30 deg incident wave tilt from normal) are 8.481 and 8.363 GHz, respectively. At the operation fre-

quency of 8.415 GHz, a differential phase shift of 11.3 deg and an ellipticity of 1.75 dB are predicted. Actual measured ellipticity was 1.84 dB. The reflected energy level is -18 dB at 8.415 GHz.

The approach taken to cure the dichroic plate depolarization described above was to make the holes slightly noncircular in cross section, thus introducing a differential E- and H-plane phase shift within the plate to counteract the 11.3-deg phase shift. This change is in the nature of a perturbation on the original design, rather than a redesign; the original plate thickness and hole center spacing are retained. The particular hole cross section selected is "Pyleguide" (Ref. 3). This type of guide, circular with a pair of flats on opposite sides, is used by JPL in the 64-m antenna feed system polarizers. Pyle's (1964) analysis (Ref. 3) is approximate. It is now practical to numerically solve the wave equation in a cylindrical waveguide of arbitrary cross section, yielding highly accurate guide wavelength numbers as a function of geometry. An excellent computer program for this purpose was developed by Knud Pontoppidan, formerly of the Technical University of Denmark (Ref. 4). The Pontoppidan program was modified for use on the JPL Scientific Computing Facility (SCF) Univac 1108 and set up for Pyleguide calculations.

Figures 2a and 2b show the cutoff wavelength  $\lambda_c$  as a function of Pyleguide geometry for the E- and H-planes. The design procedure for the Pyleguide dichroic plate was to adjust the guide geometry (using the Pontoppidan computer program) until the plate electrical thickness at 8.415 GHz for the E- and H-planes corresponded to those in the original circular hole plate at 8.481 and 8.363 GHz, respectively. The resulting geometry is shown in Fig. 3. The hole diameter is 0.013 cm larger than the original circular hole design, and the flat depth is 0.043 cm. Thus, the redesign is only a small perturbation on the original design.

To test the Pyleguide dichroic plate design, a sample section of plate 35 × 53 cm in size was fabricated. The holes were made with a broach, allowing tight tolerances ( $\pm 0.005$  cm) to be held on all hole dimensions. Although performance of this type of dichroic plate is relatively noncritical with regard to tolerances, the strict control was imposed both as an experiment in fabrication technique (there were no problems) and also to provide a good check between predicted and measured performance. Figure 4 is a photograph of the sample Pyleguide dichroic plate. The following section describes the measured performance.

## II. Experimental Results

The X-band performance of the Pyleguide dichroic plate sample was measured in the JPL Mesa Antenna Range anechoic chamber facility. Complete pattern data were taken at the design (and operational) frequency of 8.415 GHz; frequency-scanned pattern data were taken in the reflex feed symmetry plane. Optimum performance was observed at the design frequency of 8.415 GHz. No pattern distortion, grating lobe response, or other unexpected behavior was observed.

Figure 5 shows the radiation pattern of the corrugated feedhorn by itself. Figure 6 illustrates the pattern of the feedhorn/tilted dichroic plate combination in the plane containing the horn axis and the plate normal (symmetry plane). For these patterns, the horn was circularly polarized and the illuminator was linearly polarized but rapidly rotating about its axis. Thus, at each point in the radiation patterns, the ellipticity is displayed as a rapidly modulated signal level. As seen in Fig. 6, the ellipticity nulls out at a point 3 deg off axis and is 0.4 dB on axis. From symmetry considerations, the antenna secondary pattern axial ellipticity will be nearly the same as the feed system axial ellipticity.

In Fig. 6, the large lobe in the region of 120 deg is the reflection from the horn side of the dichroic plate. This reflection gives rise to a noise temperature contribution from ground thermal radiation when the antenna is at low elevation angles. The power-average level for the Pyleguide dichroic plate is -24.5 dB, yielding a maximum noise temperature contribution of 0.7 K. The original round-hole plate has a power-average reflection lobe level of -18.6 dB, yielding a noise contribution of 2.7 K. This latter figure has been experimentally observed at DSS 14 (see Fig. 8 of Ref. 1).

## III. Conclusion

A different type of hole, "Pyleguide," has been incorporated into the reflex feed dichroic plate design to alleviate polarization degradation and noise temperature contribution due to plate mismatch (reflection). The plate ellipticity degradation has been reduced thereby from 1.8 to 0.4 dB; the maximum noise temperature contribution has been reduced from 2.7 to 0.7 K. The ideal hole shape is a function of its location on the plate. The Pyleguide plate tested had all identical holes. Further performance improvement, if required, appears possible by use of non-identical holes. The ability to perform this type of design entirely analytically has been demonstrated.

## References

1. Potter, P. D., "S- and X-band RF Feed System," in *The Deep Space Network Progress Report*, Technical Report 32-1526, Vol. XV, pp. 54-62, Jet Propulsion Laboratory, Pasadena, Calif., June 15, 1973.
2. Chen, C. C., "Transmission of Microwave Through Perforated Flat Plates of Finite Thickness," *IEEE Transactions on Microwave Theory and Techniques*, Vol. MTT-21, No. 1, pp. 1-6, Jan. 1973.
3. Pyle, J. R., "Cutoff Wavelengths of Waveguides with Unusual Cross Sections," *IEEE Transactions on Microwave Theory and Techniques*, Vol. MTT-12, No. 5, pp. 556-557, Sept. 1964, Correspondence.
4. Pontoppidan, Knud, "Finite-Element Techniques Applied to Waveguides of Arbitrary Cross Sections, Parts I and II," Ph.D. Thesis, The Technical University of Denmark, Lyngby, Denmark, Sept. 1971.

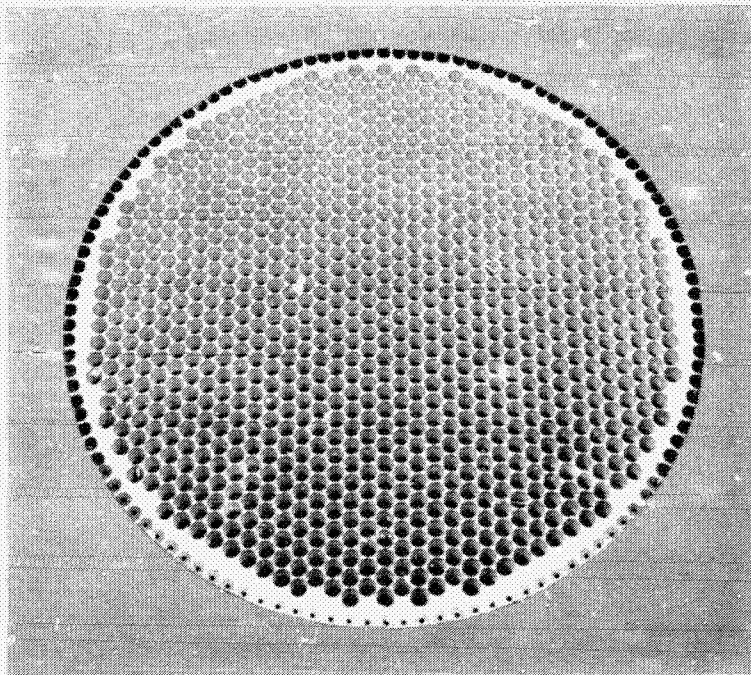


Fig. 1. Original DSS 14 dichroic reflector



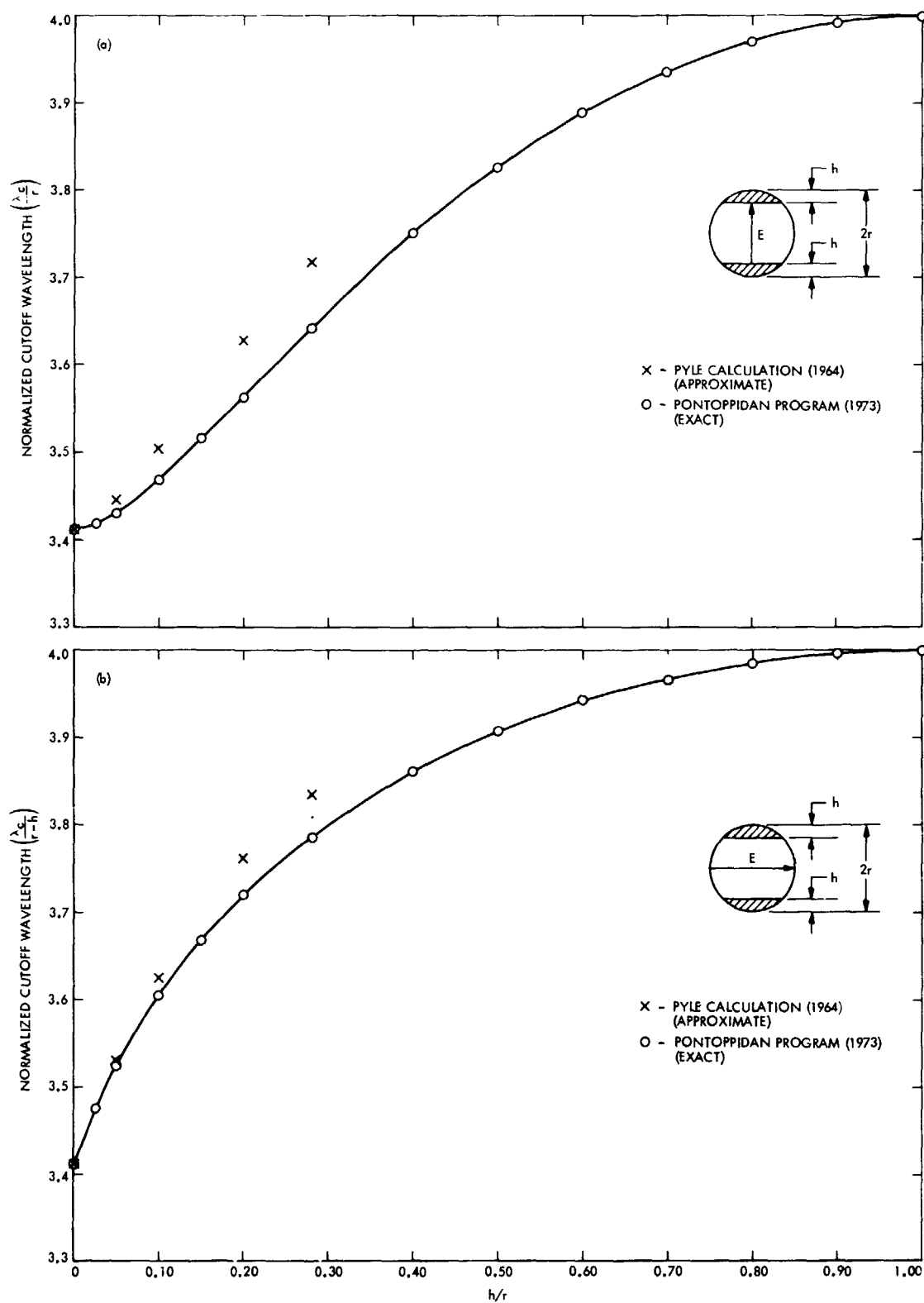


Fig. 2. Normalized cutoff wavelength of Pyleguide (a) Flats in the electric plane (b) Flats in the magnetic plane

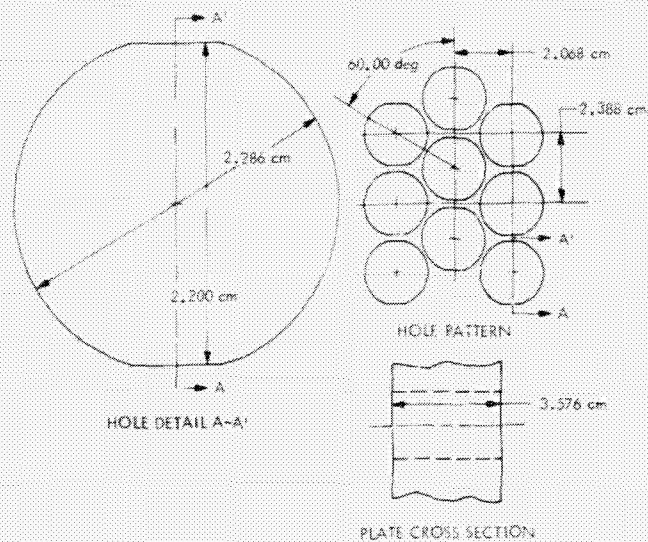


Fig. 3. Pyleguide dichroic plate geometry, 8.415 GHz

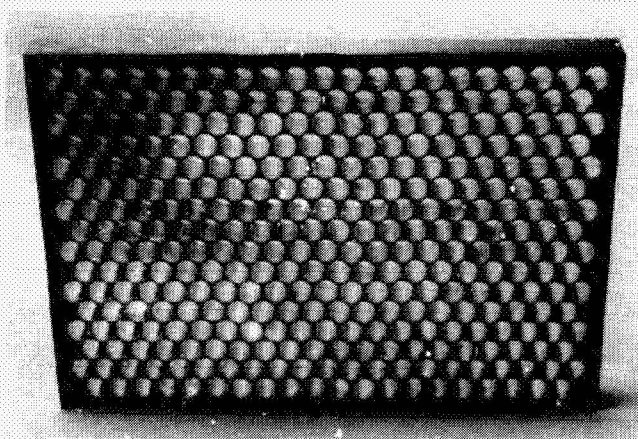


Fig. 4. Pyleguide dichroic plate sample

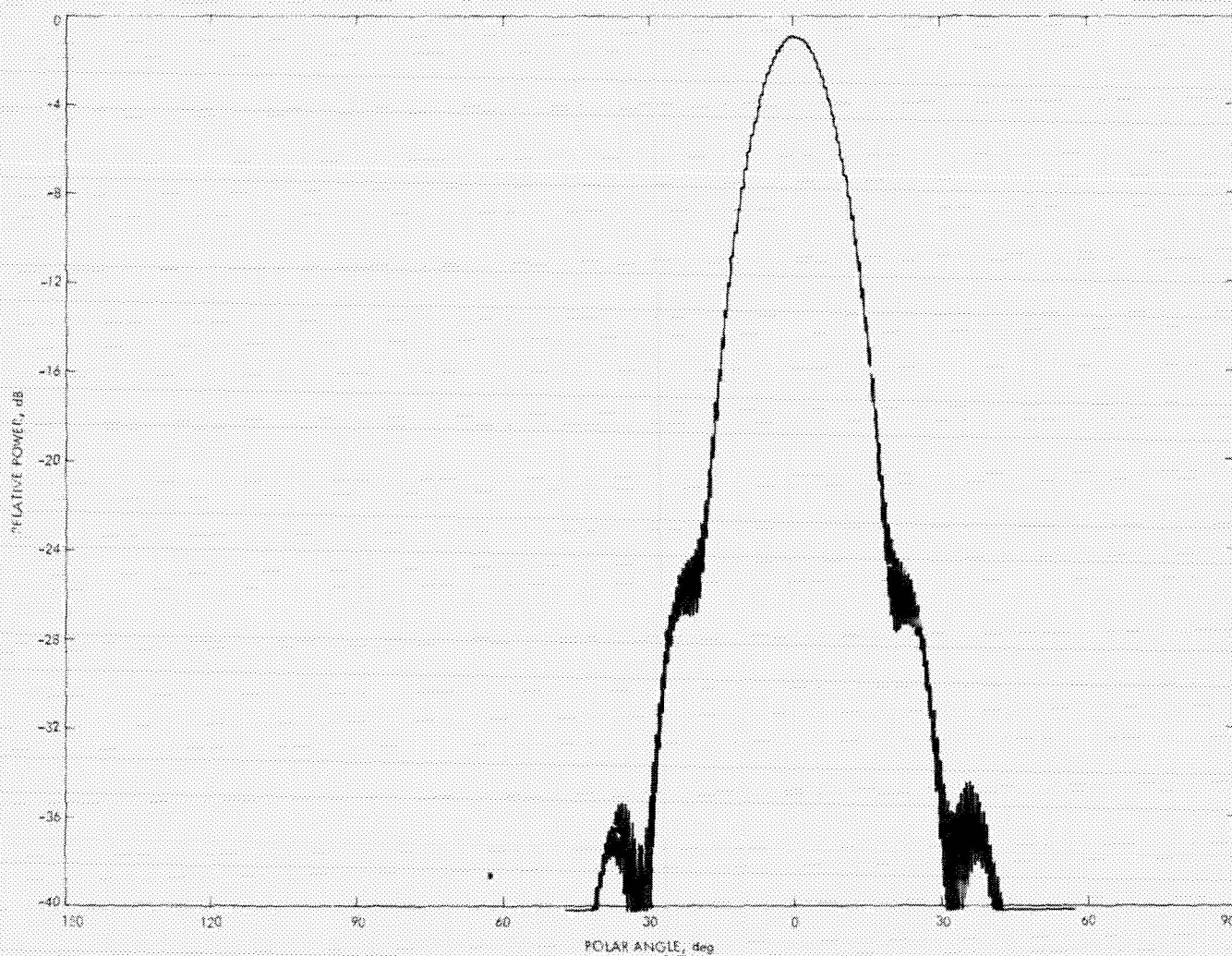


Fig. 5. Corrugated feedhorn radiation pattern, 8.415 GHz

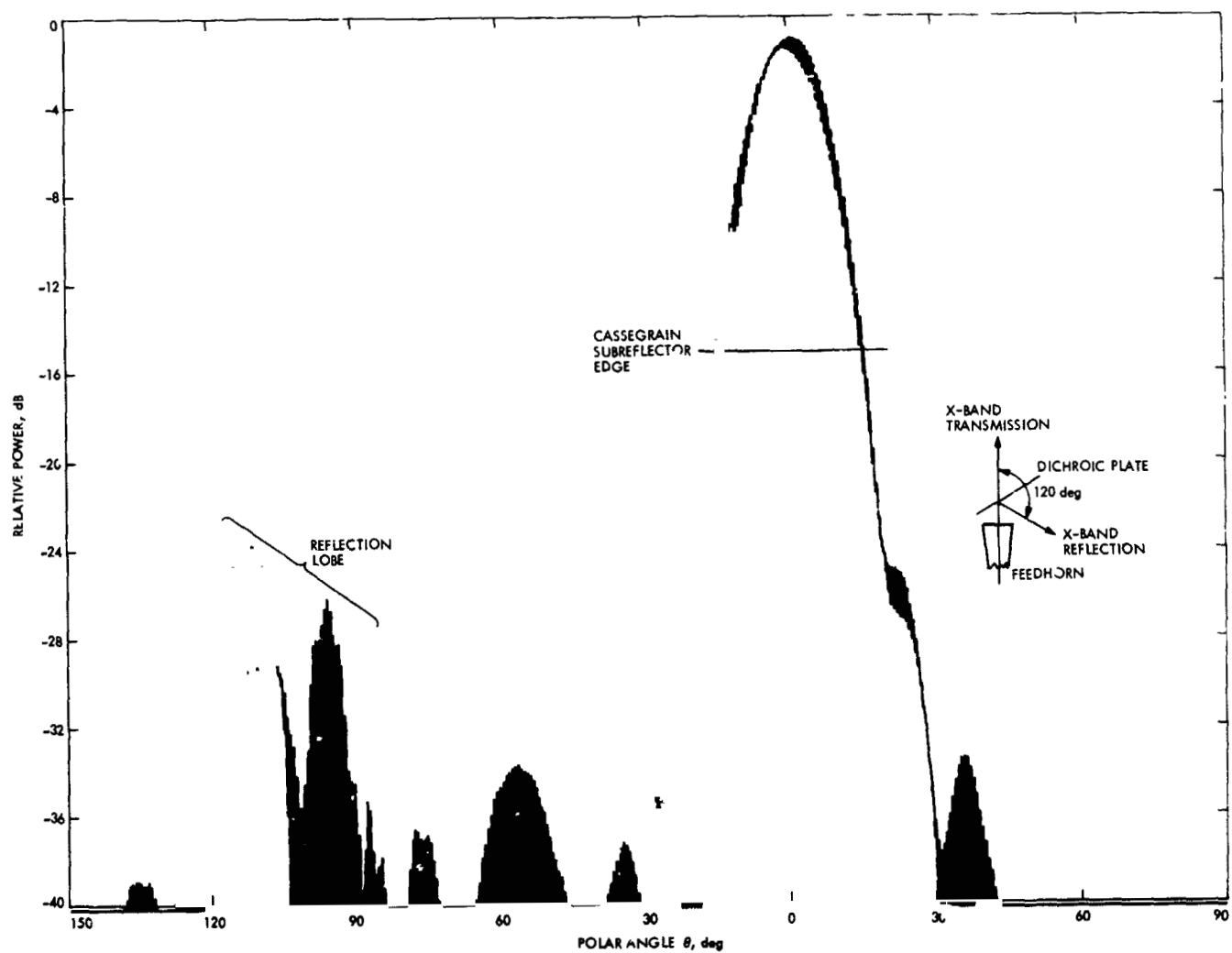


Fig. 6. Corrugated feedhorn/Pyleguide dichroic plate radiation pattern, symmetry plane, 8.415 GHz



# Range Measurements to Pioneer 10 Using the Digitally Controlled Oscillator

A. S. Liu

*Analysis of the new doppler data from DSS 14 using the Digitally Controlled Oscillator (DCO), has established that ramping the carrier frequency by the DCO will enable us to obtain range measurements to Pioneer 10 without the use of a ranging system per se. The accuracy of these measurements is on the order of 10 km.*

## 1. Introduction

The tuned oscillator range analysis (TORA) experiment utilizes the new DSN programmed oscillator device at DSS 14. This new equipment was added to DSS 14, Goldstone, California, and DSS 43, Canberra, Australia, for the purpose of tracking Pioneer 10 during Jupiter flyby. It was noted that ranging information could be obtained when the transmitted frequency was ramped by means of a digitally controlled oscillator (DCO). The returned signal shows a pattern that is dependent upon the round-trip light time, enabling measurements to be made of the distance from the station to the spacecraft.

Since the primary purpose of the installation of the DCOs was to support Pioneer 10 commanding during Jupiter encounter, training exercises were scheduled to permit station operators to become familiar with the new equipment and to establish working procedures for the Jupiter flyby. Data taken from DSS 14 were utilized during several of these training exercises, and processing of the data was begun to see if range information could be extracted. Supplied with information about the fre-

quency rates and initiation times of the DCO during those passes, the data were successfully analyzed and several round-trip range estimates of the Pioneer 10 spacecraft were made.

The concept of using ramped frequency doppler for ranging is analogous to inferring distances by an echo. By ramping the carrier frequency, a unique correspondence between time of transmission and frequency of transmission is established. Further, by noting the time and frequency of reception, one can then associate a time of transmission with that frequency, thus a time delay, or round-trip distance, is inferred.

Figure 1 is an illustration of this principle. It shows the Doppler counter readings after subtraction of reasonable estimates of shifts due to Earth and spacecraft motion, etc., computed as ordinary doppler at the initial transmitted frequency. The dashed line indicates the tuning profile of the exciter at DSS 14 as a function of time. The exciter is also used as a reference signal to heterodyne the time-delayed received signal from Pioneer 10 (effects on residuals shown as a solid line). The difference between

the reference frequency and the received signal is interpreted as Pioneer 10 "doppler data," to be used in the orbit determination process. The effects of the ramps on the received signal (solid line) are also shown, but with a delay of about 1 h, which is the time required for the signal to reach the spacecraft and return to the ground. As can be seen, the difference between the received signal and the ground reference produces the doppler residuals, which are on the order of 200 kHz.

## II. Data Analysis

Two sets of DSS 14 Pioneer 10 data were analyzed. The ramp patterns are tabulated in Tables 1 and 2. The first pass of data (Pass I) was taken on June 19, 1973, and the second (Pass II) on July 10, 1973.

### A. Pass I

To analyze this pass, we used the initial conditions of Pioneer 10, supplied by Pioneer Project Navigation. Based upon this orbit, round-trip light times for each data point were computed. The extra cycles were removed from the data according to the required light time transit.

The result is presented in Fig. 2. It is interesting to note the step residuals due to the misplacement of Pioneer 10 in this assumed trajectory by approximately 250 km. The ramped doppler data provide an additional measurement dimension not readily or directly available from conventional doppler. The unramped doppler yields a solution of the orbit by inference through the acceleration dynamics after sufficient spatial motion has occurred (about 6 weeks or longer).

The step biases are due to a trajectory round-trip light-time error times a ramp rate. Since we may regard the orbit error to be a constant over one pass, the offsets are due only to differing ramp rates. Thus, the largest offset is due to a ramp rate of 150 Hz/s. Halfway between, one sees a bias of half that caused from a ramp rate of 74.9984 Hz/s. Centered about zero are the two offsets caused by a ramp rate of  $\pm 30$  Hz/s.

### B. Pass II

A second set of data, taken on July 10, 1973, was analyzed. In the intervening period, a trim maneuver had taken place. This necessitated a solution for the new orbit. Additions were made to the code in the Planetary Orbiter Error Analysis Study (POEAS) program, which included the new data and partial derivatives required for an automatic least-squares differential-correction process. The July 10 data were sent through POEAS, and auto-

matic iterations for the solution of the new orbit were begun. After the first iteration (the best available solution was not used), the Doppler data were centered about zero, but the range was still in error by an amount equivalent to 0.5 Hz (Fig. 3). Since the ramp rates for this pass were all 100 Hz/s at S-band, the offsets were the same size and centered about zero. After the second iteration all of the biases disappeared, indicating the data derivative formulation and program coding to be correct and thus causing the solution to converge. There was a reported programmed oscillator control assembly (POCA) initiation time error of 5 s, causing residuals of 500 Hz to appear in the middle of this pass. For the sake of this demonstration rather than correcting the time inputs to the program, these data were eliminated from the data set used for the orbit solution.

When the "blunder points" were removed, we were able to adjust the orbit so that the data residuals were on the order of 1/1000 Hz. Figure 4 shows the result of this solution.

The figure shows the level to which the ramp frequency data can be fit when all the blunder points have been removed. It is evident that the only noise component remaining is the high-frequency component, and when the ramp pattern is included in the data analysis, the new DCO doppler data residuals look the same as the conventional unramped data residuals.

## III. Conclusions and Summary

Based on the analysis of two sets of Pioneer 10 ramping doppler data from DSS 14, the system shows promise of providing a new measurement dimension (i.e., range) from doppler data. The problems at present seem tractable.

Our interpretation of the data seems sound, and its incorporation into computer programs yielded reasonable results. The prototype program furnishes us with insights into the procedures for developing the navigation programs to account for this new data type in a logical manner.

In summary, as a demonstration exercise, we have

- (1) Obtained some understanding of the POCA.
- (2) Developed the software required to analyze the data from an orbital correction approach.
- (3) Interpreted our results in terms of a new data type corresponding to topocentric range to the spacecraft.

**Table 1. Ramp test pattern for June 19, 1973;  
start time  $T_0 = 9:40:00$**

Ramp No.	Ramp on time ( $T_0 - T$ )			Ramp rate (S-band) at exciter, Hz/s
	n	min	s	
1	0	0	0	150
2	0	3	20	75 <sup>a</sup>
3	0	10	00	30
4	1	27	47	0
5	1	32	47	-30
6	2	50	34	-75 <sup>a</sup>
7	2	57	14	-150
8	3	00	34	0
9	3	05	47	-150
10	2	09	07	-75 <sup>a</sup>
11	3	15	47	-30
12	4	33	34	0
13	4	38	34	30
14	5	56	21	75 <sup>a</sup>
15	6	03	01	150
16	6	06	21	0

<sup>a</sup>Actual S-band rate  $\pm 74.9984$  Hz/s.

**Table 2. Ramp test pattern for July 10, 1973**

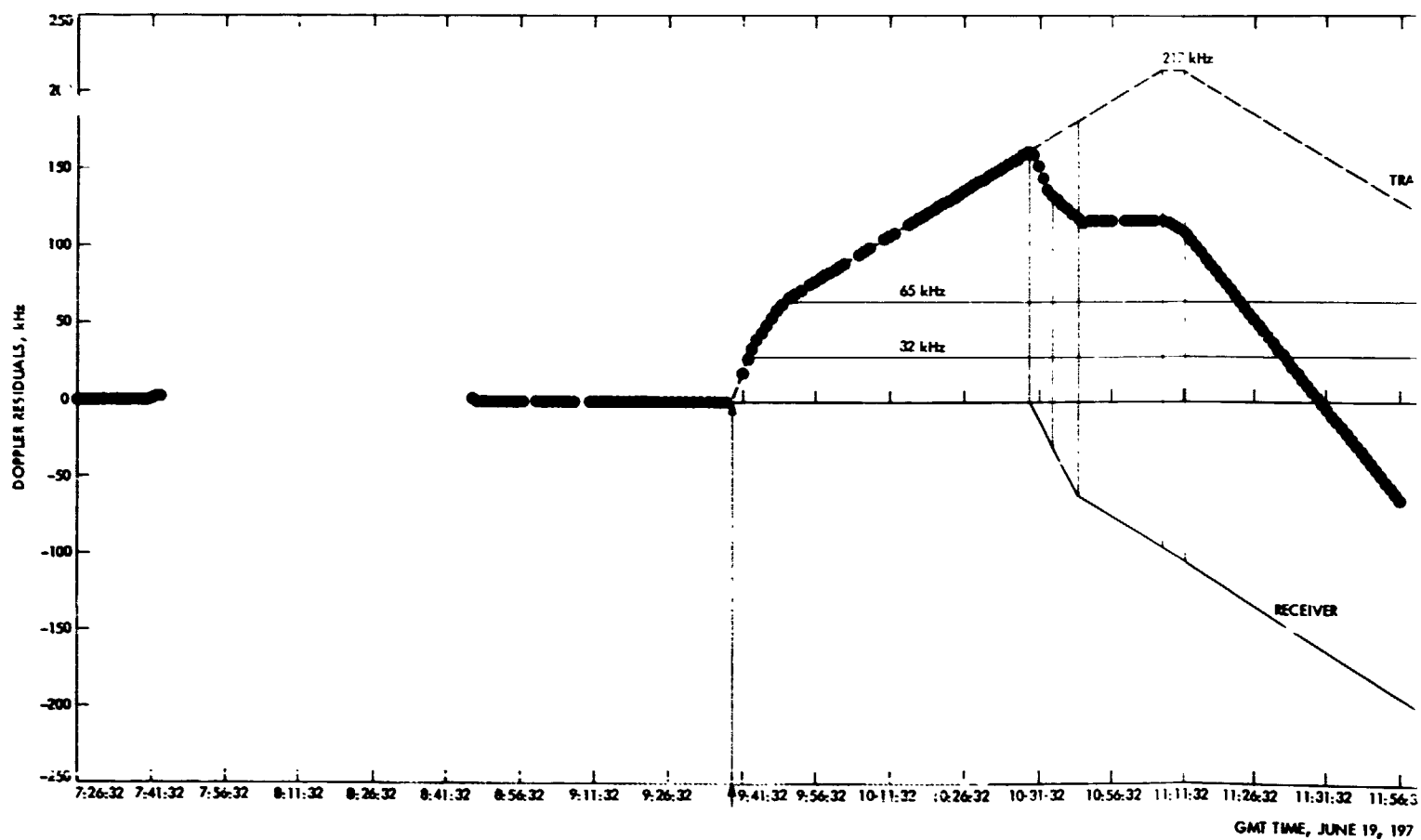
Ramp No.	Ramp on time, GMT			Ramp rate (DCO) <sup>a</sup> at exciter, Hz/s
	n	min	s	
1	06	30	00	3.125
2	06	46	40	0
3	07	09	43	-3.125
4	07	26	23	0
5	07	47	03	-3.125
6	08	03	43	0
7	08	26	46	+3.125
8	08	43	28	0
9	09	04	06	+3.125
10	09	20	46	0
11	09	43	59	-3.125
12	10	00	39 <sup>b</sup>	0
13	10	21	19	-3.125
14	10	37	59	0
15	11	01	02	+3.125
16	11	17	42	0
17	11	38	22	+3.125
18	11	55	02	0
19	12	18	04	-3.125
20	12	34	44	0

<sup>a</sup>S-band rate =  $32 \times$  DCO rate = 100 Hz/s.

<sup>b</sup>Suspected time error of -5 s.







PRECEDING PAGE BLANK NOT FILMED

JPL TECHNICAL REPORT 32-1526, VOL XIX

FOLDOUT FRAME

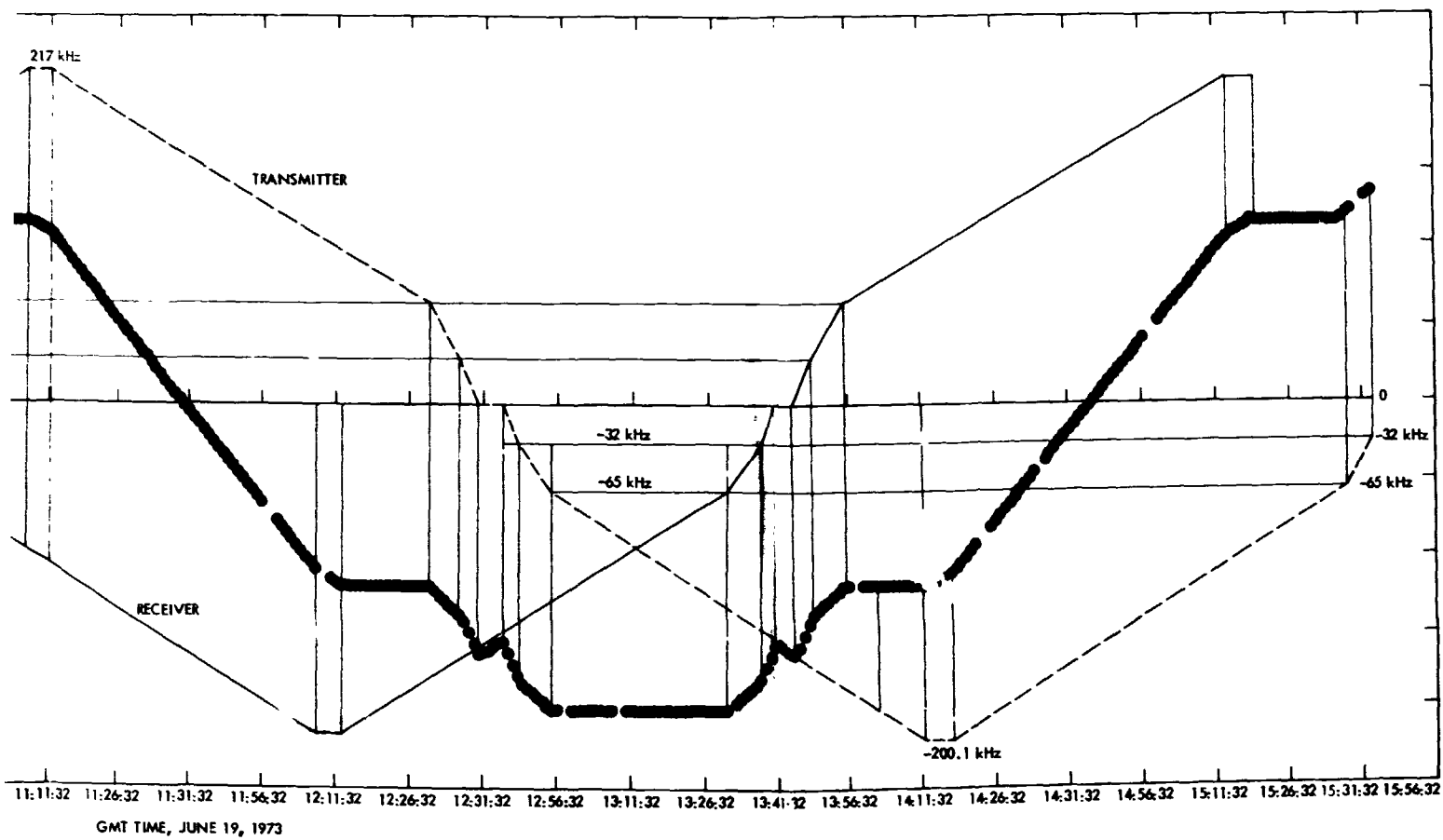


Fig. 1. Tora experiment, June 19, 1973—DSN 14 Pioneer 10 doppler residuals (effects of ramps not modeled)

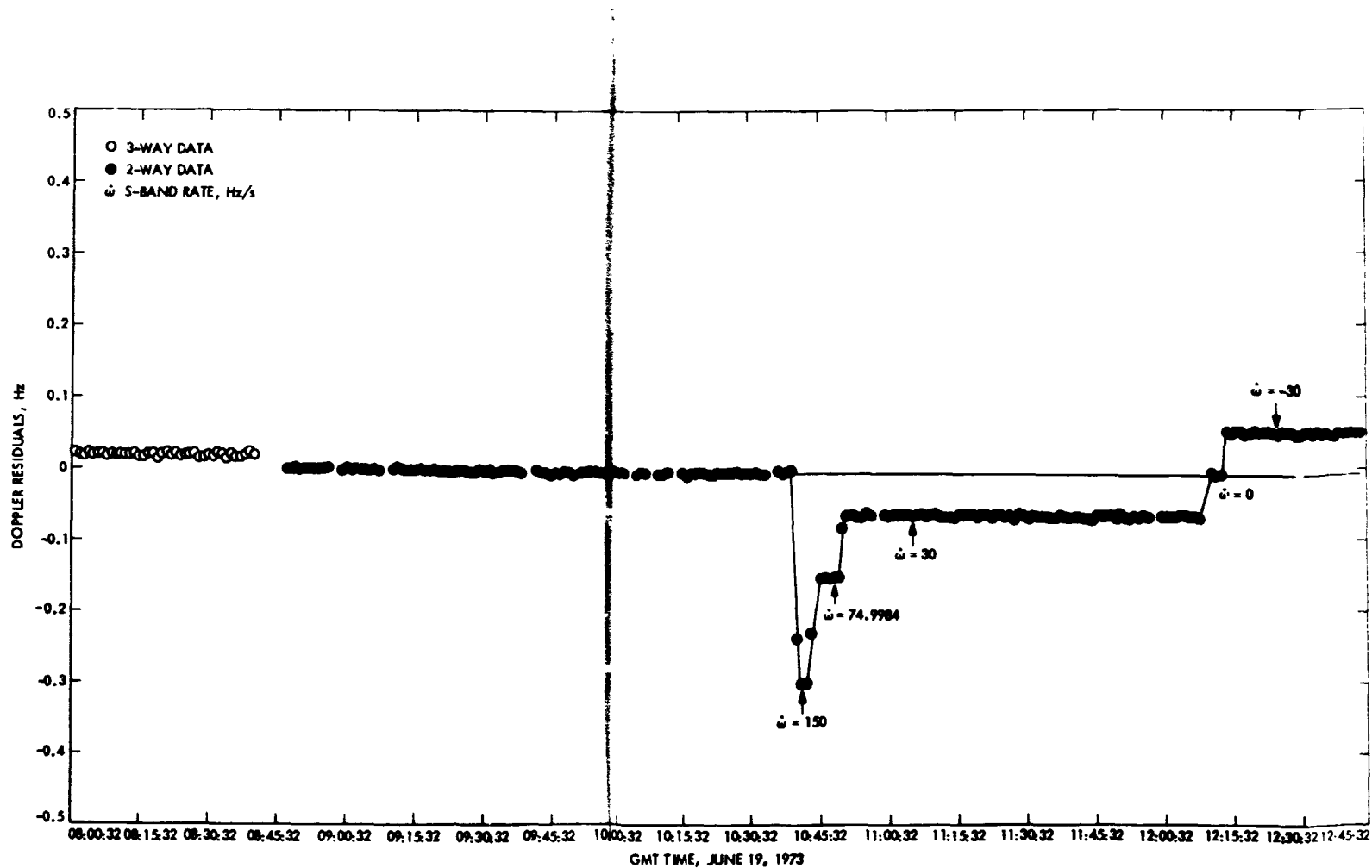
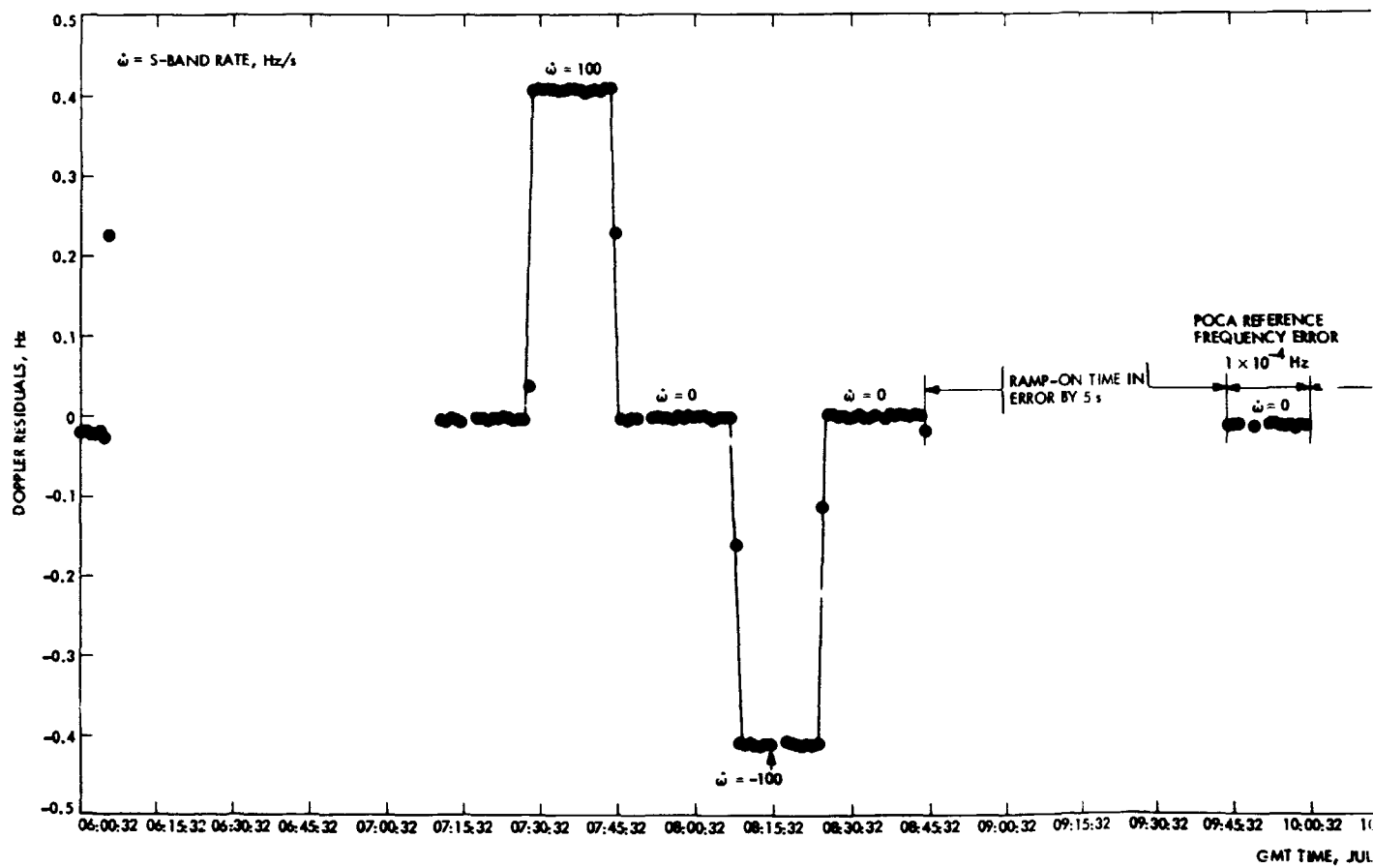


Fig. 2. Tora experiment, June 19, 1973—DSN 14 Pioneer 10 residuals (ramp effects modeled)

FOLDOUT FRAME



JPL TECHNICAL REPORT 32-1526, VOL. XIX

FOLDOUT FRAME

1

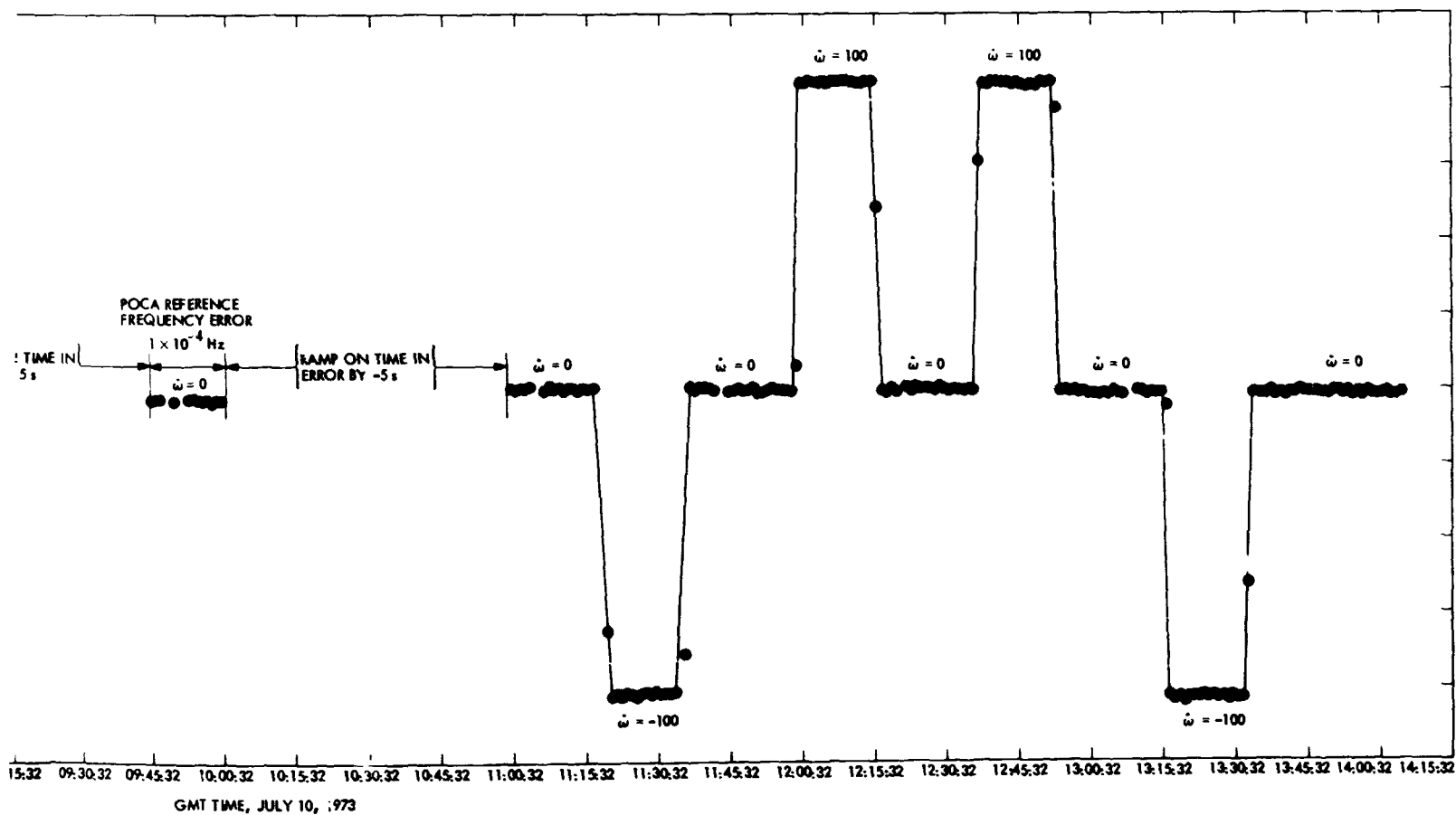


Fig. 3. Tora experiment, July 10, 1973—DSN 14 Pioneer 10 data with orbit and ramp corrections, second iteration.

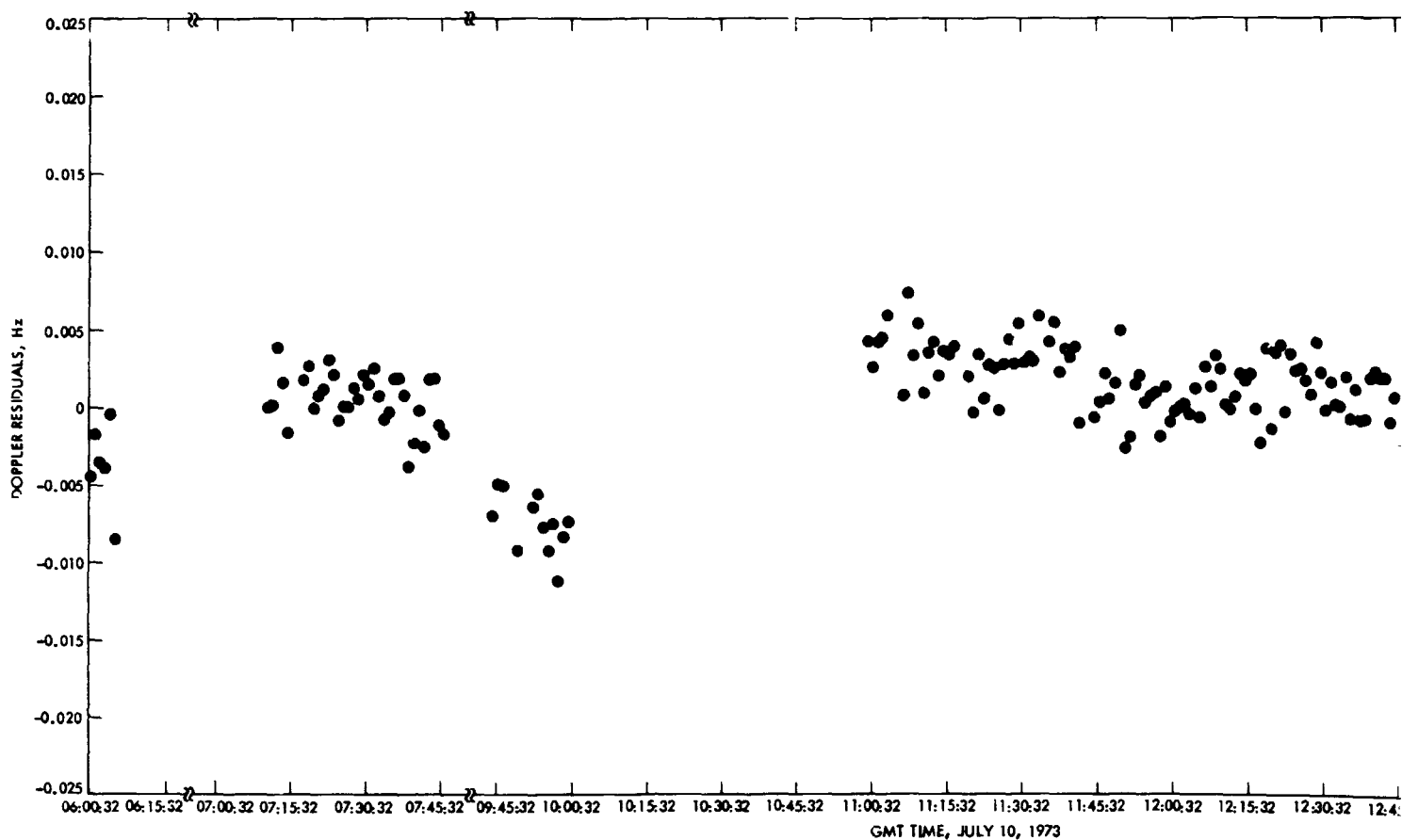
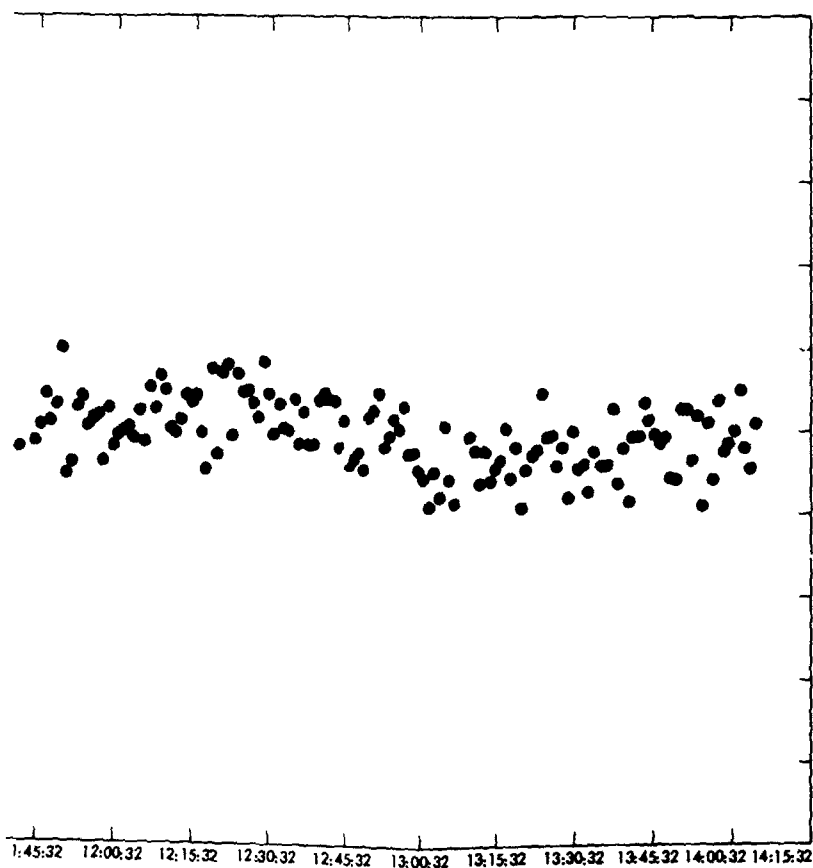


Fig. 4. Tora experiment, July 10, 1973—DSN 14 Pioneer data with orbit and ramp corrections, final iteration.



JPL TECHNICAL REPORT 32-1526, VOL. XIX

FOLDOUT FRAME

2

# S/X Open-Loop Receiver

H. G. Nishimura

R. F. Systems Development Section

*An operational DSN S-band receiver having two independent channels was modified to provide capability for coherent reception at S- and X-bands simultaneously. Coherence at both bands was accomplished by using a base-frequency multiplier which was common to both the S- and X-band local oscillator multiplier chains.*

## I. Introduction

In order to meet the occultation experiment requirements for coherent downlink phase information from a spacecraft at S- and X-bands, the DSN S-band open-loop receiver at DSS 14 was modified. Presently, the open-loop receiver has two independent S-band channels. Channel 2 was modified to receive at X-band. This modification was made without disturbing either S-band link. To meet the requirements, Channel 2 was preceded by an X- to S-band down-converter. Switching networks were added so that in the new S/X-band mode, occultation experiments can be carried out simultaneously at S- and X-bands. Coherence requirements for the two downlink signals were met by utilizing a common base-frequency for both the S- and X-band local oscillator (LO) chains. Whenever possible, components and modules

already designed or in DSN use were employed in order to minimize replacement spares and cost.

## II. Physical Description

The S/X open-loop receiver consists basically of two assemblies mounted in the tricone at DSS 14. One assembly, called the S/X open-loop receiver panel (panel), contains the times sixteen ( $\times 16$ ) base-frequency multiplier and other lower-frequency multipliers to generate the LO signal for the existing S-band mixers (see Fig. 1). The panel, mounted in receiver cabinet 9, is 43 cm wide, 51 cm long, and 10 cm high.

The other assembly, S/X open-loop receiver box (box), consists of a weather-resistant enclosure containing the



components required in the generation and conversion of the higher X-band frequency (Fig. 2). The Box measures approximately  $41 \times 51 \times 15$  cm deep.

### III. Development

Figure 3 shows a block diagram of the S/X open-loop receiver. Basically, the system consists of two reference frequency sources which drive frequency multiplier chains to supply the LO signals for the existing S-band mixers and the new X-band mixer. The  $\times 16$  base-frequency multiplier, which is common to both multiplier chains, has dual outputs. One output provides the drive for the S-band LO chain, while the other provides the drive for the X-band LO chain. Coaxial RF switches select either normal S-band operation or the new S/X-band mode. In the normal S-band mode, the existing S-band LO signals are switched into the existing S-band mixers. In the S/X-band mode, the new coherent S-band LO is switched to the existing Channel 1 S-band mixers, and simultaneously, the X-band LO is switched to the new X-band mixer in Channel 2.

Starting at the upper left in Fig. 3, reference frequency source  $f_1$  drives the dual output  $\times 16$  base multiplier. One output of the  $\times 16$  multiplier drives a  $\times 3$  multiplier, which generates the nominal 2245-MHz LO for the existing S-band mixers. This LO signal is split by a 3-dB hybrid and followed by bandpass filters FL1 and FL2. Switches S1 and S2 are operated simultaneously and, for S/X-band operation, select the new coherent LO generated by the  $\times 16$  and  $\times 3$  multipliers. For normal S-band operation, S1 and S2 select the existing S-band LO signals. Either set of LOs is applied to the existing S-band mixers in Channels 1 and 2.

The other output from the  $\times 16$  base multiplier is used to further develop the LO for the new X-band mixer. At the left in Fig. 3, reference frequency source  $f_2$  drives a  $\times 1/3$  frequency multiplier. The output is mixed with the output from the  $\times 16$  multiplier. The resultant sum frequency, a nominal 765 MHz, is further multiplied by a  $\times 8$  multiplier to provide the 6120-MHz LO drive for the X-band mixer. The LO is processed through bandpass filters and isolators HY2, FL3, HY3, FL4, and HY4 before being applied to the X-band mixer. The X-band downlink signal, nominally at 8415 MHz, comes in through the preselector filter and mixes with the 6120-MHz X-band LO in X-band mixer M1. The resulting difference intermediate frequency at 2295 MHz is amplified by AR1. Switch S3 operates together with switches

S1 and S2, and when it is in the S/X-band mode, selects the 2295-MHz S-band IF generated by the X- to S-band mixer. When the switch is in the normal S-band mode, it selects the normal 2295-MHz S-band signal to Channel 2. The signal is then fed to the S-band mixer in Channel 2. The various signal frequencies are shown in the diagram.

Perhaps the most significant area of development dealt with the suppression of spurious signals generated by the 6120-MHz  $\times 8$  frequency multiplier in the X-band LO chain.

Intermodulation products are generated in the mixer following the  $\times 8$  multiplier due to mixing of harmonics and sidebands of the  $\times 8$  multiplier output. Since the S- and X-bands are coherently related, the  $\times 3$  sideband at the output of the  $\times 8$  multiplier is at the same frequency as the IF from the X-band mixer. In addition, the  $\times 5$  and  $\times 11$  sidebands mix with the  $\times 8$  output also to generate an interference signal at the same frequency. The interference signals could mask the real signals if they were not adequately attenuated. Faced with these possibilities, the best approach was to suppress every harmonic of the  $\times 8$  input frequency appearing at the multiplier output except the required LO for the X-band mixer.

Bandpass filters FL3, FL4 and wideband isolators HY2, HY3, HY4 were used for this purpose. Typical microwave filters are of the reflective type, wherein high voltage standing wave ratio (VSWR) is exhibited in the reject band. The addition of an isolator at the input port allows the isolator to absorb the out-of-band reflected signals by an order of about 20 dB per unit. The isolator also helps in creating a better match for the in-band frequencies.

Before one can realize higher orders of suppression, RF leakage must be eliminated or at least minimized. Therefore, special precautions were taken in packaging the  $\times 8$  multiplier, isolator HY2, and filter FL3 (Fig. 4). The  $\times 8$  multiplier and HY2 were mounted within an RF-shielded enclosure. The input interface of FL3 was mounted flush against one exterior surface of the enclosure, with the input connector protruding into the enclosure through a clearance hole. The two mounting surfaces were machined smooth in order to minimize leakage. With this arrangement, the filter input was virtually RF-isolated from its output. Skin currents at the input were

contained within the enclosure. Test results confirmed excellent containment of leakage in the area of the  $\times 8$  and FL3.

Before the filtering was added, the interference signal levels were approximately  $-85$  dBm following the X- to S-mixer. With the addition of HY2 and FL3, this level was reduced to  $-141$  dBm, a reduction of 56 dB. A second suppression stage, consisting of HY3 and FL4 was added, and this reduced the spurious levels well below threshold signal levels. Because of reactive coupling between FL4 and the X-band mixer, HY4 was added to insure a better VSWR.

Certain precautionary measures had to be observed when working with these high attenuation levels:

- (1) Connectors had to be clean at their mating surfaces. Slight amounts of foreign matter can easily influence test results. In this respect, the smaller connectors, such as SMA, are notorious for generating metal flaking from their threads. Both connector ends should always be examined for cleanliness before mating.
- (2) SMA connections easily become loose during the course of testing and development. Best results

were obtained when these connections were torqued to about 12.4 g.cm (9 in.-lb) before starting tests.

#### IV. Discussion

The S/X modification is an R & D type of installation. Work will shortly be under way to provide a permanent unit at DSS 14 which will replace the R&D system. An S/X open-loop receiver will also be provided at DSS 43.

Because of the space limitations in receiver cabinet 9, the present S/X open-loop receiver panel will be reconfigured, possibly by relocating the  $\times 1/3$  multiplier-mixer to the box assembly.

Additional trimmer attenuators may be added to further balance the S-band LO signals. A crystal detector monitor will be added to provide control room personnel with an indication of the X-band and LO signal.

The  $\times 8$  multiplier will be replaced by a  $\times 2$  multiplier, followed by a  $\times 4$  multiplier. This change in the  $\times 8$  multiplier chain should reduce the levels of undesirable S-band signals appearing at the output of the X-band mixer.

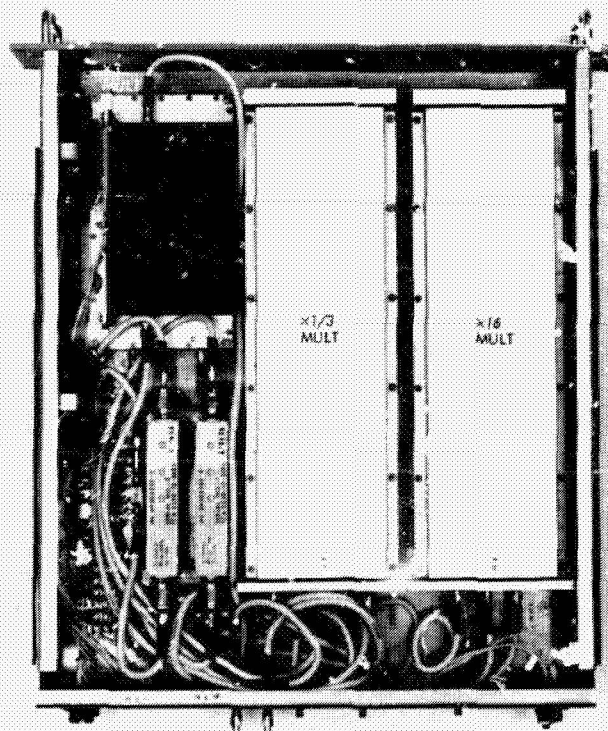


Fig. 1. S/X open-loop receiver panel



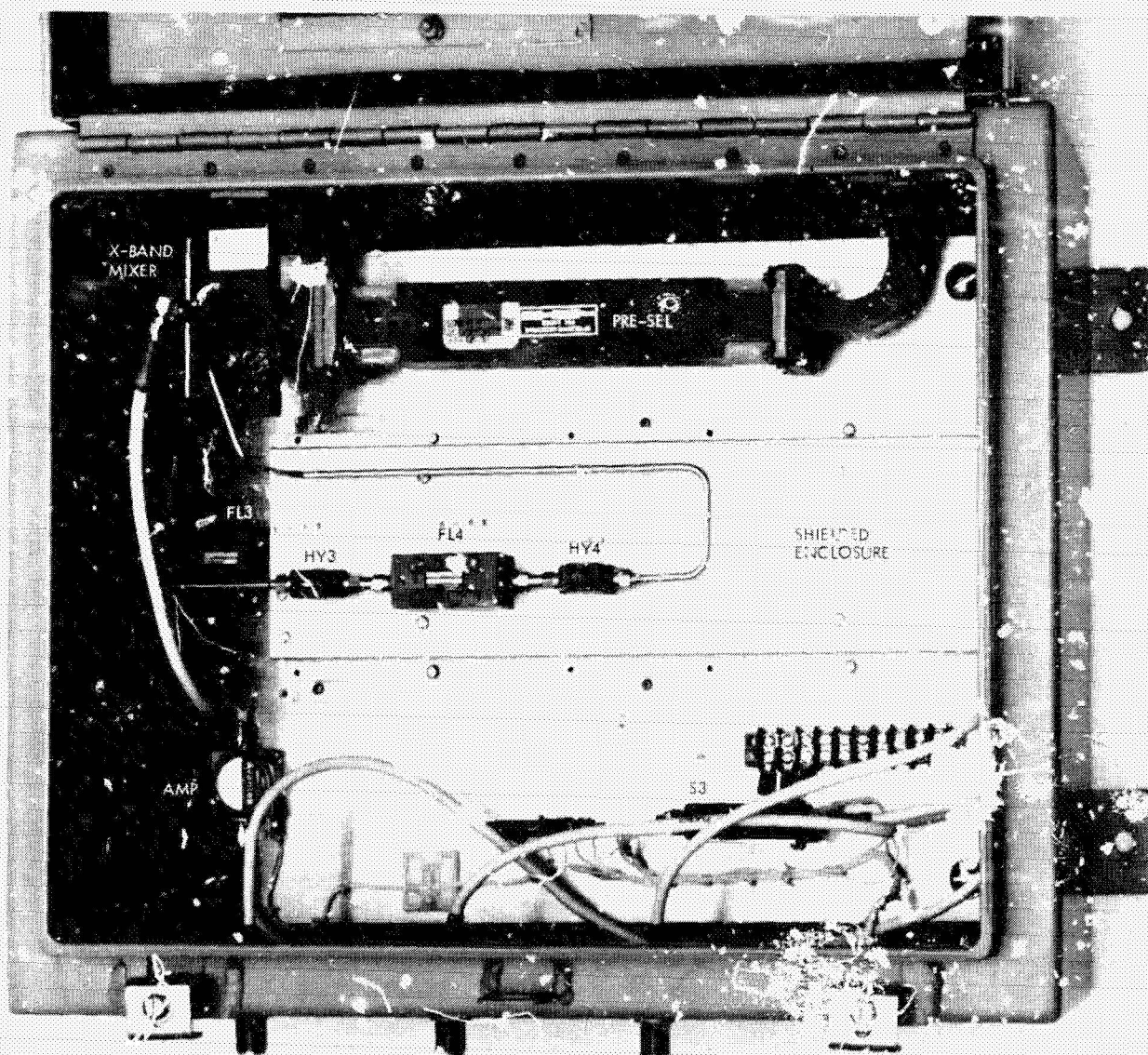


Fig. 2. S/X open-loop receiver box

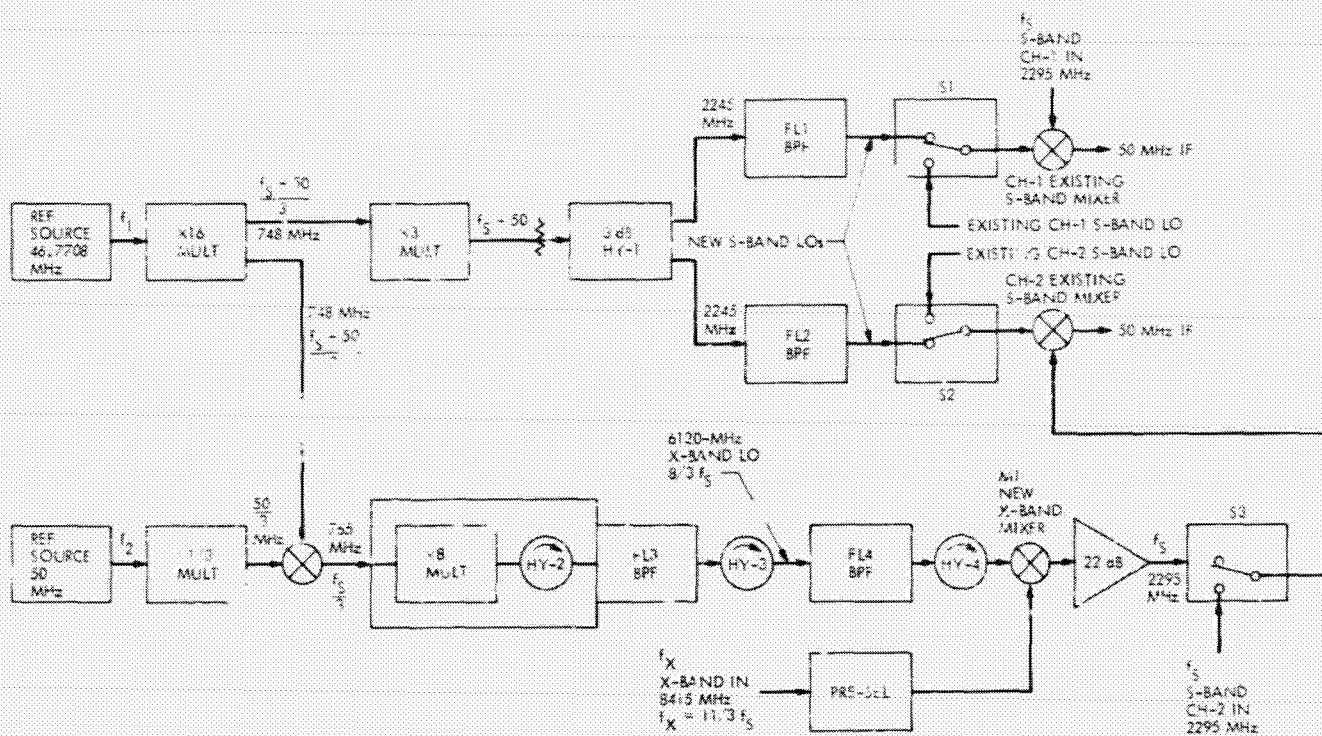


Fig. 3. S/X open-loop receiver (S1, S2, S3 shown in S/X-band mode)

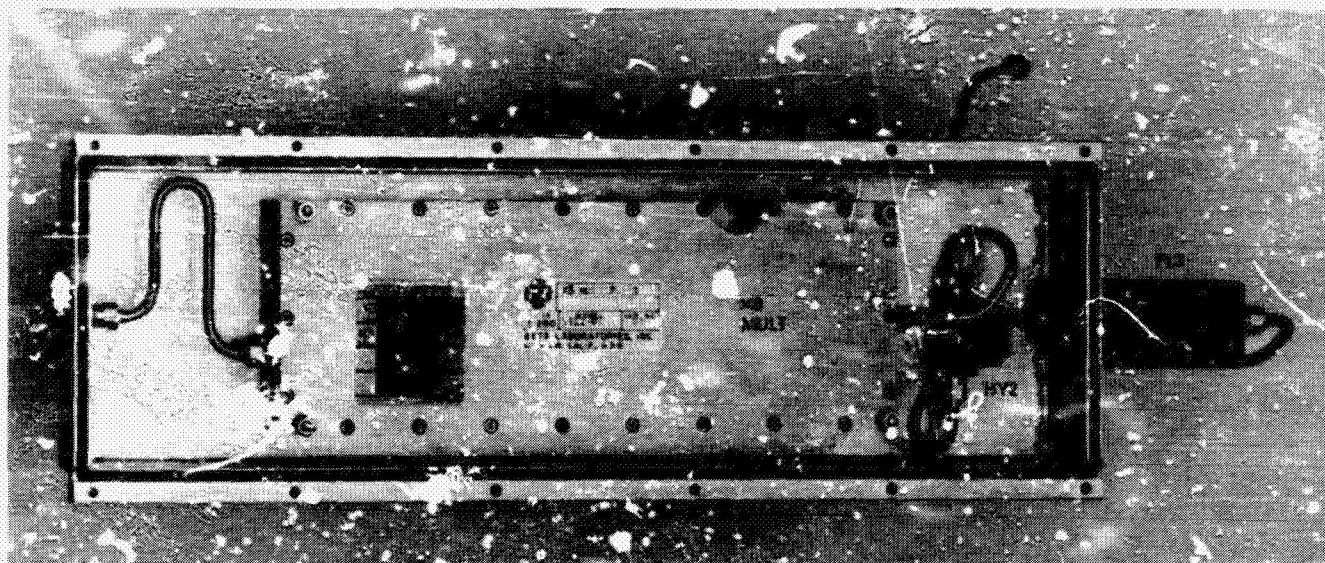


Fig. 4. X8 multiplier



# X-Band Radar System

R. L. Leu

R. F. Systems Development Section

*The radar development effort will provide the technology necessary for wider bandwidths at increased ranges. This technology will be applicable for use in uplink and downlink communications with future spacecraft.*

## I. Introduction

The radar development effort will provide the technology necessary for wider bandwidths at increased ranges. This technology will be applicable for use in uplink and downlink communications with future spacecraft.

The increased antenna gain (approximately 7 dB) will decrease the observation time for radar targets by a factor of 20. The wider bandwidth will allow faster range codes for improved ranging resolution. The first use of the new radar system will be to study the rings of Saturn as a possible hazard to navigation. This opportunity will start in December 1974.

Although there have been some developmental problems with the 250-kW klystrons, waveguide couplers, and several control assemblies, the scheduled operational date of December 1974 appears realistic. In addition to the technical difficulties discussed in this article, the other major obstacle is obtaining sufficient antenna time for installation and checkout on the 64-m antenna at DSS 14.

## II. Radar System

The radar system as discussed in Ref. 1 has undergone some changes. The system specifications are given in Table 1, and a block diagram is presented in Fig. 1. The radar will use a two-feed arrangement as shown only if a high-power polarizer (more specifically, the rotary joints in the polarizer) cannot be developed prior to the radar installation for the rings of Saturn opportunity. The transmit feed (Fig. 1, feed A) will be used as the transmit-receive feed, and the receiver feed (B) will be used as a backup. The two-feed arrangement is undesirable for optimum performance and will be used only as a last resort.

With a two-feed system and the present subreflector pin locations, the radar will have worst-case antenna degradation of approximately 1.3 dB. The 64-m antenna subreflector was not designed for continual focusing operation. It will have to remain in a fixed position and not moved between the transmit and receive feeds. If the subreflector is focused at a point midway between the feeds (Fig. 2), the degradation will be approximately 0.5 dB. As the radar is switched

from receive to transmit mode or reversed mode, the antenna pointing will be changed automatically with the computer-oriented antenna pointing system to correct for the convergence of the transmit and receive antenna beams. The software required to perform this operation was developed for another project. To improve the performance of a two-feed system, a configuration worth considering would locate the two feeds side by side (Fig. 2b). This would require reconfiguration of the cone layout and provision of new pin locations for the subreflector. The performance degradation would be 0.25 dB.

As indicated in Table 1, the transmit-receive cycle will vary in duration depending on the target being observed. The round-trip time for the rings of Saturn is  $2\frac{1}{2}$  h. During the transmit cycle, the radiated RF power must be switched on and off at a 30-s rate. This is disastrous to the klystron amplifiers, as discussed in Ref. 2. References 2 and 3 discuss an approach being implemented in the radar system for switching the radiated RF power on and off. A second method, now being used in the S-band radar, that shifts the RF carrier in frequency (about 1 MHz) at a 31-s rate, will also be available.

### III. Transmitter

At the time of this writing, three 250-kW klystrons, six waterloads, three dual directional waveguide couplers, and most of the electronic assemblies have been delivered. One klystron was operated at 225 kW for a short time before failure. One of the waveguide couplers was defective, and the other two malfunctioned at 125 to 150 kW. The malfunction was due to improper design of the terminations in the secondary arms of the couplers. They have been rebuilt and will be retested. Because of the shortage of materials and components in the electronic industry, several of the electronic control and monitor assemblies are late in delivery. This is not expected to cause any delay in the schedule.

### IV. Microwave Components

Two hybrid combiners (Ref. 4) have been delivered, and one unit was tested in excess of 225 kW at one port. Testing of the hybrid with two 200-kW inputs will take place in the third quarter of FY74. Waveguide switches, waveguide test equipment (slotted line, precision sliding load, sliding short, etc.) and waveguide components have been delivered. The switches and some waveguide components will be tested at 250 kW by January 1, 1974.

### V. Feed

The basic feed horn design has been completed and is presently being fabricated. The feed horn will be ready for RF power testing by January 1974. The polarizer, including rotary joints, will be ready for testing in February 1974.

The polarizer is the primary suspect area for breakdown from arcing and corona in the feed system. As discussed previously, should the rotary joints not handle the 400-kW power, they will be temporarily replaced with straight sections of waveguide in order to meet the December 1974 operational date. Development of the polarizer would continue, and it would be installed at a later time. The feed horn design will be the same for both feeds (transmit and receive). The receive feed will use the movable polarizer as a backup for the transmit/receive feed.

### VI. Exciter

The exciter is required to generate the 8.495-GHz frequency and  $\pm 10$ -MHz phase modulation bandwidth for the radar. The output of the exciter drives the buffer amplifier assembly, which drives the dual klystron amplifiers. The exciter is an extension of the Block IV exciter that has a switched output (530 MHz) for the X-band radar. This output drives a multiplier ( $\times 16$ ) to obtain 8.495 GHz. The  $\times 16$  multiplier has been designed, procured, and delivered and will be located in the buffer amplifier assembly, as shown in Fig. 1.

### VII. Receiver

The receiver will consist of the existing Block IV receiver X-band channel and the X-band traveling-wave maser (TWM) now located in the multi X-band/K-band (MXK) feed cone at DSS 14. The Block IV receiver is presently being tested at DSS 14 and will be available in time for the December 1974 operational date.

### VIII. Cooling

Cooling water is required for the klystron, waterloads, waveguide components, and feed. The coolant is provided by modification to the existing transmitter coolant assembly and the waveguide coolant assembly. The modification to the former has been completed, and the waveguide coolant system modification will be ready prior to the radar installation.

## References

1. Wiggins, C. P., "X-band Radar Development," in *The Deep Space Network Progress Report*, Technical Report 32-1526, Vol. XII, pp. 19-22, Jet Propulsion Laboratory, Pasadena, Calif., Dec. 15, 1972.
2. Wiggins, C. P., Buchanan, H. R., Leu, R. L., "High Power Microwave Transmitter Switch," in *The Deep Space Network Progress Report*, Technical Report 32-1526, Vol. XVII, pp. 21-27, Jet Propulsion Laboratory, Pasadena, Calif., Oct. 15, 1973.
3. Kolbly, R. B., "High Power Switching and Combining Technique," in *The Deep Space Network Progress Report*, Technical Report 32-1526, Vol. XVI, pp. 105-109, Jet Propulsion Laboratory, Pasadena, Calif., Aug. 15, 1973.
4. Hartop, R. W., "X-Band Hybrid Combiner," in *The Deep Space Network Progress Report*, Technical Report 32-1526, Vol. XVI, pp. 42-46, Jet Propulsion Laboratory, Pasadena, Calif., Aug. 15, 1973.



**Table 1. X-band radar system specifications**

System	Specifications
Frequency	8495 $\pm$ 25 MHz
RF output	400 kW ( + 86 dBm )
RF stability	$\pm$ 0.5 dB
Phase modulation	0-100% carrier suppression, 50 kHz to 10 MHz
Phase jitter system	5 deg RMS
Transmit-receive cycle	3 min to 2.5 h
Modulation	On/off during transmit at 10 s to 30 min
Received mode	Polarization diversity
Subreflector focusing	Transmit/receive

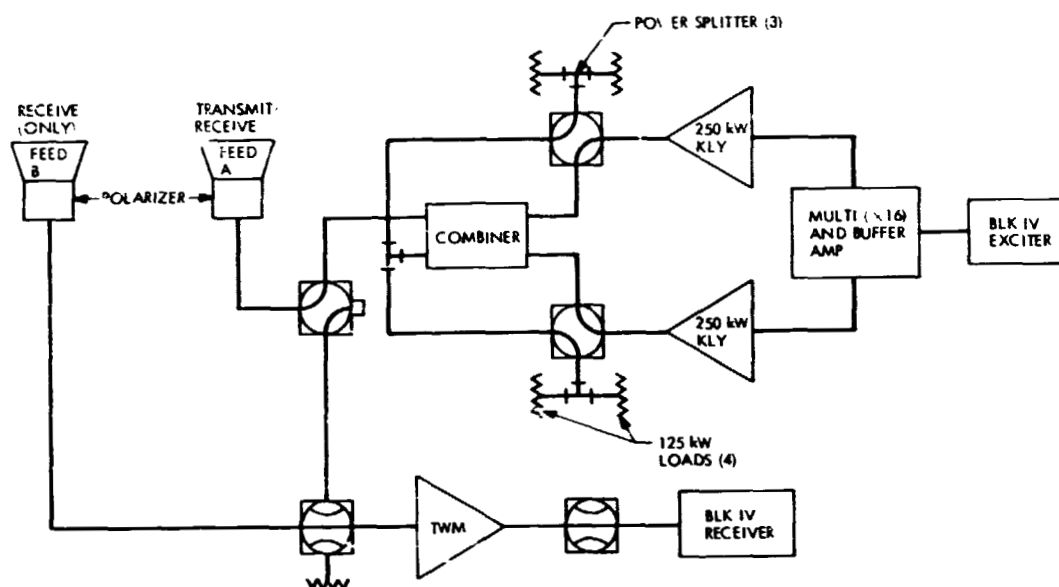


Fig. 1. X-band radar system block diagram

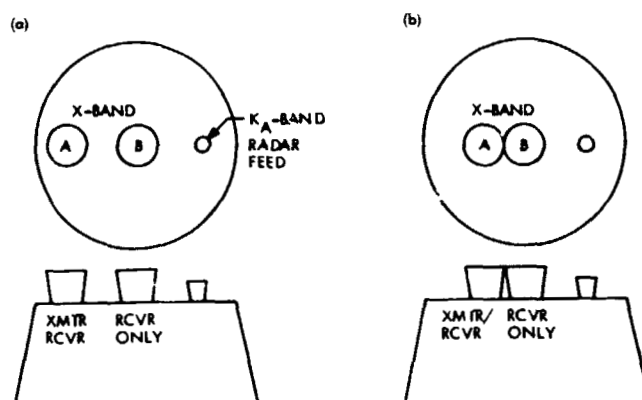


Fig. 2. X-band radar feed location: (a) present, (b) possible dual-feed arrangement

# An Algorithm for the Computation of Linear Forms

J. E. Savage<sup>1</sup>

Communications Systems Research Section

*Many problems, including matrix-vector multiplication and polynomial evaluation, involve the computation of linear forms. An algorithm is presented here that offers a substantial improvement on the conventional algorithm for this problem when the coefficient set is small. In particular, this implies that every polynomial of degree  $n$  with at most  $s$  distinct coefficients can be realized with  $O(n/\log_s n)$  operations. It is demonstrated that the algorithm is sharp for some problems.*

## I. Introduction

How many operations are required to multiply a vector by a known matrix or evaluate a known polynomial at one point? Such questions are frequently asked and Winograd (Ref. 1) has shown the existence of real matrices and polynomials (containing indeterminates over the rationals, for example) for which the standard matrix-vector multiplication algorithm and Horner's rule for polynomial evaluation are optimal. That is,  $n^2$  real multiplications and  $n(n-1)$  additions are required for some  $n \times n$  matrices to multiply the matrix by an  $n$ -vector, and  $n$  multiplications and  $n$  additions are required by some polynomials of degree  $n$  to evaluate the polynomial. In this paper, we present an algorithm for the computation of "linear forms" to show that the  $n \times n$  matrix-vector multiplication problem and the polynomial evaluation problem can be solved with

$O(n^2/\log_s(n))$  and  $O(n/\log_s(n))$  operations, respectively, when the matrix entries and the polynomial coefficients are known and drawn from a set of size  $s$  (even when the entries and coefficients are variables). These results are obtained by exhibiting potentially different algorithms for each matrix and each polynomial.

The algorithm presented here for the computation of "linear forms" is very general and can be applied to many problems including matrix-matrix multiplication, the computation of sets of Boolean minterms, of sets of product over a group, as well as the two problems mentioned above. Applications of this sort are discussed in Section III.

We now define "linear forms." Let  $S$  and  $T$  be sets and let  $R$  be a "small" finite set of cardinality  $|R| = s$ . Let  $\cdot : R \times S \rightarrow T$  be any map (call it multiplication) and let  $+$  :  $T \times T \rightarrow T$  be any associative binary operation (call

<sup>1</sup>Consultant from Brown University; Division of Engineering.

it addition). Then the problem to be considered is the computation of the  $m$  "linear forms" in  $x_1, x_2, \dots, x_n$

$$a_{i1} \cdot x_1 + a_{i2} \cdot x_2 + \dots + a_{in} \cdot x_n, \quad 1 \leq i \leq m$$

where  $a_{ij} \in R$  and  $x_i \in S$ . The elements in  $R$  shall be regarded as symbols that may be given any interpretation later. For example, in one interpretation,  $R$  may be a finite subset of the reals and, in another,  $R$  may consist of  $s$  distinct variables over a set  $Q$ , say.

An algorithm is given in the next section that for each  $m \times n$  matrix of coefficients  $A = \{a_{ij}\}$  evaluates the set

$$L_A(x) = \left\{ \sum_{i=1}^n a_{ij} x_i, 1 \leq j \leq m \right\}$$

of linear forms with  $O(mn \log_2(m))$  operations, when  $m$  is large where  $s = |R|$ . The conventional direct evaluation of  $L_A(x)$  involves  $mn$  multiplications and  $m(n-1)$  additions, so an improvement is seen when  $s$  is small relative to  $m$ .

Polynomial evaluation is examined in Section IV and the algorithm for linear forms is combined with a decomposition of a polynomial into a vector-matrix-vector multiplication to show that every polynomial of degree  $n$  whose coefficients are taken from a set of  $s$  elements can be realized with about  $\sqrt{n}s$  scalar multiplications,  $2\sqrt{n}$  nonscalar multiplications, and  $O(n \log_2(n))$  additions, when  $n$  is large. The polynomial decomposition is similar to one used by Paterson and Stockmeyer (Ref. 2), and it achieves about the same number of nonscalar multiplications but uses fewer scalar multiplications and additions.

In Section V, a simple counting argument is developed to show that the upper bounds derived in earlier sections are sharp for matrix-vector multiplications by "chains," that is, straight-line algorithms.

## II. The Algorithm

The algorithms for computing  $L_A(x)$ , where  $|R| = s$ , will be given in terms of an algorithm  $\mathcal{B}$  for the construction of all distinct linear forms in  $y_1, y_2, \dots, y_k$  with coefficients from  $R$ . That is,  $\mathcal{B}$  computes  $L_B(y)$  where  $B$  is the  $s^k \times k$  matrix with  $s^k$  distinct rows and entries from  $R$ . The algorithm  $\mathcal{A}$  for  $L_A(x)$  will use several versions of  $\mathcal{B}$ .

The algorithm  $\mathcal{B}$  has two steps. Let  $R = \{\alpha_1, \alpha_2, \dots, \alpha_s\}$ . Then,

Step 1: form  $\alpha_i \cdot y_j$ ;  $1 \leq i \leq s, 1 \leq j \leq k$ .

Step 2: let  $S(i_1, i_2, \dots, i_t) =$

$$\alpha_{i_1} \cdot y_1 + \alpha_{i_2} \cdot y_2 + \dots + \alpha_{i_t} \cdot y_t; \\ 1 \leq i \leq k, 1 \leq j \leq s.$$

Each element of  $L_B(y)$  is equal to  $S(i_1, i_2, \dots, i_k)$  for some set  $\{i_1, i_2, \dots, i_k\}$  of not necessarily distinct integers in  $\{1, 2, \dots, s\}$ . Construct  $S(i_1, i_2, \dots, i_t)$  recursively from

$$S(i_1) = \alpha_{i_1} \cdot y_1$$

and

$$S(i_1, i_2, \dots, i_t) = S(i_1, i_2, \dots, i_{t-1}) + \alpha_{i_t} \cdot y_t$$

for  $2 \leq t \leq k$ .

The first step uses  $\pi_B = ks$  scalar multiplications. Let  $N(s, t)$  be the number of additions to construct all linear forms  $S(i_1, i_2, \dots, i_t)$ . Then, from step 2, it follows that

$$N(s, 1) = 0$$

$$N(s, t) = N(s, t-1) + s^t$$

From this we conclude that

$$N(s, t) = [(s^{t+1} - 1) / (s - 1)] - (s + 1) \leq s^{t+1} \\ \geq s^t$$

for  $s \geq 2$  and  $t \geq 2$ .

Therefore, the number  $\sigma_B$  of additions to form  $L_B(y)$  satisfies  $s^k \leq \sigma_B \leq s^{k+1}$ .

Partition  $A$  into

$$A = [B_1, B_2, \dots, B_p]$$

where  $B_1, \dots, B_{p-1}$  are  $m \times k$ ,  $B_p$  is  $m \times (n - (p-1)k)$ , and  $p = \lceil n/k \rceil$ . Similarly, partition  $x = y^1, y^2, \dots, y^p$  where  $y^r = (x_{(r-1)k+1}, \dots, x_{rk})$  for  $1 \leq r \leq p-1$  and  $y^p$  is suitably defined. It follows that

$$Ax = B_1 y^1 + B_2 y^2 + \dots + B_p y^p \quad (*)$$

where  $+$  denotes column vector addition.

The algorithm  $\mathcal{A}$  for  $L_A(x)$  has two steps.

Step 1: construct  $L_{B_r}(y^r)$ ,  $1 \leq r \leq p$ , using  $\mathcal{B}$ , that is, identify the linear forms corresponding to rows of  $B_r$  and choose the appropriate forms from those generated by  $\mathcal{B}$  on  $y^r$ .

Step 2: construct  $L_A(x)$  by adding as per  $(*)$  above.

The number of multiplications used by  $\mathcal{A}$  is  $\pi_A = ns$ . The number of additions used in step 1 is no more than  $p\sigma_B$ , and in step 2 it is no more than  $m(p-1)$ . Therefore, the number of additions used by  $\mathcal{A}$  satisfies

$$\sigma_A \leq p s^{k+1} + m(p-1)$$

where  $p = \lceil n/k \rceil$ . Ignoring diophantine constraints and with  $k = \log_s(m/\log_s(m))$ , we have

**THEOREM 1.** For each  $m \times n$  matrix  $A$  over a finite set  $R$  of cardinality  $|R| = s$ , the  $m$  "linear forms"

$$L_A(\mathbf{x}) = \{a_{i1} \cdot x_1 + \cdots + a_{in} x_n : 1 \leq i \leq m\}$$

can be computed with  $\pi_A = ns$  multiplications and  $\sigma_A \leq O(mn \log_s(m))$  additions when  $m$  is large relative to  $s$ .

**Proof:** Ignoring diophantine constraints, we have

$$\sigma_A \leq n \left( \frac{s^{k+1} + m}{k} \right)$$

and  $s^k = m/\log_s(m)$ . Therefore,

$$\sigma_A \leq \frac{nm}{\log_s(m)} (1 + \epsilon_1)/(1 - \epsilon_2)$$

where  $\epsilon_1 = s/\log_s(m)$  and  $\epsilon_2 = \log_s \log_s(m)/\log_s(m)$ . If  $\epsilon_2 < 1/2$ , it is easily shown that  $(1 - \epsilon_2)^{-1} \leq 1 + 2\epsilon_2$ . Also,

$$(1 + \epsilon_1)(1 + 2\epsilon_2) \leq 1 + 2(\epsilon_1 + \epsilon_2)$$

if  $\epsilon_2 < 1/2$ , which holds for  $m \geq 16$  when  $s \geq 2$ . It follows that

$$\sigma_A \leq \frac{nm}{\log_s(m)} (1 + 2(\epsilon_1 + \epsilon_2))$$

when  $m \geq 16$ . Since  $\epsilon_1$  and  $\epsilon_2$  approach zero with increasing  $m$ , the conclusion of the theorem follows. Q.E.D.

When  $m \gg s$ , this result represents a distinct improvement over the conventional algorithm for evaluating  $L_A(\mathbf{x})$ , which uses  $m$  scalar multiplications and  $m(n-1)$  additions. It should be noted that the reduction in the number of additions by a factor of  $\log_s(m)$  obtained with algorithm  $\mathcal{A}$  follows directly from a reduction by a factor of about  $k$  in algorithm  $\mathcal{B}$ . The obvious algorithms for  $L_B(\mathbf{y})$  uses  $ks^k$  additions, but  $\mathcal{B}$  computes it with no more than  $s^{k+1}$  additions.

Although algorithm  $\mathcal{A}$  (and  $\mathcal{B}$ ) was discovered independently by the author, it does represent a generalization of an algorithm of Kronrod reported in Arlazarov, et al. (Ref. 3). His result applies to the multiplication of two arbitrary Boolean matrices. The heart of algorithm  $\mathcal{A}$  is algorithm  $\mathcal{B}$  and this was known to the author (Ref. 4) in the context of the calculation of all Boolean minterms in  $n$  variables. This will be discussed in the next section.

### III. Applications

In the set  $L_A(\mathbf{x})$  of linear forms, the elements  $a_{ij}$  and  $x_j$  are uninterpreted as are the operations of multiplication and addition. By attaching suitable interpretations, it is seen that algorithm  $\mathcal{A}$  for linear forms has applications to many different problems, several of which are now described.

#### A. Multiplication of a Vector by a Known Matrix

Let  $R$  be a set of  $s$  variables over  $S$ ,  $R = \{z_1, z_2, \dots, z_s\}$ , and let  $S = T = \{\text{reals}\}$ . Let  $+$  and  $\cdot$  be addition and multiplication on the reals. Then  $L_A(\mathbf{x})$  represents multiplication of  $\mathbf{x} = (x_1, x_2, \dots, x_n)$  by a known (but not fixed) matrix  $A$ . That is,

$$L_A(\mathbf{x}) = \{z_{k_{i1}} \cdot x_1 + z_{k_{i2}} \cdot x_2 + \cdots + z_{k_{in}} \cdot x_n : 1 \leq i \leq m\}$$

where the  $m \times n$  matrix of indices  $\{k_{ij}\}$  is fixed. For any given matrix  $\{k_{ij}\}$ ,  $L_A(\mathbf{x})$  can be computed using  $ns$  real multiplications and  $O(mn/\log_s(m))$  real additions.

Independent evaluation of the  $m$  forms requires a total of at least  $m(n-1)$  operations for any  $s$ , since each form consists of  $n$  functionally independent terms.

**Special Cases:**

- (1)  $z_1, z_2, \dots, z_s$  are assigned distinct real values.
- (2)  $s = 2$ ,  $z_1 = 0$ ,  $z_2 = 1$ . Then,  $L_A(\mathbf{x})$  is a set of subset sums such as

$$\{x_1 + x_3, \quad x_2 + x_3 + x_4\}$$

**NOTE:** Concerning Case (1), Winograd (Ref. 1) has shown that there exist fixed real (and unrestricted)  $m \times n$  matrices and vectors  $\mathbf{x}$ , such that  $mn$  real multiplications and  $m(n-1)$  real additions are required for their computation with "straight-line" algorithms. Thus, a significant savings is possible if the matrix entries can assume at most  $s$  distinct real values, and  $s$  is small relative to  $m$ .

## B. Matrix-Matrix Multiplication $AX$ , $A$ Known

Let  $R$  and  $S$  be as above and let  $T$  be the  $p$ -fold cartesian product  $Q^p$ ,  $Q = \{\text{reals}\}$ . Let  $\cdot$  be conventional scalar multiplication (consisting of  $p$  real multiplications) and let  $+$  be vector addition on the reals (consisting of  $p$  real additions). Then,  $L_A(x)$  represents multiplication of the  $n \times p$  matrix  $X$  over the reals by a known (but not fixed)  $m \times n$  matrix  $A$ . That is,

$$L_A(x) = \{z_{k_{i1}} \cdot \bar{x}_1 + z_{k_{i2}} \cdot \bar{x}_2 + \cdots + z_{k_{in}} \cdot \bar{x}_n : 1 \leq i \leq m\}$$

where  $\bar{x}_i$  denotes the  $i$ -th row of  $X$  and the  $m \times n$  matrix of indices  $\{k_{ij}\}$  is fixed. For any given matrix  $\{k_{ij}\}$ ,  $L_A(x)$  can be computed using  $nps$  real multiplications and  $O(mnp/\log_2(m))$  real additions.

NOTE: When  $n = m = p$ , Strassen's algorithm (Ref. 5) for matrix-matrix multiplication can be used at the cost of at most  $(4.7)n^{1.0857}$  binary operations. As a consequence, Strassen's algorithm is asymptotically superior to algorithm  $\mathcal{A}$  for this problem. However, when  $s = 2$ , algorithm  $\mathcal{A}$  is the superior algorithm for  $n \leq 10^{10}$ !! (Warning: beware of arguments based upon asymptotics.)

## C. Boolean Matrix Multiplication

Let  $R = S = \{0, 1\}$ ,  $T = \{0, 1\}^p$ , let  $\cdot$  be Boolean vector conjunction, and let  $+$  be Boolean vector disjunction. Then,  $L_A(x)$  represents the multiplication of a known Boolean  $m \times n$  matrix  $A$  by an arbitrary Boolean  $n \times p$  matrix  $X$ . That is,

$$L_A(x) = \{a_{i1} \cdot \bar{x}_1 + a_{i2} \cdot \bar{x}_2 + \cdots + a_{in} \cdot \bar{x}_n : 1 \leq i \leq m\}$$

where  $\bar{x}_i$  is the  $i$ -th row of the  $n \times p$  matrix  $X$ . The algorithm for computing  $AX$  uses no multiplications and  $O(mnp/\log_2(m))$  additions.

NOTE: If  $A$  is an arbitrary Boolean matrix and if the selection procedure of step 1 of algorithm  $\mathcal{B}$  can be executed without cost, the algorithm of Kronrod (Ref. 3) results. The number of operations performed, exclusive of selection, equals that given above. The Kronrod algorithm uses more operations because of a poor choice of the parameter  $k$ .

## D. Boolean Minterms

Let  $R = S = T = \{0, 1\}$ , let  $+$  be the Boolean conjunction, and let  $\cdot$  be defined by

$$\alpha \cdot x = \begin{cases} x & \alpha = 1 \\ \bar{x} & \alpha = 0 \end{cases}$$

where  $\bar{x}$  denotes the Boolean inverse. Then,  $L_A(x)$  represents a set of minterms such as

$$\{\bar{x}_1 x_2 x_3, \bar{x}_1 x_2 \bar{x}_3, x_1 \bar{x}_2 \bar{x}_3\}$$

NOTE: The set of all  $2^n$  distinct minterms, suitably ordered, represents a map from the binary to positional representation of the integers  $\{0, 1, 2, \dots, 2^n - 1\}$ . This map can be realized with at most  $2^{n+1}$  conjunctions and is a map that is useful in many constructions, such as those in Ref. 4.

## E. Products in a Group $G$

Let  $R = \{-1, 0, 1\}$ ,  $S = T = G$ , let  $\alpha \cdot x = x^\alpha$  (raise to a power), and let  $+$  be group multiplication. Then  $L_A(x)$  represents a set of  $m$  products of  $n$  terms each. For example,

$$\{a b^{-1} c d^{-1}, b c^{-1}, a^{-1} c^{-1} d^{-1}\}$$

is such a set, where  $x^{-1}$  is the group inverse of  $x$  and  $x^0$  is the group identity that is suppressed.

## IV. Polynomial Evaluation

We turn next to the evaluation of polynomials of degree  $n$ . Let

$$p(x) = a_0 + a_1 \cdot x^1 + a_2 \cdot x^2 + \cdots + a_n x^n$$

where  $+$  and  $\cdot$  represent vector addition and scalar multiplication, where  $x^1 = x$ ,  $x^i = x \cdot x^{i-1}$ , and  $\cdot$  represents vector multiplication. Let  $a_i \in R$ ,  $x \in T$  and

$$\cdot : R \times T \rightarrow T$$

$$+ : T \times T \rightarrow T$$

$$\cdot : T \times T \rightarrow T$$

where  $+$  and  $\cdot$  are associative and  $\cdot$  distributes over  $+$ . We shall construct an algorithm  $\mathcal{P}$  for polynomial evaluation, which employs algorithm  $\mathcal{A}$  for linear forms.

Algorithm  $\mathcal{P}$  has three steps. Without great loss of generality, let  $n = kt - 1$ , and assume that  $a = (a_0, a_1, \dots, a_n)$  has entries from a set of size  $s$ .

Step 1: construct  $x^2, x^3, \dots, x^t$ .

Step 2: construct the  $k$  linear forms in  $1, x, x^2, \dots, x^{l-1}$

$$\begin{bmatrix} r_0(x) \\ r_1(x) \\ \vdots \\ r_{k-1}(x) \end{bmatrix} = \begin{bmatrix} a_0 a_1 \cdots a_{l-1} \\ a_1 a_2 \cdots a_{l-1} \\ \vdots \\ a_{(k-1)l} \cdots a_{kl-1} \end{bmatrix} \begin{bmatrix} 1 \\ x \\ \vdots \\ x^{l-1} \end{bmatrix}$$

using algorithm  $\mathcal{A}$ .

Step 3: construct  $p(x) = r_0(x) + r_1(x) * x^l + \dots + r_{k-1}(x) * x^{(k-1)l}$  using Horner's rule. Let  $\sigma_p$  denote the number of vector additions used by  $\mathcal{P}$ ,  $\pi_p$  the number of scalar multiplications and  $\mu_p$  the number of vector multiplications. Since the forms required in step 1 can be realized with  $l-1$  vector multiplications and step 3 with  $k-1$  such multiplications and  $k-1$  additions, we have

$$\sigma_p \leq O((n+1)/\log_s(k)) + k - 1$$

$$\pi_p = ls$$

$$\mu_p = l + k - 2$$

since  $kl = n+1$ . If we ignore diophantine constraints and choose  $k = \sqrt{n+1}$ , to minimize  $\mu_p$  we have:

**THEOREM 2.** For each  $\mathbf{a} = (a_0, a_1, \dots, a_n) \in R^{n+1}$  with  $R$  a set of cardinality  $|R| = s$ ,  $p(x) = a_0 + a_1x + \dots + a_nx^n$  can be evaluated with  $\sigma_p$  vector additions,  $\pi_p$  scalar multiplications and  $\mu_p$  vector multiplications where

$$\sigma_p \leq O(n/\log_s(n))$$

$$\pi_p \leq s\sqrt{n+1}$$

$$\mu_p \leq 2\sqrt{n+1} - 2$$

when  $n$  is large relative to  $s$ .

Horner's rule, which is the optimal procedure for evaluating an arbitrary polynomial on the reals, uses  $n$  multiplications and  $n$  additions. Even when  $\mathbf{a}$  and  $x$  assume fixed real values, there exist vectors  $\mathbf{a}$  and values  $x$  for which Horner's rule is still optimal (Ref. 1). When the coefficients are drawn from a set of size  $s$ , however, Horner's rule can be improved upon by a significant factor when  $n$  is large relative to  $s$ .

The decomposition of  $p(x)$  used by algorithm  $\mathcal{P}$  is very similar to that used by Paterson and Stockmeyer (Ref. 2) in their study of polynomials with rational coefficients. They have shown that  $O(\sqrt{n})$  vector multiplications

are necessary and sufficient for such polynomials, but their algorithms use  $O(n)$  additions. Algorithm  $\mathcal{P}$  achieves  $O(\sqrt{n})$  vector multiplications but requires only  $O(n/\log_s(n))$  additions when  $n$  is large relative to  $s$ . Clearly, algorithm  $\mathcal{P}$  can be applied to any problem involving polynomial forms.

## V. Some Lower Bounds

The purpose of this section is to demonstrate the existence of problems for which the performance of algorithm  $\mathcal{A}$  can be improved upon by at most a constant factor. To do this, we must carefully define the class of algorithms that are permissible. Then, we count the number of algorithms using  $C$  or fewer operations and show that if  $C$  is not sufficiently large, not all problems of a given type (such as matrix-vector multiplication) can be realized with  $C$  or fewer operations.

A chain  $\beta$  is a sequence of steps  $\beta_1, \beta_2, \dots, \beta_L$  of two types: *data steps*, in which  $\beta_i \in \{y_1, y_2, \dots, y_n\} \cup K(y_i/K, y_i \neq y_j, i \neq j \text{ and } K \subset Q \text{ is a finite set of constants})$ , or *computation steps*, in which

$$\beta_i = \beta_j \circ \beta_k \quad j, k < i$$

and  $\circ : Q \times Q \rightarrow Q$  denotes an operation in a set  $Q$ .

Associated with each step  $\beta_i$  of a chain is a function  $\bar{\beta}_i$ , which is  $\beta_i$  if  $\beta_i$  is a data step and

$$\bar{\beta}_i = \circ(\bar{\beta}_j, \bar{\beta}_k)$$

if  $\beta_i$  is a computation step. Clearly,  $\bar{\beta}_i : Q^n \rightarrow Q$ . A chain  $\beta$  is said to *compute*  $m$  functions  $f_1, f_2, \dots, f_m, f_i : Q^n \rightarrow Q$  if there exists a set of  $m$  steps  $\beta_{i_1}, \dots, \beta_{i_m}$  such that  $\bar{\beta}_{i_l} = f_l, 1 \leq l \leq m$ .

We now derive an upper bound on the number  $N(C, m, n)$  of sets of  $m$  functions  $\{f_1, \dots, f_m\}$  that can be realized by chains with  $C$  or fewer computation steps.

**LEMMA.**  $N(C, n) \leq v^{uv}, v = C + n + m + |K| + 1$  if  $C \geq |\Omega| \geq 2$

**Proof:** A chain will have  $1 \leq \bar{a} \leq n + |K|$  data steps and without loss of generality they may be chosen to precede computation steps. Similarly, the order of their appearance is immaterial, so there are at most

$$\binom{n + |K|}{d} \leq 2^{n + |K|}$$

ways to arrange the  $d$  data steps.

Let the chain have  $t$  computation steps. Each step may correspond to at most  $|\Omega|$  operations and each of the two operands may be one of at most  $t + d$  steps. Thus, there are at most  $|\Omega|^t (t + d)^{2t}$  ways to assign computation steps and at most  $2^{n+|K|} |\Omega|^t (t + d)^{2t}$  chains with  $d$  data steps and  $t$  computation steps. A set of  $m$  functions can be assigned in at most  $(t + d)^m$  ways.

Combining these results, we see that the number of distinct sets of  $m$  functions that can be associated with chains that have  $C$  or fewer computation steps is at most

$$N(C, m, n) \leq \sum_{d=1}^{n+|K|} \sum_{t=1}^C 2^{n+|K|} |\Omega|^t (t + d)^{2t+m} \\ \leq (n + |K|) C 2^{n+|K|} |\Omega|^C (C + n + |K|)^{2C+m}$$

But

$$(n + |K|) 2^{n+|K|} \leq (C + n + |K|)^{C+n+|K|}$$

if  $C \geq 2$ , and

$$|\Omega|^C \leq (C + n + |K|)^C$$

if  $C \geq |\Omega|$ , from which it follows that

$$N(C, m, n) \leq (C + n + |K|)^{4C+n+|K|+m+1} \\ \leq v^{4v}$$

where  $v = C + n + m + |K| + 1$ . Q.E.D.

In the interest of deriving a bound quickly, the counting arguments given above are loose. Nevertheless, the bound can at best be improved to about  $v^v$ . As seen below, this means a factor of about 4 loss in the complexity bound.

Consider the computation of  $m$  subset sums of  $\{x_1, x_2, \dots, x_n\}$ ,  $x_i \in \{\text{reals}\}$ , as defined in Special Case (2) of Subsection III-A. In the chain defined above let  $Q = \{\text{reals}\}$  and let  $\Omega = \{+, \text{addition on the reals}\}$ . There are  $2^n$  distinct subset sums and the number of sets of  $m$  distinct subset sums is the binomial coefficient

$$F = \binom{2^n}{m}$$

Fix  $0 < \epsilon < 1$ . If  $C$ ,  $n$ , and  $m$  are such that  $N(C, n, m) \leq F^{1-\epsilon}$ , then there exists at least one set of  $m$  distinct subset sums that require  $C$  or more additions.

**THEOREM 3.** Algorithm  $\mathcal{D}$  is sharp for some problems, that is, there exist problems, namely, the computation of  $m$  subset sums over the reals, that require  $O(mn/\log_2(m))$  operations with any chain or "straight-line" algorithm, when  $m = O(n)$ .

**Proof:** Set  $v^{4v} = F^{1-\epsilon}$  where  $v = C + n + m + |K| + 1$ . Then,  $N(C, m, n) \leq F^{1-\epsilon}$ . For large  $F$ , the solution for  $v$  is

$$v = \left( \frac{1}{4} \ln F^{1-\epsilon} \right) / \ln \left( \frac{1}{4} F^{1-\epsilon} \right)$$

Since  $m = O(n)$ , it can be shown from Stirling's approximation to factorials and an examination of the binomial coefficient  $F$  that  $\ln F$  is asymptotic to  $nm \ln(s)$ . From this the conclusion follows. Q.E.D.

The counting argument given above could also be applied to matrix-vector multiplication, Subsection III-A, and to polynomial evaluation on the reals, as described in Section IV, to show that the upper bounds given for these problems are also sharp.

## VI. Conclusions

The algorithm presented here for the evaluation of a set of linear forms derives its importance from the minimal set of conditions required of the two operations. In fact, the only condition required is that addition be associative. As a consequence, the algorithm applies to a large class of apparently disparate problems having in common the fact that they can be represented in terms of linear forms of this general nature.

The algorithm allows us to treat two important problems, matrix multiplication with a known matrix and polynomial evaluation with a known polynomial. In both cases an algorithm is constructed that depends explicitly on the matrix entries and the polynomial coefficients. When the entry set of the matrix or of the polynomial coefficients is fixed and the dimensions of either problem are large, a sizable savings in the number of required computations is obtained.

The generality of the algorithm for evaluation of linear forms suggests that it may have application to many important problems not mentioned in this paper.



## Acknowledgment

The author acknowledges several important conversations with Dr. Charles M. Fiduccia, which resulted in the generalization and clarification of the principal algorithm for linear forms.

## References

1. Winograd, S., "On the Number of Multiplications Necessary to Compute Certain Functions," *Comm. Pure and Applied Math.*, Vol. 23, pp. 165-179, 1970.
2. Paterson, M., and Stockmeyer, L., "Bounds on the Evaluation Time for Rational Polynomials," in *Proceedings of the Twelfth IEEE Symposium on Switching and Automata Theory*, pp. 140-143, Oct. 1971.
3. Arlazarov, V. L., et al., "On Economical Construction of the Transitive Closure of an Oriented Graph," *Soviet Mathematics Doklady*, Vol. 11, No. 5, pp. 1209-1210, 1970.
4. Savage, J. E., "Computational Work and Time on Finite Machines," *J. Assoc. Comput. Mach.*, Vol. 19, No. 4, p. 673, Oct. 1972.
5. Strassen, V., "Gaussian Elimination is Not Optimal," *Numer. Math.*, Vol. 13, pp. 354-356, 1969.

# Radio Metric Applications of the New Broadband Square Law Detector

R. A. Gardner, C. T. Stelzried, and M. S. Reid  
Communications Elements Research Section

*Previous articles have discussed the development and performance of a new constant law detector. The new detector has a wider dynamic range and a more accurate square law response than has been available in the past. This article discusses the use and performance of this detector in a noise-adding radiometer system at DSS 13.*

## I. Introduction

Previous articles (Refs. 1, 2) have discussed the development and performance of a new constant law detector. This new detector has a wider dynamic range and a more accurate square law response than has been available in the past. Other desirable characteristics of the detector are high-level dc output with immunity to ground loop problems, fast response times, ability to insert known time constants, and good thermal stability. This article discusses the use and performance of the new detector in a noise-adding radiometer (NAR) (Ref. 3) system.

## II. The Noise-Adding Radiometer System

In a total-power radiometer, the output system noise temperature  $T_{op}$  is given by

$$T_{op} = GKV$$

where  $G$  is the system gain,  $V$  is the voltage output from the square law detector, and  $K$  is a scaling constant. In the total-power radiometer system, gain changes cannot be distinguished from real antenna temperature changes. In

order to desensitize a receiving system from gain changes, a noise-adding radiometer may be used. If a known and constant amount of noise is added to the system and used as a reference, then it is possible to obtain a ratio of output powers (Y-factors) with the noise reference source on and off. Thus,

$$Y = \frac{G(T_{op} + T_N)}{G(T_{op})}$$

and

$$T_{op} = \frac{T_N}{Y - 1}$$

where  $T_N$  is the equivalent noise temperature of the noise reference. It has been found that a temperature-stabilized solid-state noise diode is sufficiently stable for noise-adding radiometer applications (Ref. 3). If the Y-factors are measured at a rate much faster than the gain changes in the receiving system, the effect of gain fluctuations is cancelled.

A noise-adding radiometer system has been designed and constructed at DSS 13 for operation with a 26-m antenna. The maser amplifier operates in a closed-cycle

refrigerator (CCR). The CCR compressor cycles at a 1.2-Hz rate which is determined by the ac power-line frequency. Since the maser gain fluctuates at this rate, it is desirable to switch  $T_N$  at a rate greater than 8 Hz. It is also important to choose a rate that will not cohere with the 1.2-Hz CCR rate. The resolution of the radiometer, for a switching rate of 8 Hz (which corresponds to a measurement time of 0.125 s), is given by

$$\Delta T = \frac{2T_{op} \left(1 + \frac{T_{op}}{T_N}\right)}{\sqrt{\tau B}} = \frac{2(20) \left(1 + \frac{20}{117}\right)}{\sqrt{40 \times 10^{-3} \times 10 \times 10^6}} \approx 0.1K$$

where  $\tau$  is the measurement time for one Y-factor and  $B$  the system bandwidth. Thus, the resolution is 0.1K for a single measurement of  $T_{op}$  from one Y-factor for the DSS 13 radiometer. This resolution is improved, by averaging a number of individual measurements, by the factor  $1/\sqrt{N}$ . This results in a radiometer system with a measurement resolution on the order of a milli-Kelvin.

Figure 1 shows a block diagram of the DSS 13 NAR system. In the figure, ND is the solid-state noise diode in an oven. The detector is the unit described in Refs. 1 and 2. Any detector departure from true square law has two effects: (1) measurement inaccuracy and (2) susceptibility to gain fluctuation. Thus, all measurements are corrected by a factor  $\alpha$ , as described in Ref. 2, so that the measurement Y-factor is given by

$$Y = \frac{T_{op} + T_N}{T_{op}} = \frac{V_2 + \alpha(V_2)^2}{V_1 + \alpha(V_1)^2}$$

where  $V_1$  and  $V_2$  are the detector output voltages with the noise diode off and on, respectively. The IF bandwidth at the input to the detector is 5 MHz. The frequency output from the detector is fed to the computing counter.

The computing counter is Model H.P. 5360A, and the computing counter programmer is Model H.P. 6376A. These two units comprise a small computing system with input/output capability, which is capable of executing 200 program steps with an average execution time of 15  $\mu$ s per step. It is also capable of accepting input data in BCD form, reading an externally generated frequency, and performing various external functions by means of TTL-type signal levels. In addition, six-digit constants are available in thumbwheel form for use in the program. The programmer commands the noise source driver which turns the noise diode on and off.

The programmed controller, Model 601, commands the computing counter and interfaces with the station

XDS 910 computer, as shown in the figure. The programmed controller commands the 910 with azimuth and elevation offset functions, and the 910 drives the antenna servo in the usual way. The programmed controller is described in detail in Ref. 4.

### III. Method of Operating the NAR System

The detector correction factor  $\alpha$  is first measured and then set on the thumbwheels as a system constant for the duration of the NAR observing period. To determine the correct value for the correction factor, the  $\alpha$ -thumbwheels are first set to zero, the waveguide switch is switched to the ambient load, the NAR is run, and the detected output level is set to 1.8 V, with the noise diode on. The ambient load is connected to the maser input to ensure a constant system temperature during the measurement of  $\alpha$ . There is the possibility of radio sources passing into or out of the antenna beam if the maser were connected to the horn at this time. The IF input level to the detector is then reduced by 10 dB, and a new system temperature is computed. If the system temperature at the lower gain setting is lower than the system temperature at the higher gain, a greater value for  $\alpha$  is required. The correct value for  $\alpha$  is found experimentally by determining that value of  $\alpha$  which produces the same value of  $T_{op}$  for both gain settings.

The second system constant that must be determined is the correct value for  $T_N$ . When this is found, it is entered in the second set of thumbwheels and held constant for the duration of the experiment. With the ambient termination on the maser input, the system temperature is given by

$$T_{op} = T_P + T_M + T_F$$

where

$T_P$  = physical temperature of the ambient termination measured with a quartz thermometer probe.

$T_M$  = equivalent input noise temperature of the maser.

$T_F$  = equivalent input noise temperature of the follow-up receiver.

If the maser is turned on and off, a Y-factor ratio  $Y_{on}$  is measured. This ratio is given by

$$Y_{on} = \frac{T_P + T_M + T_F}{T_P + T_F}$$

With a knowledge of  $T_M$  and  $T_P$  and a measurement of  $Y_{on}$ ,  $T_F$  can be calculated. The system temperature with the ambient termination on the maser input is then known.

CR

The  $T_N$  thumbwheel is adjusted until the NAR computes the correct system temperature. The maser input is then switched to the antenna, and the NAR computes the system temperature on the antenna.

The third thumbwheel constant to be determined is  $N$ , the number of measurements which are averaged to yield the output system temperature  $T_{op}$ . Since measurement certainty is given by

$$\Delta T_{RMS} = \frac{\Delta T}{\sqrt{N}}$$

where  $\Delta T$  is the measurement resolution as stated above, a value for  $N$  may be chosen that will produce the desired radiometer resolution. If the antenna is moving in eleva-

tion during the measurement,  $N$  should be kept sufficiently small so that the real change in antenna temperature does not exceed the desired  $\Delta T_{RMS}$ .

The noise diode is enclosed in a constant-temperature (50°C) oven. Repeated measurements over an extended period of time have shown that the value of  $T_N$  varies approximately  $\pm 2\%$  in a 24-h period in S-band systems. This fluctuation in the value of  $T_N$  seems to follow ambient temperature variations. Recent laboratory work indicates that the coupling factor of the waveguide coupler used to inject  $T_N$  varies as a function of ambient temperature. Further work is in progress on this problem.

A number of NAR programs are available for various engineering and radio science applications.

## References

1. Reid, M. S., Gardner, R. A., and Stelzried, C. T., "A New Broadband Square Law Detector," in *The Deep Space Network Progress Report*, Technical Report 32-1526, Vol. XVI, pp. 78-86, Jet Propulsion Laboratory, Pasadena, Calif., Aug. 15, 1973.
2. Reid, M. S., Gardner, R. A., and Stelzried, "Improvement in the Accuracy of the New Broadband Square Law Detector," in *The Deep Space Network Progress Report*, Technical Report 32-1526, Vol. XVIII, pp. 94-98, Jet Propulsion Laboratory, Pasadena, Calif., Dec. 15, 1973.
3. Batelaan, P. D., Goldstein, R. M., and Stelzried, C. T., "A Noise-Adding Radiometer for Use in the DSN," in *The Deep Space Network*, Space Programs Summary 37-65, Vol. II, pp. 66-69, Jet Propulsion Laboratory, Pasadena, Calif., Sept. 30, 1970.
4. Parham, O. B., "The Design and Performance of a Programmed Controller," in this issue.

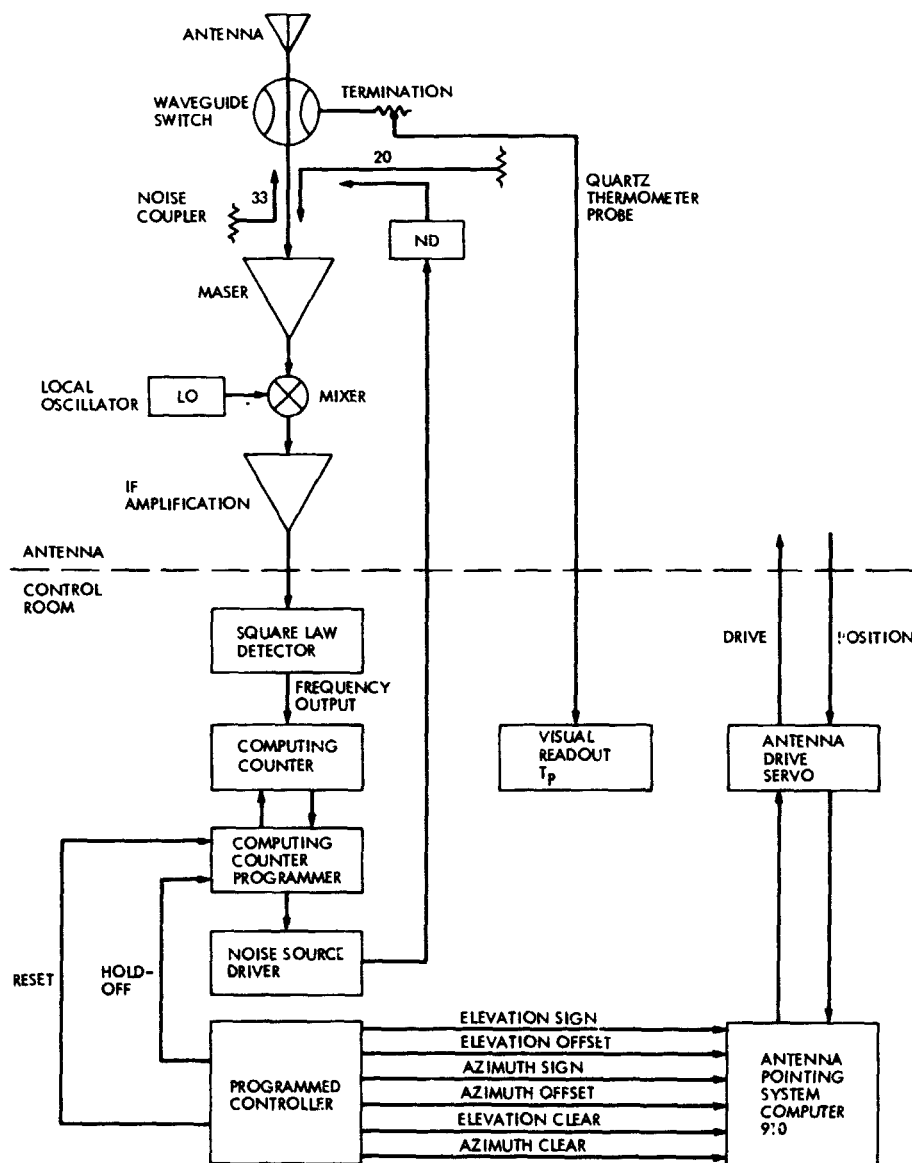


Fig. 1. Block diagram of DSS 13 NAR system

# Low-Noise Receivers: Microwave Maser Development

R. Clauss and E. Wiebe  
Communications Elements Research Section

*Two S-band maser systems with equivalent input noise temperatures of 2.1 K have been supplied to the Deep Space Network. These masers will be used on 34-m antennas at Deep Space Stations 14 and 43 to meet special requirements of the Mariner Venus/Mercury (MVM73) mission. The masers use a new shortened and cooled signal input transmission line to reduce noise and are equipped with superconducting magnets to provide the best possible stability performance.*

## I. Introduction

Special requirements for the Mariner Venus/Mercury mission showed a need for S-band masers with improved sensitivity and stability characteristics. Two new systems for DSSs 14 and 43 have been built in response to these requirements. The maser systems have new shortened and cooled input transmission lines which reduce the noise temperature as compared to previous systems. Superconducting magnets are used to improve maser gain, phase, and group delay stability. Optimum maser performance is achieved at 2295 MHz; the maser equivalent input noise temperature is 2.1 K at 2295 MHz. An overall system temperature of 8.3 K was measured during the evaluation of these new systems.

## II. Input Transmission Line

A new signal input transmission line has resulted in a substantial reduction of maser equivalent input noise tem-

perature. Previously reported systems (Refs. 1 and 2) were measured to have maser input noise temperatures of between 4 and 8 K at the S-band waveguide interface (2.1 K was contributed by the signal input transmission line). The new signal input transmission line described below contributes 0.4 K to the maser noise temperature. The improvement is achieved by cooling the center conductor of the coaxial line to 4.5 K, by shortening the line length to 18 cm, and by using a very-low-loss vacuum seal.

The new transmission line, assembled with an S-band maser and closed-cycle helium refrigerator (CCR), is shown in Fig. 1. The superconducting magnet, radiation shields, and the vacuum jacket cover have been removed. Figure 2 is a sketch identifying important features of the assembly.

A fused quartz dome provides part of the vacuum seal. The quartz dome is attached and sealed to the WR 430 input waveguide with flexible epoxy. An O-ring vacuum

seal is used between the waveguide and the adapter plate. The waveguide and fused quartz dome assembly can be replaced without disturbing other input line components; it is a field-replaceable assembly.

The coaxial transmission line outer conductor is made of thinwall (0.25-mm) stainless steel tubing; the inside is plated with 0.0025-mm copper and 0.0003-mm gold. This combination gives low microwave loss and adequate thermal isolation. Mechanical support for the transmission line is obtained by clamping a flange at the room temperature end of the outer conductor, between the adapter plate and the WR 430 waveguide. Thermal connections to the 80-K and 4.5-K CCR stations are made with flexible copper straps.

The transmission line center conductor contacts the outer conductor at the 4.5-K SMA connector and at the support clamp (which is thermally connected to the 4.5-K CCR station). A vacuum, common to the CCR vacuum jacket, provides thermal insulation between the coaxial line center conductor and its surrounding parts (outer conductor and quartz dome). The center conductor is made of gold-plated, polished copper. Refrigeration capacity measurements show that the total heat transferred to the 4.5-K CCR station (by radiation to the center conductor and by conduction through the outer conductor) is approximately 100 mW. The voltage standing wave ratio (VSWR) of the transmission line and waveguide assembly is less than 1.15 to 1 from 2050 to 2650 MHz. Q measurements, insertion loss, and temperature gradient calculations were used to determine the 0.4-K noise contribution of this transmission line assembly.

The new transmission line assembly is adaptable to all S-band maser systems presently used in the DSN. The conversion requires installation of a superconducting magnet.

### III. Superconducting Magnet

The use of a superconducting magnet, rather than a large, external permanent magnet, has several advantages: (1) it improves maser gain, signal phase, and group delay stability (Ref. 3); (2) the overall package weight can be reduced from 200 to 90 kg; and (3) the size reduction permits connection of the signal input waveguide in close proximity to the 4.5-K CCR station. A Block III maser system (Ref. 1) has been retrofit with a superconducting magnet and is currently used for two-way tracking on the 64-m antenna at DSS 14. (This maser system does not have the new input transmission line.)

### IV. Maser for SMT Cone

The maser currently in use in the S-band megawatt transmit (SMT) cone at DSS 14 uses the new input transmission line and achieves a noise temperature of 2.1 K at 2295 MHz. The maser comb structure is of the Block III type, with modified ruby shape (loading) to achieve a wide tuning range. The maser can provide more than 40 dB net gain at any frequency between 2250 and 2400 MHz. A maximum gain/bandwidth product is obtained when the maser is centered at 2285 MHz. Excess gain can be traded for bandwidth by use of field staggering coils within the superconducting magnet. A frequency response flat within 1 dB from 2270 to 2300 MHz is available at 42 dB net gain.

### V. Maser for DSS 43

A second maser with a noise temperature of 2.1 K has been built for use at DSS 43. A previously built maser comb structure (Ref. 2) was used to save on system construction time and cost. The maser is not capable of the large gain bandwidth product achieved by the maser for the SMT cone. The maser provides an 8-MHz, 1-dB bandwidth at 44 dB net gain at 2295 MHz center frequency. The pump klystron used with the DSS 43 system is identical to those presently used with Block III maser systems and does not provide 2388-MHz operation. The low forward loss of this particular maser is equal to that of the SMT cone unit, and identical noise performance at 2295 MHz is achieved.

### VI. Noise Temperature Measurements

Comparative system temperature measurements of masers described here have been made. A photograph of the maser/CCR package for the SMT cone, with horn and ambient temperature microwave-absorbing material, is shown in Fig. 3. Precision power measurements with and without the absorber material over the horn resulted in a total operating system noise temperature of 8.4 K. Best estimates of noise contributions for the parts of the system are given in Table 1. Measurements of the maser system previously used with the SMT cone showed a total operating system temperature of 10.7 K. Laboratory measurements using a liquid-helium-cooled waveguide termination indicated a 4.4-K maser noise temperature for the older SMT maser (Ref. 2).

Measurements of the maser for DSS 43 gave the lowest overall noise temperature values. The system was measured in the same configuration as that planned for in-

stallation on the 64-m antenna at DSS 43. A calibrating coupler and polarizer were included in the waveguide system. The slight loss of these components was offset by

the use of a better horn than was used in the earlier tests. A total operating system temperature of 8.3 K was measured.

## References

1. Trowbridge, D. L., "Block III Maser Implementation Program," in *The Deep Space Network Progress Report*, Technical Report 32-1526, Vol. XVIII, pp. 130-135, Jet Propulsion Laboratory, Pasadena, Calif., Dec. 15, 1973.
2. Clauss, R., and Quinn, R., "Low Noise Receivers: Microwave Maser Development," in *The Deep Space Network*, Space Programs Summary 37-58, Vol. II, pp. 50-52, Jet Propulsion Laboratory, Pasadena, Calif., July 31, 1969.
3. Clauss, R., Wiebe, E., and Quinn, R., "Low Noise Receivers: Microwave Maser Development," in *The Deep Space Network Progress Report*, Technical Report 32-1526, Vol. XI, pp. 71-80, Jet Propulsion Laboratory, Pasadena, Calif., Oct. 15, 1972.



**Table 1. Noise contributions for the SMT  
maser evaluation system**

Part of system	Noise contribution, K
Sky (includes atmosphere and cosmic background)	4.9
Horn and mode generator	1.2
Maser	2.1
Follow-up receiver	0.2
Total operating system temperature	8.4

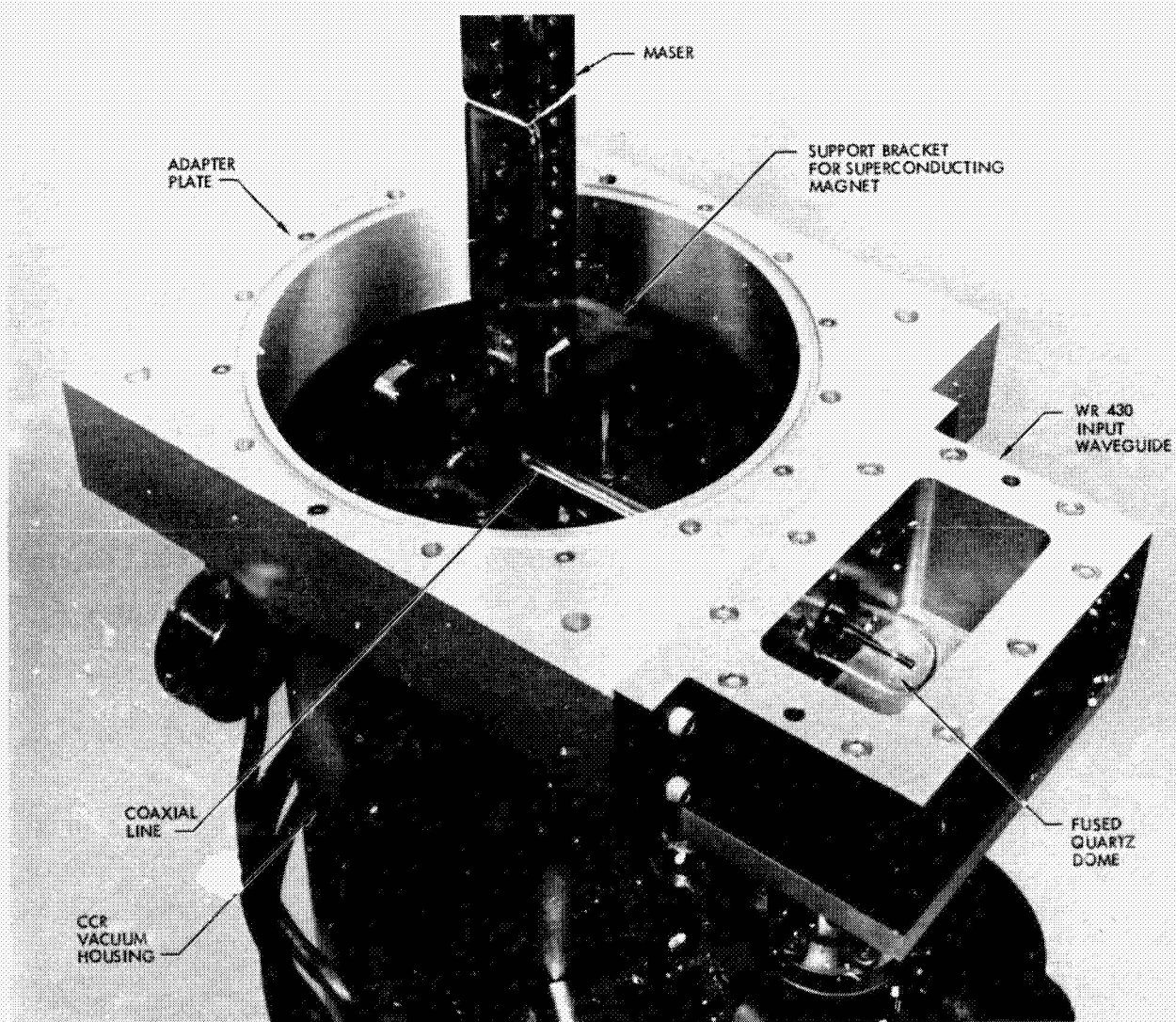
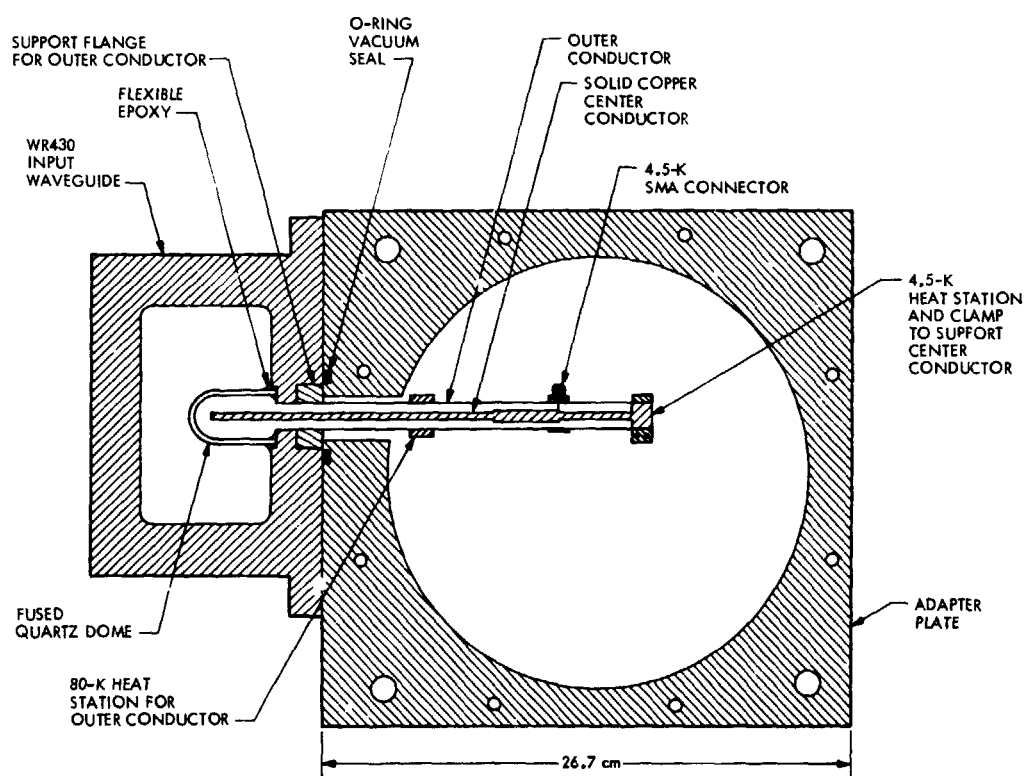


Fig. 1. Signal input transmission line for 2.1-K S-band maser



**Fig. 2. Important features of the transmission line assembly**

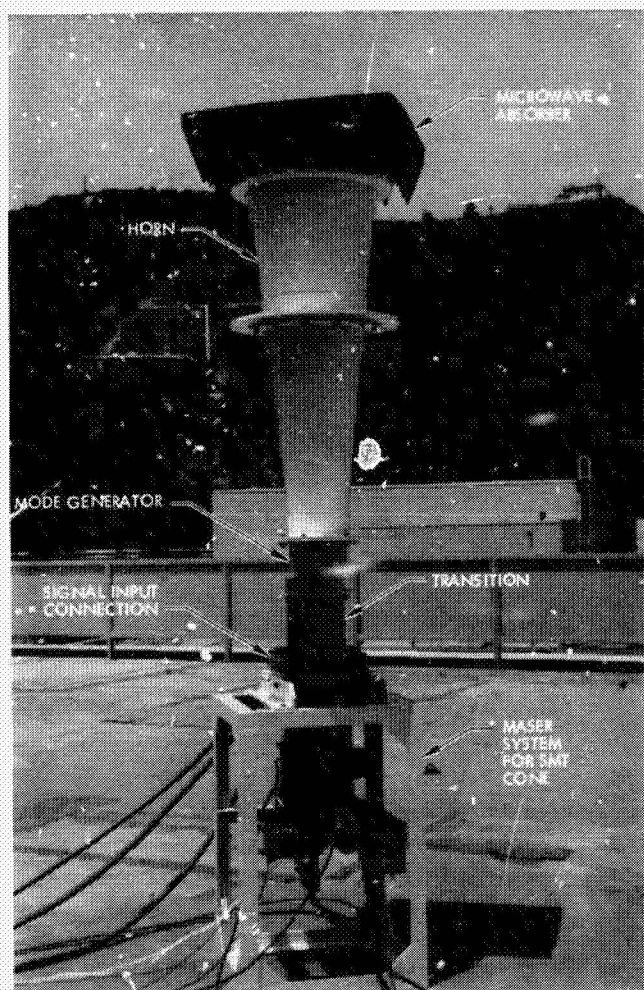


Fig. 3. SMT maser system used for noise temperature evaluation

# System Noise Temperature Calibrations of the Research and Development Systems at DSS 14

M. S. Reid and R. A. Gardner  
Communications Elements Research Section

*This article reports recent precision system noise temperature measurements made with the X- and S-band systems as they will be used for the Mariner Venus/Mercury 1973 (MVM'73) mission. Elevation and azimuth profiles for both the S-band and X-band systems are also presented. A summary of the zenith system noise temperature measurements for calendar year 1973 for the duplexed S-band systems at DSS 14 is described and plotted.*

In a previous article (Ref. 1), system temperature measurements were made at DSS 14 of the S-band Megawatt Transmit (SMT) cone S-band system and the multifrequency X- and K-band (MXK) cone X-band system. These measurements were elevation profiles with the reflex feed system both extended and retracted. Since these measurements were made, certain improvements (Ref. 2) have been made to the maser in the SMT cone, the effect of which has been to reduce the SMT system operating noise temperature. Other improvements since previous reports

(Ref. 3) have included the taping of the 64-m antenna surface. This article reports recent precision system temperature measurements made with the X- and the improved S-band systems, as they will be used for the MVM'73 mission. The present measurements were made with the Noise-Adding Radiometer (Ref. 4) and the ambient load terminations. Verification tests of the ambient load were made with a microwave absorber over the horn, and voltage standing wave ratios of the ambient load and horn were checked.

Figure 1 shows elevation profiles for the S- and X-band systems. The S-band data were obtained with maser serial number 80S2 in the SMT cone and the X-band data with maser serial 150X2 in the MXK cone. The dichroic feed system was extended, the atmosphere was clear, and the antenna azimuth was fixed at 180 deg. The masers were tuned to 2295 and 8415 MHz, respectively, and the follow-up receiver contribution was measured as less than 0.1 K in each case.

Table 1 is a summary of the system operating noise temperature performance of the SMT and MXK cones. The dichroic feed system does not degrade the S-band system temperature at high elevation angles (above 30 deg). The S- and X-band system temperature at zenith was measured as 12.4 and 21.1 K, respectively, with the dichroic feed system extended.

Figure 2 shows S-band azimuth profiles for three different elevation angles. The azimuth angles were chosen to correspond approximately to the angles at which the MVM73 spacecraft will be tracked. These profiles were

made with the SMT cone system tuned to 2295 MHz and the dichroic feed system extended.

Figure 3 shows similar X-band profiles for the same three elevation angles and the same azimuth angles. These profiles were made with the MXK system tuned to 8415 MHz and the dichroic feed system extended.

Table 2 lists the horizon mask data in tabular form for reference.

Figure 4 shows a summary of zenith system noise temperature measurements for calendar year 1973 for the S-band systems at DSS 14. The crosses are the data for maser serial number 96S3 in the polarization diversity S-band (PDS) cone operating in the diplexed mode. The circles are the data for the maser in the Module 3 area operating in the diplexed mode through the "A" cone. All these measurements (most of which were made by station personnel at DSS 14) were made with the Y-factor technique of switching between an ambient termination and the horn, but without regard for weather conditions.

## References

1. Reid, M. S., Gardner, R. A., and Freiley, A. J., "Precision System Temperature Measurements at Goldstone," in *The Deep Space Network Progress Report*, Technical Report 32-1526, Vol. XIV, pp. 60-67, Jet Propulsion Laboratory, Pasadena, Calif., Apr. 15, 1973.
2. Clauss, R. C., and Wiebe, E. R., "Low-Noise Receivers: Microwave Maser Development," in this issue.
3. Reid, M. S., "System Operating Noise Temperature Calibrations," in *The Deep Space Network Progress Report*, Technical Report 32-1526, Vol. X, pp. 123-128, Jet Propulsion Laboratory, Pasadena, Calif., Aug. 15, 1972.
4. Batelaan, P. D., Goldstein, R. M., Stelzried, C. T., "A Noise Adding Radiometer for Use in the DSN," in *The Deep Space Network*, Space Programs Summary 37-65, Vol. II, pp. 66-69, Jet Propulsion Laboratory, Pasadena, Calif., Sept. 1970.

**Table 1. Summary of system operating noise temperature performance of SMT and MXK cones**

Elevation angle, deg	Dichroic feed system extended		Dichroic feed system retracted	
	SMT cone 2295 MHz, K	MXK cone 8415 MHz, K	SMT cone 2295 MHz, K	MXK cone 8415 MHz, K
88	12.4	21.1	12.4	19.5
60	12.9	21.8	12.9	21.2
30	16.3	25.7	16.3	25.1

**Table 2. Horizon masks at S- and X-band for three elevation angles**

Azimuth angle, deg	Elevation angle 6 deg		Elevation angle 10 deg		Elevation angle 15 deg	
	SMT, K	MXK, K	SMT, K	MXK, K	SMT, K	MXK, K
105	30.9	47.0	24.7	38.7	20.9	33.6
115	31.0	46.8	24.7	38.5	21.2	33.6
125	31.4	47.4	25.0	39.0	21.0	33.9
135	32.1	48.8	25.4	39.6	21.2	33.9
145	33.1	50.1	26.0	39.9	21.5	34.7
155	34.4	51.6	26.2	40.8	21.6	35.2
165	33.7	51.0	26.2	40.9	21.6	35.2
175	33.3	50.9	26.1	40.7	21.6	34.9
180	33.1	50.5	26.1	40.7	21.6	35.1
185	32.8	50.0	25.8	40.5	21.4	34.9
195	32.4	49.2	25.6	39.9	21.4	34.9
205	32.2	48.4	25.5	39.5	21.3	34.8
215	32.1	48.2	25.4	39.5	21.3	34.7
225	32.1	48.8	25.6	39.7	21.3	34.7
235	32.4	49.6	25.6	40.2	21.4	34.7
245	32.3	49.0	25.6	39.9	21.3	34.6
255	32.3	49.0	25.6	39.8	21.3	34.6

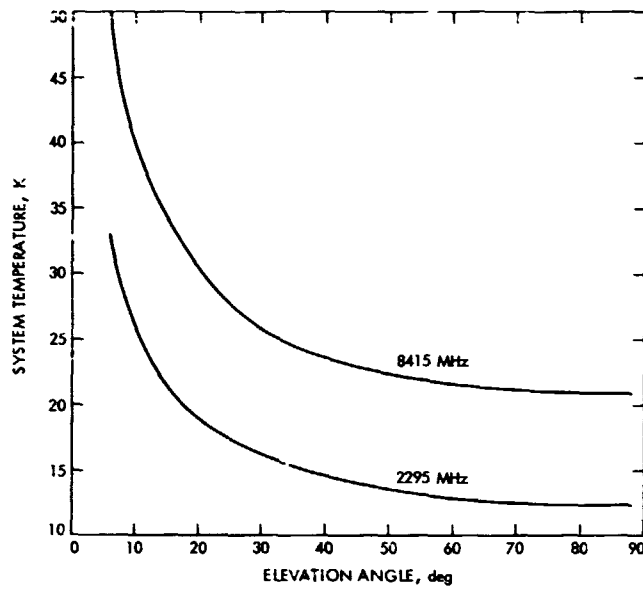


Fig. 1. S-band and X-band elevation profiles

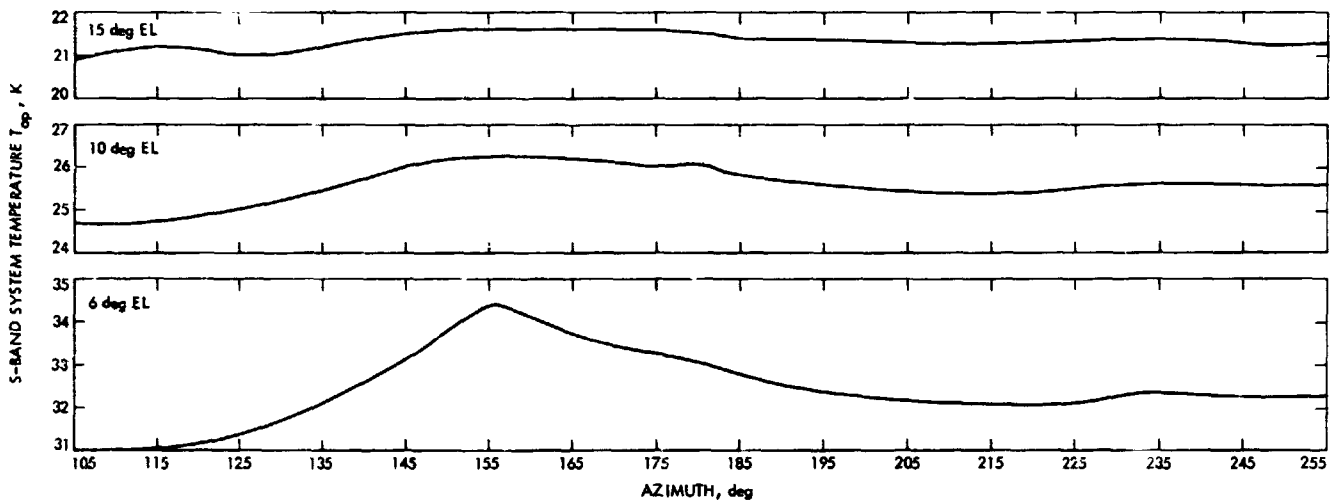


Fig. 2. S-band azimuth profiles



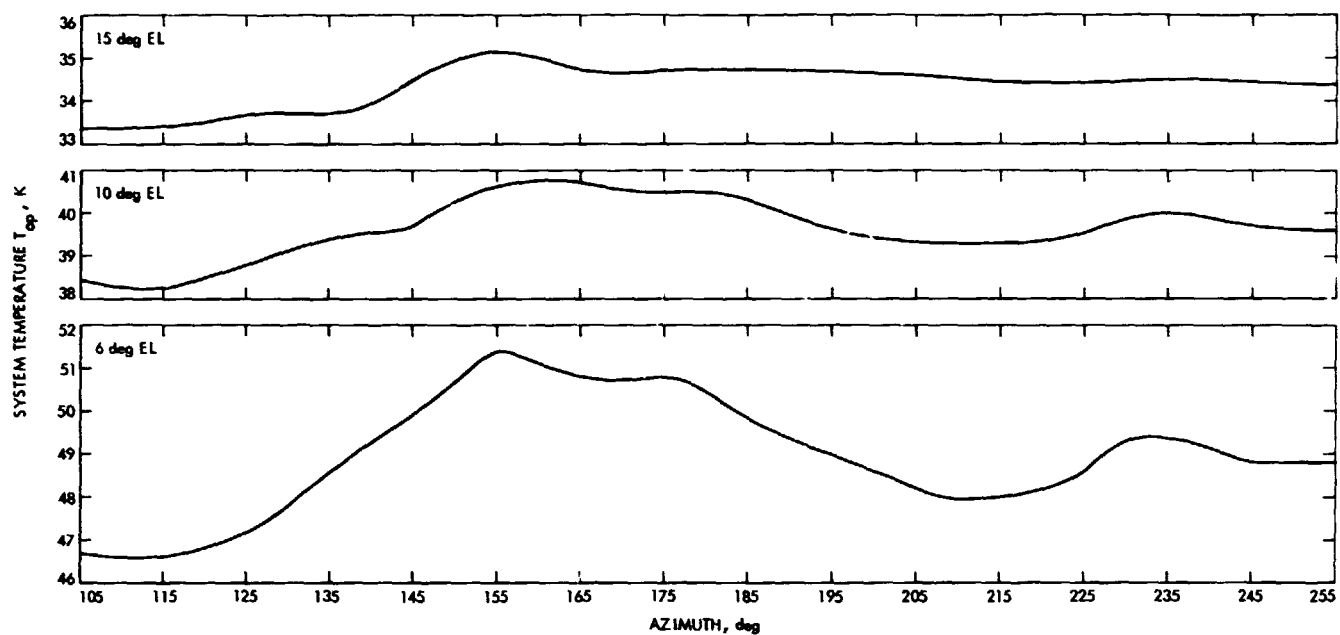


Fig. 3. X-band azimuth profiles

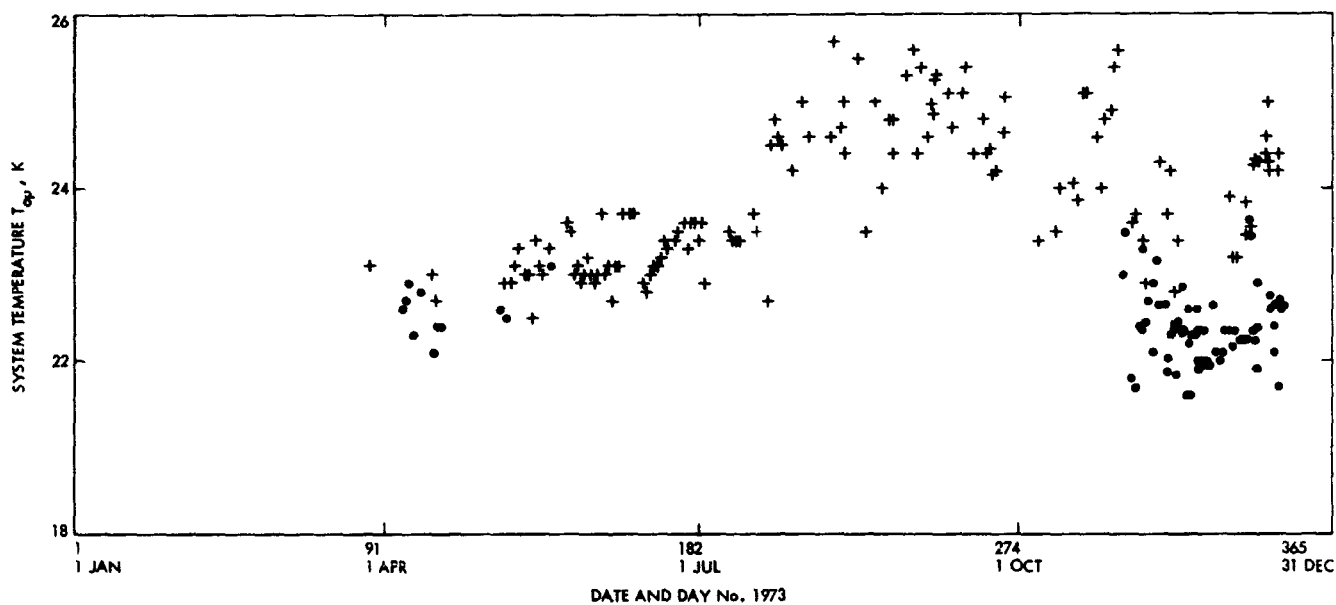


Fig. 4. Summary of DSS 14 diplexed S-band system temperatures for calendar year 1973

# The Design and Performance of a Programmed Controller

O. B. Parham

Communications Elements Research Section

*A programmed controller has been designed for operation with a Noise Adding Radiometer (NAR) for the automatic control of certain tracking station functions. These functions include the operation of the NAR, the operation of waveguide switches, and the control of the pointing of the 28-m antenna. This article describes the design and operation of the programmed controller.*

The Model 601 programmed controller was designed for the automatic control of certain tracking station functions, including the operation of the NAR (Ref. 1), the operation of waveguide switches, and the control of the pointing of the 28-m antenna. The controller provides sixteen timed contact closures. The contact closures and timing are programmed by eight-level USASCII punched paper tape.

The controller consists of four functional sections: tape reader, timer, relay register, and control (Fig. 1).

The tape reader is a low-cost photoelectric unit with stepper motor drive that reads the program tape at 100 cps.

The timer section is a three-digit, double buffered, pre-settable down counter that is programmed by the time field of the instruction. When reset to the programmed time and started, it decrements at a rate of 10 Hz until it equals zero. The maximum programmable time interval is 99.9 s and the minimum is 0 s.

The relay register is also double buffered, and provides the outputs in the form of isolated contact closures. It is programmed by the pattern field of the instruction in the form of A 1 for a closed contact and A 0 for an open contact.

The control section instructs the tape reader when to read, and controls the flow of data to the timer and relay register input buffers. It recognizes E, P, S, and T as control characters, and the digits 0-9 as data characters. All other characters are ignored and not loaded. Additionally, all characters including control and data within parentheses are ignored. This allows the program tape, without affecting its operation, to contain a title, statement numbers, or any other comments that may assist an operator when the tape is punched or listed on a teletype.

The B character is a multi-purpose control character. If the front panel halt switch is in the enable position, the tape reader will stop when an S is read. When the front panel reset switch is closed, the tape advances, ignoring

all instructions, and halts on the next S character. At this point, the program may be started by closing the front panel start switch. Additionally, an alarm, that can be enabled by front panel control, is provided to signal an operator that the tape is stopped on a halt. With one S character located at the beginning of a program tape, these functions allow an operator to load a program tape at any position in the program, initialize the program tape to the beginning, and execute the program continuously, or once and halt.

The contents of the timer and the relay register are displayed on the front panel for operation verification. An additional front panel control, the mode switch, is provided to allow program checking. Each time it is closed in the step position, an instruction is read and displayed.

In normal operation, with the mode switch in the run position, as an instruction is read, the characters following a P character are loaded one at a time into the right end of the relay register input buffer. As each new character is read in, the previously loaded characters are shifted left one place. This process continues until a T or E character is read. The characters following a T are loaded into the timer input buffer in the same fashion as the relay register was loaded. Again this action continues until a P or E character is read.

When an E is read, this indicates the end of the instruction. First, the contents of the timer input buffer are loaded into the timer and, at the same time, the relays

are set; then, a few microseconds later, the timer is started and both input buffers are cleared.

The tape reader continues, reading the next instruction until another T is read. At this point, the timer is tested. If the timer has reached zero, the rest of the instruction is read and executed, and the following instruction is read. If the timer has not reached zero when the T character is read, the tape reader stops and waits. When the timer reaches zero, the tape reader restarts and finishes reading the instruction.

The program tape is normally in the form of an endless loop. The instruction format is flexible in that the time and pattern fields may be interchanged, and the data in each field are right-justified as they are read. The omission of unnecessary zeros allows the instructions to be compact. Table 1 shows some examples of various program instructions.

Figures 2 and 3 are photographs of the standard rack-mounted Model 601 programmed controller.

A Model 601 programmed controller is currently being used at DSS to control the operation of an NAR, the operation of waveguide switches, and the pointing of the computer-driven 26-m antenna. Programs for the configuration include bore-sighting, on-source/off-source tracking, radio source drift curve generation, and radiometer calibration. This has been described in an accompanying article (Ref. 2).

## References

1. Batelaan, P., Goldstein, R. M., and Stelzried, C. T., "A Noise Adding Radiometer for Use in the DSN," in *The Deep Space Network*, Space Programs Summary 37-65, Vol. II, pp. 66-69, Jet Propulsion Laboratory, Pasadena, Calif., Sept. 1970.
2. Gardner, R. A., Stelzried, C. T., Reid, M. S., "Radio Metric Applications of the New Broadband Square Law Detector," in this issue.

**Table 1. Examples of program instructions**

Example	Instruction
1 P1111T37.5E	Close contacts 1, 2, 3, and 4 for 37.5 s. The decimal point in the time field is ignored by the controller and is inserted only for clarity.
2 P000000000001111T375E	Functionally equivalent to example 1.
3 T375P1111E	Also equivalent to example 1.
4 P1T5E	Close contact 1 for 0.5 s.
5 TE	Open all contacts and continue to the next instruction.
6 P110T5331E	Close contacts 2 and 3 for 33.1 s. The 5 was punched in error and will be ignored.

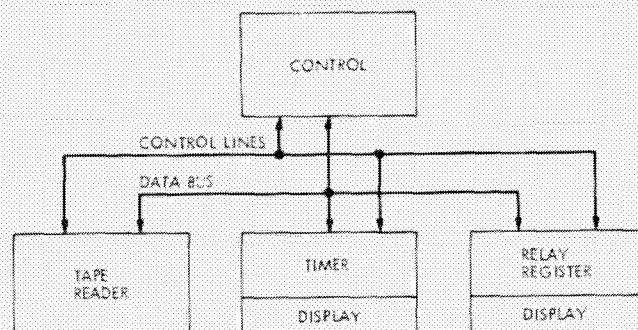


Fig. 1. Block diagram of the programmed controller



Fig. 2. Photograph of Model 601 programmed controller



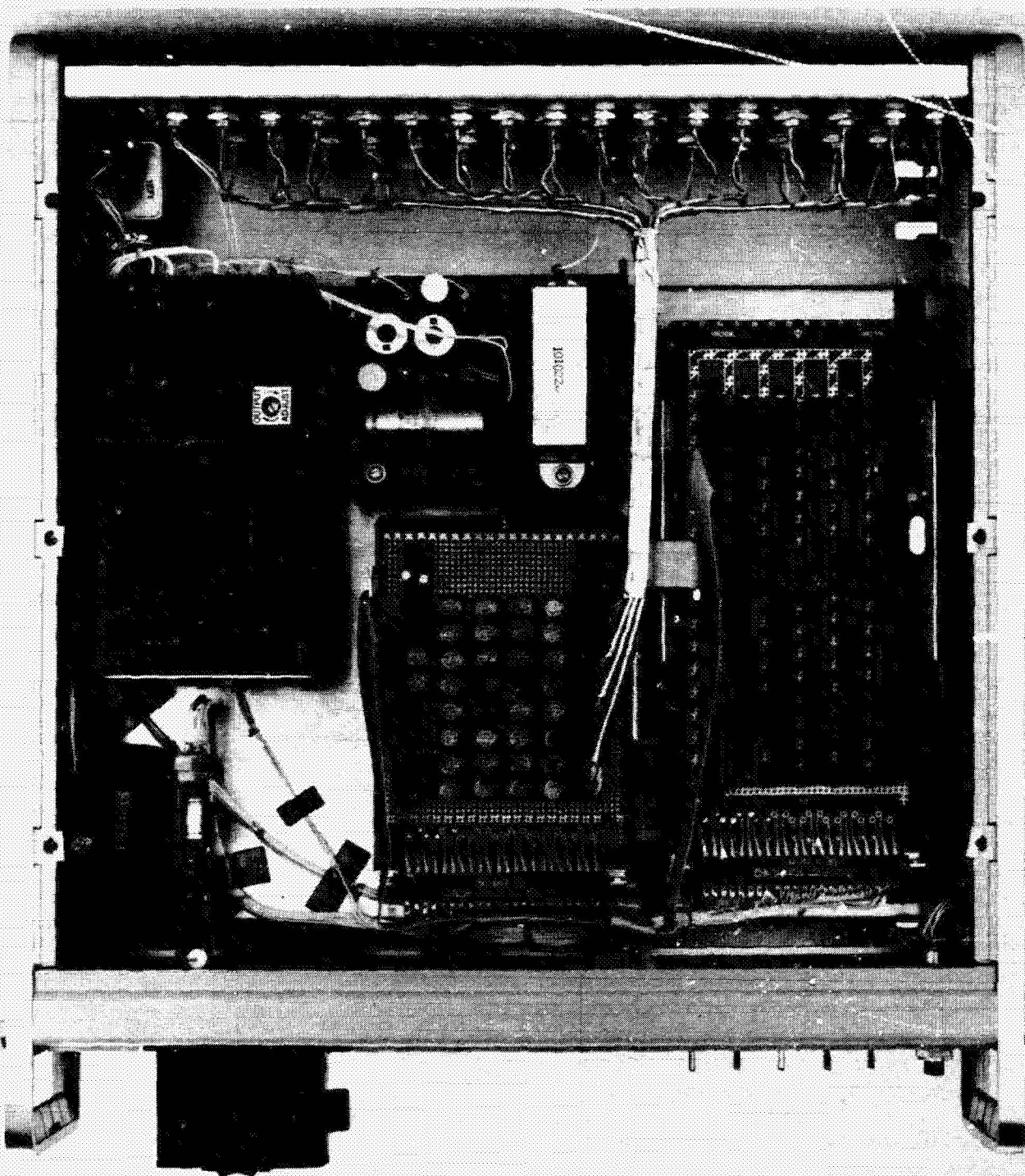


Fig. 3. Photograph of Model 601 programmed controller, top cover removed

# Radio Frequency Performance of DSS 14 64-m Antenna at 3.56- and 1.96-cm Wavelengths

A. J. Freiley

Communications Elements Research Section

*During February and March 1973, the DSS 14 64-m antenna was fitted with major structural braces, and other structural modifications were made to improve low angle elevation system gain performance at centimeter wavelengths. The new system performance, as defined by the radiometric measurements of May 1973, is compared to the previous performance, with respect to system efficiency, sub-reflector focus, and equivalent radio frequency (RF) surface tolerance. The evaluation shows that the predicted effect of the structural braces has been achieved; however, either the main reflector or subreflector surface tolerance, or both, have been degraded. The degradation is well defined at X- and Ku-band frequencies; at S-band the effect is nearly negligible.*

## I. Introduction

The radio frequency (RF) performance of the DSS 14 64-m antenna was measured to evaluate the effectiveness of the antenna modifications undertaken during February-March 1973. These modifications consisted of the installation of major structural braces and other modifications to the structure for noise abatement (Refs. 1, 2). To obtain the total antenna performance, radiometer measurements of selected radio sources were undertaken at X- and Ku-bands prior to and after the modifications. These radio sources were selected to eliminate the uncertainty associated with less accurately known sources and to maintain consistency with previous measurements. The results show a pronounced change in the antenna RF

performance, most likely attributable to a change in antenna surface tolerance.

## II. Antenna Modifications

Three major activities occurred during February-March 1973: The first was the installation of the structural braces (Refs. 1, 2) to improve the RF surface tolerance at elevation angles between 6 and 45 deg. Another activity was the resetting of the main reflector panels after the installation of the structural braces. The third activity was the welding of the panels of the subreflector to reduce the noise associated with diplexed high-power microwave transmission.

### III. Radio Sources

The performance characteristics were measured using two systems: (1) the X-band system at 8.415 GHz (3.56 cm) and (2) the Ku-band system at 15.3 GHz (1.96 cm). The radiometer measurements were made of 3C123 and Saturn at X-band and Ku-band, respectively. Noise adding radiometers were used at each frequency. Table 1 describes the source characteristics used.

### IV. Radiometer Technique

The radiometer technique used consists of three parts: The first is the boresighting of the antenna about the half-power points of the beam. Care was taken to insure both speed and accuracy of the boresights. At these frequencies, the axial focus of the system is important. Therefore, before each set of data was taken, the antenna was focused in the axial direction. To accomplish this, the analog output of the total power noise adding radiometer (NAR) was displayed on a chart recorder. While the antenna beam was on source, the subreflector was slewed from the out position to the in position and back again to determine the optimum indicated position. The third portion of the radiometer technique consists of the on-off source operating system temperature measurements. From two off source and one on source measurements, the off source operating system temperature and the source temperature can be determined for a particular elevation angle. By knowing the flux density of the observed source, one can calculate the antenna efficiency.

### V. Radiometer Data

The base performance of the antenna system is defined by measurements made in January 1972 at Ku-band and in January 1973 at X-band. The antenna system performance as determined by the May 1973 measurements is directly comparable. The same sources were observed with the same systems.

The antenna axial focus is an elevation angle dependent function. The fitted curves representing the optimum position for the January X- and Ku-band systems agree very well (Figs. 1, 2). The agreement is within approximately 2.5 mm indicated control room position. The fitted curves representing the optimum position for the May X- and Ku-band systems also agree very well—within approximately 5 mm indicated control room positions. Significant differences occur between the January and the May data. The February–March 1973 modifications have caused the focal length change of the system to be-

come greater as the antenna is moved in elevation. Therefore, the axial focus of the antenna has become more critical for all users.

The off source operating system temperature for clear weather was not affected by the antenna modifications (Fig. 3). The Ku-band operating system temperature is 25 K at zenith, and the X-band operating system temperature is 23 K at zenith, which includes 1.5 K at zenith contributed by the dichroic feed, used during both data periods at X-band (Ref. 3).

The intent of the structural braces was to improve the RF surface tolerance at elevation angles between 6 and 45 deg, which would also improve the RF system efficiency between those angles. The system efficiencies as derived from Table 1 and the radio metric measurements are presented in Figs. 4 and 5. The system efficiencies in the figures are as would be observed in spacecraft and radio science missions; the efficiencies have not been corrected for the atmospheric loss effects ( $I_{at}$ ) nor the waveguide loss effects ( $L_w$ ) but have been corrected for the effect of source size. The results following the structure modifications are lower than expected. The modifications have, in fact, generally decreased the system efficiency, as summarized in Table 2. As shown in Figs. 4 and 5, the modifications have decreased the peak system efficiencies but have improved the change in system efficiency as a function of elevation angle, as was predicted (Ref. 1). The net result is that the peak system efficiency is lower but the system efficiency at 10 deg elevation is about the same as before.

The desirable effect of decreasing the change of system efficiency from the peak was offset by a decrease in the peak system efficiency. To determine a possible cause for the effects seen, one should examine the RF surface tolerance. By assuming a flat-Earth atmospheric loss approximation and using the information given in Table 3 for the calculated system efficiency for 100% efficient reflecting surfaces, and by measuring the actual system efficiency, it is possible to determine the loss due to the surface tolerance. This loss has been converted to an equivalent RMS surface tolerance by the method of Ruze (Ref. 4) and is represented for all cases in Figs. 6 and 7. The RMS surface tolerance of the antenna before the February–March modifications was 1.15 mm at 45 deg elevation, which increased to approximately 1.65 mm at 15 deg elevation. After the modifications, the RMS surface tolerance is approximately 1.46 mm, which increases to 1.62 mm at 15 deg elevation.



## VI. Conclusions

The modifications to the DSS 16 64-m antenna accomplished during February–March 1973 have been evaluated at X- and Ku-bands using radiometer techniques. The peak system efficiency at 45 deg elevation angle has decreased at both bands, but the change in system efficiency with elevation angle has been improved.

The conclusions reached are that (1) the structural braces have decreased the effect of the RMS surface tolerance change with elevation angle, and (2) the combination of the main reflector reset and the welding of the sub-reflector has increased the overall RMS surface tolerance. Another way of stating this is to say that the dynamic

distortions (elevation angle dependent gravity induced deformations to the main reflector backup structure) have been improved; the static distortion component (elevation angle independent setting precision of either one or both reflector panels) has been degraded. The reason for the increased axial focus sensitivity as a function of elevation angle is not understood.

The peak system efficiency at 45 deg elevation angle has been reduced 0.5 dB at X-band and 1.6 dB at Ku-band. Using the surface tolerance values obtained from these short-wavelength observations, a predicted change of 0.04 dB at S-band at 45 deg elevation angle is obtained. This loss is reduced at lower elevation angles.

## References

1. Katow, M. S., "210-ft-diam Antenna Reflector Upgrade Study—Phase 1," in *The Deep Space Network*, Space Programs Summary 37-62, Vol. II, pp. 109–113, Jet Propulsion Laboratory, Pasadena, Calif., March 31, 1970.
2. Lobb, V. B., and Katow, M. S., "64 Meter-Diameter Antenna with New Braces: Installation Description and Computed Performance for Gravity Loads," in *The Deep Space Network Progress Report*, Technical Report 32-1526, Vol. XVII, pp. 93–99, Jet Propulsion Laboratory, Pasadena, Calif., Oct. 15, 1973.
3. Bathker, D. A., "Dual Frequency Dichroic Feed Performance," presented to the XXVI Meeting of the Avionics Panel, NATO/AGARD, Munich, Germany, November 26–30, 1973.
4. Ruze, J., "Antenna Tolerance Theory—A Review," *Proc. IEEE*, Vol. 54, No. 4, April 1966.

**Table 1. Radio sources**

Source	S or $T_B$	Source size, arcsec	Source structure	Antenna half-power beamwidth, arcsec	Antenna polarization
3C123 @ 8.415 GHz	9.4 FU	Two point sources <sup>a</sup>	Close double Sept. 13, arcsec	137	RCP
Saturn @ 15.3 GHz Jan 72 May 73	145 K	  20 × 18 17 × 15	  Planet (disk)	  76	  RCP

<sup>a</sup>Source size correction factor ( $c_s$ ) = 1.003.

**Table 2. 64-m system: efficiency summary**

System	Jan 1973, 45-deg elevation	May 1973 45-deg elevation
X-band	51.3%	46.1%
Ku-band	35.1% <sup>a</sup>	24.1%

<sup>a</sup>January 1972 data.

**Table 3. Antenna constants**

Constant	X-band	Ku-band
Feed and blockage efficiency $\eta_0$ (Ref. 4)	0.6196	0.6411
Waveguide loss $L_w$ , dB	0.14	0.10
Atmospheric attenuation $L_0$ at zenith, dB	0.037	0.047

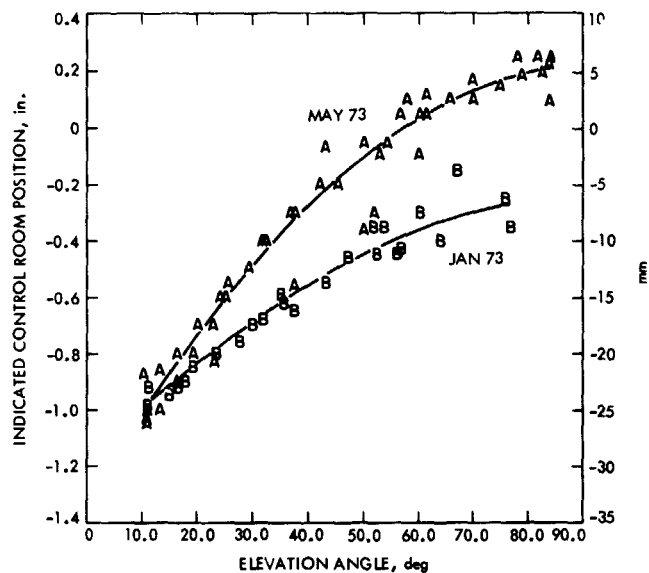


Fig. 1. Axial focus, X-band

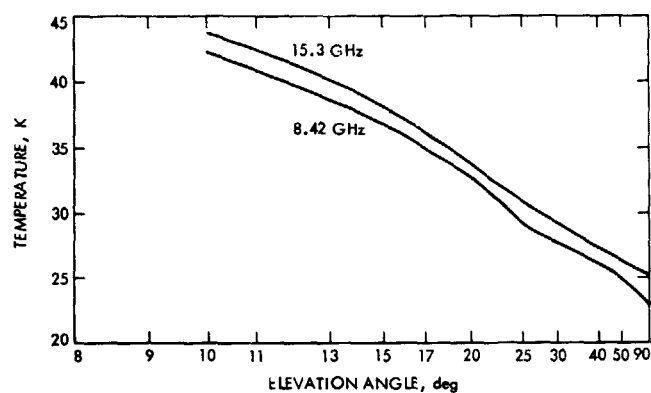


Fig. 3. Operating system temperature

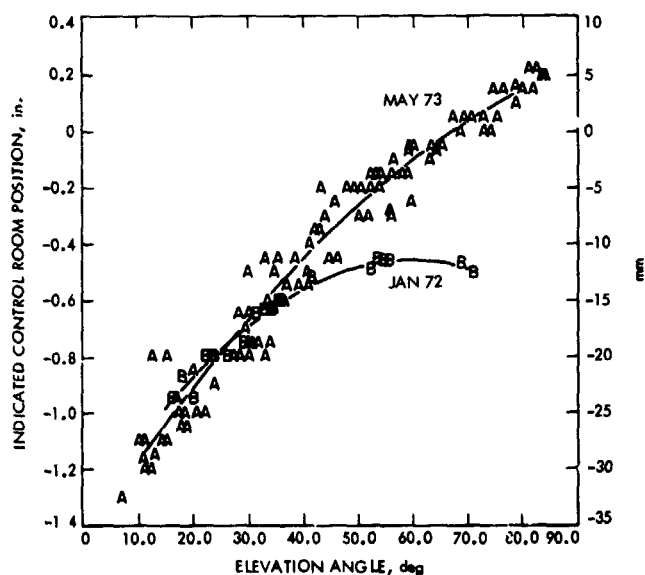


Fig. 2. Axial focus, Ku-band

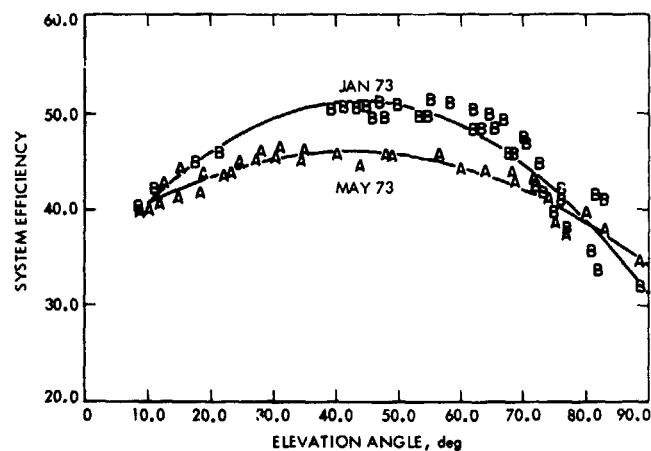


Fig. 4. System efficiencies X-band, 8.42 GHz

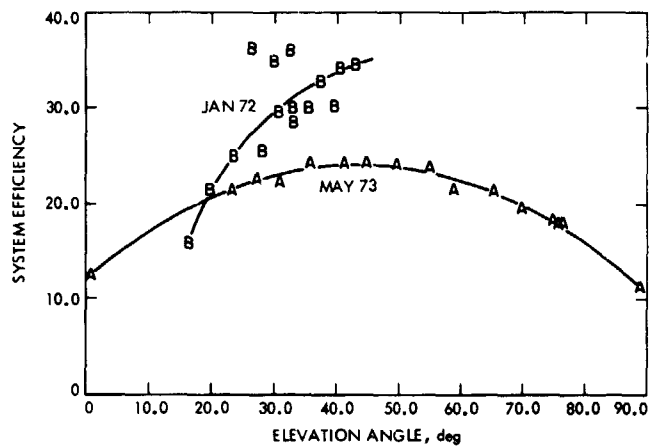


Fig. 5. System efficiencies, Ku-band, 15.3 GHz

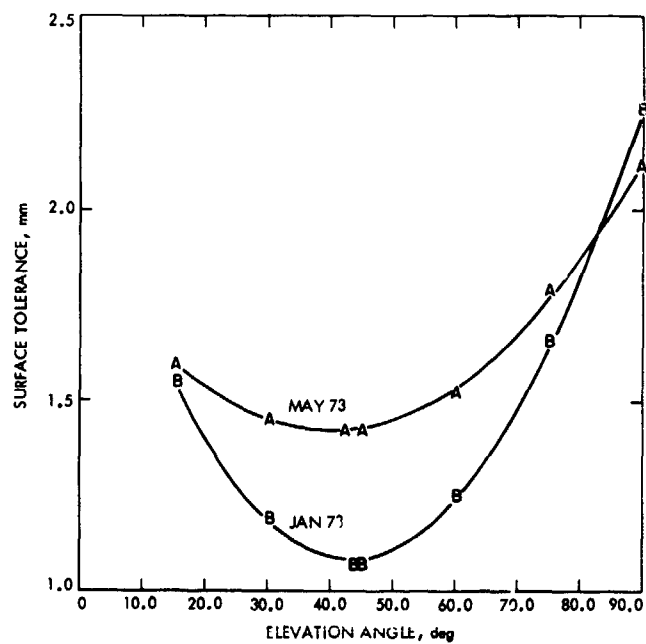


Fig. 6. System surface tolerance from X-band tests

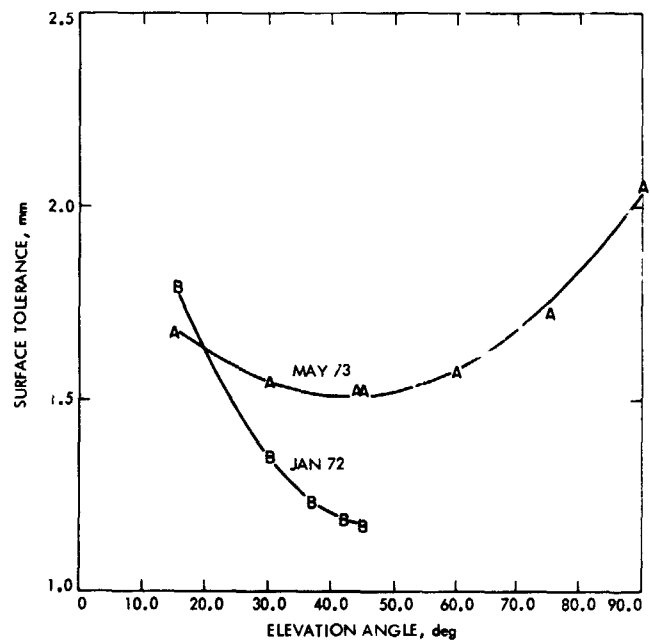


Fig. 7. System surface tolerance from Ku-band tests

# Optimal Station Location for Two-Station Tracking

E. R. Rodemich  
Communications Systems Research Section

*A problem related to the optimal placement of three tracking stations for purposes of two-station tracking is formulated and solved.*

## I. Introduction

It is known (and easy to see) that three tracking antennas, however they are placed on the globe, cannot provide total coverage of the celestial sphere. However, since most interesting deep-space phenomena (spacecraft and natural astronomical objects) have small declinations, this fact is of little practical importance. For example, the DSN's 64-m antennas cannot "see" certain points on the celestial sphere at declinations of 28 deg or so.

Of course there is typically much overlap in the coverage of the celestial sphere provided by three stations, and this overlap can be used to good advantage: since simultaneous two-station tracking is possible in these doubly-covered regions. Two-station tracking is useful for a variety of reasons. For example, since the diurnal doppler amplitude is proportional to the cosine of the declination, accurate determination of spacecraft declination using doppler is quite difficult at declinations near zero. Two-

station tracking can however be used for accurate goniometry at all declinations. Also, accurate tracking of constantly accelerating spacecraft could best be done with two stations. Finally, important astronomical knowledge can be gained from interferometric data.

Thus it is desirable to have as much of the celestial sphere as possible doubly covered. It is easy to see, however, that if no point on the celestial sphere is visible from all *three* stations simultaneously, the total area that is doubly covered is always the same. We therefore arrive at the question answered in this article: What is the maximum overlap possible between the coverages of the celestial sphere provided by *two* of the antennas, given that all *three* cover all celestial declinations that are less than a fixed amount?

More precisely, let us assume that the three antennas each cover a circular cap of angular radius  $\beta$  on the celestial sphere, and that it is required that the three circular

caps cover all objects with declinations in the range  $[-\alpha, \alpha]$ . Then we wish to maximize the region of intersection of two of the caps. Surprisingly, the optimal configuration does not always have all three stations centered on the equator.

In the case of the 64-m net,  $\beta = 84^\circ$  and  $\alpha$  is about  $28^\circ$ . It will turn out that there is a configuration of three  $\alpha = 84^\circ$  circular caps covering the band of declinations between  $\pm 28^\circ$  with two of the stations separated by only  $27^\circ$  on the globe. (This configuration has all three stations on the equator.) However, the closest pair of stations on the 64-m net (Goldstone and Madrid) are separated by  $82^\circ$ . Thus as far as two-station tracking is concerned, the 64-m net is far from optimally arranged.

## II. Solution to the Problem

Three spherical caps of angular radius  $\beta$  ( $0 < \beta < \pi/2$ ) are to cover the band on the sphere with latitudes between  $-\alpha$  and  $\alpha$  ( $0 \leq \alpha < \pi/2$ ). We want to maximize the area of the region of intersection of two of the caps.

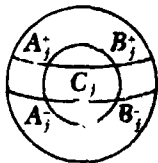
Denote latitude on the sphere by  $\delta$ , and let  $\phi$  measure longitude west from some reference point. Let the cap  $C_j$  have center at  $(\delta_j, \phi_j)$ . Since each cap covers less than half the equator, following the equator around we see the caps in a cyclic order  $C_1, C_2$ , and  $C_3$  such that  $0 < \phi_j - \phi_{j-1} \pmod{2\pi} < \pi$ . It can be shown that the caps cover the whole band in the same order that they cover the equator: if  $C_j$  intersects the band in the region  $S_j$ , then the band is the union of six disjoint regions  $S_1 - S_2 - S_3, S_1 \cap S_2, S_2 - S_1 - S_3, S_2 \cap S_3, S_3 - S_1 - S_2$ , and  $S_3 \cap S_1$ , each of which extends across the band.

$C_j$  contains the points  $(\delta, \phi)$  that satisfy the inequality

$$\cos \delta_j \cos \delta \cos(\phi - \phi_j) + \sin \delta_j \sin \delta \geq \cos \beta$$

The boundary of  $C_j$  intersects the boundaries of the band in four points  $A_j^+, A_j^-, B_j^+$ , and  $B_j^-$ , with coordinates

$$\left. \begin{aligned} A_j^+ : \delta = \pm \alpha, \phi = \phi_j + \cos^{-1} \frac{\cos \beta \mp \sin \delta_j \sin \alpha}{\cos \delta_j \cos \alpha} \\ B_j^+ : \delta = \pm \alpha, \phi = \phi_j - \cos^{-1} \frac{\cos \beta \mp \sin \delta_j \sin \alpha}{\cos \delta_j \cos \alpha} \end{aligned} \right\} \quad (1)$$



We have a covering if  $A_j^+$  and  $A_j^-$  are in  $C_{j+1}$ , and  $B_j^+$  and  $B_j^-$  are in  $C_{j-1}$ .

Our problem is to maximize the area of  $C_1 \cap C_2$ . This is equivalent to maximizing the cosine of the angle between the centers of  $C_1$  and  $C_2$ , which is

$$\cos \theta_{12} = \cos \delta_1 \cos \delta_2 \cos(\phi_1 - \phi_2) + \sin \delta_1 \sin \delta_2 \quad (2)$$

There is an extremal covering for this problem, if  $\alpha$  and  $\beta$  are such that some coverings exist. Hence it is sufficient to consider only those coverings for which there is no obvious variation that increases  $\cos \theta_{12}$ .

If we move each cap  $C_j$  to a position centered on the equator at  $(0, \phi_j)$ , we preserve the covering of the band. For, if we denote the points  $A_j^+$ , etc., in the new position by bars,  $\bar{A}_j^+$  and  $\bar{B}_j^-$  are diametrically opposite on the cap, hence

$$\begin{aligned} \cos^2 \alpha \cos[\phi(\bar{A}_j^+) - \phi(\bar{B}_j^-)] - \sin^2 \alpha = \\ \cos 2\beta \leq \cos^2 \alpha \cos[\phi(A_j^+) - \phi(B_j^-)] - \sin^2 \alpha \end{aligned} \quad (3)$$

and

$$\phi(\bar{A}_j^+) - \phi(\bar{B}_j^-) \geq \phi(A_j^+) - \phi(B_j^-)$$

By symmetry, this is equivalent to

$$\phi_j - \phi(\bar{B}_j^-) \geq \frac{1}{2} [\phi_j - \phi(B_j^-) + \phi_j - \phi(B_j^+)]$$

Similarly

$$\phi(\bar{A}_{j-1}^+) - \phi_{j-1} \geq \frac{1}{2} [\phi(A_{j-1}^+) - \phi_{j-1} + \phi(A_{j-1}^-) - \phi_{j-1}]$$

If we started with a covering of the band,  $C_j$  and  $C_{j-1}$  meet on each boundary of the band, which makes

$$\phi_j - \phi(B_j^+) + \phi(A_{j-1}^+) - \phi_{j-1} \geq \phi_j - \phi_{j-1}$$

Hence adding the preceding inequalities, we get

$$-\phi(\bar{B}_j^-) + \phi(\bar{A}_{j-1}^+) - \phi_{j-1} \geq \phi_j - \phi_{j-1}$$

Since  $C_j$  and  $C_{j-1}$  overlap on each boundary of the band, this proves the assertion, that the new configuration covers the band. By Eq. (3),

$$\phi(\bar{A}_j^+) - \phi(\bar{B}_j^-) = 2 \cos^{-1} \frac{\cos \beta}{\cos \alpha}$$

The upper boundary of the band can be covered by three arcs with this change in longitude only if

$$2 \cos^{-1} \frac{\cos \beta}{\cos \alpha} \geq \frac{2\pi}{3}$$

or

$$\cos \beta \leq \frac{1}{2} \cos \alpha \quad (4)$$

This is a necessary and sufficient condition for the existence of coverings.

One way to increase  $\cos \theta_{12}$  is to move the center of  $C_1$  directly toward the center of  $C_2$ . The covering is preserved unless  $A_3^+$  or  $A_3^-$  goes out of  $C_1$ . Hence, for an extremal covering, one of these points must lie on the boundary of  $C_1$ , so that  $A_3^+ = B_1^+$  or  $A_3^- = B_1^-$ . Similarly,  $B_3^+ = A_2^+$  or  $B_3^- = A_2^-$ .

By reflecting across the equator, we can make  $A_3^- = B_1^-$ . Suppose first that the only other one of these relations that holds is  $B_3^+ = A_2^+$ . Move the center of  $C_3$  along the great circle equidistant from  $A_2^+$  and  $B_1^-$ . There is a nearby position where  $A_2^+$  and  $B_1^-$  fall inside  $C_3$ , unless the center of  $C_3$  is on the great circle arc from  $A_2^+$  to  $B_1^-$ . Then,  $A_2^+$  and  $B_1^-$  are at the ends of a diameter of  $C_3$ , so  $\delta_3 = 0$ . Since  $A_2^+$  and  $B_1^-$  are inside  $C_3$ ,  $\delta_1 > 0$  and  $\delta_2 < 0$ . If we go to the covering with centers on the equator at  $(0, \phi_1)$  as described above, then by Eq. (3),  $\cos \theta_{12}$  is increased. Hence we are not at an extremal covering.

This shows that we need only consider coverings with  $A_3^- = B_1^-$  and  $B_3^- = A_2^-$ . Since  $B_1^+$  and  $A_2^+$  are in  $C_3$ ,

$$\delta_1 \geq -\delta_3, \quad \delta_2 \geq \delta_1 \quad (5)$$

Now we prove a lemma.

**LEMMA.** A covering with  $\delta_3 < 0$ ,  $A_3^- = B_1^-$ ,  $B_3^- = A_2^-$  and  $\delta_1 > -\delta_3$  cannot be extremal unless  $A_1^- = B_2^-$  and  $\delta_1 = \delta_2$ .

**Proof:** First suppose  $A_1^- \neq B_2^-$ . Then  $C_1$  can be rotated about  $A_3^-$  in either direction without destroying the covering. If the covering is extremal,  $\cos \theta_{12}$  is at a stationary point under this rotation, which implies that the center of  $C_1$  lies on the great circle through  $A_3^-$  and the center of  $C_2$ .

If  $\delta_1 > -\delta_3$ , we find likewise that this circle goes through  $B_3^-$ . By symmetry,  $\delta_2 = \delta_1$  and  $\phi_3 - \phi_2 = \phi_1 - \phi_3$ . Then by Eq. (3),

$$\begin{aligned} \cos \theta_{12} &= \cos^2 \delta_1 \cos [2\pi - 2(\phi_1 - \phi_3)] + \sin^2 \delta_1 \\ &= 1 - 2 [\cos \delta_1 \sin (\phi_1 - \phi_3)]^2 \end{aligned}$$

If we vary  $\delta_1$  and  $\delta_2$ , keeping  $\delta_1 = \delta_2$  and the hypotheses of the lemma,  $\cos \delta_1 \sin (\phi_1 - \phi_3)$ , which is the distance of the center of  $C_1$  from the vertical plane through the center of the sphere and the center of  $C_3$ , has a relative maximum for the given configuration. Hence  $\cos \theta_{12}$  is at a relative minimum, and can be increased by varying  $\delta_1$  in either direction.

For  $\delta_2 = -\delta_3$ ,  $B_3^+ = A_2^+$ , and we can only rotate  $C_2$  upwards about  $B_3^-$ . If this does not increase  $\cos \theta_{12}$ , the great circle through the centers of  $C_1$  and  $C_2$  must pass above  $B_3^-$ . Let the highest point on this circle have longitude  $\phi_4$ , and let it cross  $\delta = -\alpha$  at  $\phi_5$  after passing through the center of  $C_2$ . Then we have  $\phi_5 - \phi_4 = \phi_4 - \phi(A_3^-)$ . Since  $\delta_1 > \delta_2$ ,  $|\phi_1 - \phi_4| < \phi_2 - \phi_4$ , and so  $\phi_5 - \phi_2 < \phi_1 - \phi(A_3^-)$ . Also,  $\delta_1 > \delta_2$  implies  $\phi(B_3^-) - \phi_2 > \phi_1 - \phi(A_3^-)$ , hence  $\phi_5 - \phi_2 < (B_3^-) - \phi_2$ . But this makes the circle pass below  $B_3^-$ , a contradiction.

Now we know that  $A_1^- = B_2^-$ . The circle  $\delta = -\alpha$  is partitioned by  $C_1$ ,  $C_2$ , and  $C_3$  into three parts. On each part, the variation in  $\phi$  can be found from Eq. (1). Since the total variation is  $2\pi$ , we get

$$(\phi(A_1^-) - \phi_1) + (\phi(A_2^-) - \phi_2) + (\phi(A_3^-) - \phi_3) = \pi$$

or

$$\begin{aligned} \cos^{-1} \frac{\cos \beta + \sin \delta_1 \sin \alpha}{\cos \delta_1 \cos \alpha} + \cos^{-1} \frac{\cos \beta + \sin \delta_2 \sin \alpha}{\cos \delta_2 \cos \alpha} \\ + \cos^{-1} \frac{\cos \beta + \sin \delta_3 \sin \alpha}{\cos \delta_3 \cos \alpha} = \pi \end{aligned} \quad (6)$$

Then  $\phi_1 - \phi_2 = \phi(A_1^-) - \phi_1 + \phi(A_2^-) - \phi_2 = \pi - (\phi(A_3^-) - \phi_3)$ , which is fixed when we vary  $\delta_1$  and  $\delta_2$  subject to Eqs. (5) and (6). Differentiating Eq. (6), we get

$$\frac{d\delta_2}{d\delta_1} = - \frac{\sin \alpha + \sin \delta_1 \cos \beta}{\cos^2 \delta_1 \sqrt{1 - u_1^2}} \bigg/ \frac{\sin \alpha + \sin \delta_2 \cos \beta}{\cos^2 \delta_2 \sqrt{1 - u_2^2}} < 0 \quad (7)$$

where  $u_j = (\cos \beta + \sin \delta_j \sin \alpha) / (\cos \delta_j \cos \alpha)$ . Hence the range of  $\delta_1$  satisfying Eqs. (5) and (6) is an interval with  $\delta_2 > \delta_1 = |\delta_3|$  at one end,  $\delta_1 > \delta_2 = |\delta_3|$  at the other end. Differentiate Eq. (2) with respect to  $\delta_1$ :

$$\begin{aligned} \frac{d \cos \theta_{12}}{d\delta_1} &= \\ &[-\cos \delta_1 \sin \delta_2 \cos (\phi_1 - \phi_2) + \sin \delta_1 \cos \delta_2] \frac{d\delta_2}{d\delta_1} \\ &- \sin \delta_1 \cos \delta_2 \cos (\phi_1 - \phi_2) + \cos \delta_1 \sin \delta_2 \end{aligned}$$

By using Eq. (7) and the relation

$$\begin{aligned}\cos(\phi_1 - \phi_2) &= \cos[(\phi(A_1^-) - \phi_1) + (\phi(A_2^-) - \phi_2)] \\ &= u_1 u_2 - \sqrt{1-u_1^2} \sqrt{1-u_2^2}\end{aligned}$$

this can be reduced to

$$\frac{d \cos \theta_{12}}{d \delta_1} = (\text{positive quantity}) \cdot (\sin \delta_2 - \sin \delta_1)$$

It follows that  $\cos \theta_{12}$  has a maximum at  $\delta_1 = \delta_2$ , which proves the lemma.

Now we continue with considering all coverings for which  $A_1^- = B_1^+$  and  $B_3^- = A_2^-$ . There are essentially three classes:

- class (I):  $A_2^+$  and  $B_1^+$  interior to  $C_1$
- class (II):  $A_2^+ = B_3^+$ ,  $B_1^+$  interior to  $C_1$
- class (III):  $A_2^+ = B_3^+$  and  $B_1^+ = A_3^+$

For a covering in class (I), the center of  $C_3$  may be moved along its meridian to bring  $A_2^-$  and  $B_1^-$  inside  $C_3$ , unless the center is already at the closest point to  $A_2^-$  and  $B_1^-$ . Then  $A_3^-$  and  $B_3^-$  are at the ends of a diameter of  $C_3$ , which occurs for

$$\delta_4 = -\sin^{-1}(\sin \alpha / \cos \beta) \quad (8)$$

The hypotheses of the lemma are satisfied, so  $A_1^- = B_2^-$  and  $\delta_2 = \delta_1$ . Equation (6) becomes

$$2 \cos^{-1} \frac{\cos \beta + \sin \delta_1 \sin \alpha}{\cos \delta_1 \cos \alpha} + \cos^{-1} \frac{\cos \beta + \sin \delta_3 \sin \alpha}{\cos \delta_3 \cos \alpha} = \pi$$

Transpose the last term on the left and take the cosine of each side. By the use of some trigonometric formulas, the result is

$$2 \left( \frac{\cos \beta + \sin \delta_1 \sin \alpha}{\cos \delta_1 \cos \alpha} \right)^2 + \frac{\cos \beta + \sin \delta_3 \sin \alpha}{\cos \delta_1 \cos \alpha} = 1 \quad (9)$$

From Eq. (2),

$$\cos \theta_{12} = \sin^2 \delta_1 - \cos^2 \delta_1 \cdot \frac{\cos \beta + \sin \delta_3 \sin \alpha}{\cos \delta_3 \cos \alpha} \quad (10)$$

This gives a possible extremal covering.

For a covering in class (II), the center of  $C_3$  can be varied along the great circle equidistant from  $A_1^-$  and  $B_2^-$ . If  $\delta_3 > 0$ , varying in the direction of decreasing latitude

brings all the points  $A_1^-$ ,  $B_2^-$ , and  $B_3^-$  inside  $C_3$ . Hence  $\delta_3 \leq 0$ . If  $\delta_3 = 0$ ,  $\delta_2 = 0$  and  $\delta_1 > 0$ . Then moving the center of  $C_1$  to  $(0, \phi_1)$  gives a covering for which  $\cos \theta_{12}$  is larger. If  $\delta_3 < 0$ ,  $\delta_1 > \delta_2 = -\delta_3$ . The lemma applies, and gives a contradiction. Hence there are no extremal coverings in class (II).

For a covering in class (III),  $\delta_1 = \delta_2 = -\delta_3$ . We can reflect the covering in the equator to make  $\delta_1 \geq 0$ . Then we have a covering if  $C_1$  and  $C_2$  overlap on the lower boundary of the band. The condition for this is

$$2 \cos^{-1} \frac{\cos \beta + \sin \delta_1 \sin \alpha}{\cos \delta_1 \cos \alpha} + \cos^{-1} \frac{\cos \beta - \sin \delta_1 \sin \alpha}{\cos \delta_1 \cos \alpha} \geq \pi \quad (11)$$

The left side of Eq. (11) is a decreasing function of  $\delta_1 \geq 0$ , so we have an interval  $0 \leq \delta_1 \leq \delta_{10}$  to consider, where equality occurs in Eq. (11) at  $\delta = \delta_{10}$ .

Put

$$u = (\cos \beta + \sin \delta_1 \sin \alpha) / (\cos \delta_1 \cos \alpha)$$

$$v = (\cos \beta - \sin \delta_1 \sin \alpha) / (\cos \delta_1 \cos \alpha)$$

and

$$\begin{aligned}\gamma &= \phi_1 - \phi_2 \\ &= (\phi_1 - \phi(R_1^-)) + (\phi(A_3^-) - \phi_3) \\ &= \cos^{-1} u + \cos^{-1} v\end{aligned}$$

By symmetry,  $\phi_2 - \phi_1 + 2\gamma = 2\pi$ , and

$$\begin{aligned}\cos \theta_{12} &= \cos^2 \delta_1 \cos(2\pi - 2\gamma) + \sin^2 \delta_1 \\ &= 1 - 2 \cos^2 \delta_1 \sin^2 \gamma\end{aligned}$$

Let

$$\begin{aligned}R &= (1 - \cos \theta_{12})/2 \\ &= \cos^2 \delta_1 \sin^2 \gamma \\ &= \cos^2 \delta_1 [u \sqrt{1-v^2} + v \sqrt{1-u^2}]^2\end{aligned} \quad (12)$$

Eliminating radicals,

$$\begin{aligned}[R + \cos^2 \delta_1 (2u^2 v^2 - u^2 - v^2)]^2 &= 4u^2 v^2 \cos^4 \delta_1 \\ &\quad \times (1 - u^2)(1 - v^2)\end{aligned} \quad (13)$$

In the range of  $\delta_1$  of interest,  $u^2$  and  $v^2$  are less than 1, and Eq. (13) has real roots for  $R$ . The right side of Eq. (13) becomes negative when we pass  $\delta_1 = \beta - \alpha$ , where  $u$  be-



comes greater than 1. Those points  $(\delta_1, R)$  with  $0 \leq \delta_1 \leq \beta - \alpha$ , which satisfy Eq. (13), form one connected curve in the  $\delta_1 R$  plane. If we multiply Eq. (13) by  $\cos^4 \alpha \cos^2 \delta_1$ , it can be put in the form

$$\begin{aligned} \cos^4 \alpha \cos^2 \delta_1 R^2 + 4R [(\cos^2 \beta - \sin^2 \alpha + \sin^2 \alpha \cos^2 \delta_1) \\ - \cos^2 \alpha \cos^2 \delta_1 (\cos^2 \beta + \sin^2 \alpha \\ - \sin^2 \alpha \cos^2 \delta_1)] + 16 \cos^2 \beta \sin^2 \alpha \\ \times (\cos^2 \delta_1 - \cos^4 \delta_1) = 0 \end{aligned} \quad (14)$$

where the left side is a quadratic function of  $\cos^2 \delta_1$ .

The points of the  $\delta_1 R$  plane with  $0 \leq \delta_1 \leq \beta - \alpha$  which satisfy Eq. (14) lie on a curve with its end points on  $\delta_1 = 0$ , at  $R = 0$  and  $R = R_0 = 4 \cos^2 \beta (\cos^2 \alpha - \cos^2 \beta) / \cos^4 \alpha$ . Since Eq. (14) is quadratic in  $\cos^2 \delta_1$ , each value of  $R$  can correspond to at most two values of  $\delta_1$ . This implies that the curve passes through  $0 < R < R_0$  just once, monotonically.

An extremal covering minimizes  $R$ .  $R_0$  is the value for a covering with  $\delta_1 = 0$ . Since there is no local minimum on  $(0, R_0)$ , only  $\delta_1 = 0$  or  $\delta_1 = \delta_{10}$  can give extremal coverings.

This gives the following three coverings to consider:

- (1)  $\delta_1 = \delta_2 = \delta_3 = 0$ . Here  $\cos \theta_{12} = 1 - 2R_0 = 1 - 8 \cos^2 \beta (\cos^2 \alpha - \cos^2 \beta) / \cos^4 \alpha$
- (2)  $\delta_1 = \delta_2 = -\delta_3 > 0$ . We need equality in Eq. (11). Then Eq. (9) applies with  $\delta_3 = -\delta_1$ , or  $2u^2 + v = 1$ . Then from Eq. (12),

$$\begin{aligned} \cos \theta_{12} &= 1 - 2 \cos^2 \delta_1 (1 - u^2) \\ \cos \theta_{12} &= 1 - 2 \cos^2 \delta_1 \\ &\quad + 2 (\cos \beta + \sin \delta_1 \sin \alpha)^2 / \cos^2 \alpha \end{aligned} \quad (15)$$

The condition of Eq. (9) is

$$\begin{aligned} 2 (\cos \beta + \sin \delta_1 \sin \alpha)^2 \\ + \cos \delta_1 \cos \alpha (\cos \beta - \sin \delta_1 \sin \alpha) = \cos^2 \delta_1 \cos^2 \alpha \end{aligned} \quad (16)$$

We also have the covering found in class (I):

- (3)  $\delta_3 = -\sin^{-1} (\sin \alpha / \cos \beta)$ ,  $\delta_1 = \delta_2 > -\delta_3$ . Here  $\delta_1$  satisfies Eq. (9) and  $\cos \theta_{12}$  is given by Eq. (10).

For any  $\alpha, \beta$ , the optimal covering must be one of these three. The covering (2) is better than (1) if

$$\begin{aligned} \Delta = \frac{4 \cos^2 \beta (\cos^2 \alpha - \cos^2 \beta)}{\cos^4 \alpha} - \cos^2 \delta_1 \\ + \frac{(\cos \beta + \sin \delta_1 \sin \alpha)^2}{\cos^2 \alpha} > 0 \end{aligned}$$

where  $\delta_1$  satisfies Eq. (16). Equation (16) leads to a 4th-degree equation in  $\sin \delta_1$ . If we eliminate  $\sin \delta_1$  between this equation, and the equation  $\Delta = 0$ , we get a relation between  $\alpha$  and  $\beta$  that holds on the curve separating the regions where (1) or (2) is better. This equation has the following parametric solution:

$$\left. \begin{aligned} y &= \frac{9x^3 - 6x^2 + x}{10x^3 - 13x^2 + 8x - 1} \\ t &= x(y - 1) \\ \sin \alpha &= \sqrt{t} \\ \cos \beta &= \cos \alpha \sqrt{t/y} \end{aligned} \right\} \quad (17)$$

The curve is generated by  $3 \leq x \leq 3 + \sqrt{8}$ .

When the covering (3) exists,  $\sin \alpha \leq \cos \beta$ , which already implies that (2) is better than (1). Hence the region of  $(\alpha, \beta)$  for which (3) is extremal lies in the region where (2) is better than (1). Whenever (3) exists, the value of  $\delta_1$  for (2) is greater than  $\sin^{-1} (\sin \alpha / \cos \beta)$ . This implies that (2) is not extremal, for varying  $\delta_1$  toward 0 in (2) brings the points  $B_1^*, A_2^*$  inside  $C_3$ . Hence (3) is extremal when it exists, and the boundary of the region of  $(\alpha, \beta)$  for which this occurs is the curve on which Eq. (15) is satisfied by  $\delta_1 = \sin^{-1} (\sin \alpha / \cos \beta)$ , or

$$\begin{aligned} 2 (\cos^2 \beta + \sin^2 \alpha)^2 + \cos \alpha (\cos^2 \beta - \sin^2 \alpha)^{3/2} = \\ \cos^2 \alpha (\cos^2 \beta - \sin^2 \alpha) \end{aligned}$$

Rationalizing, we get a 4th-degree equation for  $\cos^2 \beta$  in terms of  $\alpha$ . This equation has the parametric solution

$$\left. \begin{aligned} y &= \frac{(1-x^2)(3x+5)}{26x^3 + 52x^2 + 42x + 8} \\ &\quad - \frac{(1-x)^2 \sqrt{9x^2 + 14x + 9}}{26x^3 + 52x^2 + 42x + 8}, \quad 0 \leq x \leq 1 \\ \sin \alpha &= \sqrt{xy} \\ \cos \beta &= \sqrt{y} \end{aligned} \right\} \quad (18)$$

In Fig. 1, the region  $\cos \beta \leq 1/2 \cos \alpha$  is shown, divided into the regions where each configuration is optimal.

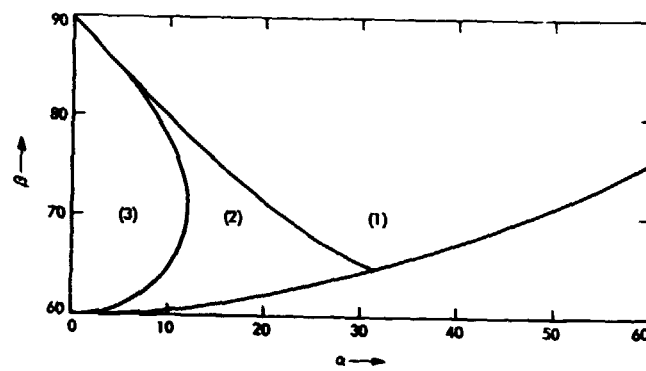


Fig. 1. The regions where each configuration is optimal

## Bandwidth Selection for Block IV SDA

R. B. Crow

R.F. Systems Development Section

*A review of the bandwidth selection for the Block III Subcarrier Demodulator Assembly (SDA) is given, along with the design philosophy as implemented in the engineering model of the Block IV SDA.*

Historically, the Block III SDA bandwidths were chosen for a number of reasons. The  $wl_0 = 0.03$  Hz loop bandwidth was the narrowest loop that could be efficiently obtained in terms of hardware stability, cost, and acquisition time, while the 1.5-Hz loop bandwidth was compatible with the Block III receiver  $wl_0 = 152$  Hz and was required for high-acceleration tracking at launch. The  $wl_0 = 0.375$  Hz loop bandwidth was a compromise in an effort to retain reasonable noise performance in the presence of dynamic signal input (i.e., doppler rate).

During the past 6 years, mission requirements have undergone considerable change, and S-band doppler rates as high as 180 Hz/s can be expected in close flybys of the larger planets (e.g., Pioneer 1.3-radius, Jupiter flyby).

The basic philosophy regarding bandwidth selection for the Block IV SDA requires

- (1) A narrow bandwidth ( $wl_0 = 0.03$  Hz), so that no penalty is suffered in using the Block IV SDA at low symbol rates.
- (2) A wide bandwidth that is as narrow as possible while still maintaining sufficient gain (at design point) to handle the maximum doppler rate at the highest subcarrier frequency.
- (3) An adaptive gain control that can be raised quickly to improve the loop acquisition characteristic but lowered slowly at a rate depending on which bandwidth is being used, thus offering a convenient

means of increasing the loop gain (i.e., bandwidth), which can be smoothly reduced (to reduce the phase transient due to loop gain change).

- (4) A loop gain increase of 10:1 to give a reasonable increase in tracking acquisition performance without increasing the loop jitter beyond usable limits. (At design point, the narrow-bandwidth loop has a jitter of 4 deg RMS, while the narrow-acquisition-bandwidth loop will have 11 deg RMS phase jitter.)

Figure 1 is a plot of loop bandwidth vs. input sideband signal-to-noise energy ratio per bit ( $ST_{sb}/N_b$ ) for both the Block III and IV SDAs. It can be noted that a more adaptive bandwidth is available in the Block IV design because of a different IF bandwidth and a different ratio of input

limit level/virtual input signal (i.e.,  $v$ ) (Ref. 1). It is also apparent that the narrow bandwidth is approximately the same for Blocks III and IV up to  $ST_{sb}/N_b \simeq +10$  dB, while the Block III medium bandwidth is approximately the same as the Block IV wide bandwidth.

From Fig. 1 and Tables 1 and 2, it is apparent that many missions previously handled by the Block III medium bandwidth can now be handled by the Block IV narrow-bandwidth loop (because of increased gain).

All other missions requiring high doppler rate tracking can use the Block IV wide bandwidth (with little increase in noise degradation compared to the Block III medium and with large improvement in rate tracking error).

## Reference

1. Brockman, M. H., "An Efficient and Versatile Telemetry Subcarrier Demodulator Technique for Deep Space Telecommunications," Paper No. A-1, 2, Fourth Hawaii International Conference on System Science, Jan. 1971, University of Hawaii, Honolulu, Hawaii.

**Table 1. Gain comparison between Block III and IV SDAs  
at design point**

Loop bandwidth	Design point loop gain, $s^{-1}$	
	Block III	Block IV
Narrow	10	56.8
Narrow-acquisition	10	568
Medium	250	—
Wide	500	59,700
Wide-acquisition	—	597,000

**Table 2. Gain comparison between Block III and IV SDAs  
at  $ST_{sig}/N_0 = +25$  dB**

Loop bandwidth	Loop gain at $ST_{sig}/N_0 = +25$ dB, $s^{-1}$	
	Block III	Block IV
Narrow	23	2,756
Narrow-acquisition	—	27,560
Medium	2,675	—
Wide	2,549	329,544
Wide-acquisition	—	3,295,440

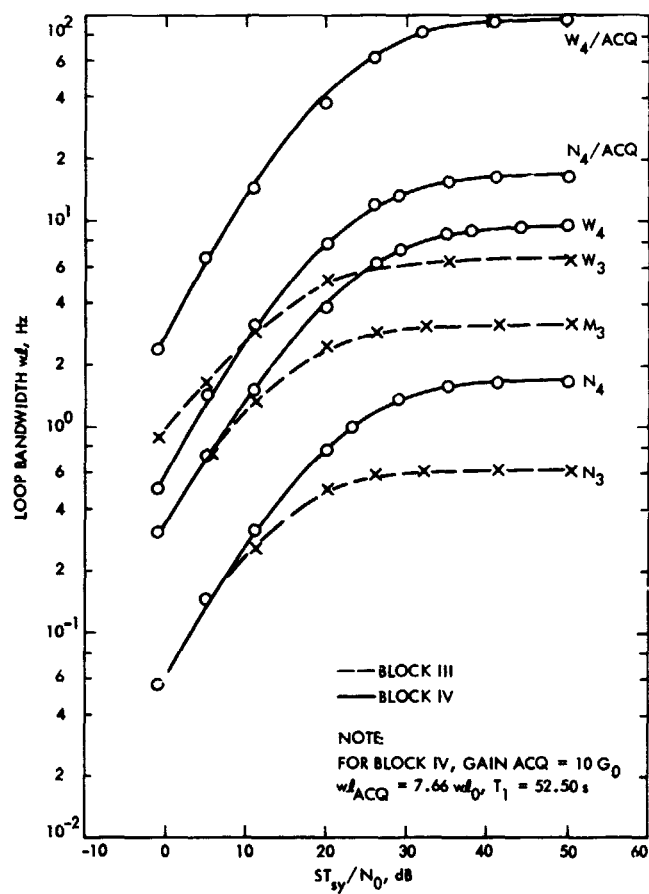


Fig. 1.  $ST_{sy}/N_0$  vs.  $w_0$  for Block III and IV SDAs for  $R_{sy} = 40$  SPS

# Frame Synchronization Performance Analysis for MVM'73 Uncoded Telemetry Modes

B. K. Levitt

Communications Systems Research Section

*This paper describes a practical frame synchronization (sync) acquisition and maintenance algorithm based on the Hamming distance metric, which is a generalization of the scheme developed for the 1973 Mariner mission to Venus and Mercury (MVM'73). For the special case of uncoded phase-shift-keyed data received over the binary symmetric channel, formulas are derived for computing an upper bound on the probability of false sync acquisition, the mean time to sync acquisition, and the mean time to the subsequent loss of sync, as a function of the bit error rate, frame length, sync word length, and algorithm parameters. These formulas are directly applicable to the uncoded MVM'73 telemetry modes, and a numerical example relating to the 117.6 kilobits/s real time TV mode is included.*

## I. Introduction

The problem of establishing frame synchronization (sync) usually involves the identification of received sync words periodically interspersed with random data (Ref. 1). For uncoded binary signals received over the additive white Gaussian noise channel, the frame sync words are often located by finding segments of the received data that are highly correlated with the transmitted sync word (Ref. 2). Massey (Ref. 3) has in fact shown that the optimum sync word search requires the addition of a correction term to this correlation rule. If hard decisions are made on the received data prior to the acquisition of frame synchronization, the problem is reduced to detecting the sync words in uncoded data received over the

binary symmetric channel: in this case, the optimum frame sync decision is based on the Hamming distance metric.

This article examines the performance of a practical frame sync acquisition and maintenance algorithm for uncoded phase-shift-keyed (PSK) data received over the binary symmetric channel. Because the detected PSK data necessarily have a binary phase ambiguity that cannot be resolved until frame sync is established, the algorithm bases its sync decision on a modified Hamming distance rule. Instead of making a hard sync decision over a single frame of received data, the algorithm scans the detected bit stream, searching for a sequence whose Hamming distance from the sync word satisfies a threshold test. When

the bit error rate is high and the threshold is stringent, the reliability of the sync decision is improved at the expense of delaying that decision for several frames. For additional reliability, a hard sync decision is made only when two received sequences one frame apart both satisfy the threshold test.

The frame sync algorithm described herein is not exceptionally innovative, and variations on the same approach have been used on past Mariner missions. It is in fact a two-threshold generalization of the particular acquisition and maintenance algorithm that was developed for use with the uncoded and biorthogonally coded telemetry modes of the Mariner 10 spacecraft (MVM73). The principal purpose of this article is to document the performance analysis of this algorithm for uncoded PSK data received over the binary symmetric channel. Markov models are employed in this analysis to derive formulas for computing an upper bound on the probability of false sync acquisition, as well as the mean time to sync acquisition, and the mean time to the subsequent loss of sync, for arbitrary bit error rates, frame lengths, sync word lengths, and threshold values. These formulas are directly applicable to the uncoded MVM73 telemetry modes, and, as a numerical example below, they are used to determine optimum threshold values as a function of the channel bit error rate for the high-rate (117.6 kilobits/s) real time TV data mode. It should be noted here that the author has extended the algorithm performance analysis to include the MVM73 telemetry modes employing a (32,6) biorthogonal code, although the work has not been published to date. However, numerical results for the 22.05 kilobits/s coded TV telemetry mode have been used to select proper algorithm threshold values for the MVM73 mission.

## II. Frame Sync Algorithm

The operation of the acquisition and maintenance modes of the frame sync algorithm are detailed in the flow diagrams of Figs. 1 and 2. A brief description of the algorithm now follows to establish some notation that will be needed later for the performance analysis.

Assume that the transmitted information is organized into  $M$ -bit frames composed of an  $L$ -bit sync word followed by  $M - L$  statistically independent, equally likely data bits. The detected bit stream contains independent bit errors: a particular bit will be incorrect with probability  $\epsilon$ .

Let the received bit stream be represented by the binary sequence  $r_1, r_2, r_3, \dots$ , and define an arbitrary

$L$ -tuple  $\rho_m = (r_m, r_{m+1}, \dots, r_{m+L-1})$ . The frame sync objective is to identify which of the  $\rho_m$ 's are received frame sync words. When a binary PSK signal is demodulated using a carrier reference derived from the modulated signal, there is an inherent binary phase ambiguity in the detector output: that is, the received bit stream can be inverted data ( $\overline{\text{data}}$ ) with probability  $1/2$ . Consequently, for low bit error rates, if a particular  $\rho_m$  is in fact a received sync word, its Hamming distance  $d_m$  from the transmitted sync word is equally likely to be near 0 or  $L$ . As indicated in Figs. 1 and 2, the algorithm threshold test reflects this property.

Suppose the receiver is out of sync, and the acquisition mode is initiated. The overlapping  $L$ -bit received sequences  $\rho_1, \rho_2, \rho_3, \dots$  are examined in succession, and the corresponding Hamming distances  $d_1, d_2, d_3, \dots$  from the sync word are computed. The algorithm uses two threshold tests:  $d_m \leq T_1$ , and  $d_m \geq L - T_1$  (the latter indicating the detection of  $\overline{\text{data}}$ ). If it finds a sequence  $\rho_{\hat{m}}$  which satisfies either threshold test, and if the sequence  $\rho_{\hat{m}+M}$  one frame ahead satisfies the *same* threshold test, frame sync is established. That is, a hard decision is made that  $\rho_{\hat{m}}$  is a received sync word, the data polarity is deduced according to which of the two threshold tests was satisfied by  $\rho_{\hat{m}}$  and  $\rho_{\hat{m}+M}$ , and the maintenance mode is entered.

If the communication link consisted only of a binary symmetric channel, there would be no need for a frame sync maintenance mode. If bit synchronization could be maintained perfectly once frame sync was acquired, a simple bit counter could maintain frame sync indefinitely. Unfortunately, in practice, interface buffers within the overall communication link typically result in random deletions and insertions of bits in the received data stream. It is the function of the frame sync maintenance mode to detect these occurrences, and to signal the resulting loss of frame sync.

Referring to the flow diagram in Fig. 2, it is seen that the data polarity decision made when frame sync was established confines the maintenance mode to one of the two threshold tests,  $d_m \leq T_2$  and  $d_m \geq L - T_2$ . (Note that the acquisition and maintenance modes use different thresholds in general.) In the acquisition mode, it was decided that  $\rho_{\hat{m}}$  was a received frame sync word, since  $d_{\hat{m}}$  and  $d_{\hat{m}+M}$  satisfied the same  $T_1$  threshold test. The maintenance mode examines only presumed received sync words of the form  $\rho_{\hat{m}+kM}$ , where  $k$  is a positive integer. If  $T_2 \geq T_1$  (see discussion below),  $d_{\hat{m}}$  and  $d_{\hat{m}+M}$  must satisfy the  $T_2$  threshold test; consequently, the mainte-



nance mode can start with  $\hat{p}_{m+2M}$ , as indicated in the diagram. When two consecutive sequences that should be received sync words fail the threshold test, the receiver is declared to be out of sync, and the algorithm reverts to the acquisition mode.

The following design objectives influence the selection of the thresholds  $T_1$  and  $T_2$ . For convenience, use the following terminology:

$Pr[FS]$ : probability of false sync acquisition.

$MTS$ : mean time to sync acquisition, in frames (expected value of  $\hat{m}/M$ ), conditioned on a correct sync decision (assuming  $Pr[FS] \ll 1$ ).

$MTLS$ : mean time to loss of sync following correct sync acquisition, in frames, neglecting bit insertions or deletions.

Ideally, we would like  $Pr[FS]$  and  $MTS$  to be small, while  $MTLS$  is large. However, for fixed values of  $\epsilon$ ,  $L$ , and  $M$ ,  $Pr[FS]$  decreases while  $MTS$  increases monotonically as  $T_1$  decreases, and the reverse condition also holds. So the selection of  $T_1$  involves a tradeoff between  $Pr[FS]$  and  $MTS$ . Typically  $T_1$  is made relatively small, favoring  $Pr[FS]$ , so that when a frame sync decision is made, it is likely to be correct. Fortunately, it will be evident in the numerical examples below that  $T_1$  does not have to be too large for  $MTS$  to be near the minimum value of  $\frac{1}{2}$ .

With regard to the selection of  $T_2$ , it should be noted that following the acquisition of frame sync, there are two situations that would cause the maintenance mode to decide that sync is lost. If one or more bits are erroneously deleted or inserted into the received data stream, thereafter, the received sync words would not coincide with the  $L$ -bit sequences examined by the maintenance mode. If the sync word is a Barker (Ref. 1) or a Neuman-Hofman (Ref. 4) sequence, its correlation properties would ensure that the Hamming distances of the  $L$ -bit received sequences from the sync word are likely to be near  $L/2$ . In this case, a threshold  $T_2$  on the order of  $L/4$  would be small enough to signal the loss of sync. On the other hand, if the channel state is such that no bit deletions or insertions are occurring, the maintenance mode will still declare a loss of sync, falsely, if two consecutive received sync words contain more than  $T_2$  bit errors. In this circumstance, relating only to the binary symmetric channel model, that is measured by the parameter  $MTLS$  defined above. (To include the random deletions and insertions in the channel model, a multi-state Markov approach would be required; this complication is avoided

in this article.) To maximize  $MTLS$ ,  $T_2$  should be as large as possible; a threshold near  $L/4$  is compatible with this objective. In conclusion,  $T_2$  should be near  $L/4$ , and  $T_1$  should be closer to zero.

### III. Algorithm Performance

The following formulas relating to the performance of the frame sync algorithm for uncoded PSK data received over the binary symmetric channel are derived in the Appendix:

$$Pr[FS] \leq (M-1) \frac{\gamma^2}{4} + \min \left[ A, (M-1) A \frac{\gamma^2}{2} + \frac{3}{2}(L-1) \gamma^2 \right] \quad (1)$$

where it is assumed that  $M \gg L$ , and

$$\gamma \equiv 2^{-(L-1)} \sum_{i=0}^{T_1} \binom{L}{i} \quad (2)$$

$$\eta(T) \equiv 1 - \sum_{i=0}^T \binom{L}{i} \epsilon^i (1-\epsilon)^{L-i} \quad (3)$$

$$A \equiv \frac{\eta(T_1) [3 - 2\eta(T_1)]}{[1 - \eta(T_1)]^2} \quad (4)$$

$$MTS = \frac{M+1}{2M} + A \text{ frames; } Pr[FS] \ll 1 \quad (5)$$

$$MTLS = \frac{1 + \eta(T_2) - \eta^2(T_2)}{\eta^2(T_2)} \text{ frames} \quad (6)$$

Parameters  $\gamma$  and  $\eta(T)$  have physical interpretations:

- $\gamma$ : the probability that a particular  $L$ -bit received sequence, composed of independent, equally likely 1's and 0's, satisfies either acquisition threshold test (probability of a "false alarm").
- $\eta(T)$ : the probability that a particular received sync word (or complemented sync word if data is detected) has more than  $T$  bit errors, and fails the corresponding threshold test (probability of a "miss").

A numerical example will serve to demonstrate the behaviour of  $Pr[FS]$ ,  $MTS$ , and  $MTLS$  as a function of threshold values for fixed  $L$ ,  $M$ , and  $\epsilon$ . The 1973 Mariner 10 mission to Venus and Mercury has a high-rate (117.6 kilobits/s), uncoded PSK telemetry mode for

transmitting real time TV data to Earth. This mode has a frame length  $M = 7056$  bits, and a sync word length  $L = 31$  bits (a pseudo-noise or PN sequence). As the spacecraft-to-Earth range varies during the mission, so does the bit error rate  $\epsilon$ ; it is anticipated that during the primary mission,  $\epsilon$  will not exceed  $\frac{1}{20}$ . On this mission, the acquisition and maintenance thresholds are identical, and are denoted by  $T$ . For bit error rates in the range  $\frac{1}{20} \leq \epsilon \leq \frac{1}{500}$ , the frame sync algorithm performance is summarized in Table 1. A single TV picture is composed of 700 frames of data; one of the design objectives in selecting  $T$  was that  $MTLS$  exceed 700, so that frame sync would be likely to be maintained over a TV picture. Subject to this constraint, as well as the threshold trade-offs discussed earlier, the recommended values of  $T$  are circled in Table 1. It is evident from the table that if  $T$  is adjusted for changes in  $\epsilon$ ,  $MTS$  will be near  $\frac{1}{2}$ ,  $MTLS$  will exceed 700, while  $Pr[FS]$  is less than  $2 \times 10^{-6}$ , for  $\epsilon$  less than  $\frac{1}{20}$ .

#### IV. Summary

This paper has considered the problem of acquiring and maintaining frame synchronization in uncoded PSK data received over the binary symmetric channel. To this end, a practical algorithm was described that computes the Hamming distances of  $L$ -bit segments of the received

bit stream from the  $L$ -bit sync word, and applies these distances to a threshold test.

In the acquisition mode, the algorithm ensures a reliable frame sync decision by requiring that two consecutive  $L$ -bit received sequences one frame apart satisfy a stringent threshold test. The maintenance mode is designed to flag the loss of frame sync due to random deletions or insertions of bits in the received data stream; at the same time, its threshold test allows sufficient errors in the received sync words to pass so that the loss of sync is not likely to be declared falsely.

The performance of this algorithm was analyzed with the aid of Markov models of the threshold test operation. An upper bound for the probability of false sync acquisition, the mean time to sync acquisition, and the mean time to loss of sync were computed as a function of the bit error rate, frame length, sync word length, and algorithm threshold values.

This algorithm is a generalization of the scheme developed to provide frame synchronization on the Mariner 10 spacecraft-to-Earth telemetry link. As a numerical example, the derived formulas were used to predict the algorithm performance for the spacecraft's high-rate, real-time TV data mode.

#### References

1. Barker, R. H., "Group Synchronization of Binary Digital Systems," *Communication Theory*, Edited by Jackson. Butterworth, London, pp. 273-287, 1953.
2. Stiffler, J. J., *Theory of Synchronous Communications*. Prentice-Hall, Englewood Cliffs, N.J., 1971.
3. Massey, J. L., "Optimum Frame Synchronization," *IEEE Trans. Commun.*, Vol. COM-20, pp. 155-169, Apr. 1972.
4. Neuman, F., and Hofman, L., "New Pulse Sequences With Desirable Correlation Properties," *Proc. Nat. Telemetry Conf.*, Washington, D.C., pp. 277-282, Apr. 1971.

Table 1. Frame sync algorithm performance for  $M = 7056$ ,  
 $L = 31$  (note that  $Pr[FS]$  is actually an upper bound)

$\epsilon$	$T$	$Pr[FS]$	MTS, frames	MTLS, frames
1/20	5	$7 \times 10^{-8}$	0.51	$7 \times 10^4$
	④	$2 \times 10^{-8}$	0.55	3179
	3	$6 \times 10^{-6}$	0.70	236
1/30	4	$2 \times 10^{-6}$		$9 \times 10^4$
	③	$4 \times 10^{-8}$	0.56	2839
	2	$6 \times 10^{-10}$	0.78	155
1/40	4	$2 \times 10^{-6}$	0.50	$1 \times 10^5$
	③	$4 \times 10^{-8}$	0.52	$2 \times 10^4$
	2	$5 \times 10^{-10}$	0.63	597
1/50	3	$4 \times 10^{-8}$	0.51	$9 \times 10^4$
	②	$4 \times 10^{-10}$	0.57	1822
	1	$3 \times 10^{-12}$	0.96	69
1/100	3	$4 \times 10^{-8}$	0.50	$2 \times 10^7$
	②	$4 \times 10^{-10}$	0.51	$8 \times 10^4$
	①	$2 \times 10^{-12}$	0.62	704
	0	$5 \times 10^{-15}$	1.73	17
1/200	2	$4 \times 10^{-10}$	0.50	$4 \times 10^5$
	①	$2 \times 10^{-12}$	0.53	9064
	0	$3 \times 10^{-15}$	1.03	54
1/500	2	$4 \times 10^{-10}$	0.50	$8 \times 10^5$
	①	$2 \times 10^{-12}$	0.51	$3 \times 10^5$
	0	$2 \times 10^{-15}$	0.70	292

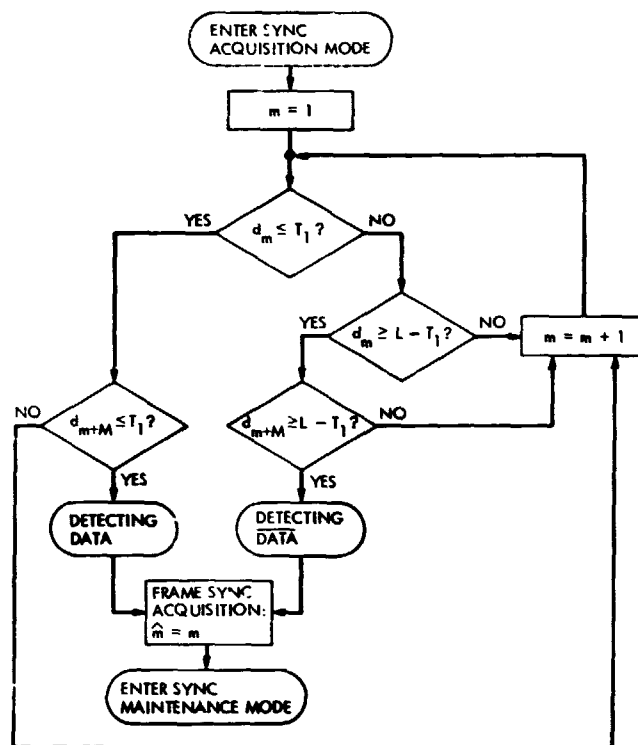


Fig. 1. Frame sync algorithm: acquisition mode flow diagram

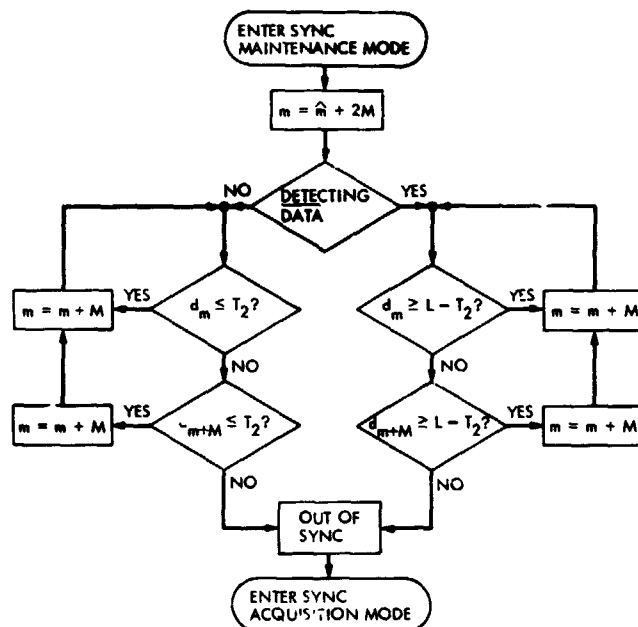


Fig. 2. Frame sync algorithm: maintenance mode flow diagram  
(assumption:  $T_1 \leq T_2$ )

## Appendix

### Derivation of Algorithm Performance Formulas

#### I. Probability of False Sync Acquisition

Assume that the received sync words are  $\rho_{m^*}, \rho_{m^*+M}, \rho_{m^*+2M}, \dots$ , where  $m^*$  is uniformly distributed:

$$Pr[m^*] = \frac{1}{M}; \quad 1 \leq m^* \leq M \quad (\text{A-1})$$

Define the following events, conditioned on a particular sync index  $m^*$ :

$$P \equiv \bigcup_{m=1}^{m^*-1} (\hat{m} = m)$$

$$R_k \equiv (\hat{m} \neq m^* + kM)$$

$$V_k \equiv \bigcup_{m=m^*+(k+1)M+1}^{m^*+kM+L-1} (\hat{m} = m)$$

$$W_k \equiv \bigcup_{m=m^*+kM+L}^{m^*+(k+1)M-L} (\hat{m} = m)$$

$$Y_k \equiv \bigcup_{m=m^*+(k+1)M-L+1}^{m^*+(k+1)M-1} (\hat{m} = m)$$

$$X_k \equiv \bigcup_{m=m^*+kM+1}^{m^*+(k+1)M-1} (\hat{m} = m) = V_k \cup W_k \cup Y_k$$

where  $\hat{m}$  denotes the frame sync acquisition decision.

There are two approaches to bounding the probability of false sync acquisition (FS) used in this paper. The first is based on the events  $\{X_k\}$ :

$$Pr[FS|m^*] = Pr[P \cup (R_0 \cap X_0) \cup (R_0 \cap R_1 \cap X_1) \cup \dots]$$

By the familiar union bounding technique,

$$Pr[FS|m^*] \leq p + \sum_{k=0}^{\infty} \mu_k \quad (\text{A-2})$$

where

$$p \equiv Pr[P]$$

$$\mu_k \equiv Pr[R_0 \cap R_1 \cap \dots \cap R_k \cap X_k]$$

To compute  $p$ , (still conditioned on  $m^*$ ), the union bound is again applied:

$$p = Pr\left[\bigcup_{m=1}^{m^*-1} (\hat{m} = m)\right] \leq \sum_{m=1}^{m^*-1} Pr[\hat{m} = m | m \neq m^*]$$

Under the assumption that a Barker or Neuman-Hofman frame sync word is used, it will be assumed that all of the received sequences  $\rho_m$  for  $1 \leq m \leq m^* - 1$ , including those that overlap  $\rho_{m^*}$ , can be treated as uniformly random binary  $L$ -tuples. Then

$$\begin{aligned} Pr[\hat{m} = m | m \neq m^*] &= Pr[(d_m \leq T_1) \cap (d_{m+M} \leq T_1)] \\ &\quad \cup [(d_m \geq L - T_1) \\ &\quad \cap (d_{m+M} \geq L - T_1)] | m \neq m^*] \\ &= \{Pr[d_m \leq T_1 | m \neq m^*] \\ &\quad \times Pr[d_{m+M} \leq T_1 | m \neq m^*]\} \\ &\quad + \{Pr[d_m \geq L - T_1 | m \neq m^*] \\ &\quad \times Pr[d_{m+M} \geq L - T_1 | m \neq m^*]\} \end{aligned}$$

and each of the four terms above equals  $\gamma/2$ , where

$$\begin{aligned} \gamma &\equiv Pr[(d_m \leq T_1) \cup (d_m \geq L - T_1) | m \neq m^*] \\ &= 2^{-L} \left[ \sum_{i=0}^{T_1} \binom{L}{i} + \sum_{i=L-T_1}^L \binom{L}{i} \right] = 2^{-(L-1)} \sum_{i=0}^{T_1} \binom{L}{i} \end{aligned}$$

$$\therefore Pr[\hat{m} = m | m \neq m^*] = \frac{\gamma^2}{2}, \quad \text{independent of } m \quad (\text{A-3})$$

and

$$p \leq (m^* - 1) \frac{\gamma^2}{2}$$

Since Eq. (1) implies that

$$\bar{m}^* = \frac{1}{2} (M + 1) \quad (\text{A-4})$$

it follows that

$$p^{m^*} \leq (M - 1) \frac{\gamma^2}{4} \quad (\text{A-5})$$

The computation of bounds on  $\mu_k$  is somewhat more involved. Note that  $X_k$  is independent of  $R_0, R_1, \dots, R_{k-2}$ , but is correlated with  $R_{k-1}$  and  $R_k$ , for  $k \geq 2$ . Since

$$Pr[E_1 \cap E_2] \leq \min\{Pr[E_1], Pr[E_2]\}$$

for arbitrary events  $E_1$  and  $E_2$ , it follows that

$$\mu_k \leq \begin{cases} \min\{Pr[R_0 \cap R_1 \cap \dots \cap R_k], Pr[X_k]\}; & k = 0, 1 \\ \min\{Pr[R_0 \cap R_1 \cap \dots \cap R_k], \\ Pr[R_0 \cap R_1 \cap \dots \cap R_{k-2}] Pr[X_k]\}; & k \geq 2 \end{cases}$$

As in the computation of  $p$ ,

$$Pr[X_k] \leq (M-1) \frac{\gamma^2}{2}; \quad k \geq 0$$

$$\therefore \mu_k \leq \begin{cases} \min\left[P_k, (M-1) \frac{\gamma^2}{2}\right]; & k = 0, 1 \\ \min\left[P_k, P_{k-2} (M-1) \frac{\gamma^2}{2}\right]; & k \geq 2 \end{cases}$$

where

$$P_k \equiv Pr[R_0 \cap R_1 \cap \dots \cap R_k]; \quad k \geq 0$$

We want to compute an upper bound for

$$\sum_{k=0}^{\infty} \mu_k$$

It will be seen later that it is difficult to determine a general expression for  $P_k$ , whereas

$$\sum_{k=0}^{\infty} P_k$$

has a simple closed form expression. Consequently, we will use the bound

$$\sum_{k=0}^{\infty} \mu_k \leq \min\left[\sum_{k=0}^{\infty} P_k, (M-1) \frac{\gamma^2}{2} \left(2 + \sum_{k=0}^{\infty} P_k\right)\right] \quad (\text{A-6})$$

The Markov model of Fig. A-1 is used to calculate

$$\sum_{k=0}^{\infty} P_k$$

Recall that  $\hat{\rho}_m$  is declared to be a received sync word if and only if it is the first sequence  $\rho_m$  satisfying one of two threshold tests

$$d_m \leq T_1 \quad \text{or} \quad d_m \geq L - T_1$$

and  $\hat{\rho}_{m+M}$  satisfies the same test as  $\hat{\rho}_m$ . And

$$P_k = Pr[\hat{m} \neq m^* + lM; 0 \leq l \leq k]$$

Consider a particular received sync word  $\rho_{m^*+lM}$ : conditioned on the detection of (noninverted) data,

$$\begin{aligned} Pr[d_{m^*+lM} \geq L - T_1 | \text{data}] &= \sum_{j=L-T_1}^L \binom{L}{j} \epsilon^j (1-\epsilon)^{L-j} \\ &= \epsilon^{L-T_1} \sum_{j=0}^{T_1} \binom{L}{j} \epsilon^{T_1-j} (1-\epsilon)^j \end{aligned}$$

If  $T_1$  is much smaller than  $L$ , as recommended earlier, and  $\epsilon$  is not unusually high, the probability above is negligible in comparison with

$$Pr[d_{m^*+lM} \leq T_1 | \text{data}]$$

and

$$Pr[T_1 < d_{m^*+lM} < L - T_1 | \text{data}]$$

Similarly, conditioned on the detection of  $\overline{\text{data}}$ ,

$$Pr[d_{m^*+lM} \leq T_1 | \overline{\text{data}}] = \epsilon^{L-T_1} \sum_{j=0}^{T_1} \binom{L}{j} \epsilon^{T_1-j} (1-\epsilon)^j$$

which can be neglected. The conclusion is that although there are two sync acquisition threshold tests with respect to the received sync words, only one of these tests is pertinent, conditioned on the detection of data or  $\overline{\text{data}}$ , and the probability that a particular received sync word fails this pertinent test is given by

$$\eta(T_1) = 1 - \sum_{l=0}^{T_1} \binom{L}{l} \epsilon^l (1-\epsilon)^{L-l} \quad (\text{A-7})$$

independent of the data/ $\overline{\text{data}}$  conditioning.

Now, referring to Fig. A-1, suppose the receiver is in the 'bad' state, B. With probability  $\eta(T_1)$ ,  $\rho_{m^*}$  fails the pertinent threshold test, and the receiver remains in state B. With probability  $1 - \eta(T_1)$ ,  $\rho_{m^*}$  passes this test, and the receiver transfers to the 'good' state, G, which is really a conditional sync acquisition state. If  $\rho_{m^*+M}$  subsequently satisfies this threshold test, the receiver is in sync, with  $\hat{m} = m^*$ . However, if  $\rho_{m^*+M}$  fails the test,  $\hat{m}$  cannot equal  $m^*$  or  $m^* + M$ , and the receiver reverts to state B. Therefore, with respect to this model,

$P_k = Pr[\text{not in SYNC after } (k+2) \text{ transitions from B}]$

$$\Downarrow$$

$$P_k = \eta(T_1) P_{k-1} + \eta(T_1) [1 - \eta(T_1)] P_{k-2}; \quad k \geq 0 \quad (\text{A-8})$$

This recursion formula for  $P_k$  has initial conditions

$$P_{-1} = P_{-2} = 1$$

It yields a complicated expression for larger values of  $P_k$ . However, summing both sides of Eq. A-8,

$$\begin{aligned} \sum_{k=0}^{\infty} P_k &= \eta(T_1) + \eta(T_1) \sum_{k=0}^{\infty} P_k + 2\eta(T_1) [1 - \eta(T_1)] \\ &\quad + \eta(T_1) [1 - \eta(T_1)] \sum_{k=0}^{\infty} P_k \\ &\Downarrow \\ \sum_{k=0}^{\infty} P_k &= \frac{\eta(T_1) [3 - 2\eta(T_1)]}{[1 - \eta(T_1)]} \equiv A \quad (\text{A-9}) \end{aligned}$$

From Eqs. A-5, A-6, and A-9, the probability of false sync acquisition, averaged over  $m^*$ , is given by

$$Pr[FS] \leq (M-1) \frac{\gamma^2}{4} + \min \left[ A, (M-1) \frac{\gamma^2}{2} (A+2) \right] \quad (\text{A-10})$$

The second bounding approach involves the events  $\{V_k\}$ ,  $\{W_k\}$ , and  $\{Y_k\}$

$$\begin{aligned} Pr[FS | m^*] &= Pr[P \cup (R_0 \cap V_0) \cup (R_0 \cap W_0) \cup (R_0 \cap Y_0) \\ &\quad \cup (R_0 \cap R_1 \cap V_1) \cup (R_0 \cap R_1 \cap W_1) \\ &\quad \cup (R_0 \cap R_1 \cap Y_1) \cup \dots] \\ &\leq p + \sum_{k=0}^{\infty} \alpha_k + \sum_{k=0}^{\infty} \beta_k + \sum_{k=0}^{\infty} \zeta_k \quad (\text{A-11}) \end{aligned}$$

where

$$\begin{aligned} \alpha_k &\equiv Pr[R_0 \cap R_1 \cap \dots \cap R_k \cap V_k] \\ \beta_k &\equiv Pr[R_0 \cap R_1 \cap \dots \cap R_k \cap W_k] \\ \zeta_k &\equiv Pr[R_0 \cap R_1 \cap \dots \cap R_k \cap Y_k] \end{aligned}$$

To bound  $\alpha_k$ , note that  $V_k$  is independent of  $R_0, R_1, \dots, R_{k-2}$  for  $k \geq 2$ , and

$$Pr[V_k] \leq (L-1) \frac{\gamma^2}{2}; \quad k \geq 0$$

$$\begin{aligned} \therefore \alpha_k &\leq \begin{cases} \min [P_k, (L-1) \frac{\gamma^2}{2}]; & k = 0, 1 \\ \min [P_k, P_{k-2} (L-1) \frac{\gamma^2}{2}]; & k \geq 2 \end{cases} \\ &\Downarrow \\ \sum_{k=0}^{\infty} \alpha_k &\leq \min \left[ A, (L-1) \frac{\gamma^2}{2} (A+2) \right] \quad (\text{A-12}) \end{aligned}$$

With regard to  $\beta_k$ , it is noted that  $W_k$  is independent of  $R_0, R_1, \dots, R_k$  for  $k \geq 0$ , and

$$\begin{aligned} Pr[W_k] &\leq (M-2L+1) \frac{\gamma^2}{2} \\ \therefore \beta_k &\leq P_k (M-2L+1) \frac{\gamma^2}{2} \\ &\Downarrow \\ \sum_{k=0}^{\infty} \beta_k &\leq A (M-2L+1) \frac{\gamma^2}{2} \quad (\text{A-13}) \end{aligned}$$

As for  $\zeta_k$ , it is evident that  $Y_k$  is independent of  $R_0, R_1, \dots, R_{k-1}$  for  $k \geq 1$ , and

$$\begin{aligned} Pr[Y_k] &\leq (L-1) \frac{\gamma^2}{2}; \quad k \geq 0 \\ \therefore \zeta_k &\leq \begin{cases} \min \left[ P_k, (L-1) \frac{\gamma^2}{2} \right]; & k = 0 \\ \min \left[ P_k, P_{k-1} (L-1) \frac{\gamma^2}{2} \right]; & k \geq 1 \end{cases} \end{aligned}$$

$$\Downarrow$$

$$\sum_{k=0}^{\infty} \zeta_k \leq \min \left[ A, (L-1) \frac{\gamma^2}{2} (A+1) \right] \quad (\text{A-14})$$

Combining Eq. A-5 and Eqs. A-11 through A-14,

$$\begin{aligned} Pr[FS] &\leq (M-1) \frac{\gamma^2}{4} + \min \left\{ \left[ 2 + (M-2L+1) \frac{\gamma^2}{2} \right] A, \right. \\ &\quad \left[ 1 + (M-L) \frac{\gamma^2}{2} \right] A + (L-1) \frac{\gamma^2}{2}, \\ &\quad \left. A(M-1) \frac{\gamma^2}{2} + \frac{3}{2} (L-1) \gamma^2 \right\} \quad (\text{A-15}) \end{aligned}$$

Comparing Eqs. A-10 and A-15, and noting that we generally have  $L \ll M$ , the final bound is

$$\begin{aligned} Pr[FS] &\leq (M-1) \frac{\gamma^2}{4} + \min \left[ A, (M-1) A \frac{\gamma^2}{2} \right. \\ &\quad \left. + \frac{3}{2} (L-1) \gamma^2 \right] \quad (\text{A-16}) \end{aligned}$$

## II. Mean Time to Sync Acquisition

If  $T_1$  is relatively small, the probability that two incorrect  $L$ -bit received sequences one frame apart satisfy the acquisition threshold test (false alarm) is negligibly small. In this case,  $Pr [FS] \ll 1$ , and with high probability  $\hat{m} = m^* + kM$  for some integer  $k$ . Since the probability  $\gamma$  of a false alarm is negligible, it is the probability  $\eta(T_1)$  of a miss that is the dominant factor in making  $k$  nonzero. Therefore, the Markov model of Fig. A-1 can be used to compute the mean time to sync

$$MTS = \frac{\bar{m}}{M} = \frac{\bar{m}}{M} - k \quad (A-17)$$

To this end, define

$b \equiv$  number of transitions from state B to SYNC

$g \equiv$  number of transitions from state G to SYNC

If we start in state B, and the first transition depends on  $\rho_{m^*}$ ,

$$\bar{k} = \bar{b} - 2 \quad (A-18)$$

From the model of Fig. A-1,

$$\begin{aligned} \bar{b} &= \eta(T_1)(\bar{b} + 1) + [1 - \eta(T_1)](\bar{g} + 1) \\ \bar{g} &= \eta(T_1)(\bar{b} + 1) + [1 - \eta(T_1)] \\ &\Downarrow \\ b - 2 &= \frac{\eta(T_1)[3 - 2\eta(T_1)]}{[1 - \eta(T_1)]^2} \equiv A \end{aligned} \quad (A-19)$$

From Eqs. A-4 and A-17 through A-19, it follows that

$$MTS = \frac{M + 1}{2M} + A; \quad Pr [FS] \ll 1 \quad (A-20)$$

## III. Mean Time to Loss of Sync

It is assumed below that the frame sync acquisition mode has made a correct sync decision, and random bit

deletions and insertions are neglected. That is, the maintenance mode examines only received sync words. Since  $\rho_{\hat{m}}$  and  $\rho_{\hat{m}+M}$  satisfy the stringent acquisition threshold test, if  $T_2 \geq T_1$  as recommended earlier, they must also satisfy the maintenance threshold test. Consequently, the frame of received data between  $\rho_{\hat{m}}$  and  $\rho_{\hat{m}+M}$  is in sync, and the time to loss of sync is at least one frame. In general, if  $\rho_{\hat{m}+kM}$  and  $\rho_{\hat{m}+(k+1)M}$  are the first two consecutive received sync words to fail the maintenance threshold test, the time to loss of sync, measured by the number of good data frames accepted by the maintenance mode, is  $k - 1$ . Accordingly, the mean time to loss of sync is given by

$$MTLS = \bar{k} - 1 \quad (A-21)$$

Using the Markov model of Fig. A-2, define

$g \equiv$  number of transitions from G to SYNC LOST

$b \equiv$  number of transitions from B to SYNC LOST

Starting in state G, the first transition reflects the outcome of the  $T_2$  threshold test applied to  $\rho_{m^*+2M}$ ; then the time to loss of sync is  $g - 1$ , so that

$$\bar{k} = \bar{g} \quad (A-22)$$

From the model, it can be seen that

$$\begin{aligned} \bar{g} &= [1 - \eta(T_2)](1 + \bar{g}) + \eta(T_2)(1 + \bar{b}) \\ \bar{b} &= [1 - \eta(T_2)](1 + \bar{g}) + \eta(T_2) \\ &\Downarrow \\ \bar{g} &= \frac{1 + \eta(T_2)}{\eta^2(T_2)} \end{aligned} \quad (A-23)$$

$$\therefore MTLS = \frac{1 + \eta(T_2) - \eta^2(T_2)}{\eta^2(T_2)} \quad (A-24)$$



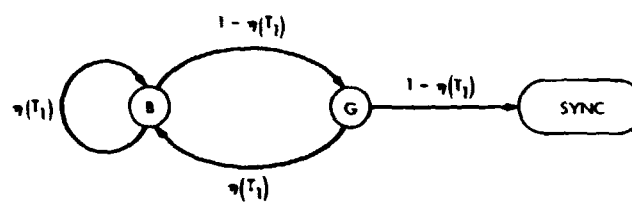


**Fig. A-1. Markov model relating to examination of received sync words in acquisition mode**

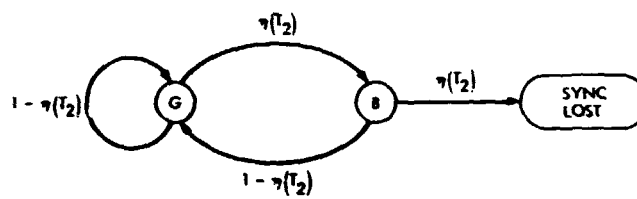


**Fig. A-2. Markov model for examination of received sync words in maintenance mode**

# DSN Research and Technology Support

E. B. Jackson

R. F. Systems Development Section

*The activities of the Development Support Group in operating and maintaining the Venus Station (DSS 13) are discussed and progress noted. Activities included planetary radar experiments (Venus and Mercury), radio source sky survey using the 26-m antenna, Faraday rotation data collection, weak radio source flux density measurement, X-band 400-kW radar development and testing, Block IV receiver/exciter installation and testing/checkout, 26-m antenna receiving system temperature improvement, differential very long baseline interferometry (VLBI) experiments, clock synchronization transmissions, DSS 14 high-power transmitter maintenance support, and Pioneer 10 science support.*

During the two month period ending December 15, 1973, the Development Support Group operated the Venus Station (DSS 13) and performed the following activities.

## I. In Support of Section 331

### A. Planetary Radar

For a total of five and one-half hours, DSS 13 supported the ranging of the planet Venus to gather data for use by the MVM73 project. Pseudonoise (PN) code and code timing pulses were supplied, via microwave link, to DSS 14 for use as a modulating signal for the 400-kW R&D transmitter, and to synchronize the demodulating

system. In addition to these ranging efforts, five and one-half hours of special Mercury ranging were supported in a similar fashion, with 10 data runs being completed. Additionally, preliminary testing, with DSS 14 transmitting and both DSS 14 and DSS 13 receiving, of a proposed "active VLBI" experiment was performed. This experiment, with Greenbank Radio Observatory as the cooperating station, is scheduled for early in 1974.

### B. Station Monitor and Control (RTOP-68)

As part of the work being done under Research and Technology Operating Plan 68 (RTOP-68), the SDS-930 computer and DSS 13 26-m antenna were used for six hours to continue testing of a developmental conical

scanning antenna drive program destined to be used at DSS 14.

## **II. In Support of Section 333**

### **A. Sky Survey**

Using the noise adding radiometer (NAR) and the 26-m antenna in a fixed position (usually  $180^\circ$  az and  $80-87^\circ$  el), data are collected on the total antenna system temperature as the Earth's rotation sweeps the antenna beam across the sky. This observing, conducted automatically during the hours when the station is closed (nights, holidays, and weekends) collected a total of 534 hours of data during this period.

### **B. Faraday Rotation**

In anticipation of the launch of the MVM73 spacecraft, it was decided to provide backup for the single receiver being used to collect Faraday rotation data. Purchase orders have been placed for two more receivers for evaluation but, pending their arrival, a receiver was obtained on loan from Teledyne Corporation. After extensive modification of the antenna previously used with the Smythe receiver, the Teledyne receiver was placed into service and is currently collecting data. Stanford Research Institute delivered and installed a second receiver but the antenna drive mechanism failed and this receiver is currently not functioning. At the end of the period, both the Teledyne and one Stanford receiver are collecting data from Applications Technology Satellite 1 (ATS-1), data that will be used by the MVM73 project to provide ionospheric correction for the spacecraft ranging and doppler data.

### **C. Weak Source**

With the reinstallation of the S-band radar operational (SRO) feedcone onto the DSS 13 26-m antenna and the relocation of the maser/refrigerator from the electronics room into this feedcone, the resulting low receiving system temperature has made it feasible to again measure the strength of weak radio sources. Late in November this project was resumed with 13 hours of data being collected on radio sources 3C123, 3C138, 3C147, 3C353, NGC7027, PO 237-23, and PO 2345-23.

In anticipation of full-scale resumption of the associated antenna gain measurement portion of this program, the standard gain feedhorn was removed from the 26-m antenna and returned to Section 333 for examination and calibration.

## **III. In Support of Section 335**

### **A. X-Band Radar (400 kW)**

The first klystron (VA-949J) was installed into the modified test bed and tested at a power output of just over 200 kW. During this testing, three directional couplers failed, two with overheated internal matching loads and one with water leaks in the cooling tubing. On December 6, 1973, this first klystron apparently failed and was removed from the test setup.

A replica of the inside framework of a 64-m-type feedcone has been constructed at DSS 13. A dual klystron power amplifier with combiner, water loads, and couplers, as required for complete testing, will be constructed in this replica. Available space is limited and integration of the two klystron power amplifiers into the cone will be difficult. Pending the availability of the actual feedcone, this replica will enable construction, fitting, and testing to take place.

### **B. Block IV Receiver/Exciter**

We continued to provide support to the installation and checkout of the Block IV receiver/exciter at DSS 14. Installation is now complete and, working until the configuration at DSS 14 was frozen for MVM73 launch, testing and checkout were supported with a total of 273 manhours. The Block IV receiver/exciter is now partially operational and is being used to support MVM73.

### **C. Antenna Pointing (26-m)**

Inasmuch as we were resuming normal receive capability operation, and reinstallation of the SRO feedcone may have resulted in a change in the agreement of the radio frequency axis of the antenna with the mechanical axis, some test tracking was done with the scan and correct using receiver (SCOUR) computer program. In three hours of tracking using Cassiopeia A and Cygnus A as sources, a new set of preliminary azimuth and elevation offsets was obtained for use during other tracking activities.

### **D. Receiving System Temperature Improvement (26-m)**

With the completion of the first phase of the dual uplink carrier testing, it was felt that the maser/refrigerator could be relocated from the electronics room into the feedcone and thus improve the receiving system temperature from 29 K to approximately 17 K at zenith. This relocation was effected and the maser compressor was also reinstalled into the closed cycle refrigerator

(CCR) room on the antenna (vice the outboard elevation bearing platform). Unfortunately this compressor soon failed and was replaced by the spare. The failed unit has been repaired and is ready for reinstallation if necessary.

#### **IV. In Support of Section 391**

In an investigation of its application to spacecraft positioning, a differential very long baseline interferometry (VLBI) experiment was carried out with Pioneer 10 and a radio source as signal sources; the cooperating stations were DSS 13 and DSS 42. A total of 18½ hours on four separate passes were spent observing, in the VLBI mode, the spacecraft Pioneer 10 and radio source OW-174.

#### **V. In Support of Section 422**

##### **A. Clock Synchronization Transmissions**

Regular clock synchronization transmissions have not yet been scheduled by DSN scheduling but special transmissions were made to DSSs 42 and 43. These transmissions, along with the regularly scheduled maintenance, disclosed some system problems. Marginal radio frequency (RF) drive to the 100-kW klystron was corrected by replacement of the  $\times 14$  multiplier in the exciter chain. A synthesizer failed and was replaced in the programmed oscillator used for frequency control. A total of nine transmissions have been made during the last two months.

##### **B. DSS 14 High-Power Transmitter Maintenance**

In preparation for the launch of the MVM73 spacecraft, the complex spare 20-kW klystron was installed at the Microwave Test Facility and correct operation assured. Some minor tuning was accomplished, then the klystron, with a complete set of operational data, was shipped to DSS 14 in case of need.

During a routine checkout, the 100-kW DSN transmitter was discovered to be inoperational. With the assistance of the DSS 14 staff, DSS 13 personnel replaced the klystron, socket tank and magnet, and restored the system to operational condition. Due to schedule requirements at DSS 14, this work was accomplished during four consecutive night operations.

The previously reported (Ref. 1) difficulty with reflected power on the R&D 400-kW transmitter was found to be spurious signals caused by a defective radio frequency connector in the input line to the frequency multiplier. Replacement of this connector cleared up the poorly transmitted spectrum and full 400-kW operation is now possible without reflected power "kickoffs."

##### **C. Pioneer 10 Tracking**

If the tracking load at DSS 14 can be relieved, a planetary radar experiment is planned with the comet Kohoutek as a target. It is proposed that DSS 13 take over tracking Pioneer 10 for several days during early January, 1974. In validation of DSS 13's capability to receive good data, and with the cooperation of DSS 12 for telemetry reduction, a test track was made of Pioneer 10 with the telemetry subcarrier being transmitted to DSS 12 via the intersite microwave link. Good data were obtained with the telemetry S/N ratio being 2.5 from DSS 13 vs 2.8 with DSS 12 receiving.

#### **VI. In Support of Section 825**

With the closer approach of Pioneer 10 to Jupiter, a stepped-up level of radiation monitoring was provided from DSS 13. The radiation at 2295 MHz from Jupiter was monitored for a total of 87.5 hours. Radio star calibrators, as tabulated in Table 1, were also observed for 122 hours.

### **Reference**

1. Jackson, E. B., "DSN Research and Technology Support," in *The Deep Space Network Progress Report*, Technical Report 32-1526, Vol. XVII, pp. 100-102. Jet Propulsion Laboratory, Pasadena, Calif., Oct. 15, 1973.

**Table 1. Radio star calibrators used in Pioneer 10  
science support**

3C48	3C147	3C309.1	Virgo A
3C123	3C218	3C348	NGC7027
3C138	3C286	3C353	PO237-23

# Design of a High-Speed Reference Selector Switch Module for the Coherent Reference Generator Assembly

T. K. Tucker

R. F. Systems Development Section

*Design effort was started in April 1973 to develop and fabricate a high-speed switch module for the Coherent Reference Generator Assembly. The major design goal was to develop a high-speed switch capable of switching between frequency standards in less than 400 ns in the event of a primary standard failure, thus providing a constant failsafe 1-MHz reference signal to the station clocks. This report reviews the overall design and provides a general overview of the completed module.*

The engineering model of the Coherent Reference Generator Assembly (CRG) was installed and implemented at DSS 14 during July 1973. Included in this installation was an engineering prototype of the 1-MHz clock reference switch module (switch module), which supplies 1-MHz reference signals to the frequency and timing subsystem (FTS) clock and timing circuits.

The following significant features of the Switch Module will be discussed in this report:

- (1) Design objective.
- (2) System application
- (3) Description.
- (4) Present status.

## I. Design Objective

The major design objective for the switch module was to provide a constant 1-MHz reference to the station clock by automatically switching to a backup reference source in less than 400 ns in the event of a primary source failure.

## II. System Application (Fig. 1)

Inputs to the CRG are obtained directly from the station frequency standards that, during the next few years, may be two rubidium standards (Rb) or two hydrogen maser (HM) standards.

The primary input to the FTS clock system from the CRG is a failsafe 1-MHz reference derived from either

the present rubidium standards or the future ultrastable hydrogen maser standards. Once a class of standard is chosen (either rubidium or hydrogen maser), the secondary or backup reference is derived from the same generic type (i.e., if hydrogen maser No. 2 is chosen as the prime standard, hydrogen maser No. 1 would be the backup unit).

Both the primary and secondary standard 1-MHz references are made available to the FTS so that duplicate clocks can be operated for long-term stability and standard performance determination.

### III. Description (Fig. 2)

The switch module is housed in a standard Block IV RF module and has been designed to operate without operator adjustment or alignment.

The switch module has been designed with a "failsafe" dc power system. In the event of a dc power loss from the CRG power supplies, the module automatically switches to a battery backup source located in the FTS, thus assuring continuous 1-MHz references to the station clock.

Two input references are selected, within the module, by a solid-state multiplexer that is addressed externally by the CRG control and monitor panel. The multiplexer's logic assures that the primary signal is obtained from the selected frequency standard and the secondary, or backup, is derived from the other like standard.

The key idea of the overall switch design is to use digital switching techniques to accomplish the high-speed switching. To accomplish this, both the primary and secondary standard inputs are passed through Schmitt triggers and converted to transistor-transistor logic (TTL) levels.

To detect primary standard failure, two parameters must be considered: (1) instantaneous signal presence, and (2) the average input power level.

Instantaneous failure sensing and switching is accomplished through an unusual application of a zero cross-over detector circuit, which consists of two voltage comparator integrated circuits interconnected and biased to provide full 360-deg signal presence sensing of the primary input signal.

If the input signal is present, the failure sensor remains at a logical "1" level. If the input signal should disappear

for a time interval in excess of approximately 250 ns, the sensor output assumes a logical "0" level thus initiating a failure mode signal. The 250-ns decision time is established by a simple resistor-capacitor (RC) filter in the sensor output, which prevents switch operation on minor noise disturbances.

The failure mode signal triggers a one-shot retriggerable multivibrator circuit initiating the switching gate that gates off the primary signal channel and enables the secondary in its place. The transfer from primary to secondary signal, after primary failure, is accomplished in less than 400 ns.

The one-shot multivibrator serves an essential function by assuring that once a failure has been sensed and a transfer between standards effected, approximately a one-half second delay is required before the circuit can revert back to normal operation. This prevents the switch from chattering on an intermittent input signal.

Average power sensing and switching are accomplished by measuring the primary input power with a signal level detector. If the input power remains above a preset level of approximately +9 dBm, the primary level sense signal remains at a logical "1." If, however, the input level falls below this preset level, the primary level sense signal assumes a logical "0" state initiating a switching gate to disable the primary channel and enable the secondary in its place.

Level monitor logic is also designed to provide continuous module status information to the CRG control and monitor panel. Input and output signal power levels are monitored in individual level detector circuits and are compared in an exclusive "or" circuit. If inputs are above the preset level of approximately +9 dBm, output from the module must also be present and above +9 dBm, or the module "output failure" signal will be initiated. If no inputs are present or they fall below the +9-dBm level, outputs are not expected and only the "input failure" signals will be initiated.

The TTL signals are filtered at the switch output to provide sine wave outputs, at nominal 50-ohm impedance, so that no changes to the existing FTS are required.

### IV. Status

Documentation is complete and the first production model of the switch module has been built and tested. Installation at DSS 14 will be accomplished as soon as the station operational freeze is lifted.

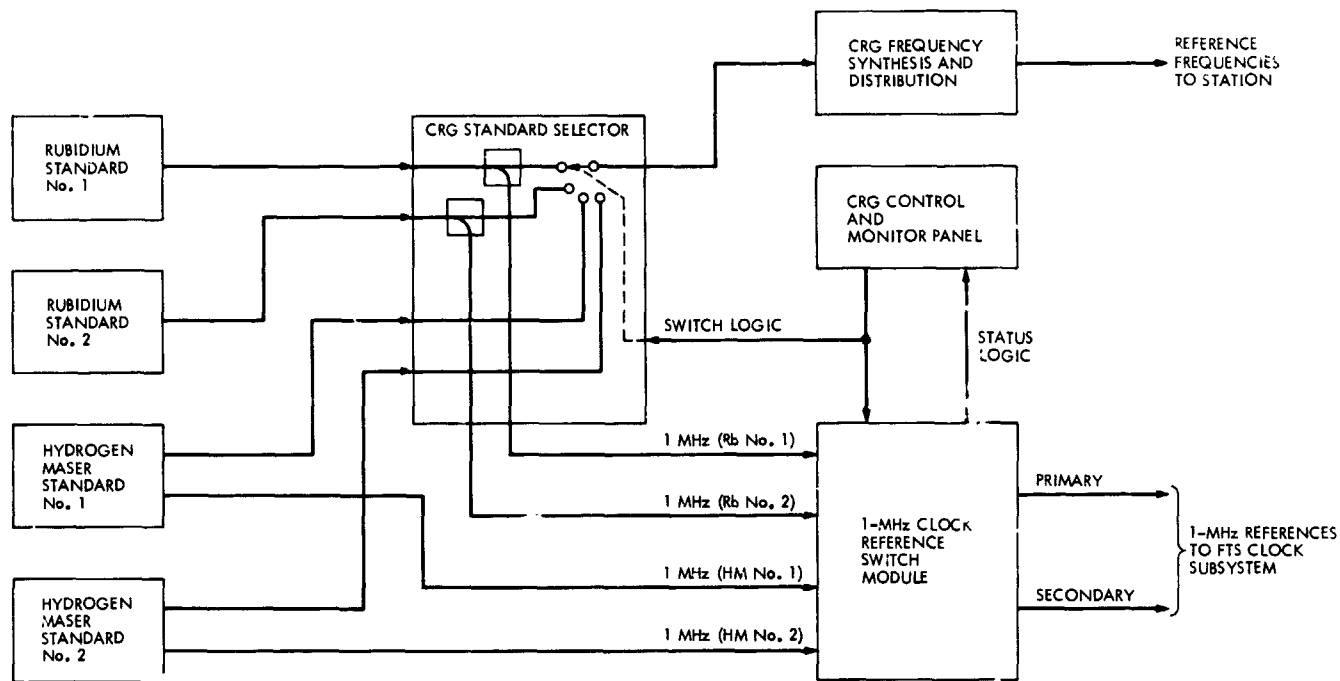


Fig. 1. System block diagram

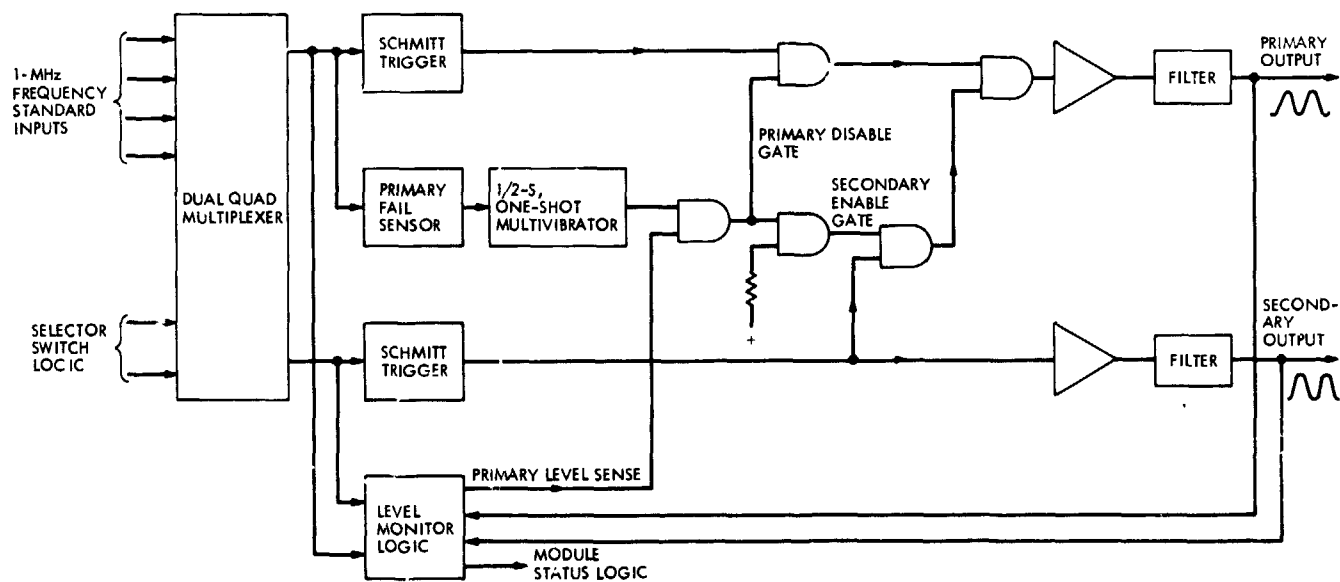


Fig. 2. Functional block diagram, 1-MHz clock reference switch



# A Scaled-Time Telemetry Test Capability for Sequential Decoding

S. Eutman, J. Layland, and J. MacConnell  
Communications Systems Research Section

R. Chernoff and N. Han  
R. F. Systems Development Section

J. Wilcher  
DSIF Digital Systems Development Section

*This article describes the motivation for, and development and initial testing of, a scaled-time telemetry test capability. The immediate need for this capability is to establish the sequential decoding performance of the data decoder assembly (DDA) for Helios and Pioneer, and the tests have been aimed at evaluating the suitability of the scaled phase-locked loop (PLL) for this task. The relevant parameters of limiter suppression, phase jitter variance, and phase jitter autocorrelation have been measured, and no discrepancy was found between the  $\times 16$ -scaled PLL and the 12-Hz loop of the DSN receiver. Comparative sequential decoding tests have also been performed for 128-bit/s data; no discrepancy was found between scaled and unscaled performance at any modulation index, either near optimum or high (70 deg), where the carrier reference noise is dominant.*

## I. Introduction

The purpose of this article is to describe the experimental setup and preliminary results of a time-scaled simulation of a convolutionally coded, sequentially decoded, coherent telemetry link. The need for such an approach arose when it became necessary to provide the Helios project as well as future Pioneer project with an accurate estimate of link performance and design trade-offs at medium data rates. Medium rates are by definition data rates of the same order of magnitude as the band-

width of the phase error process in the coherent reference signal, or more generally, data rates at which decoder memory is comparable to the memory of the phase-locked loop.

Such conditions arise at low received signal levels at end and post-end of missions and at stronger signal levels when transmission is contaminated by a turbulent medium like the solar corona, a planetary atmosphere, or during rapid descent of a probe.

Experimental performance estimation through simulation is necessary under the above conditions because accurate theoretical models of decoder behavior when the phase is not constant are not yet in existence (Ref. 1). The current state of decoding theory can accurately predict decoder performance only when the phase is constant over many constraint lengths. Finally, scaling up of the simulations to a higher speed than under normal operating conditions is necessary in order to accumulate the required amount of statistical data in a reasonable length of time. For example, to establish with reasonable confidence a bit error probability of  $10^{-5}$  requires about  $10^6$  bits. To gather this amount of data at 100 bits/s would take over 10 days. Similarly, establishing a block erasure probability (decoder overflow) of  $10^{-3}$  for blocks of 1000 bits, would take 10 days.

## II. Scaling the Tests

The block diagram in Fig. 1 depicts the system elements which require modification to provide a high-speed version of actual behavior at normal operating conditions. It is assumed that the front end noise is wideband, with a one-sided spectral density  $N_0$ . Primed variables denote scaled versions of the normal unscaled quantities, and  $x$  denotes the scale factor. There are several ways to achieve the required scaling of the system dynamics. The method we selected may be described as follows:

$N'_0 = N_0$	Wideband noise level unchanged
$P'_T = xP_T$	Total signal power scaled up
$R' = xR$	Bit rate scaled up
$\omega'_L = x\omega_L$	Loop bandwidth scaled up
$r' = r$	Damping ratio unchanged to preserve relative dynamics
$\alpha' = \alpha$	Limiter suppression factor unchanged to preserve relative dynamics
$\omega'_H = x\omega_H$	Prefilter bandwidth increase required to maintain the same input signal-to-noise ratio (SNR) to the limiter for $\alpha' = \alpha$
$\rho'_L = \rho_L$	Loop SNR unchanged
$E'_b/N'_0 = E_b/N_0$	Bit SNR unchanged
$m' = m$	Modulation index unchanged
$\tau'_i = \tau_i/x$	Loop filter time constants reduced
$K' = xK$	Loop gain increased

The above quantities obey the following relationships, which are documented by Tausworthe (Ref. 2)

$$E_b/N_0 = m^2 P/N_0 R$$

$$\rho_L = \alpha/\omega_L N_0$$

$$r = \alpha K \tau_1^2 / \tau_2$$

$$\omega_L = (1 + r)/\tau_2(1 + \tau_2/r\tau_1)$$

and

$$\alpha = \alpha(\rho_H)$$

where

$$\rho_H = (1 - m^2)P_T/N_0\omega_H$$

$$m = \sin \theta, \text{ where } \theta \text{ is the modulation angle}$$

Inserting the scaled parameters into the above formulas will verify that all the scale changes are achieved and the relative dynamics preserved where necessary.

Time-scaling of the subcarrier demodulator and symbol synchronizer assemblies (SDA and SSA) is accomplished through switch-selectable operating modes which match the actual (i.e., upscaled) data rates. Moreover, the losses in these assemblies are small and relatively insensitive to rate changes.

## III. Test Techniques

The approach followed in evaluating the scaled-time telemetry test capability, must minimize the test time required to build confidence in the correctness of the scaled parameters. The first tests therefore measured the global static PLL parameters, limiter suppression  $\alpha$ , and phase jitter variance  $\sigma_\phi^2$ , at specific signal strengths and compared these measurements with published results for the 12-Hz DSN PLL. Dynamics of the PLL behavior also influence strongly the performance of medium-rate telemetry, necessitating their measurement, in the form of the phase jitter autocorrelation function. In this case, both the 12-Hz DSN PLL and the scaled PLL had to be measured, as the desired parameters were not generally documented.

The ultimate criterion for acceptance of the results of the scaled telemetry tests is, of course, the equivalence of measured telemetry performance in both normal and scaled-time modes. This is most economically used at the mid-range data rates only (e.g., 128 bits/s), where reasonable duration tests can define the system performance. The anticipated plan is to test at 128 bits/s over a set of modulation indices near optimum, and to spot-check many data rates at one very high modulation index. For each data rate checked in this fashion, the modulation index will be set sufficiently high for the

noisy carrier reference to be the dominant source of noise, and so that performance is poor enough to be measured in reasonable time without scaling. The total received power level will be set high enough so that the desired  $10^{-4}$  deletion probability could be achieved with a lower modulation index. A successful match of performance at the high mod-index will, of course, indicate that the noisy reference losses are correctly scaled. Since we believe that the additive receiver noises will scale correctly, successful high mod-index comparison should also indicate overall success of the scaled test setup. Some prior test data (Ref. 3) exist for normal-time tests of performance near the optimum mod-index which can be compared against the scaled tests to identify any unexpected errors in the scaling assumptions.

No plans exist presently to test the scaled-time test configuration for uncoded telemetry. Since performance of sequential decoding is very critically dependent upon the adjacent-symbol correlation of the carrier reference noise, correct scaled-time performance of sequential decoding almost certainly implies that scaled-time tests of uncoded telemetry will also be correct. Future users of the scaled-time test capability for uncoded data will, of course, have the option of accepting this hypothesis or performing whatever additional tests they might need to validate the scaled-time performance for uncoded telemetry.

#### IV. The Scaled Loop Hardware Design and Initial Testing

The preceding sections have shown that, by scaling the receiver 12-Hz loop bandwidth, statistical data on bit error rates can be obtained in a time inversely proportional to the scaling number  $N$  used on the receiver. It was decided to scale the receiver loop bandwidth by 16, a factor which allowed a reasonable improvement in the speed of data acquisition without causing the data rates for the faster bit rates to exceed the capabilities of the telemetry decoding equipment.

For the scaling number under consideration (16), it was necessary only to scale the tracking filter and the predetection filter. (If extremely high scaling numbers are used, it may be necessary to increase the bandwidth of the IF amplifiers). Since  $B_L$  is being scaled, it can be shown that it is necessary to decrease  $\tau_1$  by  $(N)^2$  and  $\tau_2$  by  $N$ , where  $\tau_1 = R_1 C$  and  $\tau_2 = (R_1 + R_2)C$  in Fig. 2. For the case being evaluated ( $N = 16$ ),  $\tau_1$  becomes 9.887 s and  $\tau_2$  becomes  $8.5 \times 10^{-3}$  s. The hardware implementation of the tracking filter consisted of modifying the

values of  $R_1$ ,  $R_2$ , and  $C$  in a standard DSN tracking filter module to provide the new time constants. The only other hardware modification required was the predetection filter amplifier. The bandwidth (BW) of this amplifier must be scaled (increased) by the scaling number  $N$ . For this test, the bandwidth was increased from the normal 12-Hz loop value of 2 kHz to the new value of 32 kHz noise BW. The hardware implementation consists of a four-stage, synchronously tuned amplifier. (The gain of this filter amplifier must be the same as that of the normal amplifier in order not to disturb the automatic gain control (AGC) performance of the receiver). For future experiments, the predetection filter could be a commercial crystal filter. This would enable tighter control of the bandwidth between units, as well as better bandwidth stability vs. temperature. The changes and modules are identified in Fig. 3.

In order to verify that the receiver bandwidth had been properly scaled, several experiments were run. Input carrier power was set for all tests by the Y-Factor Technique (Ref. 4). First, the limiter suppression ( $\alpha$ ) characteristic was checked by measuring carrier power at the limiter output vs. loop threshold margin. This measurement was performed by a coherent amplitude detector and vacuum tube volt meter (VTVM). The results of the test can be seen in Fig. 4. Ideally, the scaled and unscaled  $\alpha$  curves should be identical. If the  $\alpha$  characteristic levels off at a lower margin in the scaled case, it would probably indicate an IF amplifier or limiter of insufficient bandwidth, or an insufficient noise bandwidth in the predetection filter amplifier. (If high-scaling numbers are used, it may be necessary to increase the BW of the IF amplifiers. This will prevent their influencing the predetection bandwidth, which should ideally be determined solely by the predetection filter amplifier). Since the curves for the scaled and unscaled cases are nearly identical, it appears that the predetection filter is indeed the determined BW, as desired.

The second test consisted of measuring the phase jitter ( $\sigma_\phi^2$ ) of the receiver voltage-controlled oscillator (VCO) as a function of margin. These data were obtained by employing the test translator as a signal source, and the UHF doppler detector as a dual phase detector, which allowed measuring the variance of the phase noise present on the VCO. The test configuration for this measurement is shown in Fig. 3. The UHF doppler signal (zero doppler + phase jitter) is phase detected against the station frequency standard. The phase shifter is required to set the reference phase in quadrature (to enable phase detection), with either of the two signals being

phase detected in the dual phase detector. (The other signal is being amplitude detected.) For each data point (value of margin), both channels are sampled and recorded by the digital instrumentation system (DIS). The need for sampling both channels arises when a cycle slip occurs. For each cycle slipped at S-band, there appears a 90-deg shift in the phase at the UHF doppler detector. (This is due to a  $\times 4$  multiplication between the point at which the UHF doppler is extracted and the S-band local oscillator output.) Therefore, if a cycle is slipped, the channel that was phase detecting is now amplitude detecting and vice versa. To prevent loss of phase data following cycle slip, both channels are recorded. When the tapes are processed, only the channel that is phase detecting is used. From those data, the variance ( $\sigma_n^2$ ) is calculated. As can be seen in Fig. 5, the data follow very closely those obtained with the normal 12-Hz loop. This further indicates that the receiver seems to be properly scaled.

The third test consisted of taking the autocorrelation of the phase jitter data. Each autocorrelation plot shows the time response of the loop at a particular margin. By plotting  $\tau$  from each of these plots vs. margin, a plot is obtained that illustrates loop response vs. margin. Figure 6 is such a plot for both the scaled and unscaled loops. If the loop is properly scaled, the scaled loop will have a value of  $\tau$  equal to  $1/N$  of the unscaled loop at each margin. For convenience, the time ( $\tau$ ) scales of the two data sets shown in Fig. 5 are scaled by the scaling factor  $N$ . Therefore, the two curves will coincide if the loop is properly scaled. As can be seen, there is very close agreement between these two curves.

The results of this group of three tests seem to indicate that the receiver loop bandwidth was indeed scaled the desired amount over the range of loop margins considered.

## V. Telemetry Tests

Testing of the scaled-time telemetry test capability using sequential decoding requires that several decoding test runs be performed using both the 192-Hz loop and the 12-Hz DSN receiver at identical (scaled equivalent) test conditions. To be convincing, these test runs must cover the range of data rates, SNRs, and modulation indices for which scaled tests are expected to be used. The scaling can be used at data rates of 256 symbols per second (SPS) (scaled to 4096 SPS) and lower. At scaled 512 SPS (8192 SPS) and above, the data decoder assembly (DDA) cannot operate successfully.

The test configuration for sequential decoding testing with scaling is shown in Fig. 7. It is identical to the configurations used for normal DSN testing of sequential decoding for Pioneer or Helios, except that the receiver modules for the 192-Hz loop are substituted for those of the 12-Hz DSN receiver PLL. The output from the test is a magnetic tape original data record (ODR) containing, for each data frame processed by the DDA, the number of decoding computations which were used in processing it. These ODR tapes are later analyzed off-line to determine the cumulative distribution of computations, which is then used to evaluate system performance. In the DSN station, the tests require the use of the simulation conversion assembly (SCA), the test transmitter, the antenna microwave assembly, the Y-factor assembly, a receiver and SDA, two telemetry/command processors (TCPs) with SSAs, and one DDA. The TCP-DDA-SSA string operates under control of nonstandard DSIF software—the DDA stand-alone-TCP verification program—and provides the ODR end-product of the tests. The second TCP-SSA string operates with the Mariner Mars 1971 (MM71) Test Program No. DOI-5087-T1 and acts as a monitor for the telemetry channel, to verify station setup accuracy and identify drifts in parameters.

The SCA provides a pseudo-random data sequence for the test transmitter. The subcarrier frequency used is 32,993 Hz, and data rates of interest range from 16 to 4096 SPS. The biphas-modulated subcarrier in turn phase-modulates the carrier at the test transmitter, with a modulation index which may vary from 35 to 75 deg, depending upon data rate and other factors. This simulated telemetry signal is then processed by the station receiving equipment, much like the signal from a spacecraft. The "received" signal strength is set as required using the Y-factor measurement technique (Ref. 4) prior to the start of a test. The modulation indices are set by precision attenuators. Extreme care is required in this setup because of the sensitivity of decoding performance: the decoding erasure rate can vary by an order of magnitude with a 0.5-dB change in signal strength. After setup, the Test Program 5087 output monitors channel statistics, and when stable operation of the receiver and SDA is observed, the TCP/DDA program is activated to develop the ODR of decoder performance. The format of these ODR tapes is shown in Fig. 8.

Tests with the scaling test facility have been performed and the data analyzed for a real data rate of 256 SPS (scaled for 4096 SPS). The signal strength was set to that which would provide an  $ST_s/N_o$  of 2.7 dB at 45-deg modulation index for both scaled and nonscaled tests. This value will produce an erasure rate of between  $10^{-3}$

and  $10^{-4}$  at the optimum modulation index. Figure 9 shows the results of tests at several modulation indices. The computation distribution curve shown is a rather sensitive measure of channel behavior. The minor differences between comparable curves are well within the set-up tolerance on the system, believed to be on the order of 0.4 dB. The high mod-index curves (70 deg) are interesting in that the carrier reference losses are the dominant noise source at this point. If the carrier reference losses failed to scale properly, we would expect it to be evident from these curves; since there is agreement, we conclude that the scaling of the 256-SPS data rate is successful. We expect this success to be repeated at lower data rates, but tests must yet be performed, lest some unexpected interference signal, or some other nonscaled or nonscalable artifact of the DSN receiver/SDA/SSA systems, contribute a larger than expected share to the telemetry system losses.

## VI. Summary and Future Plans

This article has described the motivation for, and development and initial testing of, a scaled-time telemetry test

capability. The immediate need for this capability is to establish the sequential decoding performance of the DDA for Helios and Pioneer, and the present tests have been aimed at evaluating the suitability of the scaled PLL for this task. The relevant parameters of limiter suppression, phase jitter variance, and phase jitter autocorrelation have been measured, and no discrepancy was found between the  $\times 16$ -scaled PLL and the 12-Hz loop of the DSN receiver. Comparative sequential decoding tests have also been performed for 128-bit/s data; no discrepancy was found between scaled and unscaled performance at any modulation index, either near-optimum or high (70 deg), where the carrier reference noise is dominant.

Further testing will be performed of the scaled-time telemetry test capability, and productive use made of it, at DSS 71, where long-duration tests are in progress to establish DDA performance. At each of the Helios data rates where scaling can be used, a very high modulation-index comparison test will be run to verify the scaling of noisy reference losses before the planned tests of several mod-indices and power levels are run.

## References

1. Layland, J. W., "A Sequential Decoding Medium Rate Performance Model," in *The Deep Space Network Progress Report*, Vol. XVIII, Technical Report 32-1526, Jet Propulsion Laboratory, Pasadena, Calif., Dec. 15, 1973.
2. Tausworthe, R. C., "Theory and Practical Design of Phase-Locked Receivers, Vol. I," Technical Report 32-819, Jet Propulsion Laboratory, Pasadena, Calif., Feb. 1966.
3. Lumb, D., Private Communication at Helios Working Group Splinter Session, Sept. 27, 1973.
4. *DSIF Program Library: Documentation for Y-Factor Computer Program*, DOI-5343-SP-B, 29 Sept. 1972 (JPL internal document).



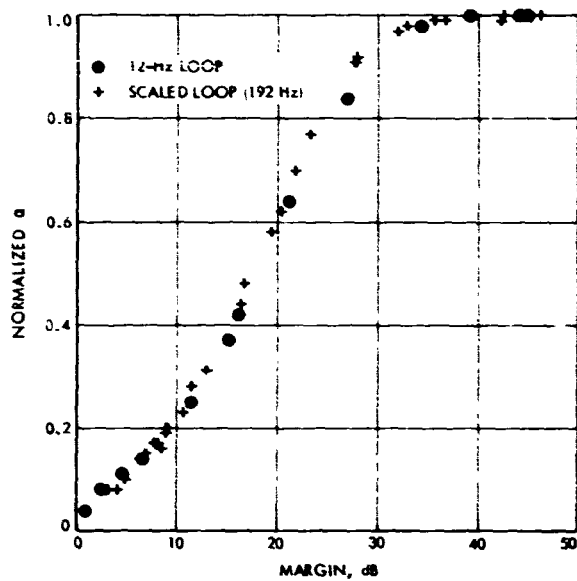


Fig. 4. Limiter suppression factor vs. loop threshold margin

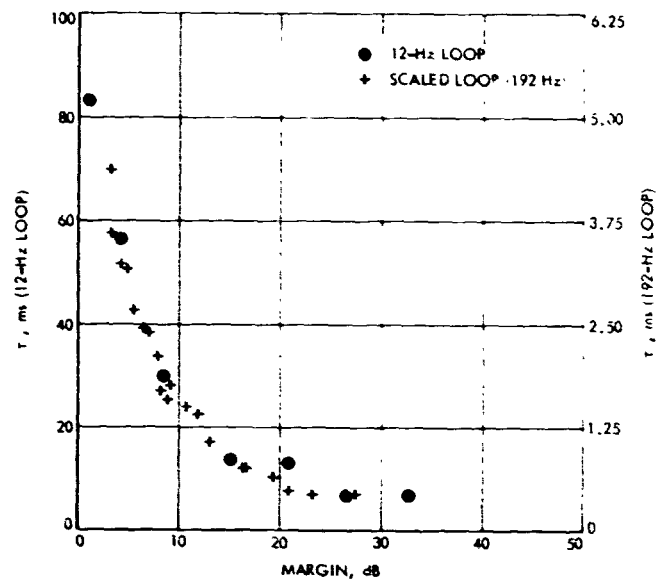


Fig. 6. Effective loop time constant vs. loop threshold margin

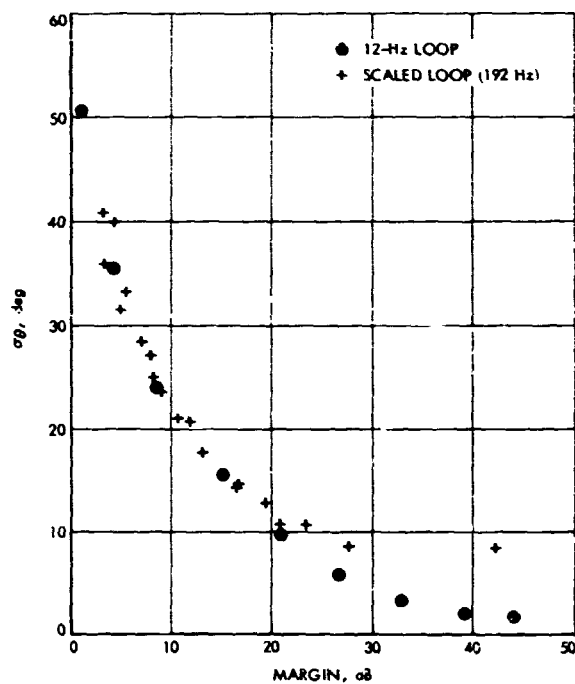


Fig. 5. Variance of loop jitter vs. loop threshold margin

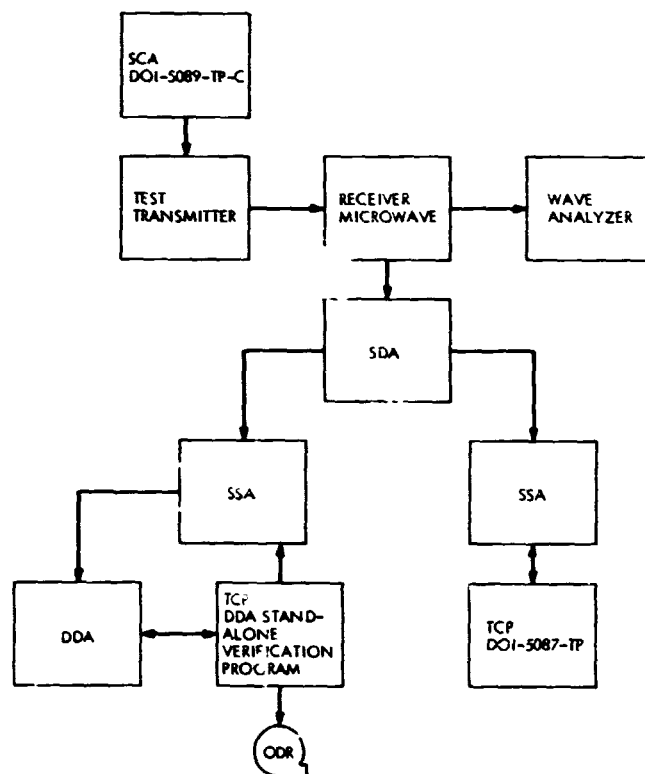


Fig. 7. Telemetry test configuration





# NCS Standard Computer Interface Hardware, Its Timing and Timing Control Logic

T. O. Anderson

*This article describes the Network Control System (NCS) Standard Computer Interface hardware, including the interface cable, the line drivers, line receivers and line terminating network. It describes in considerable detail the timing specifications for the interface timing control signals for continuous data transfer as well as for asynchronous byte transfer. A set of control logic which complies with these timing specifications has been designed for and successfully checked out in connection with the Star Switch Controller (SSC). This control logic, which includes synchronization and noise filter operations, is described in detail. Transfer rates for variable cable lengths are listed.*

## I. Introduction

The NCS standard computer interface hardware contains 14 parallel data-transmission lines. Eight of these lines are data lines, four are timing and control lines, and two are function lines (see Fig. 1).

Of the interface timing control lines for asynchronous data transmission, two are unidirectional request lines, one in each direction; one is a bidirectional half-duplex response line; and one is a bidirectional half-duplex ready line. The linear bit operation of these lines and the operation of the control logic to perform these operations is specified in detail. The control logic synchronizes the input signals to the local service clocks, and filters out spurious noise pulses of short duration. Both the control

logic and its operation are described in detail, as are the cable, line drivers, receivers, and line termination.

## II. Cable, Drivers, Receivers, and Line Termination

The NCS standard interface cable is a twisted pair cable, with line drivers and line receivers, as shown in Figs. 2 and 3. The cable itself is shown in Fig. 4. All connectors, physically and functionally, mate with connectors such as that shown in Fig. 4. Pin assignments for the timing control lines, data lines, and function lines are also shown in Fig. 4. (Figures 2, 3, and 4 are taken from JPL Specification ES506534 A, May 1973, a JPL internal document.)

As shown in the figures, twisted pair, #22-gauge, 100- $\Omega$  lines are used. The drivers are 7438 open collector, high current TTL-buffer, 2-input NAND-gates, and the receivers are regular 7400 NAND inputs. Both ends of the lines are terminated with 150  $\Omega$  to +5V and 330  $\Omega$  to ground. The common term is terminated on the GND pin of the driver and receiver chip, respectively.

### III. Signal Sync and Noise Filter

In order to combat noise and to synchronize the interface timing control signals with the internal service clock of the computer, a signal transition is recognized only upon the second consecutive sample of the internal clock. This specification is valid for transitions in either direction. Stated differently, a single noise pulse of either polarity of a duration of less than two clock periods occurring at any time will have no effect on the true operation of the line receiving logic.

### IV. Timing Control Line Operation

Figure 1 shows the selected set of computer interface timing control lines together with eight data lines. The request-to-transmit line is unidirectional, while the return response and data lines are half-duplex bidirectional. For bidirectional communication, two request-to-transmit lines are then required, one in each direction, as shown. Figure 5 is a simple block diagram and timing chart which show the detailed operation of the timing control lines. The time sequence for the various control lines, which is repeated for each linear bit or parallel byte, is listed as follows:

- (1) An outbound request line is asserted by the transmitting device.
- (2) The assertion of an inbound request line is sampled and synchronized by the recipient device.
- (3) The synchronized inbound request signal causes assertion of the outbound return response line.
- (4) The return response line inbound to the transmitting device is sampled and synchronized and causes assertion of the outbound ready line.
- (5) The ready signal inbound to the recipient device is sampled and synchronized, and used to form a data-strobe pulse for sampling the received data.
- (6) Upon sampling the received data, the inbound ready signal is used to turn off the outbound response line.

- (7) Turnoff of the outbound response line will in turn cause turnoff of the inbound ready line.
- (8) Turnoff of the inbound ready line will again cause the outbound response line to turn on, conditional on the request line being on, for receiving of the next character.
- (9) At the end of a block transmission, the request line is turned off by the transmitting device simultaneously with the ready line, outbound from the transmitting device, for the last character being turned on.

#### A. Control Logic Operation

The operation of a signal synchronizing and noise control receiving register for the transmission interface timing control signals, in general, and for the ready line register, in particular, is specified as follows:

- (1) A signal change is recognized only if the signal remains in its new state for two consecutive clock periods after the signal has remained in its prior state for at least two clock periods.
- (2) A data strobe will be generated only for a unidirectional change of the input signal.
- (3) Once a data-strobe pulse has begun to form, it will be completed independently, and the fact that it was completed will be independently reported. Independently, as used here, implies independence of what is happening on the input signal line.
- (4) A noise spike of either polarity of a duration less than two clock periods occurring at any time must not be the cause of a double data-strobe pulse, nor should such a noise spike interrupt the forming of a data-strobe pulse or the subsequent report signal that a data-strobe pulse was formed.

#### B. Request Line Sync Register

Figure 6 shows the interface timing control logic. The logic is implemented with a SN5495 universal 4-bit, shift-right, parallel-load register with no additional gating. The input signal is used as a mode control and the parallel entries are connected so that the register, when it is in the parallel load mode, will shift left. The shift-right/shift-left data entries are fixed-wired as "1" and "0," respectively. The desired output level is achieved by correlating the input mode control signal with the fixed-wired data inputs; e.g., SR = 1, SL = 0, or vice versa.

The output of stage C will change state only if the output line has been stable for two consecutive clock pulses, as described. This is true for transitions in either direction, and it is true in general. There are however, two special cases in which it is not true, and that is if the line reverses again between the first and second or the second and third clock pulses following a transition. The probability of this special case occurring is deemed exceedingly low. The output from stage B is used directly as the response term, conditional only on a ready register term. The reason that the direct connection is acceptable, as opposed to the use of an intermediate storage device, is that when the request line is turned off at the same time that the ready line is turned on, for one character transfer or for the last character in a block, the turnoff of the response line, which in turn causes the ready line to turn off, occurs at the same time that the data-strobe pulse begins to develop. The request line register and the ready line register are connected in much the same manner. Furthermore, if the same type of interface logic is used at both the transmitting and receiving ends, there is the added sync delay at the transmitting end between its inbound response line turnoff and the time that its outbound ready line is turned off. Stated differently, the request line turns off the response line, which in turn turns off the ready line. Whether it is for a single character transfer, or for the last character, the response line is turned off sooner than for a character within a block, where it is turned off at the end of the data-strobe pulse. The ready line is still turned off one clock period later than completion of the data-strobe pulse.

### C. Ready Line Sync Register

As shown in Fig. 6, the ready register is connected to shift right in either of its modes. The parallel load entries are connected to shift right; however, with certain modifications. The input signal is used as mode control; the data entry for shift right in the serial mode is a fixed 0 and for shift right in the parallel-load mode a fixed 1. By shifting in one direction only, the vector that generates the data strobe is automatically generated for a unidirectional signal change only. The external gating shown in Fig. 2 is intended primarily to prevent one-clock-period noise pulses from generating or regenerating the strobe pulse, or to interfere with its forming, or with the reporting of its having been formed.

As shown in the truth table (Fig. 7), the strobe pulse condition is ABC and the strobe pulse completion report

condition is BC, both of which can occur only for the specified conditions. In relation to the truth table, the ready register connection shown in Fig. 2 is derived from the following arguments: When the input signal is a 1, a 1 is entered to the shift-right connected entry of the register. When the signal is a 0, a "0" is entered to the serial input of the internally connected shift-right register. The content in B is always entered to C, while the entry to B is a function of the signal and the content of the register. The signal is the mode-control term, and when it is 0, the shift register is internally connected for shift right. What is in A will, in this mode, always be shifted to B. When the signal is a 1, a "1" is entered to the input of the shift register, which in this mode is connected externally to shift right to allow for vector modification. Thus, in this mode, what is in A is shifted into B in all instances except one: the 011 condition, in which case, a 1 is entered to B instead of the 0 in A.

### D. Response-Ready Register Time Share

The response and ready lines are both bidirectional but are always energized from opposite ends; the request line is always energized first and the response line second. This allows time-sharing a single synchronizing receiving register between these two lines, as shown in Fig. 8. (Figures 1, 5, 6, 7 and 8, are taken from JPL Specification ES508535 A, Appendix, a JPL internal document.) Also shown in the figure are the steering gates for time-sharing of the ready-response register through the synchronized request line. The same line is also used for added interlock of the outbound response line and the outbound ready line.

The control logic described here is duplicated in each end of a transmission path.

## V. Data Transfer Rates

The bit transfer rate for different length cables has been tabulated using the type of interface described here, where the assertion and/or release of a line is recognized only on the second clock pulse of an internal 5-MHz service clock, and using identical interface logic at both ends, with individual service clocks (Table 1).

A cable delay of 5.90 ns/m is used, and a double round-trip per byte for continuous transmission is considered. The cable length has been limited to 152.4 m so that the signal attenuation will not cause a marginal operation.

**Table 1. NCS standard computer interface transfer rates for various cable lengths<sup>a</sup>**

Cable length, m	Maximum reliable data transfer rate in kilobytes/s
3.05	530
15.24	460
30.48	400
60.96	310
152.4	185

<sup>a</sup>Asynchronous internal service clocks of 5 MHz at each end.

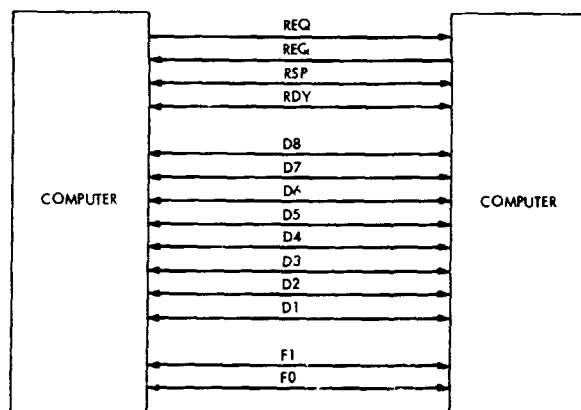


Fig. 1. NCS standard computer interface hardware lines

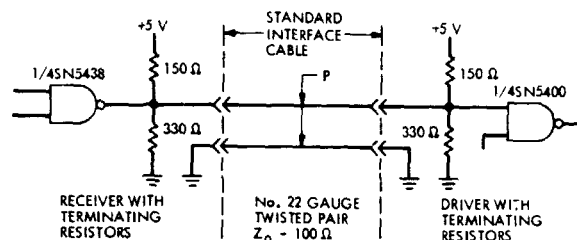


Fig. 2. NCS standard computer interface unidirectional line driver/receiver configuration

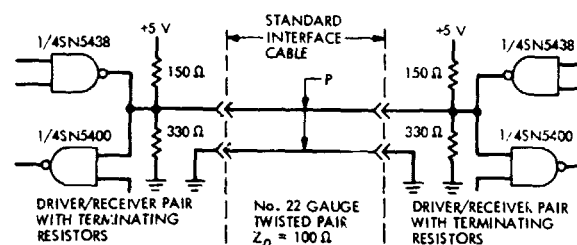


Fig. 3. NCS standard computer interface bidirectional line driver/receiver configuration

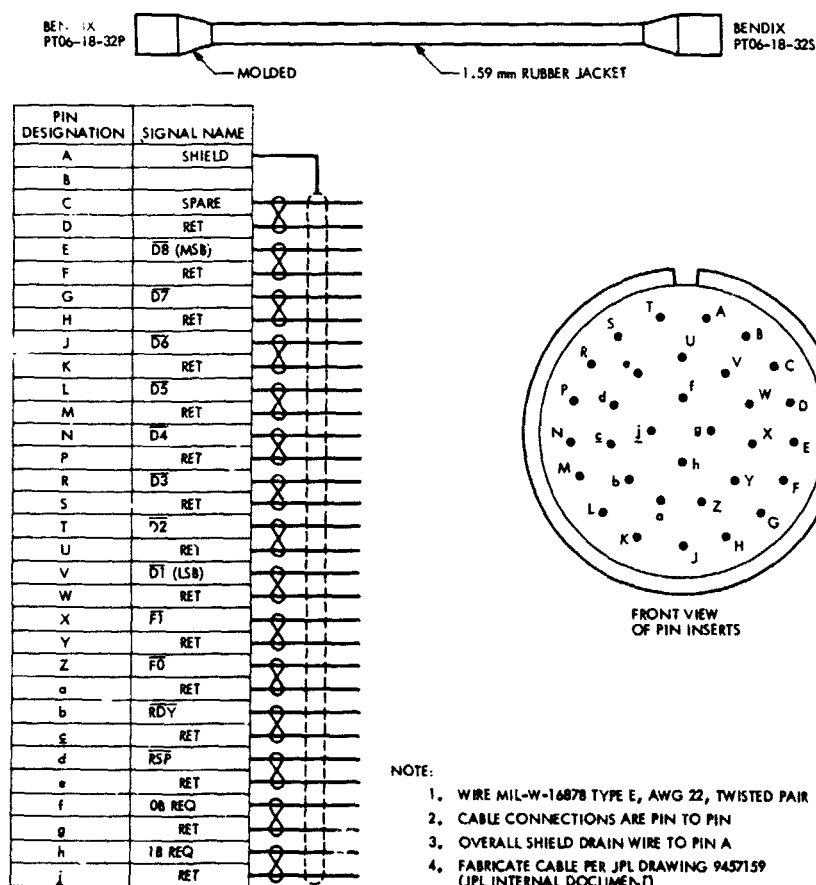


Fig. 4. NCS standard computer interface cable connector and pin assignment

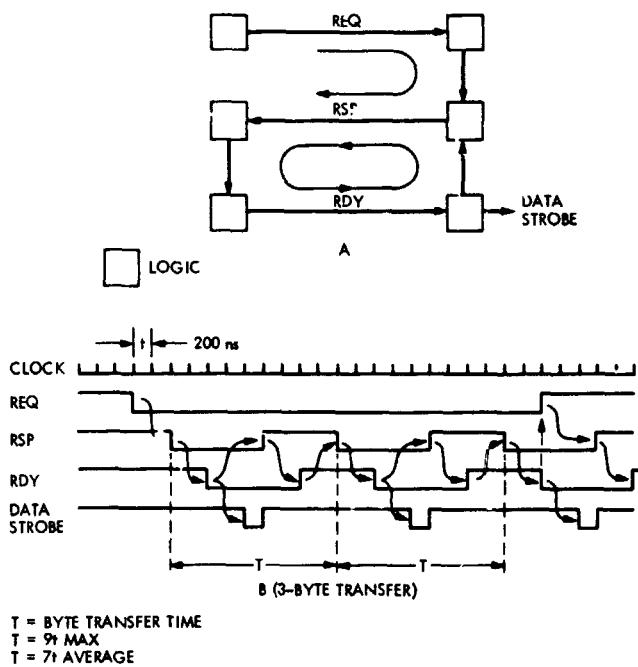


Fig. 5. NCS standard computer interface timing control line, logic, and timing diagram

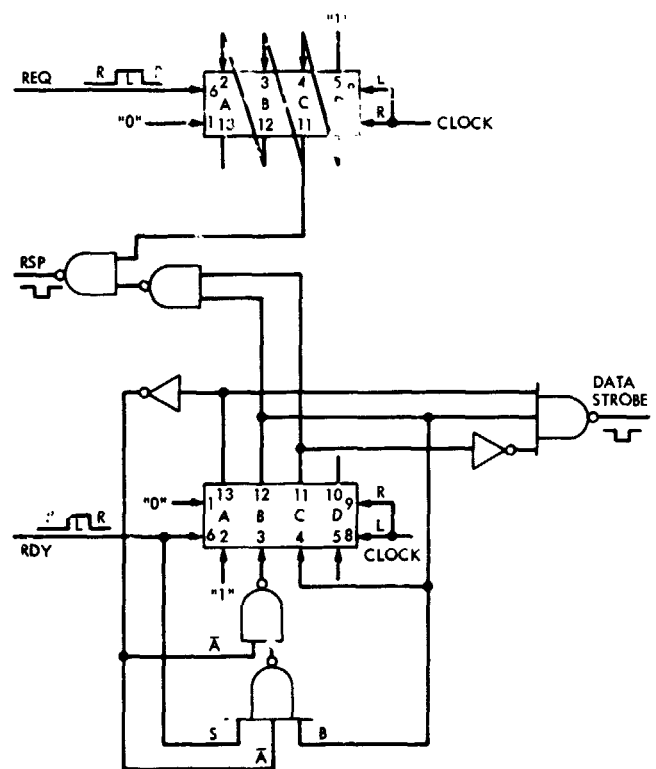


Fig. 6. NCS standard computer interface, basic interface timing control logic



S	A	B	C	S	A	B	C
0	0	0	0	1	1	1	1
1	0	0	0	0	1	1	1
1	1	0	0	0	0	1	1
0	1	1	0	1	0	0	1
0	0	1	1	1	1	0	0
1	0	0	1	0	1	1	0
1	1	0	0	0	0	1	1
0	1	1	0	1	0	0	1
0	0	1	1	1	1	0	0
0	0	0	1	1	1	1	0
0	0	0	0	1	1	1	1
0	0	0	0	1	1	1	1
1	0	0	0	0	1	1	1
0	1	0	0	1	0	1	1
1	0	1	0	0	1	1	1
0	1	0	1	1	0	1	1
1	0	1	0	0	1	1	1
0	1	0	1	1	0	1	1
0	0	1	0	1	1	1	1
1	0	1	0	0	1	0	1
1	1	0	1	0	1	1	0
1	1	1	0	0	0	0	1
1	1	1	1	0	0	0	0

Fig. 7. (contd)



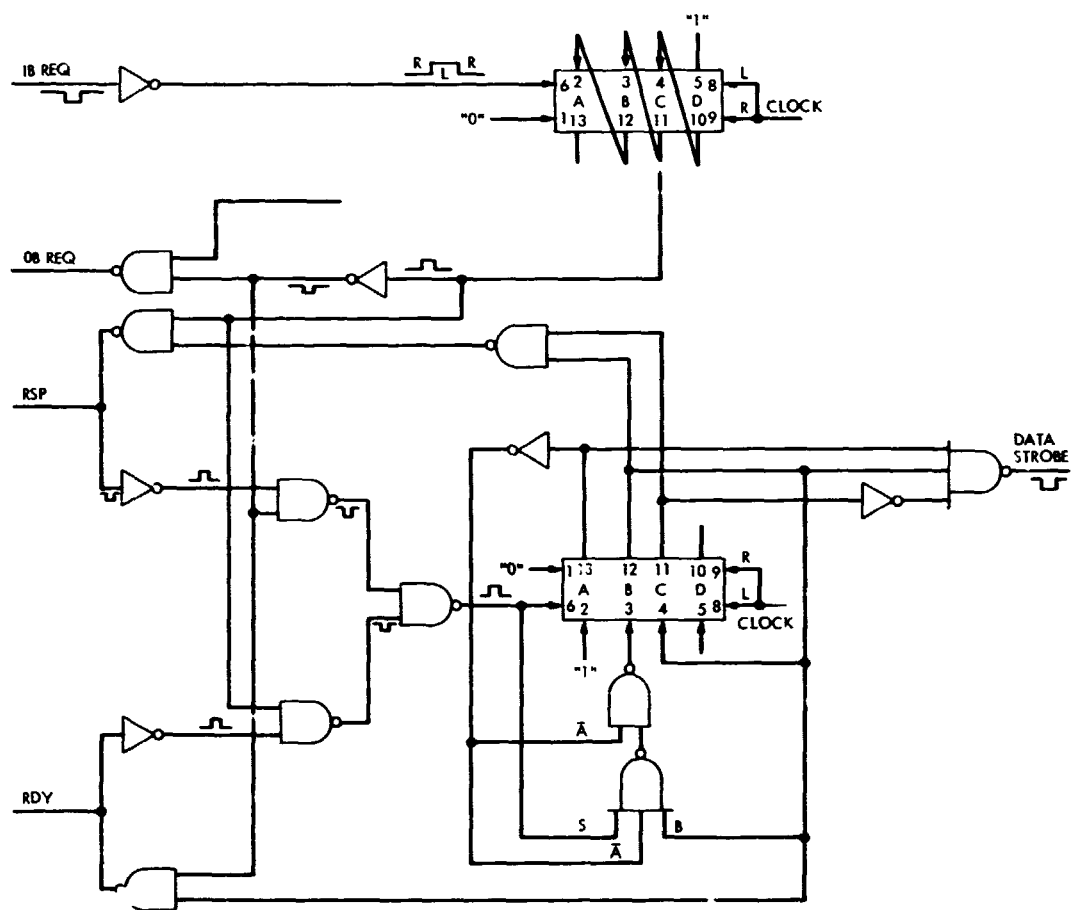


Fig. 8. NCS standard computer interface timing control logic including interlock and time share

# High-Speed Data Outage Distribution

J. P. McClure  
DSIF Digital Systems Development Section

*The outages experienced on the present Ground Communications Facility (GCF) 4800-bits/s high-speed data subsystem have been examined. An outage is defined as any interval when 10 or more consecutive high-speed data (HSD) blocks were received in error or were not received at all. For a 3-month period in 1973, outages ranged from 2.5 s to 4.8 h in length. The median outage was 15 s. Approximately 16% of the outages exceeded 1 min, and only 1.5% exceeded 15 min duration.*

## I. Introduction

The GCF provides high-speed data transmission at a rate of 4800 bits/s, using NASCOM circuits and Western Electric 203A data sets. Data are divided into 1200-bit blocks, transmitted at four blocks per second. If no data are available for transmission, the GCF generates and sends filler blocks in order to keep the circuit active and provide block synchronous operation. Before transmission, an error detection code is calculated and included in the block. At the receiving end, a GCF decoder checks the received code and sets status bits if transmission errors are present. If blocks are not received at all, the decoder goes out of lock (into search) for an integral number of block times until flow is re-established. The receive data set carrier failure signal also comes on during local circuit failures.

The information available from the GCF decoder has been studied to determine the distribution of the outages experienced in the data forwarded from the DSSs to JPL.

## II. Outages

For this study, an outage was defined as any interval when 10 or more consecutive HSD blocks were received in error or not received at all. Intervals of less than ten blocks were considered to be error bursts. This definition is a bit arbitrary; however, 10 block times ( $2^{16}$  s) is an improbably long error burst, hence there is some justification for this choice.

For outage study purposes, slightly less than three months of 1973 data were analyzed. These data were collected from the normal HSD operational circuits during regular tracking passes. No attempt was made to sort the data, though some data reflecting equipment malfunctions were discarded.

Outages ranged from 10 blocks ( $2\frac{1}{2}$  s) to 17,513 blocks (4.8 h) in length, with long outages being in the minority. Table 1 lists outage parameters for each of the DSS geo-

graphical areas, plus a total of all four DSS areas. Information on the performance of the Ames-JPL circuits is also shown.

As indicated in the tabulation, the median outages ranged from 58 to 63 blocks (14.5 to 15.75 s), a very close span considering the widely different transmission distances involved.

### **III. Distribution**

The outage distribution for the combined DSSs is shown in Fig. 1. On this plot, the abscissa indicates the percentage of the outages which had lengths equal to or less than the X-coordinate value. For instance, 71% of the outages were 100 blocks or less in length.

The abrupt breaks in the curves in the 30- and 50-block areas are caused by data set retrain characteristics. When a high data error rate condition occurs, the transmit and receive data sets interrupt the data flow and perform an internal readjustment sequence to compensate for changed circuit conditions. These interruptions cause data outages.

The GCF has a current commitment to restore service in 15 min or less. As measured, only 1.5% of the outages exceed 3600 blocks (15 min). In fact, only 16% of the outages exceed 1 min (240 blocks). A different definition of an outage would vary these findings; however, the GCF is definitely meeting its restoral commitment.

A future report will discuss the burst characteristics of faulty blocks.

**Table 1. HSD outage data and distributions**

	Canberra	Madrid	Goldstone	Johannesburg	Ames	DSS Total
Blocks transmitted ( $\times 10^6$ )	18.588	11.242	19.571	10.810	45.771	60.211
Circuit, days	53.8	32.5	56.6	31.3	132.4	174.2
Outages ( $\geq 10$ blocks)	375	163	94	246	142	878
Average interval between outages, h	3.44	4.79	14.4	3.05	22.4	4.76
% outages exceeding 1 min	13.3	18.4	18.1	15.9	16.2	16.3
% outages exceeding 5 min	2.1	3.1	5.1	4.1	3.6	3.7
% outages exceeding 10 min	1.1	0.6	3.2	1.3	2.1	1.7
% outages exceeding 15 min	0.6	0.0	3.2	1.3	2.1	1.5
% outages exceeding 30 min	0.3	0.0	1.1	0.8	0.0	0.65
Outages exceeding 1 min	50	29	17	40	23	136
Outages exceeding 5 min	8	5	5	10	5	28
Outages exceeding 10 min	4	1	3	2	3	10
Outages exceeding 15 min	2	0	3	2	3	10
Outages exceeding 30 min	1	0	1	1	0	3
Outage blocks	69829	31996	46475	57434	31485	237219
Outage duration						
Average, blocks	186.2	196.3	494	233	221	270
Average, s	46.6	49.1	123.6	58.4	55.4	67.5
Median, blocks	58	63	62	59	34	60
Median, s	14.5	15.7	15.5	14.7	8.5	15

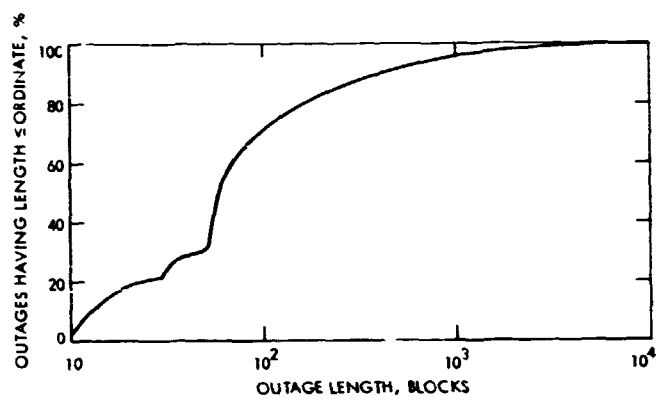


Fig. 1. HSD outage distribution, DSS to JPL

# Planetary Ranging

R. W. Tappan

DSN Data Systems Development Section

*The planetary ranging assembly (PRA) determines the range, or distance, to spacecraft that are travelling at planetary distances from Earth by measuring the time required for a radio signal to travel to the spacecraft and back. The range data are used to improve the accuracy of the calculation of the spacecraft's orbit and to provide information concerning the charged particle content of space.*

*The PRA is able to operate at the reduced signal levels because of improvements in the method of maintaining coder lock and detecting the signal in the presence of space noise. It is capable of operation with either S-band or X-band carrier frequencies and offers selectable code types to enable each project to specify the operating mode best suited to its particular mission.*

The planetary ranging assembly was installed in the Deep Space Instrumentation Facility (DSIF) to support Mariner Venus, Mercury 1973 and subsequent planetary missions. The PRA installation was necessary because the Mark 1A lunar ranging cannot operate at the signal levels received from spacecraft traveling at planetary distances. The range data are used to improve the spacecraft orbit prediction and to provide information concerning the charged particle content of space in the path between the ground station and the spacecraft.

The planetary ranging assembly contains digital hardware that performs special control and data collecting functions and a small general purpose computer that handles scheduling, computation, and data formatting.

The PRA is part of a ranging system that measures the round-trip time of a radio signal which travels from a ground tracking station to a spacecraft and back. A coded

signal is modulated on an S-band carrier and transmitted to the spacecraft, which detects and retransmits the signal to the tracking station. The signal received at the tracking station is delayed in time by its round trip through space and is shifted in frequency by the doppler effect because of the relative motion between the spacecraft and tracking station. The delay is measured by synchronizing a local model of the code with the transmitted code and then shifting it into alignment with the received signal. In order to detect alignment between the local code (receiver code) and the received signal, it is necessary to clock the receiver coder at the same bit rate that is present on the received signal. This is accomplished by adding the frequency offset due to the doppler effect to the clock frequency of the transmitted signal. The doppler signal derived from the S-band carrier is scaled and used for this purpose. Although the scaling is exact, there is a slow drift between the receiver coder and the received signal because the carrier and the modulation are not delayed by the same

amount when they pass through a medium containing charged particles. This difference, called differenced range vs integrated doppler (DRVID), is measured and output as a data type.

The PRA operates at much lower received signal levels, and therefore at greater distances, than the lunar ranging, primarily because it is implemented to use the carrier doppler signal to keep the receiver coder in step with the received signal, rather than extracting the coder clock directly from the signal. Performance has also been improved by optimizing the ranging code to improve the efficiency of detection, and employing a computer to numerically average the received signal and thus extend the signal range over which useful information can be recovered.

The elements of the PRA that communicate with the computer do so using the DSIF Standard 14-line interface. This computer interface is designed to transfer data reliably over relatively long distances in the electrically noisy environment of the tracking station. The use of a standard interface makes the equipment design independent of the computer assigned to it and enables equipment configurations to be changed more easily.

The PRA provides capability for ranging with either an S-band receiver or an X-band receiver by using the doppler signal from each receiver to generate a clock signal. Either of these clocks may be selected to drive the receiver coder; the other one automatically drives a clock generator which permits measurement of DRVID only using the receiver not selected for ranging.

A fixed-frequency relationship must exist between the transmitter coder frequency and the S-band carrier in order for the doppler rate aiding scheme to be workable. The same reference frequency that drives the S-band exciter is used to generate the transmitter coder, making the ratio between the carrier frequency and the transmitter coder frequency a fixed ratio of 1/2048. The clock that drives the receiver coder is derived in a similar manner, except that the doppler adder adds the doppler frequency offset, properly scaled. A doppler signal to which a bias reference frequency has been added is used to avoid the cycle detection problems encountered near zero-frequency doppler. The bias is removed digitally by the doppler

adder. High-frequency logic is required to implement the doppler adder, since additions and subtractions must be performed at an intermediate frequency (66 MHz) to minimize the phase jitter introduced in the receiver coder by the stepwise adjustment of its clock phase. The intermediate frequency is the highest frequency compatible with the high-speed logic used.

The transmitter and receiver coders generate both continuous spectrum and discrete spectrum codes. The code type to be used for the acquisition is selectable at the beginning of each ranging acquisition to enable each project to specify the code type best suited for its particular mission. The continuous spectrum code is a pseudo-noise code composed of six components which are combined into a composite code that is transmitted continuously to the spacecraft. The code power at any one frequency is small, minimizing the possibility of interference with other spacecraft operations; however, only a fraction of the total code power is available to align each of the individual components. The discrete spectrum code is composed of 20 square waves whose frequencies range from approximately 500 kHz to approximately 1 Hz. Each of the frequencies is sequentially transmitted to the spacecraft, so that the total code power is available to align it. The discrete spectrum code can therefore be used at lower received signal levels than the continuous spectrum code. The possibility of interference with other spacecraft operations has been reduced by mixing all components of this code with the highest frequency component.

The planetary ranging assembly was installed in the DSIF to provide range and DRVID data from spacecraft traveling at planetary distances. The measurement of range is used to improve the prediction of the spacecraft's orbit, and the DRVID data disclose information concerning the charged particle content of space.

Ranging at planetary distances is possible because of the performance improvement resulting from the incorporation of doppler rate aiding, code optimization, and numerical averaging of the received signal.

The PRA incorporates the flexibility necessary to support future missions by providing both continuous and discrete spectrum codes which may be used with either S-band or X-band carriers.

## Bibliography

1. Tausworthe, R. C., "Ranging Measurement," in *Supporting Research and Advanced Development*, Space Programs Summary 37-42, Vol. III, Jet Propulsion Laboratory, Pasadena, Calif., Nov. 30, 1966, pp. 52-56.
2. Tausworthe, R. C., "Communications Systems Development Minimizing Range Code Acquisition Time," in *Supporting Research and Advanced Development*, Space Programs Summary 37-42, Vol. IV, Jet Propulsion Laboratory, Pasadena, Calif., Dec. 31, 1966, pp. 198-200.
3. Martin, W. L., "Special Equipment for Mariner Venus 67 Ranging System," in *Supporting Research and Advanced Development*, Space Programs Summary 37-48, Vol. III, Jet Propulsion Laboratory, Pasadena, Calif., Nov. 30, 1967, pp. 63-67.
4. Lushbaugh, W. A., "Mariner Venus 67 Ranging System Digital Rack," in *The Deep Space Network*, Space Programs Summary 37-50, Vol. II, Jet Propulsion Laboratory, Pasadena, Calif., March 31, 1968, pp. 56-61.
5. Goldstein, R. M., "Ranging With Sequential Components," in *The Deep Space Network*, Space Programs Summary 37-52, Vol. II, Jet Propulsion Laboratory, Pasadena, Calif., July 31, 1968, pp. 46-49.
6. Martin, W. L., "A Binary-Coded Sequential Acquisition Ranging System," in *The Deep Space Network*, Space Programs Summary 37-57, Vol. II, Jet Propulsion Laboratory, Pasadena, Calif., May 31, 1969, pp. 72-81.
7. Lindley, I. P., *The PN Technique of Ranging as Applied in the Ranging Subsystem Mark I*, Technical Report 32-811, Jet Propulsion Laboratory, Pasadena, Calif., Nov. 15, 1965.
8. *Planetary Ranging Assembly Functional Requirements Document*, FM509136, Sept. 27, 1973 (JPL internal document).
9. *Planetary Ranging Assembly Technical Manual*, TM509201, Sept. 15, 1973 (JPL internal document).



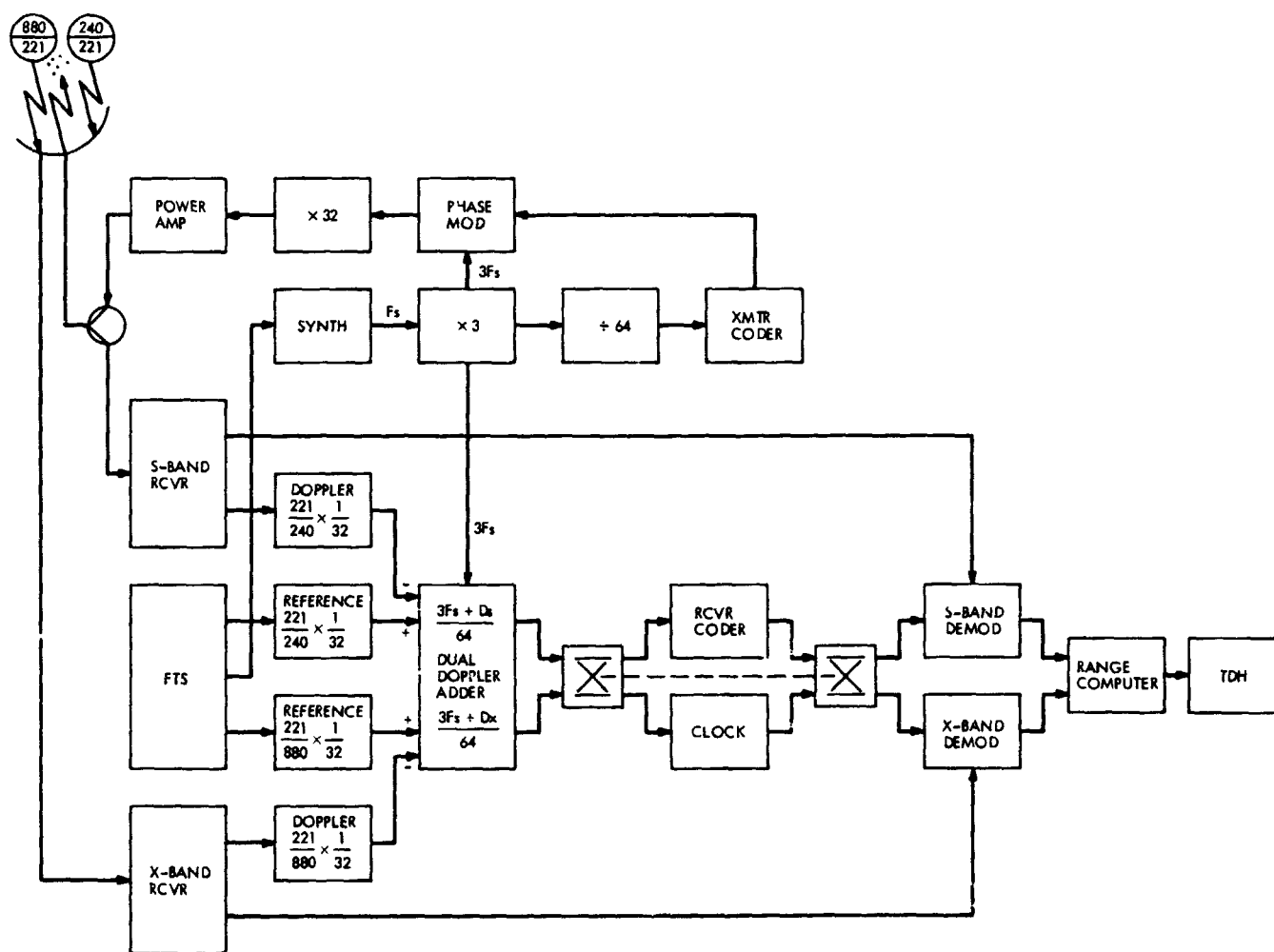


Fig. 1. Planetary ranging block diagram

# Adjustable Tuner for S-Band High-Power Waveguide

J. R. Loreman

R. F. Systems Development Section

*As part of an effort to reduce the DSN transmitter backpower at DSS 14, an adjustable S-band waveguide tuner for use at 400 kW has been developed. The tuner will be used to improve the match of the transmitter waveguide to the antenna feed system at DSS 14 in an effort to reduce transmitter back power at certain operating frequencies caused by high voltage standing wave ratio (VSWR) in the feed.*

Because of various waveguide modifications to the transmitter waveguide run at DSS 14 (Ref. 1), the waveguide match of the run has changed, causing high transmitter back power. Measurements have been conducted in an effort to determine the corrective measures required (Ref. 2). The measurements, as well as reports by operating personnel, indicated that the S-band polarization diversity (SPD) cone configuration in particular requires an effort to reduce back power at certain operating frequencies. Figures 1 and 2 show the voltage standing wave ratio plot of the waveguide from the DSN transmitter through the SPD cone in right circular polarization (RCP) and linear polarization. Calculated back power for each VSWR has been included on the charts.

Further measurements have been made at DSS 14 to determine the effect of a waveguide tuning section on the VSWR. The tuning section used was a low-power broad wall vane type tuner and, though not of a design applicable to high microwave power, its characteristics approximate deflection of the broad waveguide wall, a

technique frequently used for tuning of high-power waveguides. Figure 3 shows the match at low power through the SPD cone in linear polarization, with the tuner at the transmitter input to the waveguide. The effect on the VSWR with respect to frequency is apparent when this figure is compared with Fig. 2. From the testing, it was apparent that a simple tuner based on the controlled deflection of the waveguide broad wall would probably have sufficient tuning effect to reduce the VSWR of the SPD cone configuration to approximately 1.12 across the band of 2110 to 2120 MHz. The advantages of such a tuner are simplicity; direct application to the high-power configuration, as the tuner could be easily water-cooled; small size, as no auxiliary cavities would be required; and simple mechanical design. The main disadvantages are felt to be a limited frequency effect and limited retuning capability due to work-hardening of the copper waveguide. Both of these disadvantages may be crucial to the acceptability of such a simple design, as the changing of any one of the major reactive components in the waveguide run or cone will

require retuning, and the complex nature of the mismatch may require several tuners of this type. For these reasons, a parallel tuner development based on the coupling of a waveguide section to an adjustable cavity through the narrow wall is being pursued (Ref. 3).

Based on a simple waveguide broad wall deflection scheme, a prototype adjustable tuner has been designed and fabricated (see Fig. 4). The broad walls have been machined to approximately 0.25 cm to minimize work-hardening of the copper wall, and water-cooling ducts are provided on both narrow walls. The mechanism allows bidirectional deflection of both waveguide broad walls. Waveguide structural rigidity is provided by both the water-cooling ducts and the stainless steel deflection

bars. Laboratory tests indicate that the tuner can be adjusted from a VSWR of 1.01 to 1.15 up to four times before the copper waveguide walls begin to visually show work-hardening. Thus, it appears more tuning flexibility may exist than was expected. The prototype tuner has been operated at a power level of 400 kW for several hours with no heat buildup on the thinned broad walls of the waveguide. It appears that the tuner at its present level of development may be operationally installed. Several additional tuners have been fabricated, and one tuner will be installed at DSS 14 in the 400-kW radio science transmitter waveguide run to the SPD cone in January 1974. Based on the results of this installation, the tuner may be installed in the DSN high power transmitter waveguide run on an interim basis.

## References

1. Leu, R. L., "X-Band Filter," in *The Deep Space Network Progress Report*, Technical Report 32-1526, Vol. XVI, Jet Propulsion Laboratory, Pasadena, Calif., Aug. 15, 1973.
2. Loreman, J. R., "Waveguide Installation Measurements at DSS 14," in *The Deep Space Network Progress Report*, Technical Report 32-1526, Vol. XVI, Jet Propulsion Laboratory, Pasadena, Calif., Aug. 15, 1973.
3. Buchanan, H. R., "Variable S-Band High-Power Tuner," in *...*

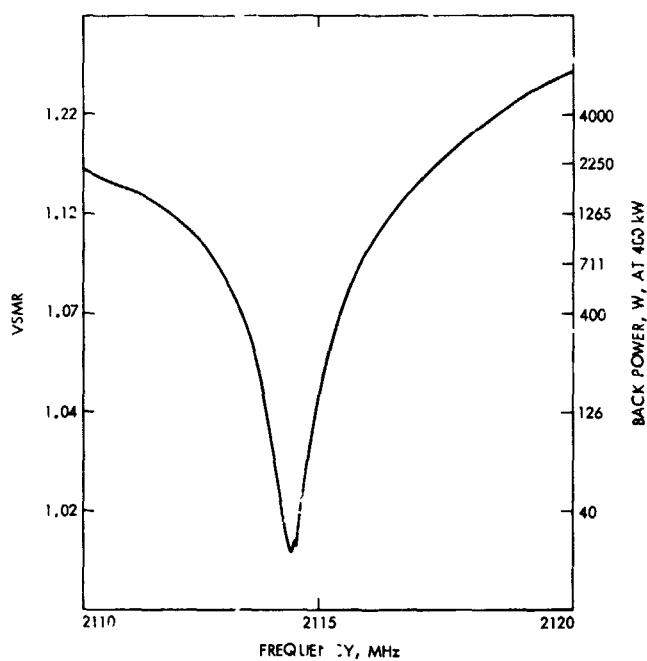


Fig. 1. VSWR 400-kW transmitter through SPD cone (RCP)

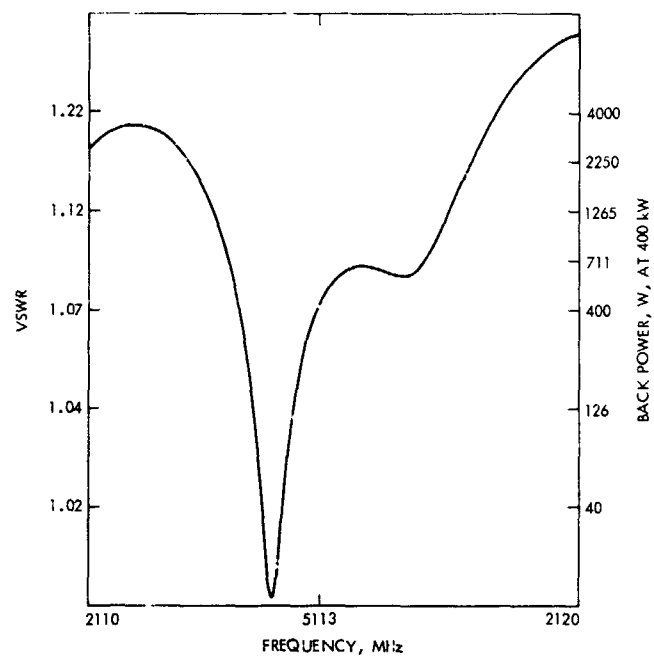


Fig. 2. VSWR 400-kW transmitter through SPD cone (linear polarization, 359 deg)

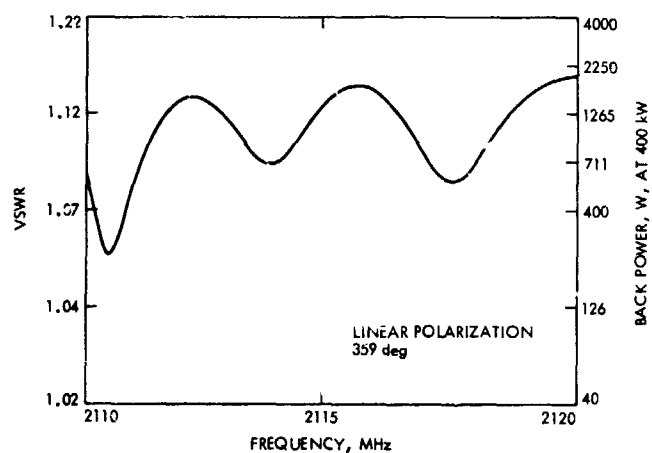


Fig. 3. VSWR 400-kW transmitter through SPD cone, vane-type tuner installed

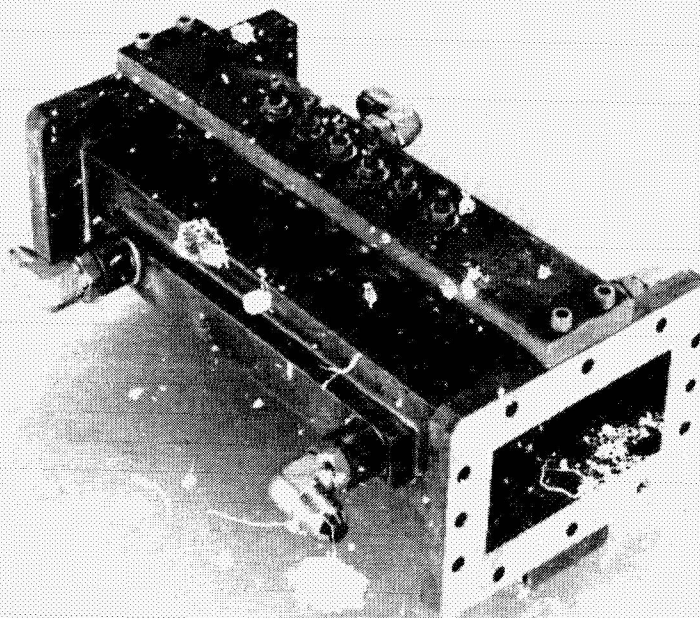
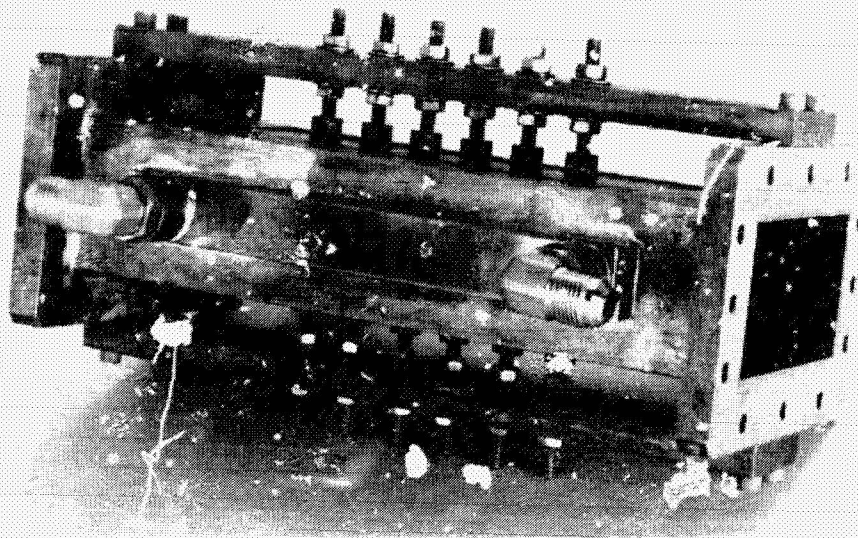


Fig. 4. Two views of prototype adjustable tuner for S-band high-power waveguide

# X-Band Antenna Feed Cone Assembly

R. W. Hartop

R. F. Systems Development Section

*The new X-band feed cone assemblies for the DSN 64-m antenna stations are under construction. The feed subassemblies have been completed, and other progress to date is reported.*

In support of Viking and future projects, the DSN must provide for X-band signal reception at the three existing 64-m antenna stations. The design of a new feed cone assembly for this purpose was described in Ref. 1.

The feed subassemblies for the three cones have now been completed and are shown in Fig. 1. The top plate, which seals the cone opening and supports the feed without additional members, is shown resting on a wooden frame that serves as a storage and transportation enclosure.

Not yet mounted on the feed assembly is the X-band waveguide switch to select either the feed or a calibrated load for the traveling wave maser. Its mounting plate may be seen at the lower end of the feed.

The lowest component in the feed, which will attach directly to the waveguide switch, is the circular-to-rectangular waveguide transition. This uniform transition is formed by electron-discharge machining of a solid

copper forging with a tool like that shown on the right in Fig. 2.

The tool illustrated is a forming tool that is a copy of a master tool generated on a programmed machine. Several of these tools are used as electrodes to form a transition such as the aluminum test piece also shown in Fig. 2. The transition, when finished, is 10.16 cm (4.000 in.) long and uniformly transforms a 3.477-cm (1.369-in.) diameter circular waveguide into a  $3.175 \times 1.587$  cm ( $1.250 \times 0.625$  in.) rectangular waveguide.

The next section above the transition is a circular waveguide section that serves as a higher-mode control between the transition and polarizer, which is the third section. Both components are made from solid copper forgings, the polarizer by electron-discharge machining, and the circular waveguide section by conventional machining.

The polarizer is a quarter-wave plate design and is the same as that used successfully in the Operational Time

Sync Microwave Subsystem (Ref. 2), except for dimensional scaling to this frequency band.

The fourth waveguide section is another circular waveguide spacer identical to the second section. Besides providing additional mode control, these two spacer sections, totaling 20.32 cm (8 in.) in length, will provide for future modifications in the feed without greatly increasing its length. For example, rotary joints for the polarizer could be added without changing the overall length by substituting shorter spacer sections along with the new rotary joints.

The feed horn is fabricated in four sections, of which the top three are aluminum for weight reduction and cost savings, and the lower section (seen with a support clamp in Fig. 1) is OFHC copper. The horn is otherwise

identical to that in the Time Sync System (Ref. 2), except that the horn throat was not modified. Thus, the 3.477-cm (1.369-in.) diameter circular waveguide is maintained throughout the feed.

The voltage standing wave ratio (VSWR) of one of the feed assemblies, complete with the transition, is shown in Fig. 3 over a wide bandwidth. The actual operation of these feeds in the near future will be over a narrow band near 8400 MHz.

The internal floors and ladders for the cone assemblies have been fabricated, along with various brackets and panels. Assembly of these parts and the feed subassemblies into the cone shells has begun, with completion scheduled before the end of the first quarter of calendar year 1974.

## References

1. Hartop, R. W., "X-Band Antenna Feed Cone Assembly," in *The Deep Space Network Progress Report*, Technical Report 32-1526, Vol. XVII, pp. 131-133, Jet Propulsion Laboratory, Pasadena, Calif., Oct. 15, 1973.
2. Hartop, R. W., "Operational Time Sync Microwave Subsystem," in *The Deep Space Network Progress Report*, Technical Report 32-1526, Vol. VI, pp. 165-167, Jet Propulsion Laboratory, Pasadena, Calif., Dec. 15, 1971.



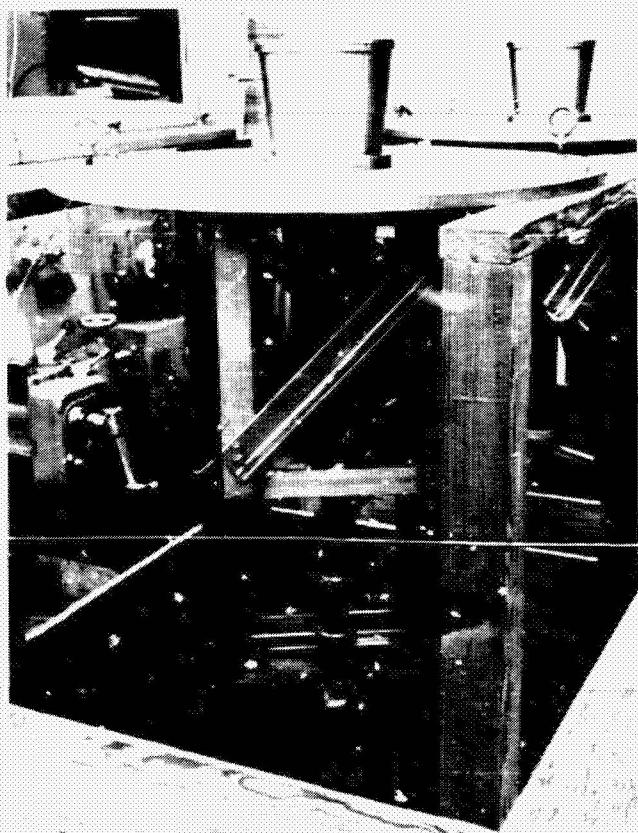


Fig. 1. X-band feed subassembly



Fig. 2. Waveguide transition and tool

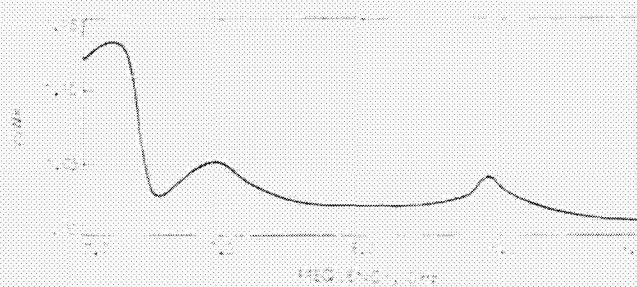


Fig. 3. XRO feed assembly VSWR



# Variable S-Band High-Power Tuner

H. R. Buchanan

R. F. Systems Development Section

*A variable, high-power waveguide tuner that can be remotely controlled is being developed. Satisfactory operation at a 400-kW power level is the goal. Progress to date is reported.*

## I. Introduction

Recent measurements of the DSS 14 transmitter waveguide installation (Ref. 1) have emphasized the need for a compact tuning device that can be used at strategic points in the waveguide system to improve the match. This device must operate at 400 kW and have the capability of correcting a mismatch in the order of 1.10 to 1.15 voltage standing wave ratio (VSWR). A manually adjustable device that can be retuned a limited number of times has been developed for the immediate need (Ref. 2). This report describes a longer range development of a variable tuner that can be adapted for remote control and, if required, programmed control.

## II. Theory of Operation

The microwave circuit of the variable tuner is depicted in Fig. 1. A portion of the main WR 430 waveguide signal is coupled to an H-plane arm terminated in a variable position short. The short is a movable, noncontacting

type with a restricted range of motion to avoid operation at or near resonance. The short is an existing design that has been used satisfactorily at 20 kW.

The power level coupled into the H-plane arm is controlled by the diameter of the circular aperture in the side wall of the main waveguide. Figure 2 indicates the theoretical coupling as a function of the hole diameter with correction for the waveguide wall thickness (Ref. 1). When the H-plane arm is terminated by a short circuit, the mismatch introduced into the main waveguide is a function of the power coupling and the short position. Figure 3 indicates the theoretical susceptance variation (Ref. 1) calculated for aperture diameters of 3.81 and 4.70 cm. It is noted that the larger aperture affords a larger tuning range with a less steep slope in the negative susceptance region.

## III. Prototype Tests

A waveguide test sample has been fabricated and tested at low power, using several coupling aperture

diameters. The coupling measurement was made with the H-plane arm terminated in a matched load. Match measurements using a waveguide slotted line were made with the H-plane arm terminated in a laboratory model sliding short. The test results are plotted in Figs. 2 and 3 for comparison with theory. The agreement appears to be quite acceptable for small apertures, but less accurate for larger apertures. Nevertheless, the theory serves as a valuable tool for laboratory development.

#### IV. Future Plans

A high-power test model is now being fabricated using a coupling hole diameter of 4.7 cm. This aperture is expected to exhibit a coupling of 17 dB, resulting in a power level in the H-plane arm of approximately 8 kW. This model will include the noncontacting short and water-cooling. Tests at 400-kW will be made and reported at a later date.

### References

1. Matthaei, G. L., Young, L., and Jones, E. M. T., *Microwave Filters, Impedance-Matching Networks, and Coupling Structures*, McGraw-Hill Book Company, New York, 1964, pp. 229-242.
2. Loreman, J. R., "Adjustable Tuner for S-band High-Power Waveguide," in *The Deep Space Network Progress Report*, this issue.

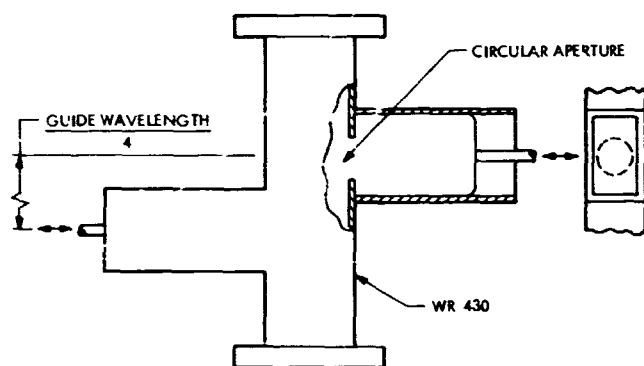


Fig. 1. High-power waveguide tuner

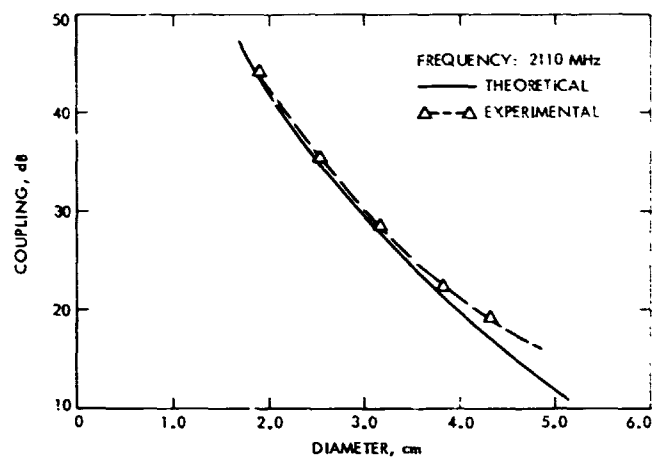


Fig. 2. Coupling vs aperture diameter

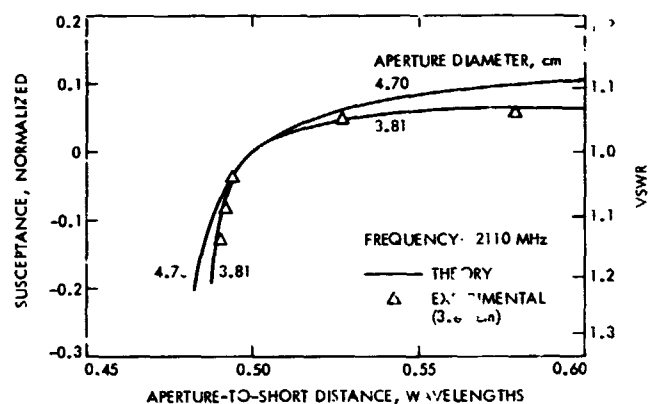


Fig. 3. Susceptance vs short position

# A No-Load RF Calorimeter

R. C. Chernoff

R. F. Systems Development Section

*A novel RF calorimeter is described and analyzed. The device combines the conservation of energy principle with the dc substitution idea to eliminate the need for RF and/or dc loads, thereby providing highly accurate "on-line" measurements of RF power at low cost. Breadboard test data are reported.*

## I. General Description

Consider any source,  $S$ , of power that accepts dc (or low-frequency) power,  $P_{dc}$ , produces output power,  $P_o$ , and rejects dissipated power,  $P_{diss}$ , to an external heat sink. If  $P_{dc}$ ,  $P_o$ , and  $P_{diss}$  are considered average values, conservation of energy implies

$$P_o = P_{dc} - P_{diss} \quad (1)$$

which in turn suggests the analog circuit of Fig. 1 for measuring  $P_o$ .

Operation of the device consists of correct adjustment of the  $P_{diss}$  scale deflection and zero of the  $P_o$  meter. A known value of  $P_{dc}$  is applied to the source. The  $P_o$  meter is then adjusted by means of potentiometer (1) to read " $P_{dc}$ ," i.e., that voltage (preferably at or near 100 mV) corresponding to  $P_{dc}$ . Secondly, the  $P_o$

meter zero is set by pot R2 under the following conditions: (1)  $P_{diss}$  inputs is reconnected, (2) some value of  $P_{dc} > 0$  is applied to the source, (3) the source is adjusted for zero output.

Since the conservation of energy principle applies to every form of energy,  $P_o$  can be any kind of power whatever; the utility of the device depends only on whether  $P_{dc}$  is easier to measure than  $P_o$ , and not on the "species" of either. But the most obvious application, and the only one considered here, is to RF power sources, although for our purposes the term "RF source" can be very broadly interpreted to include any dc (or 60- or 400-Hz) powered source of electromagnetic power,  $P_o$ , from very low frequency (VLF) to light.

The principal advantage of this device over conventional RF power measurement devices is that it enables "on-line" measurements, i.e., measurements of radiated power, with accuracy hitherto attainable only with dc substitution

calorimeters (Ref. 1). It is, in fact, a kind of dc substitution calorimeter in which the source itself serves as the dc load, but since it does not require an RF load (or an external dc load for dc substitution), it is much cheaper than a conventional RF calorimeter. For this reason one is tempted to call it a "poor man's calorimeter," but we will stick with "no-load calorimeter" (NLC) for the purposes of this article.

The principal limitations on the applicability of the NLC are: (1) source efficiency must be relatively high to obtain good accuracy, (2) it must be possible to operate the source in a  $P_0 = 0$ ,  $P_{dc} > 0$  mode to set the  $P_0$  meter zero (this is difficult or impossible for some oscillators, e.g., magnetrons), and (3) the device can only measure the power at the output port of the source, not at some remote point in a transmission line or in free space.

## II. Error Model

Figure 2 is an approximate lumped equivalent circuit for heat flow in a typical fluid cooled RF source. Most of  $P_{diss}$ , viz  $P_1$  flows from dissipation sites within the source (e.g., a tube anode) through an internal heat exchanger (e.g., coolant passages or fins in the anode) to the coolant.  $R_{11}$  represents the thermal resistance of the internal heat exchanger. The coolant then carries  $P_1$  to an external heat exchanger that rejects it to an infinite heat sink at  $T_0$  through equivalent thermal resistance  $R_{12}$ . If the cooling system is closed,  $R_{12}$  is shunted by thermal capacitance  $C$ , which represents the finite heat capacity of the circulating coolant.  $P_p$  is the fluid frictional loss in the internal heat exchanger. Heat leakage from the source is represented by the shunt  $R_2$  to the infinite heat sink at  $T_0$ .

From Eq. (1) and elementary circuit theory we have

$$P_0 = P_{dc} - (1 + \alpha)P_3 + P_e \quad (2)$$

where

$$\alpha = (R_{11} + R_{12})/R_2$$

and

$$P_e = P_p(1 + R_{11}/R_2) + (T_i - T_0)/R_2 \quad (3)$$

is an error term due to  $P_p$  plus the heat flow between sinks at  $T_i$  and  $T_0$  through leakage conductance  $1/R_2$ . In general,  $T_i$  and  $T_0$ , hence  $P_e$ , are random variables of time.

We assume that only  $P_3$ , the heat carried from the source to the external heat exchanger by the coolant, is sensed, so that the output voltage,  $v_0$ , of the NLC is

$$v_0 = aP_{dc} - bP_3 \quad (4)$$

If, at some time, say  $t = 0$ , and at some positive value,  $P_{dc}(0)$ , of  $P_{dc}$ , we adjust the zero of the  $P_0$  meter in the manner described above, we set

$$b = a(1 + \epsilon_0)/(1 + \epsilon_0) \quad (5)$$

where  $\epsilon_0 = P_e(0)/P_{dc}(0)$ , and  $P_e(0)$  is the value of  $P_e$  at that time. From Eqs. (2), (4), and (5) we find that at any future time,  $t$ ,

$$\begin{aligned} \Delta P_0 &= P_0 - v_0/a \\ &\approx \epsilon_0 [P_{dc}(0) - P_{diss}(t)] + \Delta P_e(t) \end{aligned} \quad (6)$$

where  $\Delta P_e(t) = P_e(t) - P_e(0)$ , and we have assumed  $\epsilon_0$  small enough to write  $\epsilon_0 \approx \epsilon_0/(1 + \epsilon_0)$ . From Eq. (3) we see that  $P_e$ , hence  $\Delta P_e(t)$ , is independent of  $P_{dc}$ , hence of  $P_{diss}$ , so the two terms of  $\Delta P_0$  are uncorrelated, and the rms value of  $\Delta P_0$ ,  $\text{rms}(\Delta P_0)$ , assumes its minimum value,

$$\min [\text{rms}(\Delta P_0)] = \text{rms}(\Delta P_e(t)) \quad (7)$$

at  $P_{diss}(t) = P_{dc}(0)$ . To minimize  $\text{rms}(\Delta P_0)$ , therefore, one must not only be able to estimate the value of  $P_{diss}$  but one must also rezero the  $P_0$  meter whenever  $P_{diss}$  changes. The obvious way to get around this difficulty is to add a signal proportional to  $P_e(0)$  to the analog computation of  $P_0$  as, for example, in the circuit shown in Fig. 3. The  $P_0$  meter zero is first set with the  $P_e$  compensation pot, R3, at  $P_{dc} = 0$ . Then, with  $P_{dc} > 0$ , the  $P_0$  meter is again zeroed with R2 as previously described. This adjustment eliminates the  $P_{dc}(0) - P_{diss}$  bias term from Eq. (6).

Theoretically, the  $P_e$  compensation enables one to realize  $\text{rms}(\Delta P_0) = \min [\text{rms}(\Delta P_0)] = \text{rms}[\Delta P_e(t)]$ , i.e., elimination of all errors except those due to random fluctuation of  $T_i - T_0$ . The cost is slight: one additional adjustment making three in all (R1, R2, and R3), none of which need be repeated when  $P_{dc}$  or  $P_{diss}$  change. On the other hand, the benefit may also be slight if, for example,  $\text{rms}[\Delta P_e(t)] \gg \text{ave}(P_e)$ , or if instrumentation errors swamp both.

Note that leakage conductance  $1/R_2$  enters into the error term  $P_e$  only through the relatively small gradient  $T_i - T_0$ , not through the large gradient between the

source  $P_{diss}$  and the leakage sink at  $T_1$ . This is another advantage the NLC has over a conventional dummy load calorimeter: in the latter, heat leakage contributes directly to measurement error, and there is no easy or inexpensive way to compensate for it, whereas in the NLC, leakage conductance contributes a small, easily compensatable error, and leakage power itself has no direct effect.

$C$ , the thermal capacity of the circulating coolant, is just one of the many finite heat sinks in a large power source and its cooling system, but it is included in the model because it tends to be much larger than most of the others. It can contribute a maximum error of  $(R_{12}/R_2)P_3$  if  $b$  is adjusted before  $C$  is fully charged. In most large fluid cooled sources, the coolant will be only 5 to 10°C warmer than  $T_0$ , while the internal heat source (e.g., a tube anode) will be hundreds of °C hotter than the coolant. This means that  $R_{12}$  is much smaller than  $R_{11}$ . Furthermore,  $R_{11} + R_{12}$ , the total thermal resistance of the cooling system, is always much smaller than the leakage resistance  $R_2$  in any reasonably designed large source. Therefore,  $R_{12} \ll R_2$  and the error caused by premature adjustment of  $b$  is very small. This reasoning may not hold for small sources that have relatively large heat leakage, but  $C$  is proportionally smaller for small sources and the time required to reach thermal steady state is proportionally shorter.

### III. Experimental Results

A breadboard NLC was built and used to measure the output of a 10-kW average power water cooled klystron amplifier. The  $P_{diss}$  signal was provided by resistance temperature sensors that sensed the  $\Delta T$  of the combined coolant flows in collector and body. Coolant flow appeared to be constant to within the resolution (about 1%) of the flowmeter (had coolant flow not been constant, a flow rate sensor and (flow rate)  $\times \Delta T$  multiplier would be required to provide the  $P_{diss}$  signal). The  $P_{dc}$  signal was provided by analog multiplication of the voltages appearing at the terminals of beam current and beam voltage meters installed in the klystron power supply.

The  $P_0$  meter was adjusted to 20 kW full-scale using portable standard meters to measure beam current and voltage. No calibration data were available for the kilovoltmeter used to measure beam voltage but its accuracy was assumed to be 1.0% on the basis of the manufacturer's claims. This plus the 0.25% accuracy of the beam current ammeter yields an estimated 1.25% accuracy for the  $P_{dc}$  calibration.

Two kinds of tests were used to evaluate the performance of the NLC breadboard. The first was a comparison of simultaneous measurements of RF power by this device and by a conventional dummy load calorimeter. The second was a test of "zero tracking," i.e., the ability of the NLC to retain its original zero reading as  $P_{dc}$  is varied over its operational range while the actual RF output remains fixed at zero. The zero-tracking test measures the total error due to nonlinearity and drift. It is, of course, incapable of determining what part of this total is due to instrumentation errors and what part arises in the heat transfer processes of the source itself.

The results of the zero-tracking test appear in Fig. 4. The transient following each  $P_{dc}$  step change is greatly exaggerated by integration of the  $\Delta T$  signal ( $\tau \approx 25$  s) required to suppress rapid fluctuations.

Figure 4 shows that the steady-state  $P_0$  error is less than 0.20 kW (= 1.0% of full scale). The  $P_0$  meter was initially zeroed at  $P_{dc} = 20$  kW.  $P_e$  compensation was not attempted. Were  $P_e(0)$  appreciable, we would expect to see the error increasing linearly from 0 to 20 kW, but Fig. 4 shows no clear evidence of such a trend. We conclude that the zero-tracking error is primarily due to temperature drifts ( $T_i - T_0$  fluctuations in the simplified error model) within the source and/or instrumentation drift and nonlinearities.

The bulk of the error may well be due to the offset voltage at the input of the  $\Delta T$  operational amplifier (op-amp). The  $\Delta T$  op-amp was zeroed at the beginning of the test, but the offset drifted from zero as the ambient temperature changed. We can estimate the temperature change required to produce the observed zero-tracking error as follows.

The resistance temperature bridge output,  $v(\Delta T)$ , is about 1.0 mV/°C. The coolant flow during the test was 72 l/min (19 gpm). Therefore, at  $P_0 = 0$ , the constant  $v(\Delta T)/P_{dc} = 0.2$  mV/kW. Thus the observed 0.2-kW zero-tracking error corresponds to an offset voltage of 0.04 mV. The op-amp's offset temperature coefficient specification is 15  $\mu$ V/°C max, so that the 0.2-kW error could have been caused by an ambient temperature change of only 2.7°C. Obviously, a low-drift op-amp for  $\Delta T$  would have been preferable, but this breadboard, like most, was built of the most available, not the best, components.

The results of the no-load vs conventional calorimeter measurements are shown in Fig. 5 and Table 1. Although

nothing was known about its thermal properties, the dummy load design appeared to provide excellent thermal insulation between the coolant and the waveguide envelope of the load. The coolant was pure water. Coolant  $\Delta T$  was measured with a quartz thermometer, and load flow was measured with a differential pressure flowmeter. The values recorded in Table 1 are the means of at least nine nearly simultaneous readings each of  $P_o$  and dummy load  $\Delta T$  at each power level. The dummy load flow appeared to be constant throughout the run.

The apparent negative bias in the  $P_o(\text{NLC}) - P_o(\text{CC})$  values in Table 1 may not be significant; all but one difference is less than the maximum 0.20-kW error observed in the zero-tracking test, and the largest, 0.23 kW, is only slightly larger. In other words, the results of

Table 1 are consistent with the hypothesis that the  $P_o(\text{NLC}) - P_o(\text{CC})$  discrepancies are entirely due to the previously observed zero-tracking errors.

#### IV. Conclusions

The no-load calorimeter enables on-line RF power measurements at accuracies otherwise attainable only with much more expensive off-line techniques and equipment. A simple model of heat flow in the RF source shows that the inherent accuracy of the no-load calorimeter measurement is limited essentially by random fluctuation in temperature gradients between heat sinks. Two brief breadboard tests yielded consistent results.  $\Delta T$  op-amp offset drift appears to be the major error contributor in breadboard tests.

#### Reference

1. Ginzton, E. L., *Microwave Measurements*, McGraw-Hill, 1957, p. 193.

**Table 1. Comparison of RF output measurements:  
NLC breadboard vs conventional calorimeter**

$P_o(NLC)^a$ , kW	$P_o(CC)^b$ , kW	$P_o(NOM)^c$ , kW	$P_o(NLC) -$ $P_o(CC)$ , kW	$\Delta^d, \%$
7.88	8.05	7.6	-0.17	-2.1
7.46	7.43	7.0	+0.03	0.4
10.09	10.15	9.4	-0.06	-0.6
5.15	5.38	5.0	-0.23	-4.5
3.18	3.22	3.0	-0.04	-1.2

<sup>a</sup> $P_o(NLC)$  = NLC breadboard measurements.

<sup>b</sup> $P_o(CC)$  = conventional (dummy load) measurements.

<sup>c</sup> $P_o(NOM)$  = "nominal" RF output per in-line power meter.

<sup>d</sup> $\Delta\%$  =  $\frac{P_o(NLC) - P_o(CC)}{P_o(NLC)} \times 100\%$ .



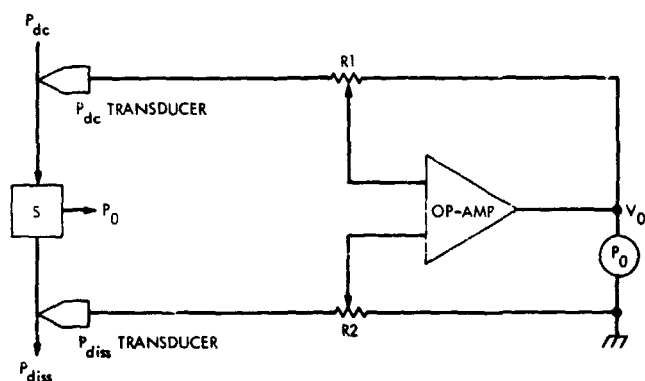


Fig. 1. No-load calorimeter

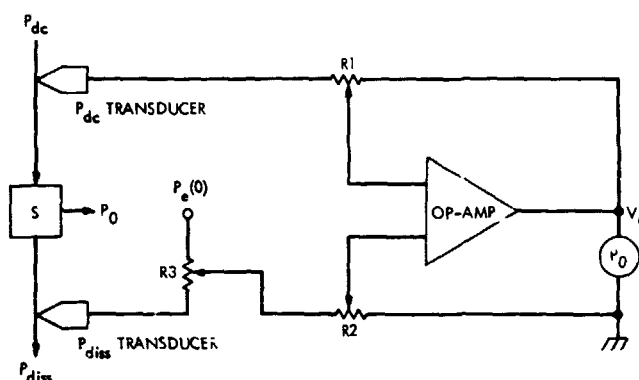


Fig. 3. NLC with  $P_e$  compensation

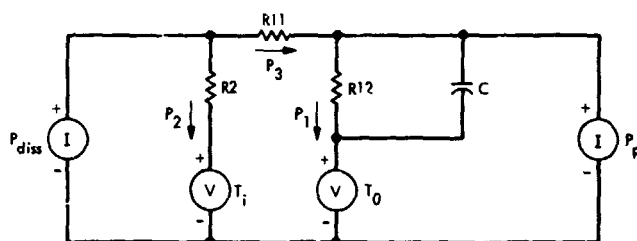


Fig. 2. Electrical analog of heat flow in an RF source

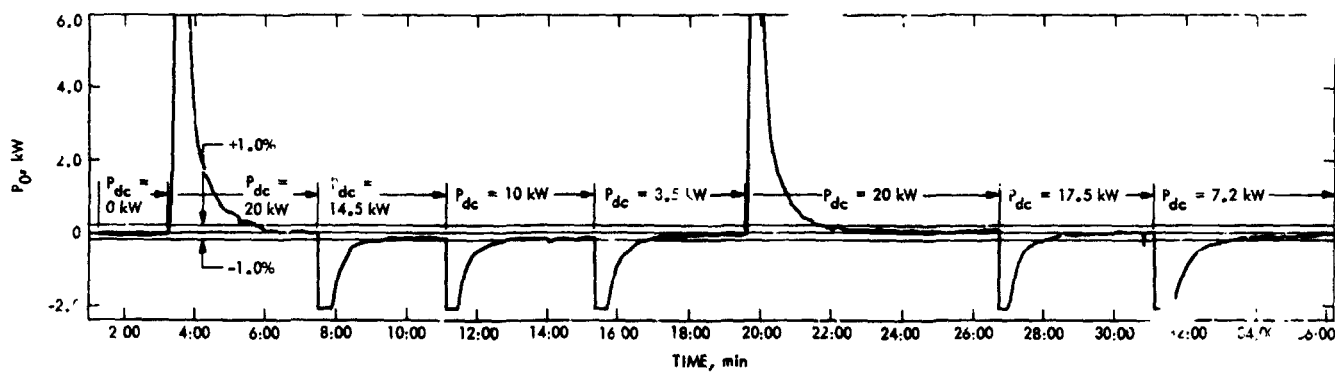


Fig. 4.  $P_0$  zero-tracking performance of the no-load calorimeter

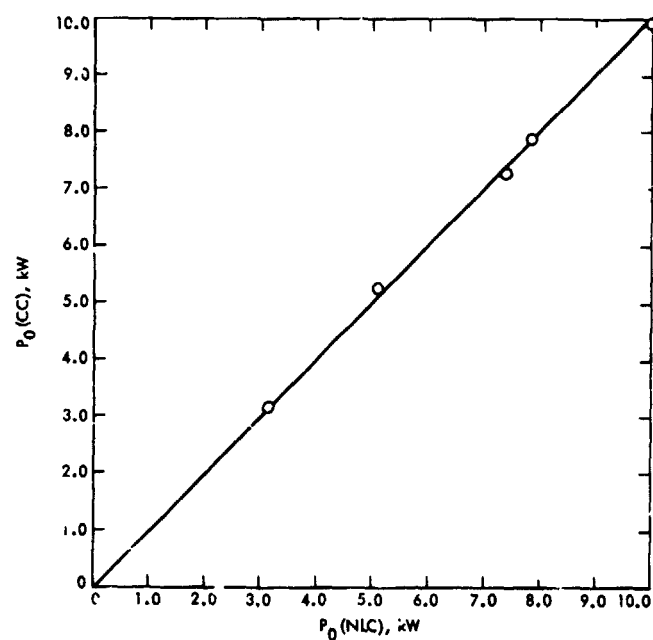


Fig. 5. Comparison of RF output measurements, no-loss calorimeter vs conventional calorimeter

# Dual Carrier Preparations for Viking

D. A. Bathker

Communications Elements Research Section

D. W. Brown

R. F. Systems Development Section

*While simultaneous transmission of two S-band carriers from a single Deep Space Station is no longer a committed operating mode for Viking Project support, the program of investigation and abatement of noise bursts and intermodulation interference has continued through the first three calendar quarters of 1973. At DSS 14, internal waveguide and external antenna work yielded major reductions in both types of interference. Supporting investigations were also conducted at JPL and at DSS 13 during this period. Conclusions and recommendations for future work are presented.*

## I. Introduction

The continuing program of investigation and abatement of interference arising from single- and dual carrier transmission from a Deep Space Station shifted emphasis to DSS 14 early in 1973. The extensive work at DSS 13 during 1972 (Refs. 1 and 2) was continued in the first half of 1973 in order to obtain long-term data and to perform specific experiments in support of the 64-m antenna effort. This work has been reported in detail by Petty and Jackson (Refs. 3 and 4). This article will emphasize results at DSS 14 and, with the aid of an extensive reference list, will serve as a final report for the 1972-1973 program.

On the whole, the effort at DSS 13 served the intended purpose of confirming prior hypotheses, identifying

sources of interference, developing remedial procedures, and establishing improved methods of instrumentation. Although significant reduction of internal sources and of selected portions of the external system at DSS 13 was achieved, little was to be gained by further work on the DSS 13 unique antenna structure.

## II. Supporting Investigations

Analysis and modeling of various aspects of the dual-carrier problem have continued, with the objective of backing the empirical field work with sound theory (Refs. 5-9). Of particular interest is the work by Higgs and others (Ref. 7), including laboratory generation of broadband noise and intermodulation products (IM<sub>n</sub>) in the receive band by means of RF-illuminated junctions of

oxidized aluminum. More recently, a quantum physics model has been applied (Ref. 9), largely confirming past hypotheses of tunneling effects in the myriad metal-oxide-metal junctions in the external antenna.

More closely allied to the field activities was the evaluation by Kent (Ref. 10) of the degradation of telemetry and doppler data in the interference environment. With the aid of a controllable IMP generator (Ref. 11), a range of performance was obtained, yielding the conclusion that, in general, for carrier loop margins near 20 dB (typical of Viking orbital operations), the presence of detectable receive band IMPs will produce detectable data degradation.

In yet a different context—Viking orbiter uplink and downlink spectrum analysis—Koerner has included the IMPs along with modulation sidebands and the multiple carriers in determining mutual interference in communication links (Refs. 12 and 13).

### III. Summary of DSS 14 Activity

As indicated at the close of the last major dual-carrier activity report (Ref. 2), a return to DSS 14 was authorized at the beginning of 1973. The initial scope was set at the accomplishment of whatever modifications could be made during the then scheduled station down time in February and March. In addition to a work plan for this period, tests were designed and scheduled for "before and after" interference performance during January and April-May. As of the end of May, the ten-fold improvement achieved (more on this in the next section) was sufficient to uncover a level and type (spectral quality) of interference which pointed strongly to the highly illuminated feed cones with their newly installed S/X-band hardware. This latter equipment was added during the aforementioned down time and consists of an ellipsoidal reflector atop the S-Band Megawatt Transmit (SMT) cone and a dichroic plate over the Multiple-frequency X- and K-Band (MXK) cone (Ref. 14). It had been anticipated that these items with their piece-part construction (rivets, etc.) and hydraulic retraction mechanisms would prove to be troublesome in the interference sense.

Because of the then approaching Mariner Venus/Mercury 1973 (MVM'73) preparations and Pioneer 10 configuration freeze, it was considered inadvisable to undertake any modifications to this critical equipment for the purposes of interference abatement. However, in order to capitalize on the gains already achieved, a plan

was devised to remove intact the SMT and MXK cones with the primary intent of evaluating the basic antenna with only the relatively simple (externally speaking) Polarization Diversity S-Band (PDS) cone in place. Evaluation in this configuration not only indicated further reduction in interference level but uncovered yet new clues pointing primarily to the quadripod apex and legs. Here again, a work plan was developed to complement an already scheduled survey and reconditioning of the main reflector. In order to maintain test configurations as orderly as possible, the re-installation of the cones was delayed somewhat, with the MXK going up near the first of August and the SMT about one month later.

More test time during and after this effort would have allowed more satisfying cause-and-effect conclusions to be drawn, but thanks to the extraordinary efforts of DSN scheduling, station personnel, and key people from Sections 332, 333 and 731, additional improvements of 100-fold and more (30 dB since January) were obtained with sufficient control to firmly establish the re-installed cones and related equipment as the limiting interference sources.

Table 1 attempts to summarize these DSS 14 activities for the purpose of establishing a time line for the discussion to follow, which will present the performance achieved at each step. The important detail behind the modification summary given above will be reported separately<sup>1</sup> (see also Ref. 15).

### IV. Performance Results At DSS 14

Considering the completion times of Table 1 as the abscissa and the IMP mean averaged over the available test periods as the ordinate, we obtain Fig. 1. As noted, all performance data are for the standard test conditions of dual 40-kW carriers at approximately 6-MHz spacing ( $N = 31$ )<sup>2</sup>.

The "pre-1973" data point is typical of observations in 1972 and perhaps earlier. The 2- to 3-dB improvement indicated in the first interval is illustrative of the concept that for many discrete interference sources, eradication of less than a majority (assuming equal intensity for each) will result in less than 3-dB reduction in overall level.<sup>3</sup> Keeping Table 1 in mind, we see a 10-dB reduction

<sup>1</sup>To be published.

<sup>2</sup> $N$  is the index of the  $N$ th spectral line above the upper carrier (Ref. 2).

<sup>3</sup>See first part of Ref. 15 for "pre-1973" modifications.

achieved in the next interval, which represents the addition of the S/X feed cones, down time modifications, and replacement of such internal waveguide items as switches and diplexer. While some data were taken in the SMT diplex mode as well as with the PDS cone, which proved helpful on a detailed diagnostic level, in general, the interference performance was essentially the same with either cone active (Ref. 16). For the purposes of this article, it is sufficient to consider all data as taken in the PDS mode.

As of late May, the IMP mean had not only been reduced to typically  $-150$  dBm (from  $-140$  dBm in January), it had also taken on a more stable character (i.e., less variance). Similarly, the single- and dual-carrier noise burst (NB) performance had made proportional improvements (Fig. 2). As noted in the preceding section, the SMT and MXK feedcones were then removed, with an immediate 6- to 10-dB improvement. By late July, minor modifications primarily near the surface of the main reflector, had yielded exceptionally interference-free performance: IMP means of  $-170$  dBm and less and NB peaks in the 3-K range, except upon mechanical agitation of the quadripod apex/subreflector assemblies. As indicated in Fig. 1, this effect had first been uncovered during the prior test period, and was a primary consideration in the formulation of the August work plan (see Table 1).

Station commitments forced the re-installation of the MXK cone during the August modifications, with a result that precluded the possibility of observing a probably stable interference level of  $-170$  dBm or less. Nonetheless, evidence in mid-August strongly indicates that the intermittence had been subdued, even though a new stable IMP level of  $-160$  dBm resulted in this configuration. By late August, with essentially all modifications complete, the IMP level had apparently risen to  $-155$  dBm. As Table 1 indicates, the main reflector had been stripped of tape and retaped during this month, but with dry weather in this period, it is believed that tape was not a factor in the August performance data.

Two apparently unrelated circumstances are of interest for this period. First, as noted in Table 1, the 400-kW klystron failed at about the time the feed cones were removed, and because spares had been temporarily consumed by other high-power transmitter problems, it was necessary to adopt the 100-kW configuration as planned for DSS 43 and 63. In order to maintain continuity of test condition, dual 40-kW operation with the 100-kW klystron was attempted and just achieved with close monitoring of operating conditions (i.e., RF drive, beam

voltage, etc.). While this mode considerably exceeded the 10% per carrier nominal operating power (Ref. 2), with resulting increased level of low-order (uplink) intermodulation sidebands in the transmitter output, special tests were conducted which indicated that the *receive band* IMPs were probably typically generated and, if anything, this configuration would yield data on the conservative side. This transmitter configuration prevailed throughout the balance of the year.

Secondly, beginning at the mid-August tests and continuing thereafter, the prevailing IMP levels of  $-160$ ,  $-155$ , and finally  $-150$  dBm in September became consistently more sensitive to carrier operating level. As seen in Fig. 3, a 3-dB reduction (to dual 20 kW) produced less receive band IMPs in ratios approaching 30 dB ( $-150$  to  $-180$  dBm). All prior experience—early 1973 as well as both DSS 13 and DSS 14 in 1972—suggested a cube law effect (approximately 9 dB per 3 dB) (see Fig. 2 of Ref. 2). The clear implications here are that the July and August effort not only subdued the dual 40-kW intermittent but achieved a lasting reduction of the cube law mechanism by as much as 20 to 30 dB (referred to the 20-kW level), and that the implied interference sources associated with cone re-installation are of intrinsically different type from those generally observed prior to that time. This conclusion reinforces earlier hypotheses concerned with loose as opposed to tight RF joints and the various intermediate solid-state junctions.

Largely unresolved at this time are the weather-dependent characteristics of the IMPs and NBs. Prior experience suggests that the August retaping of the main reflector (using latest techniques of insulation between overlapping tape junctions) will improve performance in this respect, but, as indicated by the termination of the top curve of Fig. 2, there has been no opportunity to make this evaluation.

## V. Conclusions

1. Single- as well as dual-carrier noise bursts have been diminished to insignificance to the benefit of all missions. The only reservations concern the weather (as discussed above) and the presently unknown maintenance requirements (discussed or implied in many earlier reports—Refs. 3 and 17, in particular).

2. With the DSS 14 antenna and microwave equipment in "as is" condition (September 1973), the dual-carrier performance at 20 kW is more than adequate to support the Viking application, as indicated in Fig. 4. Note that the upper curve is taken from Fig. 3 and that the worst-

case Viking frequency separation offers additional margin over the nominal test conditions (Ref. 2). Reservations are as stated in (1) above.

3. It is *possible*, at least for a short period of time, to virtually eliminate both internal and external interference on a large antenna for worst-case excitation in the DSN context.

4. It is *not* considered possible to maintain the ultimate implied by (3) under normal operations for any significant period of time. It is considered possible, and even feasible, to achieve  $-160$  to  $-170$  dBm IMP means and 3-K or less NB peaks for worst-case excitation, given redesign and/or elimination of some features of the present (DSS 14) S/X-band feed cones and a dedication to the requisite operational care and maintenance.

## VI. Recommendations

1. In order to maintain single-carrier improvements, recommendations of maintenance and modification have

been made (Refs. 3, 15, 17, 18) applicable in some degree to any antenna, and those at DSSs 43 and 63 in particular.

2. Further, in support of single-carrier performance, a program of noise burst monitoring at DSS 14 at 400 kW as well as at other nominal operating levels is recommended, especially during the winter and spring months, to complement the summer data reported here.

3. In the event dual-carrier operation is contemplated in support of, or for enhancement of, future flight projects, recommendations for more major modifications for the 64-m network are also included in Refs. 15 and 18. These relate primarily to the external antenna and have, in the course of this program, been largely accomplished at DSS 14.

4. Finally, a firm commitment to dual-carrier operation should, in addition to the above, be supported by a thorough evaluation of and response to the S/X-band feed cone and maintenance implications of conclusion (4) above.

## References

1. Bathker, D. A., and Brown, D. W., "Dual Carrier Preparations for Viking," in *The Deep Space Network Progress Report*, Technical Report 32-1526, Vol. XI, pp. 146-149, Jet Propulsion Laboratory, Pasadena, Calif., Oct. 15, 1972.
2. Bathker, D. A., and Brown, D. W., "Dual Carrier Preparations for Viking," in *The Deep Space Network Progress Report*, Technical Report 32-1526, Vol. XIV, pp. 178-199, Jet Propulsion Laboratory, Pasadena, Calif., Apr. 15, 1973.
3. *1973 Dual Carrier Work at DSS-13; Results, Conclusions, Recommendations*, IOM 3331-73-020, July 27, 1973 (JPL internal document).
4. Jackson, E. B., "Station Control and Operations Technology," in *The Deep Space Network Progress Report*, Technical Report 32-1526, Vols. XIII through XVII, Jet Propulsion Laboratory, Pasadena, Calif., 1973.
5. Butman, S., "Efficient Signal Generation for High-Power Dual-Spacecraft Command," in *The Deep Space Network Progress Report*, Technical Report 32-1526, Vol. XIII, pp. 130-132, Jet Propulsion Laboratory, Pasadena, Calif., Feb. 15, 1973.
6. Levitt, B. K., "Intermodulation Products in Dual Carrier Transmission: Power Series Analysis," in *The Deep Space Network Progress Report*, Technical Report 32-1526, Vol. XV, pp. 70-79, Jet Propulsion Laboratory, Pasadena, Calif., June 15, 1973.

## References (contd)

7. Higa, W. H., Clauss, R. C., and Dachel, P. R., "Low Noise Receivers: Theory of Noise Bursts on Large Antennas," in *The Deep Space Network Progress Report*, Technical Report 32-1526, Vol. XV, pp. 80-83, Jet Propulsion Laboratory, Pasadena, Calif., June 15, 1973.
8. Greenhall, C. A., "Dual Carrier Intermodulation Caused by a Zero-Memory Nonlinearity," in *The Deep Space Network Progress Report*, Technical Report 32-1526, Vol. XVII, pp. 108-112, Jet Propulsion Laboratory, Pasadena, Calif., Oct. 15, 1973.
9. Higa, W. H., "Quantum Phenomena on Giant Antennas," to be published.
10. Kent, S. S., "Dual Carrier Investigations at the Mars Deep Space Station," in *The Deep Space Network Progress Report*, Technical Report 32-1526, Vol. XVI, pp. 163-173, Jet Propulsion Laboratory, Pasadena, Calif., Aug. 15, 1973.
11. Kolbly, R. B., "Intermodulation Product Generator," in *The Deep Space Network Progress Report*, Technical Report 32-1526, Vol. XV, pp. 143-145, Jet Propulsion Laboratory, Pasadena, Calif., June 15, 1973.
12. *Minimum and Maximum Intermodulation Product Order for Downlink Carrier Channel Interference from an Intermodulation Product of Two Uplink Carriers*, IOM 3395-73-92, Apr. 24, 1973 (JPL internal document).
13. *Viking Uplink Carrier Channel Interference Produced by Ranging Sidebands From an Intermodulation Product of Two Viking Uplink RF Signals*, IOM 3395-73-216, Sept. 10, 1973 (JPL internal document).
14. Potter, P. D., "S- and X-Band RF Feed System," in *The Deep Space Network Progress Report*, Technical Report 32-1526, Vol. X, pp. 135-142, Jet Propulsion Laboratory, Pasadena, Calif., Aug. 15, 1972.
15. *Noise Abatement Work Completed on 64-m Antenna and Associated Hardware at DSS-14*, IOM 3324-73-077, Aug. 29, 1973, revised Sept. 26, 1973 (JPL internal document).
16. Reid, M. S. and Stelzried, C. T., "An Analysis of Noise Bursts on the 64-m Diameter Antenna at Goldstone," in *The Deep Space Network Progress Report*, Technical Report 32-1526, Vol. XIV, pp. 42-45, Jet Propulsion Laboratory, Pasadena, Calif., Apr. 15, 1973.
17. *Noise Abatement Plan for DSS-43 and DSS-63 Antenna Microwave Subsystem*, IOM 335B-73-228, Oct. 4, 1973 (JPL internal document).
18. *Suggested Plan for 64-m Antenna Noise/IMP Outdoor Abatement*, IOM 3331-73-027, Nov. 9, 1973 (JPL internal document).

**Table 1. DSS 14 configuration and modification—1973**

Time completed	Significant elements
Late January	PDS cone only; antenna modifications of 1970–72.
Late May	All feedcones; antenna welding (cones, tricone, subreflector), waveguide component maintenance and modifications.
Mid-July	PDS cone only (MXK and SMT removed); 100-kW klystron substituted for 400-kW.
Late July	PDS cone only; miscellaneous antenna modifications (minor welding, temporary removal/taping of service hardware).
Mid-August	PDS and MXK cones in place; extensive welding at apex and quad legs, dish detaped.
Late August	PDS and MXK cones; apex component shielding, more welding, new safety platform, dish retaped.
Mid-September	All feedcones in place, including S/X optics; full operating configuration.



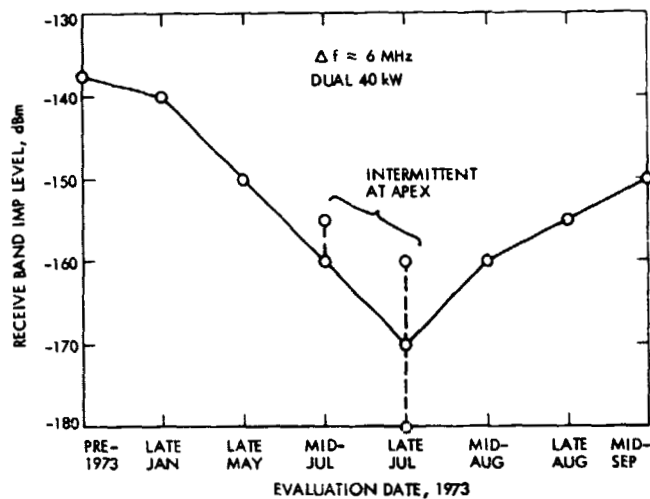


Fig. 1. DSS 14 receive band IMPs for dual 40 kW

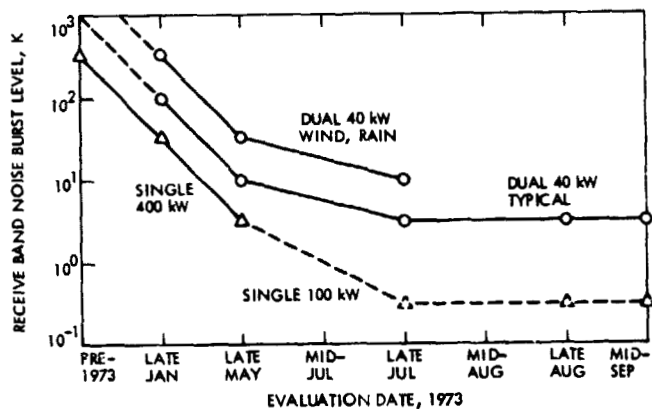


Fig. 2. DSS 14 receive band noise bursts

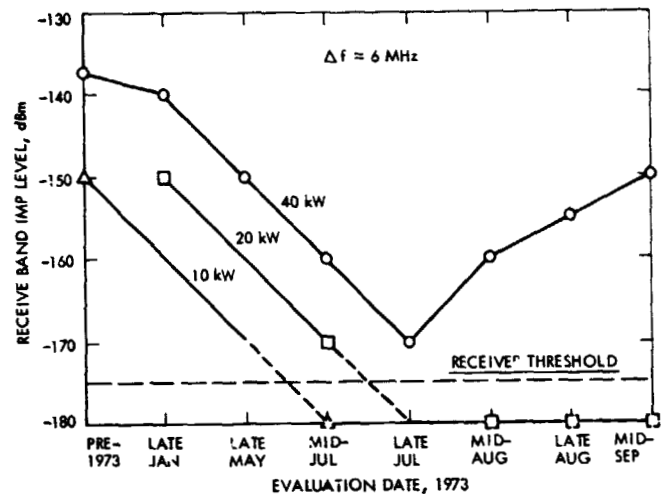


Fig. 3. DSS 14 receive band IMPs vs dual carrier power

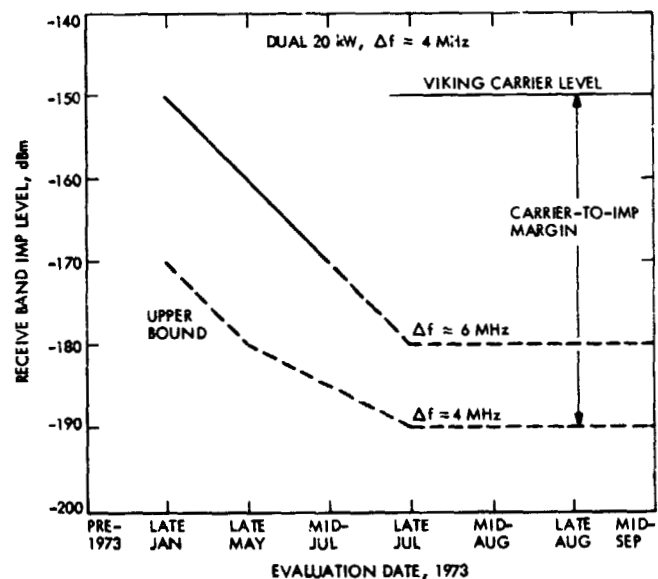


Fig. 4. DSS 14 receive band IMPs for Viking application

# Computer Program Copy-Verify and Load Check System

R. Billings  
Network Operations Office

*The Computer Program Copy-Verify and Load Check System consists of two programs, DOI-5352-SP and DOI-5379-SP. The system assures the integrity of a DSN program tape at two critical points—reproduction and loading. The Mag Tape Copy Routine DOI-5352-SP verifies the tape as it is being copied. The Mag Tape Load Check Loader Program interacts with parts of the Mag Tape Copy Routine to check the validity of a load in progress.*

## I. Introduction

Some DSN computer programs have presented a problem to the DSN Program Library because there is no direct way of reproducing their tapes. These programs are those which occupy almost all of the 16K memory locations in the XDS 920 computers; they are too large to be copied by a standard mag tape copy routine. This constraint also precludes the verification of a copied tape. The loading of these programs has also posed a problem because most of them are mission-critical real-time programs in which an unrevealed loading error could cause data loss or command malfunction. Procedures were needed to ensure that such tapes were copied accurately and loaded correctly.

The usual procedure for making mag tape copies was to incorporate a self-dump routine in the program itself; this routine dumped all of core memory as a single record on tape. The program was loaded into memory, and then a

branch was made to the self-dump routine. The routine allowed the program to be dumped as many as nine times, but there was no way of checking that the dump was correct or even whether the program was loaded accurately in the first place.

A reload routine was also incorporated in the program so that another record could be loaded in the event of a bad load or subsequent failure. The capability of reloading the program from the extra records on tape provided some insurance against bad recordings and stretching or other physical damage. However, this insurance did not prevent loss of data from program hangups and other failures, many of which were blamed on "bad loads" for want of a definite cause, although they could have stemmed from copy errors or loading errors.

From the point of view of the DSN Program Library, the procedure is unsatisfactory. The Program Library is

charged with the responsibility for the accurate duplication of mag tapes, and this procedure does not ensure accuracy. The self-dump technique provides a means of making copies of a tape, but, except for parity checking in the computer and tape units, it does not verify that the copies are 100% accurate. To ensure accurate duplication, 100% verification is considered necessary.

The self-dump routine was therefore rewritten to include a verification sequence; the new program is titled Mag Tape Copy Routine DOI-5352-SP and has been distributed to personnel engaged in programming for the Deep Space Network XDS 920 computers. The program occupies 400 locations in memory starting at location 36000. The program dumps core into mag tape as many times as requested, rewinds, and then performs a word-by-word comparison between core and the records on tape. Typewriter messages indicate successful verification or comparison errors; in the latter case, the whole procedure is restarted.

Mag Tape Copy Routine DOI-5352-SP also includes a load-check routine, which is used in conjunction with Mag Tape Load-Check Loader DOI-5379-SP to ensure a correct load. Following the load from mag tape, the program branches to the load-check routine, reads another record from tape, and compares it word by word with the record already loaded in core. Typewriter messages indicate whether or not the comparison (and, hence, the load) is successful. Together, these two programs comprise a system which ensures against copy errors and "bad loads."

## II. Program Description

Mag Tape Copy Routine DOI-5352-SP, written in XDS 920 symbol language, is essentially in two parts: a dump sequence in which a requested number of records is written on tape, and a verify sequence, in which the tape is compared word by word with core memory. The routine checks for buffer errors in the dump sequence and for comparison errors in the verify sequence. If a buffer error occurs, the tape erases backwards over the entire record, and then erases forward over half the record to get the tape quickly by any bad areas. Comparison errors are indicated by an error message; the tape rewinds to load point for another start.

No comparison is made of the area in which the copy routine is located (36000.-36377.). Since values are chang-

ing in these locations during the comparison sequence, the whole area is bypassed. Copy errors in this section would be inconsequential because tapes are ordinarily copied from a single master and not from other copies.

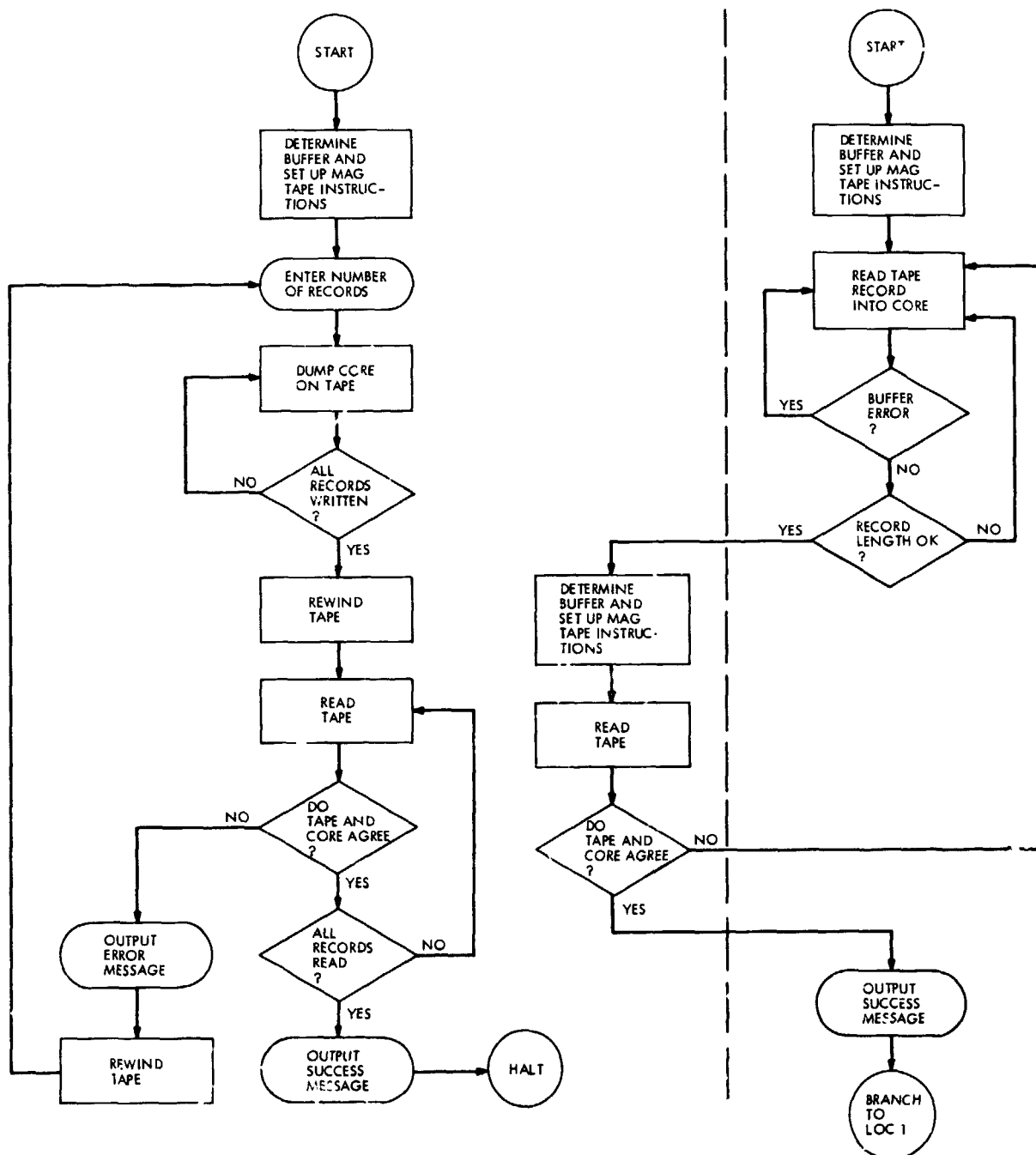
A feature of this program is that either buffer may be connected to the tape units; the program automatically determines which buffer is connected and sets up all the mag tape instructions accordingly. The buffer test is performed using the end-of-tape test as a pseudo-instruction. If the tape is not at the end of the reel, a W-buffer end-of-tape test will cause the next instruction to be executed provided the tape unit is connected to the Y-buffer, or it will cause the next instruction to be skipped if the tape unit is connected to the W-buffer.

The load-check routine is incorporated in this program and shares subroutines with the dump and verify sequences as needed. Mag Tape Load-Check Loader DOI-5379-SP branches to this routine after loading a program from mag tape. The load-check routine reads the next record from tape and compares it word by word with core memory. If the comparison is successful, a LOADCHECK OK message is typed out; if a comparison error is found, the operator is alerted with an error message and the program branches back to the loader to begin the operation again.

Some features of Mag Tape Load-Check Loader DOI-5379-SP are that it will operate with either buffer, it zeroes core memory before loading a program from mag tape, it rejects any record on tape that is shorter than normal and reads instead the next record, and it branches to location 1 (where it expects to find a branch to the beginning of the program) after loading and verifying that the proper load was achieved.

## III. Conclusion

The success obtained with this copy-verify and load-check system indicates that it is a feasible and practical way of verifying tape duplication and loading. Its use by programmers is encouraged to provide the DSN Program Library with a convenient means of verifying that tapes are copied accurately and to provide Deep Space Stations with assurance that programs are loaded correctly. The next step is to expand the system to include those tapes which are recorded with subprograms following the main records and those which are recorded in modular form.



MAG TAPE COPY ROUTINE DOI-5352-SP

MAG TAPE LOAD CHECK LOADER DOI-5379-SP

Fig. 1. Routine sharing between programs

# Network Telemetry System Performance Tests in Support of the MVM'73 Project

R. D. Key and E. T. Lobdell  
Network Operations Office

*This article presents a description of Network Telemetry System Performance Tests that were executed throughout the DSN in support of the MVM'73 project.*

## I. Introduction

System Performance Tests (SPTs) are executed throughout the DSN whenever a modification is made to the Network Telemetry System that affects its performance. This is the case when new software or hardware is added, as was required for the support of Mariner 10. The purpose of this article is to describe the effort that was undertaken in executing telemetry SPTs throughout the DSN and to present the test results. The philosophy and the objectives of the SPTs will be discussed so as to demonstrate the benefits gained by performing these tests. A description of the telemetry SPTs will be presented, along with a description of the test procedure and test software. A summary of the results and the status of the Network Telemetry System will be presented.

## II. Objectives of System Performance Testing

The development of test procedures, test software, and the execution of the telemetry SPTs are performed to accomplish certain objectives. The overall objective is to

guarantee that the Network Telemetry System can meet specified operational capabilities. These capabilities are defined in various documents; those of particular importance are given in Refs. 1 through 3. The SPT must verify that the telemetry system configurations and interface requirements are satisfied. They must also evaluate the ability of the Telemetry System to meet performance requirements.

The telemetry SPT is designed so that it can be used to locate or diagnose system problems. The problems may occur during the installation of new equipment or software, or they may be the results of system failures uncovered during DSN real time tracking operations. Some of the latter type problems have been discovered when portions of the SPT are used during countdown tests.

Use of SPTs for prepass readiness tests is another objective that requires that the SPT procedure be modular. Thus, the various classes and levels of prepass readiness tests can be accomplished by executing the appropriate sections of the procedure.

The modularity feature of the procedure enhances the capability to test modifications that may affect the capabilities of the Telemetry System. Portions of the test procedures are used to perform onsite (DSN Facility) acceptance testing of both hardware and software.

An additional objective of SPTs is to aid in the training of station personnel. The SPTs are prepared so that the configurations used are as near as possible to configurations used for real time tracking of the spacecraft. By using the test procedures, station personnel can gain experience in operating the Telemetry System and Telemetry and Command Data (TCD) software. This experience is particularly valuable when new equipment, configurations, or software have been introduced.

### III. Test Configuration

Shown in Fig. 1 is the general telemetry test configuration. Simulated data are generated in the Simulation Conversion Assembly (SCA). The simulated data called for in the tests are a 2047-bit pseudo-noise (PN) sequence; yet fixed pattern data, such as square wave data, may be used if special tests require that the data be recognized and validated by visual inspection. The SCA generates either a single channel or two channels of data, depending on the telemetry mode being tested. In the case of the single channel of data, the SCA modulates these data with a square wave subcarrier. For the two channels, the data channels are modulated with two subcarriers using the interplex scheme. The modulation indices of the subcarriers are set by using the wave analyzer at the receiver. The data on the subcarriers phase modulate a carrier generated in the test transmitter, which is interfaced to the DSN Block III receiver through ambient load and the 20-dB coupler. The test transmitter signal level is adjusted to obtain the required signal-to-noise ratio which is accurately measured at the Y-factor detector.

The Telemetry and Command Data handling software (DSN Program Library Software No. DOI-5050-OP) resides in the Telemetry and Command Processor (TCP) and in the Data Decoder Assembly (DDA), both of which are small general purpose computers. The TCD software can be configured to process data using any one of three telemetry channels. For Mariner 10 support the channels are as follows:

- (1) Channel 1 (CH1). Low-rate uncoded (LR UNC) with data rates of 8½ and 33½ bits/s. This channel interfaces the Subcarrier Demodulator Assembly (SDA) directly to the software internal bit sync loop

residing in the TCP. The TCP formats these data, records them as a digital Original Data Record (ODR), and transmits them via high-speed data (HSD).

- (2) Channel 2 (CH2). Medium-rate coded (MR C) at 490 and 2450 bits/s; LR UNC at 8½ and 33½ bits/s. The data from the SDA are synchronized and detected by the Symbol Synchronizer Assembly (SSA). The medium rate coded data are block-decoded using DDA software. These data are formatted and transmitted to the TCP where they are recorded as an ODR and transmitted via HSD. Low-rate data are accepted by the DDA from the SSA. These data are formatted and transmitted to the TCP where they are handled the same as Channel 1 data.
- (3) Channel 3 (CH3). High-rate coded (HR C) at 22.05 and 7350 kilobits/s; medium rate coded at 490 and 2450 bits/s; high-rate uncoded (HR UNC) at 117.6 kilobits/s. The high rate coded and medium rate coded data are decoded by the Block Decoder Assembly (BDA). The DDA accepts the high- or medium-rate decoded data from the BDA or high-rate uncoded data from the SSA. These data are formatted and transmitted via wide band data (WBD) lines if they are high-rate coded or via HSD lines if they are medium-rate coded. The formatted data are also recorded on the DDA 9-track high-density recorder (HDR), creating an ODR.

The transmitted data blocks (the output of the TCD) are described in detail in Ref. 4. The specifications placed on the telemetry system by these requirements are very important and must be tested.

The TCP has a 24-bit direct transfer interface with the Digital Instrumentation System (DIS). The operational telemetry software uses this interface to transfer initialization, status and calculation messages to the monitor system (Ref. 5). This interface is tested, but without the DIS monitor operational software.

The DIS is used to process the data for the test using the Telemetry and Command System Test Program (DOI-5409-SP). The data transmitted by the TCP or DDA go to the station communication center and are normally transmitted to the Mission Control and Computing Center (MCCC). To use the DIS as the processing computer, the DDA or TCP HSD/WBD lines must be patched at the station communication center to the DIS HSD/WBD lines.

#### IV. Telemetry System Test Software

The Telemetry and Command System Test Program, DOI-5409-SP, resides in the DIS computer. It contains two subprograms: a telemetry subprogram and a command subprogram, both under the control of an Executive Program. The program interfaces with the TCD string to be tested through the HSD/WBD on-site GCF equipment (station communications center), and the 24-bit monitor interface. By virtue of these interfaces, the TCD and its operational software are tested in an operational environment. That is, the telemetry system test validates data as they are transmitted externally from the TCD system.

The software receives the monitor data, and formats and prints the results selectively on the DIS I/O typewriter or line printer. Due to the greater print speed of the line printer, it is normally used during the tests. The monitor data displayed are initialization messages, status messages, and the calculation messages. These messages are validated by visual inspection for correctness and completeness in compliance with Ref. 5.

The telemetry data HSD/WBD blocks may be displayed on the line printer for visual inspection, although normal operation consists of permitting the software to output the following:

- (1) Standard block header information consisting of source, destination, data-dependent type (DDT), user-dependent type (UDT), spacecraft identification, and day of the year and the time of the block formation.
- (2) Formatted configuration and lock status with receiver AGC or signal level in dBm, and the TCD software channel in use.
- (3) The bit error rate (BER) or word error rate (WER) measured over a given period; the bit rate and data format.

In the bit error rate test, the data may be either PN or a fixed pattern. The test software synchronizes to the data and does a bit-by-bit comparison. The WER/BER accumulation may be over any chosen interval resulting in a grand total, while statistics can be displayed as interim summaries at intervals as required.

As the test is being executed, the test software will detect errors and display error messages as follows:

- (1) The  $\Delta t$  between telemetry HSD/WBD blocks are not within specified tolerances.
- (2) Excessive bit error or incorrect data type, as evidenced by the inability to achieve synchronization.

(3) Binary time and multisecond clock differences.

(4) GCF errors.

The telemetry system software is an invaluable tool, which has done much to facilitate and ease the execution of the Telemetry System Performance Tests.

#### V. Test Procedure Format

The Network Telemetry System Performance Tests for Mariner 10 were executed using Ref. 6. In this section, the format of the procedure will be presented to provide a description of the tests that are performed at the Deep Space Stations.

The overall test is divided into three main tests. Each test contains a number of subtests that are modular so that any test can be run independently. This allows the procedures to be used for prepass readiness tests, troubleshooting, and new equipment or software tests. It also allows for reduced testing when resources so demand.

The three tests are the Configuration and Interface Tests, the Telemetry Performance Tests and the Non-Real Time Capability Tests. These tests all call out a Test Preparation Section as needed. The complete test, two TCD strings, can be accomplished in 40 hours.

##### A. Configuration and Interface Tests

The Configuration and Interface Tests are performed on the three telemetry channels (CH1, CH2, and CH3). They test the telemetry operational software and hardware interfaces using all the operational configurations planned for Mariner 10 support. This test contains HSD and WBD interface tests that verify the HSD/WBD blocks. The blocks are verified by inspection of the formatted block headers, configuration and lock indicators that are formatted for ease of interpretation, and by the absence of error messages. This section contains a set of TCP-DIS monitor message verification tests that verify that the initialization, status, and calculation messages are correct as specified.

Although the AGC/dBm conversion test and the signal-to-noise ratio (SNR) calculation test are separate sections of the test procedure, they are normally run with the configuration and interface tests. The AGC/dBm conversion test verifies that software can perform a correct conversion from AGC volts to signal level in dBm. The conversion parameters are entered in the program, and accuracy of the conversion is checked to see that it is

within  $\pm 0.05$  dBm. The SNR calculation test verifies the accuracy of the software SNR estimator routine. SNRs of 15, 10, and 5 dB are set up using the Y-Factor machine. The calculation is verified to be accurate within  $\pm 0.3$  dB.

The important aspect of the configuration and interface tests is that they insure that the functional capabilities of the Telemetry System exist. (The configurations tested can be found in Fig. 3.)

### B. Telemetry Performance Test

The Telemetry Performance Tests determine the capability of the Telemetry System to meet the DSN support performance requirements. These tests are designed to evaluate telemetry performance at threshold SNRs with CH1, CH2, and CH3 configured in the Mariner support modes.

The test measures the output data Word Error Rate (WER) for coded data and the Bit Error Rate (BER) for uncoded data given an input data signal-to-noise ratio. The results are compared against predicted BER/WER, and if they are within given tolerances, the performance is considered to be acceptable. The predictions are based on available mathematical models of the Telemetry System (Refs. 7 through 10). These models are evaluated using a computer program. This program is called the Telemetry Efficiency Program, and is used primarily to generate performance parameters for the telemetry SPTs.

A strong signal test is always executed prior to a weak signal test. The strong signal test is run to detect gross errors in the HSD/WBD blocks that would invalidate the weak signal tests, which take much longer to perform. The strong signal test also confirms the set up configuration and interfaces.

The weak signal performance tests are run for all operational configurations and data rates. An accurate SNR is set using the Y-Factor machine, and the WER/BER is measured and recorded. The SNR calculation is also checked for accuracy. (The telemetry modes and performance tolerances can be obtained from Fig. 5)

During the execution of the telemetry performance tests, Original Data Records (ODRs) are created to be played back and validated in the Non-Real Time Capability Tests, with the exception of the ODR for the 117.6 kilobits/s uncoded data mode. Since the WBD lines are limited to a data rate of 28 kilobits/s, it is not possible to perform a telemetry performance test in real time. Therefore, the data are recorded, then played back at the wide-band rate, with an effective data rate of 22 kilobits/s.

(This is also normal operational procedure for supporting the 117.6 kilobits/s mode.) Performance data can then be obtained as they were for the other data modes.

### C Non-Real Time Capability Tests

The ODRs generated in the performance tests are validated in the third set of SPTs. These are the Non-Real Time Capability Tests. In the first part of these tests, the ODR playback demonstration, the digital ODRs are played back using the appropriate playback program, the 7-track playback program (DOI-504i-OP) or the 9-track playback program (P9 module of DOI-5050-OP). This demonstrates the ability to play back tapes, using both the TCD and the playback software. The HSD/WBD blocks are checked in a manner similar to the configuration and interface tests, to insure that the tapes were properly recorded.

In the second part of the Non-Real Time Capability Tests, analog tape playback demonstration analog tapes are generated at a specific SNR and then played back. The tape output SNR is obtained and compared against the set SNR. The tape output SNR must be no greater than 1 dB less than the set SNR.

Data reporting is accomplished by using four data sheets. These are presented in Figs. 2 through 5. The data sheets are:

- (1) Data Sheet 1: Test Report Log. This data sheet is used to keep a record on what tests have been performed throughout the Network (Fig. 2).
- (2) Data Sheet 2: Configuration/Interface Tests. This sheet gives a checklist of the tests performed for the Configuration and Interface Tests (Fig. 3).
- (3) Data Sheet 3: dBm Conversion and SNR Calculation Tests. Tabulates results of these tests (Fig. 4).
- (4) Data Sheet 4: Performance Tests. Tabulates results of the Performance Tests, plus results of the ODR playback (Fig. 5).

Test results are analyzed and recorded by the Telemetry System Cognizant Operations Engineer (SCOE).

## VI. MVM'73 Network Telemetry Test Status and Results

Execution of network telemetry SPTs for MVM'73 was scheduled to begin in May of this year, with a completion date of 10 August 1973. Unfortunately, these dates were not met due to the late delivery of operational software



and hardware. The tests were still being executed after the Mariner 10 launch; however, all of the Configuration and Interface Tests plus those capabilities that were required for launch had been completed prior to launch. The tests were required to be performed at the following stations:

- (1) Goldstone, California: DSS 12 and DSS 14.
- (2) Tidbinbilla, Australia: DSS 42 and DSS 43; con-joint stations.
- (3) Madrid and Ceberos, Spain: DSS 62 and DSS 63.

The tests were conducted by station personnel. In a number of cases the SPTs uncovered station problems, which, when corrected by the station personnel, required a rerun of system tests. The station personnel also made recommendations on modifications or corrections of the procedures.

Data taken during the tests were transmitted to the telemetry SCOE. The data were analyzed and saved. To evaluate the status of the Telemetry System, a Telemetry Test Status Board was created. The most recent data from each station are recorded on this Board, and are presented in Fig. 6.

The Telemetry Test Status Board presents the date that the Configuration and Interface Tests, including AGC/dBm and SNR tests, were completed. It also presents the results of the performance tests (1-1 through 7) and the date that these tests were completed. For the performance tests, the data rate, input SNR, allowable WER/SER, and allowable SNR with tolerances are presented. The Board shows which tests are not completed and due, are out of tolerance, and are not required from a particular station.

All of the Configuration and Interface Tests (including the AGC/dBm and SNR tests) were successfully completed prior to Mariner 10 launch. The Telemetry Performance Tests were not completed. Some of the tests were run, but the results were not within tolerance. These results were accepted since they were nearly within specification, and it was deemed that the station resources not be loaded by further testing except on a best efforts basis.

In some cases, data from the tests were not available. These tests were not completed due to hardware problems that were uncovered prior to or during the tests. Since the tests were run late, many problems were discovered just prior to Mariner 10 launch. The problems could not be corrected due to the Mariner configuration freeze, and then the Pioneer 10 configuration. The problems are now being corrected and the tests will be run after the termination of the Pioneer configuration freeze.

The Non-Real Time Tests were executed prior to Mariner launch with the following results:

- (1) All TCP ODRs were validated.
- (2) DDA ODRs at DSSs 14 and 63 have been validated.
- (3) Hardware problems with the DSS 43 DDA ODRs have been uncovered.
- (4) All 26-meter-antenna DSS analog tape ODRs have been validated.
- (5) Problems with the recorder track assignments of the 64-meter-antenna DSS Analog Tape ODRs have been uncovered.

Overall, the performance as demonstrated by the Telemetry SPTs, has been acceptable.

## References

1. *Deep Space Network System Requirements—Detailed Interface Design*, Document No. 820-13. Jet Propulsion Laboratory, Pasadena, Calif., Feb. 1, 1971. (JPL internal document.)
2. *Deep Space Network Support Requirements for MVM73 Project*, Document No. 615-15-Rev. A. Jet Propulsion Laboratory, Pasadena, Calif., Jan. 15, 1973. (JPL internal document.)
3. *GCF-NASCOM MVM73 Project Support Communications Capabilities, Configurations, and Operational Support Procedures—Network Operations Plan for MVM73 Project*, Document No. 615-93-01. Jet Propulsion Laboratory, Pasadena, Calif., Sept. 20, 1973. (JPL internal document.)
4. *Telemetry System Wideband and High Speed Data Interfaces*, Document No. TLM-3-5, listed in *Deep Space Network System Requirements—Detailed Interface Design*, Document No. 820-13. Jet Propulsion Laboratory, Pasadena, Calif., May 1, 1973. (JPL internal document.)
5. *DSS Monitor System Interfaces with DSS Monitor Program DOI-5046-OP*, Document No. 820-13, MON 5-4, listed in *Deep Space Network System Requirements—Detailed Interface Design*, Document No. 820-13. Jet Propulsion Laboratory, Pasadena, Calif., Feb. 28, 1973. (JPL internal document.)
6. *DSIF Standard Test Procedure Telemetry System Performance Test MVM73 Version*, Document No. 853-61; 2A-07. Jet Propulsion Laboratory, Pasadena, Calif., Dec. 28, 1973.
7. Brockman, M. H., "MMT Subcarrier Demodulator," in *The Deep Space Network*, Space Programs Summary 37-46, Vol. III, pp. 189-204. Jet Propulsion Laboratory, Pasadena, Calif., July 31, 1967.
8. Burt, R. W., "DSIF System Verification Tests," in *The Deep Space Network*, Space Programs Summary 37-51, Vol. II, pp. 132-136. Jet Propulsion Laboratory, Pasadena, Calif., May 31, 1968.
9. Edelson, R. E., *Telecommunications Systems Design Techniques Handbook*, Technical Memorandum 33-571. Jet Propulsion Laboratory, Pasadena, Calif., July 15, 1972.
10. Tausworthe, R. C., "Communications Systems Development: Efficiency of Noisy Reference Detection," in *The Deep Space Network*, Space Programs Summary 37-54, Vol. III, pp. 195-201. Jet Propulsion Laboratory, Pasadena, Calif., Dec. 31, 1968.

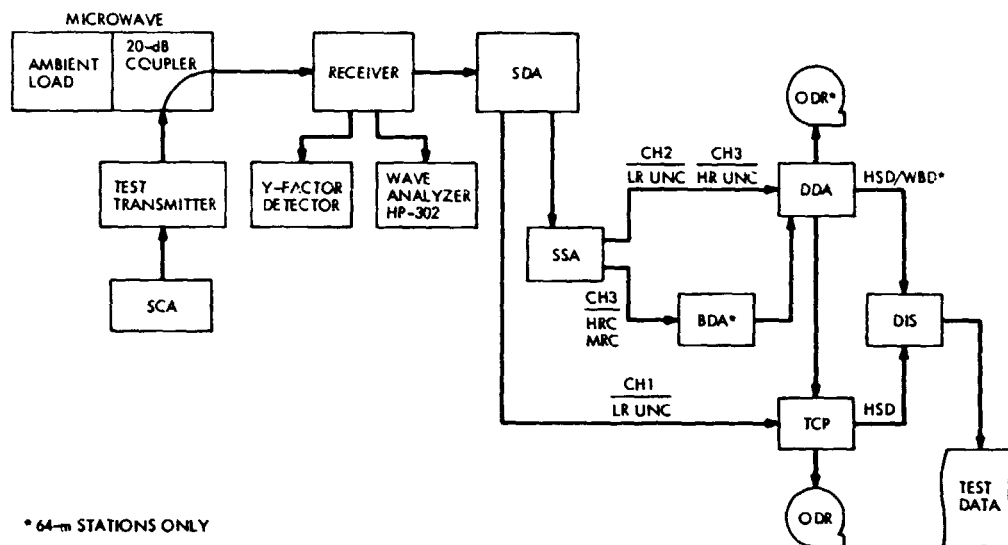


Fig. 1. Telemetry test configuration, general

DSS \_\_\_\_\_ TCD String \_\_\_\_\_  
 Test Conductor \_\_\_\_\_

Test and Paragraph No.	Dc s Conducted	Passed	Failed	Comments
Configuration/Interface —				
- Test 1 (C.2.a.)				
- Test 2 (C.2.a.)				
- Test 3 (C.2.b.)				
- Test 4 (C.2.b.)				
- Test 5 (C.2.c.)				
- Test 6 (C.2.c.)				
- Test 7 (C.2.d.)				
- Test 8 (C.2.d.)				
AGC/DBM Conversion TEST (C.3)				
SNR Calculation Test (C.4)				
Performance Test - 1 (C.5.b.)				
Performance Test - 2 (C.5.c.)				
Performance Test - 3 (C.4.d.)				
Performance Test - 4 (C.5.e.)				
Performance Test - 5 (C.5.f.)				
Performance Test - 6 (C.5.g.)				
Performance Test - 7 (C.5.a.)				
ODR Playback Demonstration (C.6.)				
Analog Tape Record/Playback (C.7)				

Fig. 2. Data Sheet 1. Test report log, MVM'73 TLM system test

DSS \_\_\_\_\_ Test Conductor \_\_\_\_\_ Date \_\_\_\_\_

26-Meter Station (Standard)												
Test No.	TCD String No.	Bit Rate bps	Configuration					Verification, Check if OK				
								Config and Lock Status		Monitor Messages		
			RCV	SDA	SSA	BDA	DDA	HSD	WBD	Init	Calc	Status
1-A	1	33.333	1	1					NA			
2-A	1	33.333	2	2					NA			
3-A	1	2450.0	1	1	1		1		NA			
4-A	1	2450.0	2	2	1		1		NA			
1-B	2	33.333	1	1					NA			
2-B	2	33.333	2	2					NA			
3-B	2	2450.0	1	1	1		1		NA			
4-B	2	2450.0	2	2	1		1		NA			
64-Meter Stations (Conjoint), *DSS 14 and CTA 21												
1-A	1	33.333	1	1					NA			
2-A	1	33.333	2	2					NA			
3-A	1	2450.0	1	1	1		1		NA			
4-A	1	2450.0	2	2	1		1		NA			
5-A	1	22.05K	1	1	1	1	1	NA				
6-A	1	22.050K	2	2	1	1	1	NA				
7-A	1	117.6K	1	1	1	1	1	NA	**			
8-A	1	117.6K	2	2	1	1	1	NA	**			
1-B	2	33.333	1	(4)2					NA			
2-B	2	33.333	2	3					NA			
3-B	2	2450.0	1	(4)2	1		1		NA			
4-B	2	2450.0	2	3	1		1		NA			
5-B	2	22.05K	1	(4)2	1	1	1	NA				
6-B	2	22.05K	2	3	1	1	1	NA				
7-B	2	117.6K	1	(4)2	1	1	1	NA	**			
8-B	2	117.6K	2	3	1	1	1	NA	**			
26-Meter Stations (Conjoint)												
1-B	2	33.333	4	5					NA			
2-B	2	33.333	3	5					NA			
3-B	2	2450.0	4	5	1		1		NA			
4-B	2	2450.0	3	5	1		1		NA			
1-C	3	33.333	3	4					NA			
2-C	3	33.333	4	5					NA			
3-C	3	2450.0	3	4	1		1		NA			
4-C	3	2450.0	4	5	1		1		NA			

\*\* Record only (DDA ODR)

Fig. 3. Data Sheet 2. Configuration/interface tests

dBM Conversion Test:

	TCP 1	TCP 2	TCP 3
AGC	_____	_____	_____
dBM	_____	_____	_____

Results should be 130 dBM  $\pm 0.5$  dB

SNR Calculation Test:

Input $ST_b/N_o$	SNR Allowable	TCP 1	TCP 2	TCP 3
15.0 dB	15.0 dB $\pm 0.3$ dB	_____	_____	_____
10.0 dB	9.3 dB $\pm 0.3$ dB	_____	_____	_____
5.0 dB	4.3 dB $\pm 0.4$ dB	_____	_____	_____

DSS \_\_\_\_\_

Test Conductor \_\_\_\_\_

Date \_\_\_\_\_

Fig. 4. Data Sheet 3. dBm conversion and SNR calculation tests

Test No.	Bit Rate and Data Type	Run Time	Input $ST_b/N_o$ dB	WER/BER Allowable	SNR Allowable dB	WER/BER Results	SNR Results dB	Start Time	Stop Time	ODR Playback Check if OK
1-1	117.6 kbps UNC	5 min	2.5	0.040 to 0.050						
1-2	2450.0 bps B.C.	30 min	*10.17	<0.00001						
2-1	22.05 kbps B.C.	5 min	2.0	0.050 to 0.070	1.4 $\pm 0.5$					
2-2	2450.0 bps B.C.	30 min	*7.7	<0.00002	7.5 $\pm 0.8$					
3-1	7350.0 bps B.C.	30 min	5.0	0.0006 to 0.002	4.8 $\pm 0.5$					
3-2	490.0 bps B.C.	30 min	*12.9	<0.00001	12.8 $\pm 0.9$					
4	2450.0 bps B.C.	30 min	3.0	0.017 to 0.035	2.0 $\pm 0.5$					
5	490.0 bps B.C.	30 min	4.0	0.013 to 0.030	2.7 $\pm 0.5$					
6	33.333 bps UNC	30 min	5.0	0.014 to 0.025	3.9 $\pm 0.5$					
7	8.333 bps UNC	2.5 h	6.0	0.020 to 0.040	3.6 $\pm 0.5$					

\* Resultant  $ST_b/N_o$  dual subcarrier interplex calculation

NOTE Reproduce this table for use as a data sheet.

DSS \_\_\_\_\_ TCD \_\_\_\_\_ (Primary)

Date \_\_\_\_\_ Test Conductor \_\_\_\_\_

Fig. 5. Data Sheet 4. Performance tests

## MVM 73 NETWORK TELEMETRY TEST STATUS

SYSTEM PERFORMANCE TESTS; 853-61; 2A-07					CTA 21						DSS 71			DSS 12			
TEST	BIT RATE (BPS) DATA TYPE	INPUT ST <sub>L</sub> /N <sub>0</sub> (DB)	WER/BER ALLOWABLE	SNR (DB) ALLOWABLE	TCP 1			TCP 2			TCP 1			TCP 1			WER
					WER/BER	SNR	DATE	WER/BER	SNR	DATE	WER/BER	SNR	DATE	WER/BER	SNR	DATE	
CONFIG INTERFACE	--	--	--	--	--	--	7-23	--	--	7-23	--	--	7-23	--	--	10-1	-
AGC/DBM	--	--	--	--	--	--	7-23	--	--	7-23	--	--	7-23	--	--	10-2	-
SNR	--	--	--	--	--	--	7-23	--	--	7-23	--	--	7-23	--	--	10-21	-
1-1	117.6 K UNC	2.5	0.040-0.050	2.0 ± 0.3	--	--	--	0.047	2.1	7-23	NR	NR	NR	--	--	--	-
1-2	2450.0 BC	10.17	<0.00001	10.0 ± 1.0	0.0	9.7	7-23	NR	NR	NR	0.0	10.5	10-17	0.0	10.43	10-15	1.2 x
2-1	22.05 BC	2.0	0.050-0.070	0.8 ± 0.3	--	--	--	0.068	0.5	7-23	NR	NR	NR	--	--	--	-
2-2	2450.0 BC	7.7	<0.00002	7.4 ± 0.8	0.0	7.3	7-23	NR	NR	NR	0.0	7.0	10-17	0.0	8.25	10-21	0.0
3-1	7350.0 BC	5.0	0.0006-0.002	4.1 ± 0.4	--	--	--	0.0012	4.0	7-23	NR	NR	NR	--	--	--	-
3-2	490.0 BC	12.9	<0.00001	12.6 ± 0.9	0.0	12.2	7-23	NR	NR	NR	0.0	13.0	10-17	0.0	13.71	10-21	0.0
4	2450.0 BC	3.0	0.017-0.035	2.0 ± 0.4	NR	NR	NR	0.022	2.4	7-23	0.024	2.0	7-23	0.0319	1.85	10-21	0.03
5	490.0 BC	4.0	0.013-0.030	2.7 ± 0.4	0.022	2.5	11-30	0.018	2.65	7-23	0.019	2.62	7-23	0.0133	2.93	10-21	0.01
6	33.333 UNC	5.0	0.014-0.025	3.9 ± 0.5	NR	NR	NR	0.0176	3.71	7-23	0.02	3.71	7-23	0.0136	4.18	10-21	0.02
7	8.333 UNC	6.0	0.020-0.040	3.6 ± 0.5	NR	NR	NR	0.03	3.62	7-23	0.03	3.37	7-23	0.027	3.5	10-21	0.02

SYSTEM PERFORMANCE TESTS; 853-61; 2A-07					DSS 43						DSS 62						
TEST	BIT RATE (BPS) DATA TYPE	INPUT ST <sub>L</sub> /N <sub>0</sub> (DB)	WER/BER ALLOWABLE	SNR (DB) ALLOWABLE	TCP 1			TCP 2			TCP 1			TCP 2			WER
					WER/BER	SNR	DATE	WER/BER	SNR	DATE	WER/BER	SNR	DATE	WER/BER	SNR	DATE	
CONFIG INTERFACE	--	--	--	--	--	--	8-3	--	--	8-3	--	--	7-23	--	--	7-23	-
AGC/DBM	--	--	--	--	--	--	8-3	--	--	8-3	--	--	7-23	--	--	7-23	-
SNR	--	--	--	--	--	--	8-3	--	--	8-3	--	--	7-23	--	--	7-23	-
1-1	117.6 K UNC	2.5	0.040-0.050	2.0 ± 0.3	X	X	X	X	X	X	--	--	--	--	--	--	0.04
1-2	2450.0 BC	10.17	0.00001	10.0 ± 1.0	X	X	X	X	X	X	0.4 x 10 <sup>-5</sup>	9.79	9-27	0.000017	10.37	9-27	1 x
2-1	22.05 K BC	2.0	0.050-0.070	0.8 ± 0.3	X	X	X	0.048	2.33	10-31	--	--	--	--	--	--	0.07
2-2	2450.0 BC	7.7	0.00002	7.4 ± 0.8	X	X	X	X	X	X	0.2 x 10 <sup>-5</sup>	7.87	9-27	0.0	7.9	9-27	9 x
3-1	7350.0 BC	5.0	0.0006-0.002	4.1 ± 0.4	X	X	X	0.0006	5.71	10-31	--	--	--	--	--	--	0.04
3-2	490.0 BC	12.9	0.00001	12.6 ± 0.9	X	X	X	X	X	X	0.0	13.2	9-27	0.0	13.27	9-27	0.0
4	2450.0 BC	3.0	0.017-0.035	2.0 ± 0.4	X	X	X	X	X	X	0.0315	1.77	9-27	0.031	1.71	9-27	0.02
5	490.0 BC	4.0	0.013-0.030	2.7 ± 0.4	X	X	X	0.02	2.32	7-20	0.019	2.75	8-2	0.018	2.75	8-2	0.04
6	33.333 UNC	5.0	0.014-0.025	3.9 ± 0.5	0.0133	3.85	7-20	0.013	4.01	7-20	0.0193	3.62	9-27	0.0169	3.83	9-27	0.0
7	8.333 UNC	6.0	0.020-0.040	3.6 ± 0.5	X	X	X	0.020	3.6	7-20	0.024	3.65	9-27	0.0217	3.66	9-27	0.02

MVM 73 NETWORK TELEMETRY TEST STATUS

		DSS 71				DSS 12						DSS 14						DSS 42					
		TCP 1			TCP 1			TCP 2			TCP 1			TCP 2			TCP 2			TCP 3			
	DATE	WER/BER	SNR	DATE	WER/BER	SNR	DATE	WER/BER	SNR	DATE	WER/BER	SNR	DATE	WER/BER	SNR	DATE	WER/BER	SNR	DATE	WER/BER	SNR	DATE	
	7-23	--	--	7-23	--	--	10-1	--	--	10-4	--	--	9-28	--	--	9-28	--	--	10-31	--	--	10-31	
	7-23	--	--	7-23	--	--	10-2	--	--	10-4	--	--	9-28	--	--	9-28	--	--	10-31	--	--	10-31	
	7-23	--	--	7-23	--	--	10-21	--	--	7-26	--	--	9-28	--	--	9-28	--	--	9-23	--	--	10-3	
	7-23	NR	NR	NR	--	--	--	--	--	0.05	2.0	9-24	X	X	X	--	--	--	--	--	--		
	NR	0.0	10.5	10-17	0.0	10.43	10-15	$1.2 \times 10^{-6}$	10.34	10-2	0.0	10.5	9-24	0.0	10.5	9-24	0.0	11.98	10-31	0.0	11.3	10-3	
	7-23	NR	NR	NR	--	--	--	--	--	0.05	1.0	9-24	0.058	1.0	9-24	--	--	--	--	--	--		
	NR	0.0	7.0	10-17	0.0	8.25	10-21	0.0	7.12	10-2	0.0	7.0	9-24	0.0	7.0	9-24	$1 \times 10^{-5}$	6.94	10-31	0.0	8.3	10-3	
	7-23	NR	NR	NR	--	--	--	--	--	0.0008	4.0	9-24	0.0007	4.3	9-24	--	--	--	--	--	--		
	NR	0.0	13.0	10-17	0.0	13.71	10-21	0.0	12.06	10-2	0.0	12.0	9-24	0.0	12.0	9-24	0.0	13.6	10-31	2.0	12.49	10-31	
	7-23	0.024	2.0	7-23	0.0319	1.85	10-21	0.0319	2.5	7-26	0.024	2.0	7-23	0.02	2.0	9-11	0.0136	2.61	10-31	0.0148	2.48	10-31	
65	7-23	0.019	2.62	7-23	0.0133	2.93	10-21	0.017	2.87	7-26	0.015	3.0	7-23	0.014	3.0	9-11	0.014	3.2	10-31	0.016	2.80	10-31	
71	7-23	0.02	3.71	7-23	0.0136	4.18	10-21	0.02	3.78	10-2	0.012	4.32	9-24	0.013	4.1	9-24	0.013	4.11	10-31	0.013	4.06	10-31	
62	7-23	0.03	3.37	7-23	0.027	3.5	10-21	0.027	3.75	10-2	0.02	3.9	9-28	0.02	3.6	9-24	0.0127	3.77	10-31	0.024	3.23	10-31	

		DSS 62						DSS 63						COMMENTS
		TCP 1			TCP 2			TCP 1			TCP 2			
SR	DATE	WER/BER	SNR	DATE	WER/BER	SNR	DATE	WER/BER	SNR	DATE	WER/BER	SNR	DATE	
--	8-3	--	--	7-23	--	--	7-23	--	--	9-7	--	--	8-10	X = NOT COMPLETED AND DUE <input type="checkbox"/> = OUT OF TOLERANCE NR = NOT REQUIRED
--	8-3	--	--	7-23	--	--	7-23	--	--	9-7	--	--	8-10	
--	8-3	--	--	7-23	--	--	7-23	--	--	9-7	--	--	8-10	
X	X	--	--	--	--	--	--	0.04	2.0	10-4	0.0425	2.0	10-4	
X	X	$0.4 \times 10^{-5}$	9.79	9-27	0.000017	10.37	9-27	$1 \times 10^{-6}$	8.9	9-7	$4 \times 10^{-6}$	8.93	9-7	
.33	10-31	--	--	--	--	--	--	0.0709	0.795	9-7	0.0667	0.744	9-7	
X	X	$0.2 \times 10^{-5}$	7.87	9-27	0.0	7.9	9-27	$9 \times 10^{-6}$	6.59	9-7	$1.4 \times 10^{-5}$	6.59	9-7	
.71	10-31	--	--	--	--	--	--	0.0015	4.05	9-7	0.00087	4.36	9-7	
X	X	0.0	13.2	9-27	0.0	13.27	9-27	0.0	12.65	9-7	0.0	12.0	9-7	
X	X	0.0315	1.77	9-27	0.031	1.71	9-27	0.024	2.04	9-7	0.022	2.15	9-7	
.32	7-20	0.019	2.75	8-2	0.018	2.75	8-2	0.021	2.60	9-7	0.013	2.92	9-7	
.01	7-20	0.0193	3.62	9-27	0.0169	3.83	9-27	0.0118	4.36	10-4	0.0119	4.2	10-4	
.6	7-20	0.024	3.65	9-27	0.0217	3.66	9-27	0.0236	3.98	10-4	0.0186	4.09	10-4	

Fig. 6. MVM'73 network telemetry status





# Analysis of Staffing and Training Policies for a DSN Tracking Station

A. Bahadur and P. Gottlieb  
Systems Analysis Section

*This article presents a method for analyzing the effects of training and staffing policies, and for selecting optimum policies which minimize the expenditures for training and salaries while maximizing the performance of the tracking station. Two models have been developed which represent increasing levels of sophistication. The first characterizes steady-state behavior under the optimization of training, average capability, and crew size. The second, which is the dynamic model, optimizes the operating policy over a sequence of time segments. Each segment is characterized by a performance requirement (dependent on the phase of the mission), turnover, and training allocation with a corresponding change in average capability. With inputs such as required minimum station performance, training availability, current crew capability, and expected turnover, the output of the model will be the change in average crew capability, the percentage of time allocated for training, and the corresponding minimum cash expenditure for salaries and training.*

## I. Introduction

This article presents a methodology for analyzing the staffing and training requirements for operating a DSN tracking station. This analysis is part of a study made to develop tools to assist the management of the Deep Space Network in the planning and operation of the tracking stations.

In order to meet tracking commitments, the management of the tracking stations allocates personnel and financial resources among operations, maintenance, and training. Training is not only for new personnel and operators of new equipment, but also for upgrading the skills of veteran personnel. This article discusses the methods

developed to assess the changing demands in these areas and to formulate an operating and training policy to satisfy requirements in a cost-effective manner.

Work is continuing, especially in the area of training effectiveness, to represent more characteristics of the staffing and training policy with our model, and to generate optimal training and staffing policies of practical value, using DSS 12 as the main example. The specific accomplishments expected in the near future from these efforts are listed in Section IX.

We begin with a discussion of the general features of the tracking station represented by our model.

## II. Characteristics of the Model

- (1) *Optimization of performance.* The performance of the tracking station in carrying out the different tasks may be measured by certain selected parameters. These parameters are treated as an output of the system, e.g., system availability, data recovery, number of data outages, etc. A maximization (or minimization) of one or more parameters provides the basis for the optimal operating policy.
- (2) *Relationship between performance (output) and capability (skills available).* There exists a relationship between the capability of the men and the quality of the station performance, which in turn is explicitly related to the parameter being optimized. These relationships between capability and performance are ultimately expressed in quantitative terms.
- (3) *Training to increase capability.* Training methods, which may be of varying effectiveness, are available to increase the capability of the men to perform their tasks. This may be either through increased proficiency in familiar subsystems or the development of proficiency in different or new subsystems.
- (4) *Constraints.* There are constraints on the system, which are parameterized and which may vary with time. Typical constraints are the type of training methods available, the amount of time and manpower available for training, minimum performance requirements, and the number of crews required.
- (5) *Costs associated with maintaining and improving performance.* These costs include operating expenses such as salaries, and some forms of capital investment such as training of new technicians.

These five features provide the basic structure and interrelationships for constructing the model. Within this basic framework, the model attempts to determine the "operating policy" which optimizes a given parameter while the tracking station is under a specified set of constraints.

## III. The External Environment of the Tracking Station

The block diagram shown in Fig. 1 illustrates the relationships between the tracking station and its environment. The rectangular area within the dashed line represents the tracking station. The area outside the rectangle is the external environment of the tracking station. The significant relationships between the tracking station and areas in its external environment are identified.

Hiring is done to either add to, or replace, the people working at the station. The "world" represents the available manpower pool, and includes former employees.

The tracking station (the operating system) transforms the inputs into a tangible, measurable quantity. This is the output or performance of the system.

Two methods of training are considered, formal training and on-the-job training. The employees at the tracking station have the same general background, since they satisfy certain basic selection and hiring criteria. Thus, it is assumed in this model that the different training methods are equally effective for all employees. Further work is necessary to delineate the difference in the effectiveness of training by method, background of the individual, and the length of his employment at the tracking station.

## IV. The Internal Environment of the Tracking Station

The people at the station may be divided into two categories:

- (1) *Administrative personnel.* This category includes the station managers, secretaries, schedulers, etc., who perform the administrative tasks at the station.
- (2) *Maintenance and operations personnel.* These include the operators and technicians who maintain and operate the station equipment.

Henceforth, for convenience, any reference to an individual at the station will imply an individual from category (2).

Station personnel, both new employees and veteran personnel, receive training to increase their operations and maintenance skills in various subsystems. As mentioned previously, two methods of training are considered: formal training and on-the-job training.

Formal training, as the name suggests, consists of classroom-type multimedia instruction. A group of trainees is taught a specific skill by a qualified instructor. Under the present Deep Space Network configuration, the Training Center develops, with the assistance of the Technical Staff, the instruction material and provides the instructors. During the time that a trainee is undergoing formal training, he cannot participate in station operations. Thus, the trainee performs no "useful work" during formal training, and all of his time is devoted to training.

On-the-job training takes place within the station. A trainee working with an already trained man acquires the necessary skills through observation and practice. Experience suggests that half the combined time of trainee and trainer results in useful work. The other half is devoted to learning, and consequently the process of on-the-job training is not as efficient timewise as formal training.

To express this distinction, we define the effectiveness of a training method to be the ratio of the time required to acquire the skill with the given method compared to a "standard" training method. For convenience, we take the more efficient formal training to be the standard. Experience suggests that trainees' time spent in on-the-job training is only 40% as effective as formal training (Ref. 1).

The operations and maintenance skills in different subsystems acquired by an individual through the process of training may be translated into a measure called the "capability" of the individual. The division of the tracking station into subsystems may be along hardware lines or along functional lines as is presently the case, with the number of subsystems ranging from 14 to 36. Henceforth, the use of the word capability will be restricted to the above definition.

The capability of an individual is measured in terms of the number of subsystems that he can operate and/or maintain. This measure is weighted by the relative difficulty factor of each subsystem, in the following manner (Ref. 2). The number of days of formal training required to train a man to operate and maintain a subsystem is determined. The capability of an individual is then determined by the subsystems that he can operate and maintain in terms of formal training days. If an individual has partial proficiency in a subsystem, the corresponding percentage of the total for that subsystem is added to his capability.

Between August 1971 and June 1972, DSS 12 was divided into 14 hardware subsystems. The average training time in a subsystem for operations and maintenance was 22 days ( $\sigma = 15.6$ ) and 70 days ( $\sigma = 42$ ), respectively. During this time period, the average individual capability varied between 191 and 241 days. Let

$K_i$  = capability of the  $i$ th individual (formal training days)

$K$  = average capability of the individuals in the station (formal training days)

$N$  = number of men in the station

then

$$K = \sum_{i=1}^N \frac{K_i}{N} \quad (1)$$

For every "pass" (the continuous tracking period of a given spacecraft), the total amount of data available for collection can be determined from the spacecraft tracking and testing schedule. This total represents the maximum output of the system.

We define the data acquisition efficiency  $\eta$  = (actual data gathered / available data) for an average view period. The two factors which have the greatest influence on data acquisition efficiency (Ref. 3) are

- (1) Capability of the station personnel
- (2) Man hours spent in actual operations and maintenance (as opposed to training)

The men at the station are divided into several crews (1 to 4), depending on the number of shifts that the station operates. If the men are divided among the crews so that the total capability of the men in each crew, called crew capability, is the same for all crews, then

$$\eta = f(\text{crew capability, percentage of time spent in operations})$$

where

$$\text{crew capability} = \frac{NK}{M}$$

$$M = \text{number of crews}$$

and

$$1 \leq M \leq 4$$

Let

$t_1$  = fractional time spent in operations by the average individual

$t_2$  = fractional time spent in formal training by the average individual

$t_3$  = fractional time spent in on-the-job training by the average individual

Clearly,

$$t_1 + t_2 + t_3 = 1 \quad (2)$$

and

$$\eta = f\left(\frac{NK}{M}, t_1\right)$$

The data collected on station operations suggest an exponential relationship between capability and performance. This relationship exhibits the characteristic "knee" (Refs. 4, 5, 6) of learning curves, and a saturation effect:

$$\eta = 1 - \exp\left(-\alpha_1 F_p \frac{NK}{M}\right) \quad (3)$$

where

$\alpha_1$  = exponential index

$F_p$  = performance factor

We choose a value of  $\alpha_1 = 0.0034$  on the basis of a best fit of the historical data.

To obtain a reasonable functional form for  $F_p(t_1)$ , we select the following empirical relationship based on historical station data:

$$F_p = \begin{cases} \sqrt{t_1} & 0.685 \leq t_1 \leq 1.0 \\ 1.2t_1 & 0 \leq t_1 \leq 0.685 \end{cases} \quad (4)$$

This relationship is a reflection of the fact that the station can devote up to 20% of its man hours to training before operations begin to be seriously affected. The effect of  $t_1$ , for  $\alpha_1 = -0.0034$ , on data acquisition efficiency  $\eta$  is shown in Fig. 2. Recall that  $(1 - t_1)$  is the fractional time spent in training.

## V. Identification of Costs

Our model is based on the cost equation

$$CVL = CH + CA + CF + CS + CT + CP \quad (5)$$

where

$CVL$  = overall cost

$CH$  = hiring cost

$CA$  = cost of attrition

$CF$  = cost of overhead personnel

$CS$  = cost of salaries of operations personnel

$CT$  = cost of training

$CP$  = cost of lost performance

Salaries:

$CF$  = average salary of administrative personnel times number of administrative personnel;

$$CF = 12 \times 3 = 36 \text{ (\$/year)} \quad (6)$$

$$CS = CK \times N \quad (7)$$

where

$CK$  = average salary of an individual of capability  $K$ ;

$$CK = \frac{8 + K}{50} \text{ (\$/year)} \quad (8)$$

This linear relationship between capability and salary fits some recent, randomly selected data fairly well (Ref. 7).

Hiring and attrition:

$CH$  = cost of hiring one man (= \$500) times number of men hired

$$CH = 0.5 \times \text{number of men hired (\$/year)}$$

$CA$  = cost of termination processing of one man (= \$50) times number of men that leave

$$CA = 0.05 \times \text{number of men that leave (\$/year)}$$

Training costs:

$CT$  = cost of training = cost of formal training + cost of on-the-job training

$$CT = N \times CS (\alpha_2 \times t_2 + t_3) \quad (9)$$

$\alpha_2$  = formal training cost factor = 2 (being twice as expensive as on-the-job training on a per-trainee-hour basis, since extra costs such as lecture preparation and instructor training must be included). This factor is determined by analysis of historical cost and operating data from the Technical Staff and Training Center.

Performance is a benefit, but one way of quantifying it is in terms of lost performance. Lost performance can be considered either in terms of inefficiency or lost data. For one optimization policy, we need to parameterize lost data by assigning a value to the available data. This value of the available data is dependent on the mission, its phase, and competing priorities (Refs. 3, 8). The cost of lost per-

formance, expressed in \$K/year, may be expressed by the following linear relationship:

$$CP = (1 - \eta) \times \text{value of available data (\$K/year)} \quad (10)$$

Since the optimal policies will be in the range of  $\eta$  greater than 80%, the assumption of linearity in the range 80% to 100% will be adequate. If one were interested in values of 50% and lower, nonlinear factors, which describe the penalty of poor performance, might have to be introduced.

## VI. Optimization Technique

Figure 3 is a detailed representation of the station operating system shown in Fig. 1. Optimization occurs at two points (Refs. 9, 10):

- (1) Distribution of time between operating and training
- (2) Distribution of training time between formal and on-the-job training

The allocation of time between the two methods of training and operating can be optimized according to one of the following policies:

- (1) Minimization of the cash expenditure ( $CE$ ), subject to a required minimum data recovery efficiency constraint, where cash expenditure is

$$CE = CH + CA + CF + CS + CT \text{ expressed in \$K/year}$$

- (2) Minimization of the overall cost ( $CVL$ ), which includes the value of lost data:

$$CVL = CE + CF$$

Turnover is treated as an independent parameter (external constraint), either as an absolute number or as a percentage of the total number of men in the station.

For convenience of illustration, we have considered the average capability of those that leave to be the same as the station average, and that of people who are hired to be zero. This assumption is in accord with past experience, but the model does have the flexibility to specify other values of capability for the departing individuals and the new hires. This implies that whenever there is turnover, new hires will have to be given training to maintain the average station capability.

## VII. The Steady-State Model

For this model, we assume that the station requirements and crew capabilities do not change with time. The dynamic model will address the problem of changing capability due to turnover and training.

The steady-state requirement implies that the number of people hired equals the number that leave and that the new hires are brought up to the average capability through the process of training. For convenience of illustration, we make the following additional assumptions:

- (1) The time period is 1 year, consisting of 250 working days for each man.
- (2) There are three crews ( $M = 3$ ).

The following examples illustrate the typical results which can be obtained with the steady state model.

### A. Minimum Cash Expenditure to Obtain a Required Efficiency

In this example, the operating policy is obtained as a result of minimizing the cash expenditure  $CE$ . For a 20% annual turnover, Fig. 3 shows the cash expenditure required to provide a minimum data recovery efficiency. This relationship is provided for a family of values of station size ( $N$ ) and average individual capability ( $K$ ).

Station size varies from 15 to 36, which corresponds to crew sizes of 5 to 12. A crew size of 5 is typical of the current staffing at DSS 12 under the operating philosophy of a central console and "operations engineers." (Refs. 11, 12, 13). A crew size of 10-12 was typical at DSS 12 in 1970 and is also typical of the larger stations, like DSS 14.

Average individual capability is considered from 50 to 200 days. Though some individuals have capability greater than 200 days, the average is unlikely to exceed that value. Thus, 200 days is used as the upper bound. In each figure, the comparisons of  $N$  and  $K$  which provide the maximum information are illustrated.

In Figure 4, values of  $K$  above 95 are bunched closely together, which indicates that increasing capability does not increase efficiency for constant  $N$ . The reason is obvious. At high turnover and high capability, most of the time is spent in training to regain the lost capability rather than in operations. Curves for  $N = 15$  to 18 terminate at the point corresponding to  $K = 200$ .

The policy of specifying a minimum required data recovery efficiency is close to the present spacecraft project procedure. It is interesting, however, to perform a more global optimization by trading off the cost of maintaining a station of high performance capability against the cost of lost data resulting from poor performance. The following examples illustrate this second optimization policy.

### B. Effect of Crew Size on Minimum Overall Cost

Turnover of three men/year ( $v$ ) and a data value of \$1200K/year (\$) are considered in Fig. 5, where the minimum overall cost is plotted against average individual capability.

For average capability less than 150 days, a station size of 21 is optimal. Between 155 and 175, a station size of 18 men is optimal. For average capability greater than 175, the optimal station size is 15 men. In general, with increasing capability a smaller station size is indicated.

The data value of \$ = 1200, 1.2 million dollars per year, is somewhere between what one might choose for the cruise and extended mission phases of a recent Mariner-type spacecraft (Ref. 3).

### C. Effect of Data Value on Crew Size

With turnover of three men/year, the station sizes which minimize the overall cost are plotted as a function of average individual capability, in Fig. 6. These curves help to quantify the intuitively obvious relationship (basically inverse) between station size and average capability. The curve for \$ = 600 turns around at  $K \approx 40$  days, indicating that it is not desirable to operate the station with average capability less than 40 days.

In Fig. 6, for an average individual capability of 120 days and a data value of \$600K/year, a station size of 16 men is indicated. When the data value is increased to \$1800K/year, the optimal station size increases to 25 men for the same *average individual capability*.

### D. Minimum Cost and Optimal Capability Contours

Figures 7 and 8 show contours of minimum overall cost and optimal capability, respectively. The turnover is 30% of station size ( $N$ ) instead of an absolute number, as in the previous case.

Figures 7 and 8 may be used in conjunction to determine the station's "operating point."

For a particular data value, either the station size or average individual capability must be selected as the starting point. Since there are greater constraints on station size than average individual capability, it is suggested that data value and station size be used as the starting point. Figure 7 then gives the minimum overall cost, and Fig. 8 provides the optimal average individual capability. If the present average individual capability is lower than the optimal, training will be required to achieve the optimal level. It must be remembered that these operating points are dependent on the assumed annual turnover, and in Figs. 7 and 8 it is 30%.

If data value is chosen at \$2M/year and a station size of 27, the minimum overall cost, from Fig. 7, is \$480K/year and the optimal average individual capability, from Fig. 8, is 128 days.

In all of the above exercises, the optimal data acquisition efficiency and training policy are determined by the model as a result of the optimization.

So far, we have seen how a wide range of information about station operation may be obtained by using the steady-state model. However, the use of the steady-state model imposes two restrictions:

- (1) There is no net change in station capability.
- (2) An averaged value is used for available data.

The dynamic model, which is an extension of the steady-state model, overcomes both of these difficulties.

## VIII. The Dynamic Model

The dynamic model exhibits the effects that changing data values, average capability, and turnover have on operating policy. The total time span is divided into a sequence of segments, with each segment, or stage, characterized by

- (1) Individual terminations with immediate replacement
- (2) Average individual capability at start of the time segment
- (3) Average individual capability at the end of the time segment, which is dependent on the turnover and training policy during the time segment
- (4) Available data value (used with the policy minimizing overall cost  $CVL$ )

Station size  $N$  is constant through all segments.

The other inputs are

$\tau$  = duration of each stage

$T$  = number of stages considered

The steady-state model, considered in the preceding section, is actually a particular case of the dynamic model with  $\tau = 1$  year and  $T = 1$ , and no change in capability.

The dynamic model provides an operating policy, resulting from optimizations based on an anticipated demand (data value profile or required minimum efficiency) under specified constraints. The operating policy, and more specifically, the training policy, is a reflection of the overall long-term needs of the station rather than the effect of one stage alone. This is the essential difference from the steady-state model. For example, an extremely high data value (or required minimum efficiency) in stage 6 may influence training policies through stages 3 to 5, as in training in preparation for a launch. Let

$\eta_t$  = data acquisition efficiency in stage  $t$

$CVL_t$  = overall cost in stage  $t$

$CVLT = \sum CVL_t$  = sum of the overall cost in each stage

$CE_t$  = cash expenditure in stage  $t$

$CET = \sum CE_t$  = sum of the cash expenditure in each stage

Three different versions of the dynamic model are used to deal with different optimization requirements and constraints:

#### *Dynamic Model 1*

Optimization: Minimize  $CVLT$

Constraints: Training availability in each stage

#### *Dynamic Model 2*

Optimization: Minimize  $CVLT$

Constraints: Training availability in each stage  
Minimum required efficiency in specified stages

#### *Dynamic Model 3*

Optimization: Minimize  $CET$

Constraints: Training availability in each stage  
Minimum required efficiency in each stage

The minimization is based on a dynamic programming technique (Refs. 14, 15), proceeding in the forward direction. The dynamic program has  $T$  stages, which are the

ends of the time segments. The state variable is the average individual capability. The boundary condition, or starting point, is the initial average individual capability at the station  $K_0$ .

Starting from  $K_0$ , there is a maximum and minimum average capability that can be achieved in any stage. This corresponds to 100% formal training and no training, respectively, and is an inherent constraint on the average individual capability.

Sample results from Dynamic Model 1 and Dynamic Model 2 are presented to illustrate the workings of the models.

Sample results from Dynamic Model 1 are illustrated in Figs. 9 and 10. A time span of 1 year is considered, divided into four stages, each of 3 months' duration.

Station size  $N$  is 30 men, and there are no constraints on training. There is no turnover during the entire time span.

In this example, the data value increases to \$2M/year in the fourth stage. Starting from an initial value of 20 days, the average individual capability levels off at 90 days. The bulk of the training is done during the first stage, when the data value is lowest, with no training in the fourth stage.

The data acquisition efficiency obtained as a result of minimizing the total overall cost  $CVLT$  is plotted in Fig. 10. The overall cost and cash expenditure per stage are also shown. The total cash expenditure  $\approx$  \$250K.

Sample results from Dynamic Model 2 are shown in Figs. 11 and 12. Station size  $N$  is 27 men, and there are no constraints on the quantity or type of training in any stage. A time span of 2 years is considered, divided into eight segments of 3 months each.

The data value profile is a sawtooth type having a value \$2000K/year in stages 2, 4, 6, and 8 and \$0K/year in the other four stages. A sawtooth data value profile is selected, since it is typical of missions. Missions are characterized by periods of high tracking requirements (launch, orbit insertion), separated by less demanding phases, such as the cruise phase.

The initial average capability  $K_0$  is 20 days.

There is a minimum efficiency constraint in stages 6 and 8. The efficiency in both of these stages must exceed 8%, corresponding typically to launch or encounter phases.

The turnover profile was generated by sampling from a Poisson distribution. The turnover through stages 1 to 8 is 3, 5, 7, 7, 2, 1, 5, 2 men, respectively. This is 81% and 37% turnover for the 2 years, respectively.

It is desired to find the operating policy to minimize the total overall cost *CVL* under the given constraints and input conditions.

Maximum capability increases to 200 by the end of stage 5 and levels off, since, in practice, individuals seldom exceed this by much.

Minimum capability decreases gradually (due to turnover) to a level of 15 and then jumps to 160 in the sixth stage. This is the effect of a minimum efficiency constraint of 99% in stage 6. A capability of less than 160 would result in the minimum efficiency constraint being violated.

The optimal capability increases, through training, to reach 160 days at the start of the sixth stage. Training follows a sawtooth pattern which is a complement of the data value profile.

In Fig. 12, the actual efficiency in stages 2 and 4 is influenced by the data value in those stages. However, in stages 6 and 8, the minimum efficiency constraint is clearly the dominating influence. The actual efficiency, in general, has a profile similar to the data value, a conclusion which is not unexpected.

The overall cost and cash expenditure through the stages are also shown in Fig. 12. The cash expenditure in

stages 1, 3 and 5 is high because of the training costs (100% training in each stage). The cash expenditure averages to \$450K/year.

Thus, the dynamic model provides an estimate of the demands that are placed upon the station, in terms of training and cash expenditure, to assist in formulating an operating policy which will meet future commitments.

## IX. Further Efforts

We are presently in the process of applying this analysis to the recent developments at DSS 12, and expect to report on the following specific items:

- (1) Statistical relationship between salary and capability (based on the new subsystem breakdown which became effective in July 1973)
- (2) Analysis of the capability lost during the actual attrition process
- (3) Analysis of the relationship between the qualification and certification program at DSS 12 and our method of measuring capability
- (4) Measures of past station performance which can be related to crew capability

We are also developing a distributed capability model which will be able to optimize the allocation of individuals at the station to crews and training programs. A preliminary report of some of this work has been given in Refs. 1 and 3.

## References

1. Bahadur, A., and Gottlieb, P., *Final Report, Maintenance and Operations Study of the DSIF*, Document 890-37, Sept. 1973 (JPL internal document).
2. Eyres, R., and Howe, J., *Building a Hardware Maintenance Team*, Datamation, Nov. 1972.
3. Bahadur, A., and Gottlieb, P., *Interim Report of Maintenance and Operations Study of DSIF*, Document 890-19 Rev. A, Jan. 1972 (JPL internal document).
4. Berelson, B., and Stebbins, R., *Human Behavior*, Harcourt, Brace and World, Inc., 1964, pp. 157-165.
5. Ghiselli, E. E., and Brown, C. W., *Personnel and Industrial Psychology*, 2nd Edition, McGraw-Hill Book Co., 1955, pp. 78-81, 258-267.

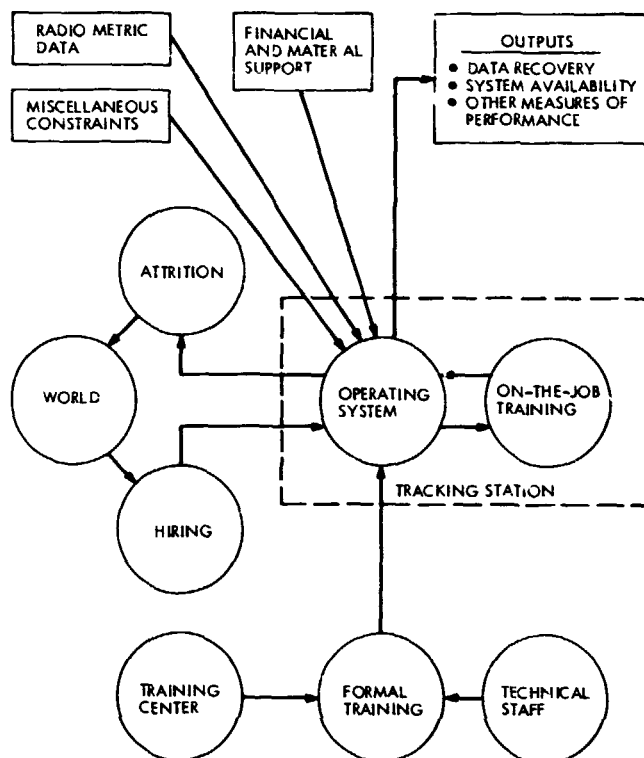


## References (contd)

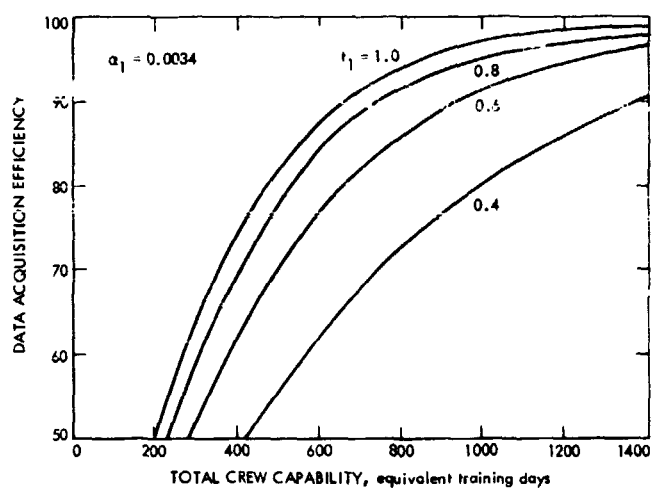
6. Deese, J., *The Psychology of Learning*, 2nd Edition, McGraw-Hill Book Co., 1958, pp. 181-199.
7. Bahadur, A., *Analysis of the Relationship Between Salary and Selected Parameters*, IOM 393.2-248, Oct. 1972 (JPL internal document).
8. Bahadur, A., Gottlieb, P., Hagen, P., and Meares, D., *Interim Report of Maintenance and Operations Systems Study*, IOM 393.2-98, June 30, 1971 (JPL internal document).
9. Klir, G. J., *An Approach to General Systems Theory*, Van Nostrand Reinhold Company, 1969.
10. Hillier, F. S., and Lieberman, G. J., *Introduction to Operations Research*, Holden-Day, Inc., 1967.
11. Younger, H., *Training of Operations Systems Engineers*, IOM 4223D-73-010, Feb. 27, 1973 (JPL internal document).
12. Bell, W., *Preliminary Plan for Training Operation System Engineers*, IOM 12-73-252, March 5, 1973 (JPL internal document).
13. Patterson, L., Burford, A., and Bearden, P., *Network Operations Performance Analysis Task SMC-75 Final Report*, 422G-5A2, July 30, 1973 (JPL internal document).
14. Kaufmann, A., *Dynamic Programming and Finite Games*, Academic Press, 1967.
15. Bellman, R. E., and Dreyfus, S., *Applied Dynamic Programming*, Princeton University Press, 1962.

Table 1. Definition of Symbols

Symbol	Definition
$\alpha_1$	Exponential index
$\alpha_2$	Formal training cost factor
$\eta$	Data acquisition efficiency, %
$\eta_t$	Data acquisition efficiency in stage $t$
$\nu$	Number of men leaving/year, men/year
$\tau$	Duration of each stage, months
$\$$	Value of available data, \$K/year
$CA$	Cost of attrition, \$K
$CE$	Cash expenditure, \$K
$CE_t$	Cash expenditure in stage $t$ , \$K
$CET$	Sum of cash expenditure in each stage, \$K
$CF$	Cost of overhead personnel, \$K
$CH$	Hiring cost
$CK$	Salary of an individual, \$K
$CP$	Cost of lost performance, \$K
$CS$	Cost of salaries of operations personnel, \$K
$CT$	Cost of training
$CVL$	Overall cost
$CVL_t$	Overall cost in stage $t$ , \$K
$CVLT$	Sum of overall cost in each stage, \$K
$F_p$	Performance factor
$K$	Average capability of individuals in the station, days
$K_0$	Initial average individual capability
$M$	Number of crews
$N$	Number of men in the station
$P$	Number of states in dynamic program
$T$	Number of stages considered
$t_1$	Fractional time spent in operating
$t_2$	Fractional time spent in formal training
$t_3$	Fractional time spent in on-the-job training



**Fig. 1. The tracking station and its environment**



**Fig. 2. Effect of training on data acquisition efficiency**

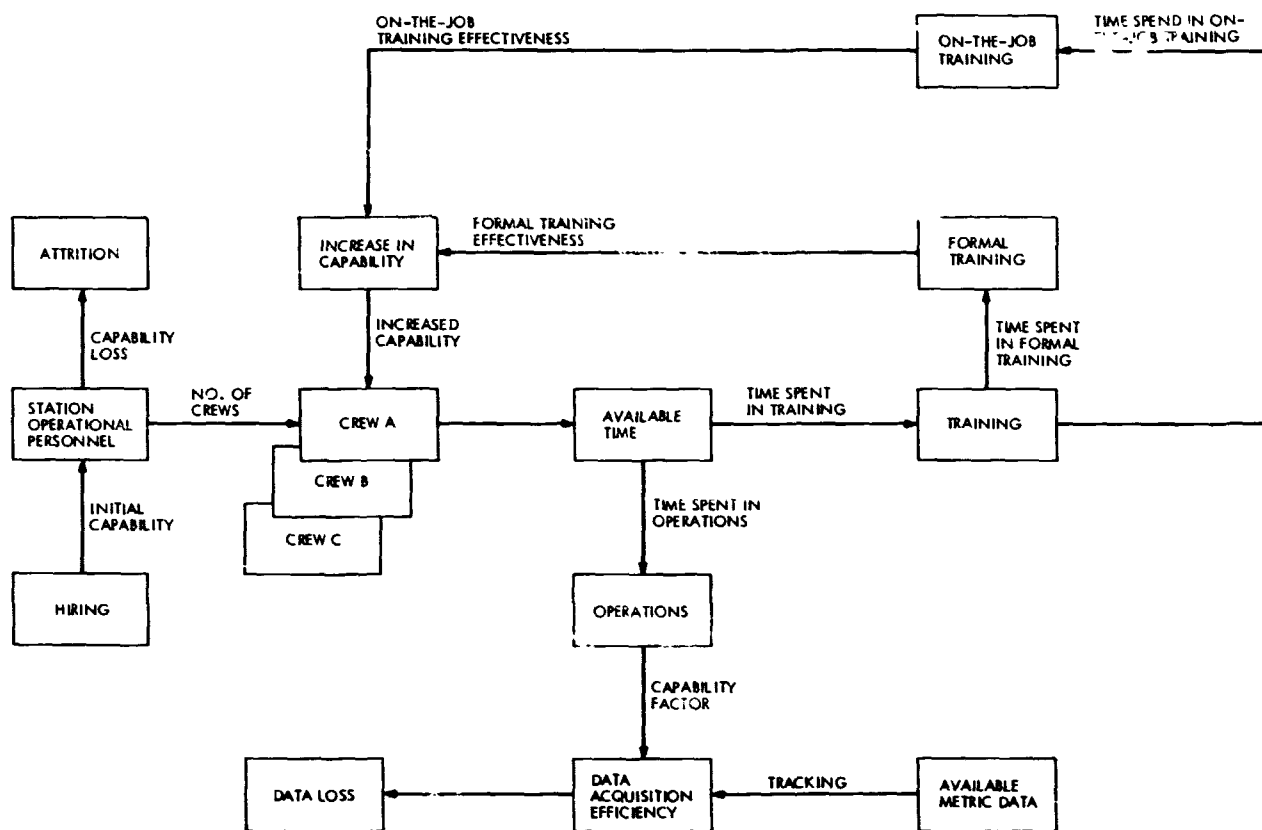


Fig. 3. Station dynamics

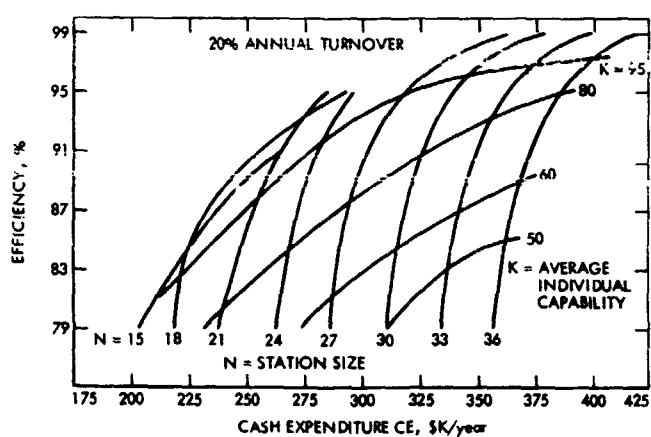


Fig. 4. Capital expenditure for data acquisition efficiency

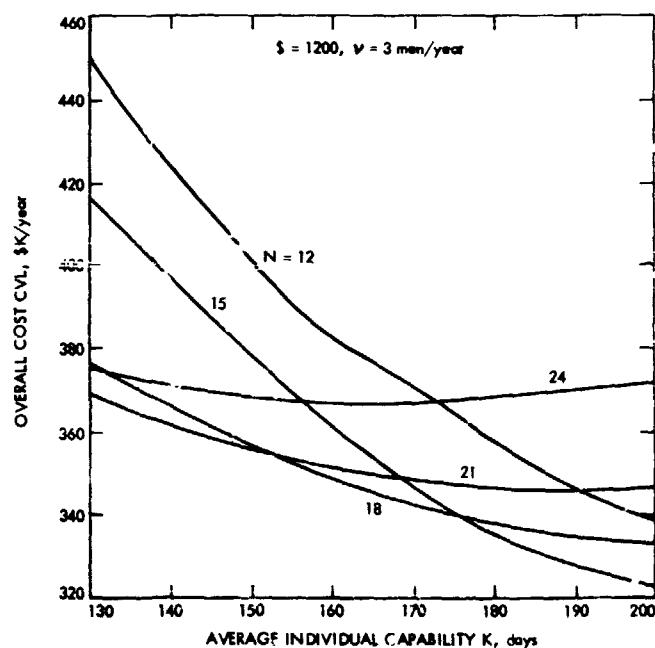


Fig. 5. Effect of crew size on overall cost

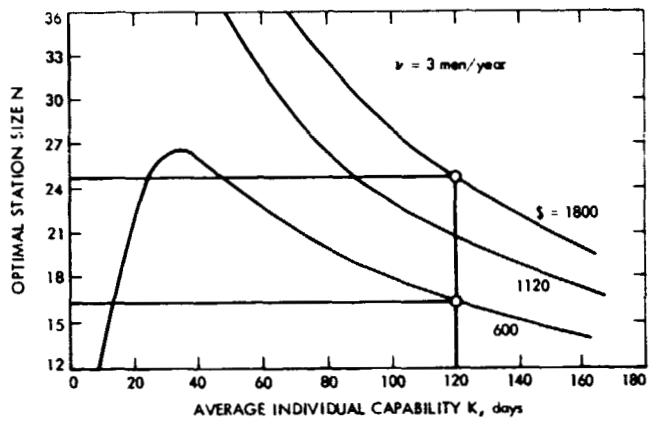


Fig. 6. Effect of data value on crew size

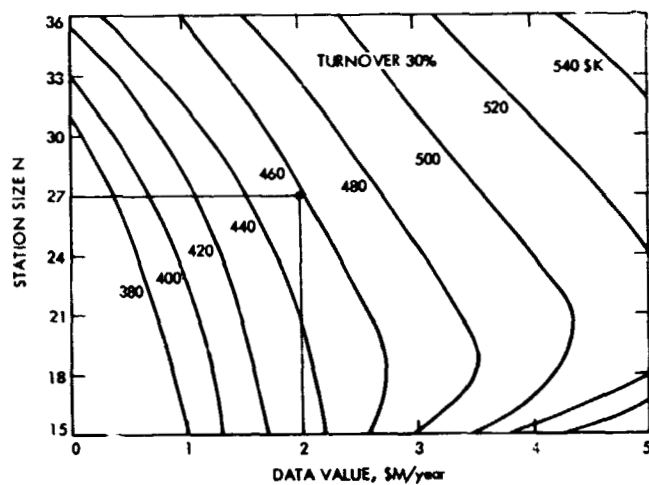


Fig. 7. Minimum overall cost contours

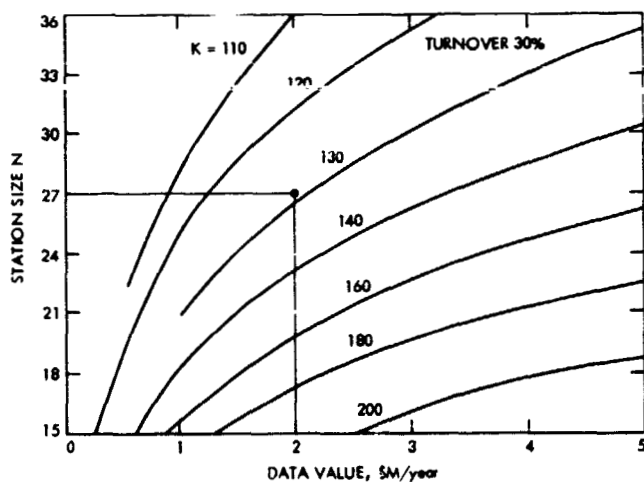


Fig. 8. Optimal capability contours

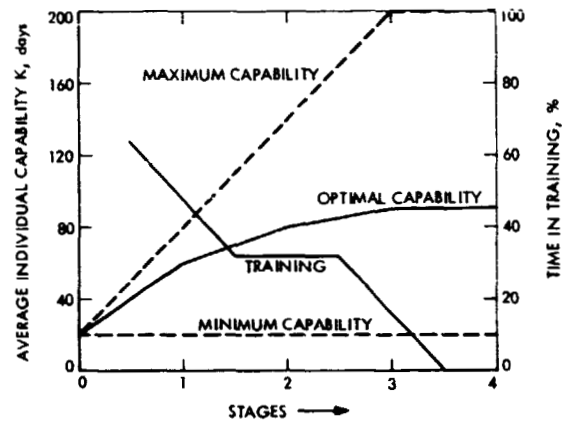


Fig. 9. Training and optimal capability

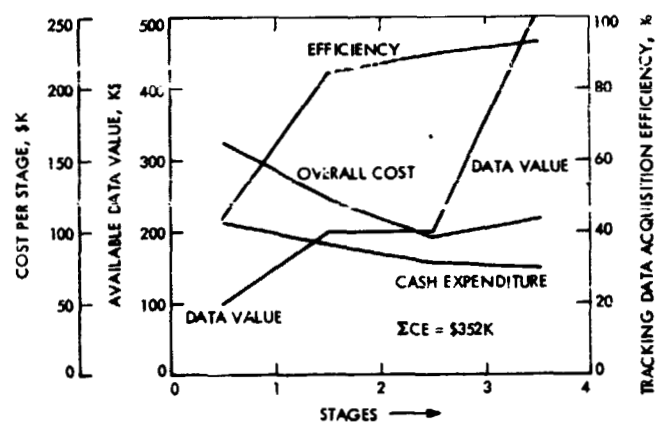


Fig. 10. Cost and efficiency

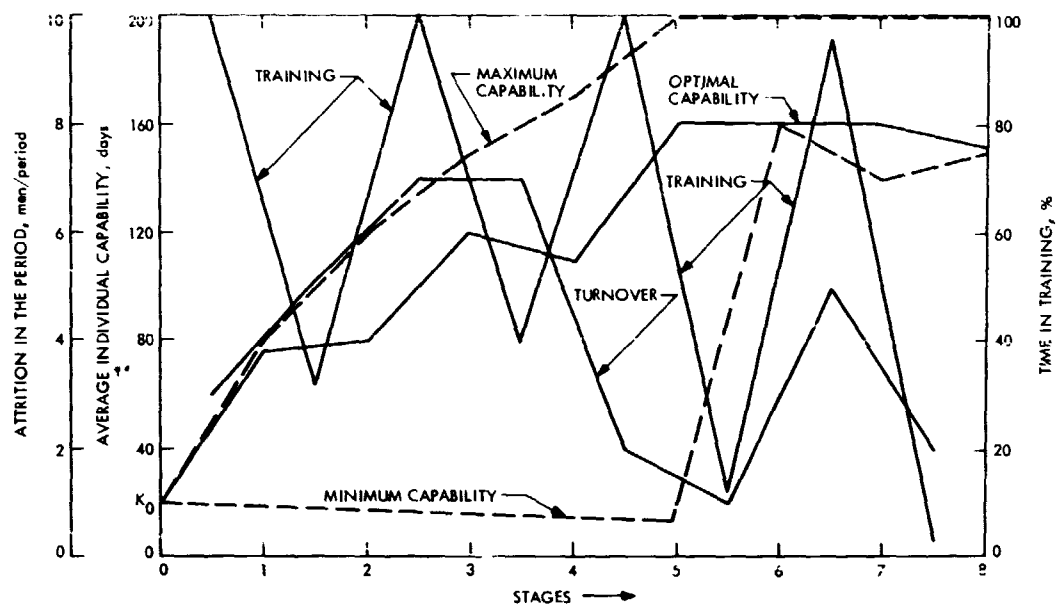


Fig. 11. Training and optimal capability

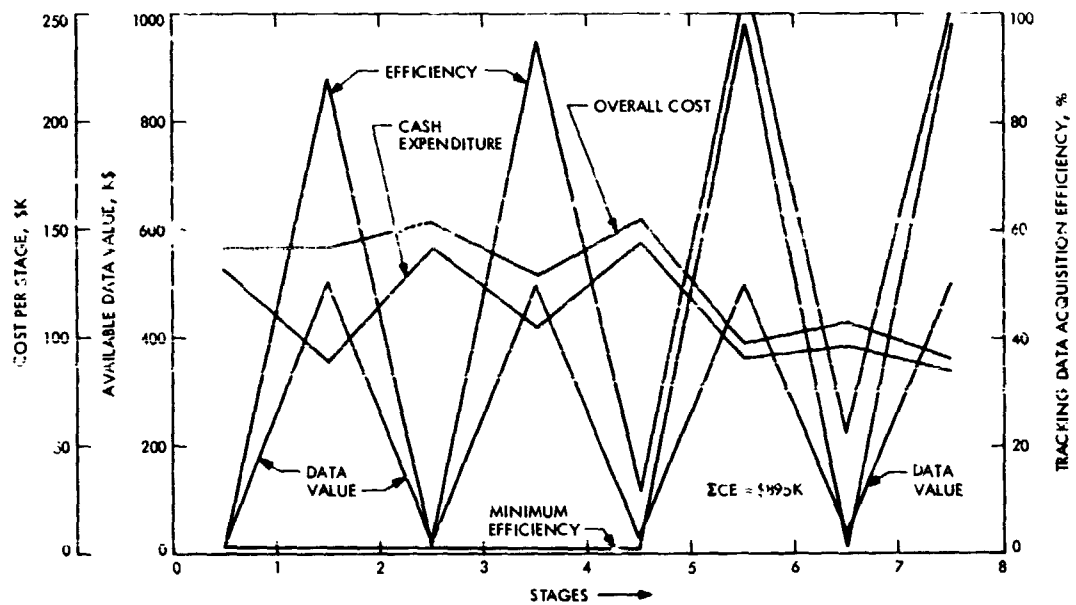


Fig. 12. Cost and efficiency

# The DSN Hydromechanical Service Program— A Second Look

R. Smith and O. Sumner  
DSN Facility Operations Office

*The DSN Hydromechanical Service Program has progressed satisfactorily along the lines originally intended. The results of oil sampling and analysis have been particularly rewarding, detecting early signs of wear and forestalling catastrophic failures.*

Since the status report in Technical Report 32-1526 (Vol. XIV, pp. 216-222), the program has progressed with gratifying results. Oil analysis is now being routinely performed for all 26 stations and, on request, at the 64-m stations.

The past year of operation (Dec. 1972-Oct. 1973) has provided many examples of the value of a centralized oil analysis program and a hydromechanical repair facility in discovering anomalous conditions and providing restorative service:

- (1) A servo pump from DSS 12 showed an increase in metal particle count and was also reported to be somewhat noisy. Disassembly and an inspection revealed a missing spring retainer pin, excessive wear in the piston and shoe assembly, excessive wear in the creep plate, bad shaft bearings, damaged hanger clevis, and splitting of the shaft seal. It can be assumed that failure was imminent and that a catastrophic failure was averted as a result of oil analysis. The pump was overhauled, tested, and returned to service.

- (2) A new 64-m antenna drive motor was received for testing prior to shipment to DSS 14. The test failed due to a seized check valve in the crosscheck manifold. The motor was returned to the manufacturer under warranty. If this motor had not been tested prior to installation, it would have resulted in a failure at DSS 14. The motor was retested after the repair and the test was satisfactory. The motor is currently in operation at DSS 14.

- (3) In December 1972, all 26-m antenna drive motors were drawn from network spares and shipped to the DSN Maintenance Center for testing prior to use in an exchange program. It was found that none of the motors was operational, and a major overhaul effort was required.

- (4) In December 1972, an analysis of DSS 12 hydraulic oil revealed a high concentration of metal from pump number two. An inspection performed by station personnel revealed a failed hanger needle bearing.

- (5) In May 1973, an analysis of DSS 62 hydraulic oil revealed a high concentration of metal from pump number two and severe depletion of oil viscosity improver. The station was subsequently requested to change the pump and to drain, clean and refill the system. The pump was returned to the DMC for maintenance.
- (6) In June 1973, an analysis of DSS 61 gear reducer oil revealed a high concentration of water in the hour-angle east gear reducer. A recommendation was made to drain the gear reducers, spray the interior with isopropyl alcohol to absorb the water, add approximately 76 l of new oil and agitate with compressed air for 2 h, then drain the gear reducer and refill with new oil. After 30 days of operations, a sample was submitted for analysis and showed water content well below the oil specifications.
- (7) In July 1973, an analysis of DSS 14 gear reducer oil revealed high metal concentration and depletion of viscosity improver. Oil was changed on all gear reducers.
- (8) In August 1973, an analysis of DSS 43 and DSS 63 gear reducer oil revealed very heavy contamination. The two systems were drained, flushed, inspected,

and refilled. An analysis of the oil presently in use will be done in the near future.

- (9) Figures 1 and 2 show the rotating group of a 64-m antenna drive motor removed from DSS 42 because of blown seals and a faulty crossfeed valve. Internal inspection revealed that a complete separation of the rotating group had occurred, resulting in severe damage to the cylinder block, seizure of one piston in the block, and separation of the piston from the shoe. A new rotating group was installed, and the motor was tested for smooth operation and static tested prior to being returned to the station.

A complete change of pumps and motors is near completion at DSSs 11 and 12. Already there has been a significant improvement in the contamination levels from these two stations during routine oil analysis.

In the near future, routine oil analysis will be facilitated for the 64-m antenna systems. The program to exchange hydraulic components with rebuilt and serialized components will continue until all stations are completed. Then the equipment will be monitored through oil analysis and recording of operational time on the components. These two factors will determine frequency of replacement.



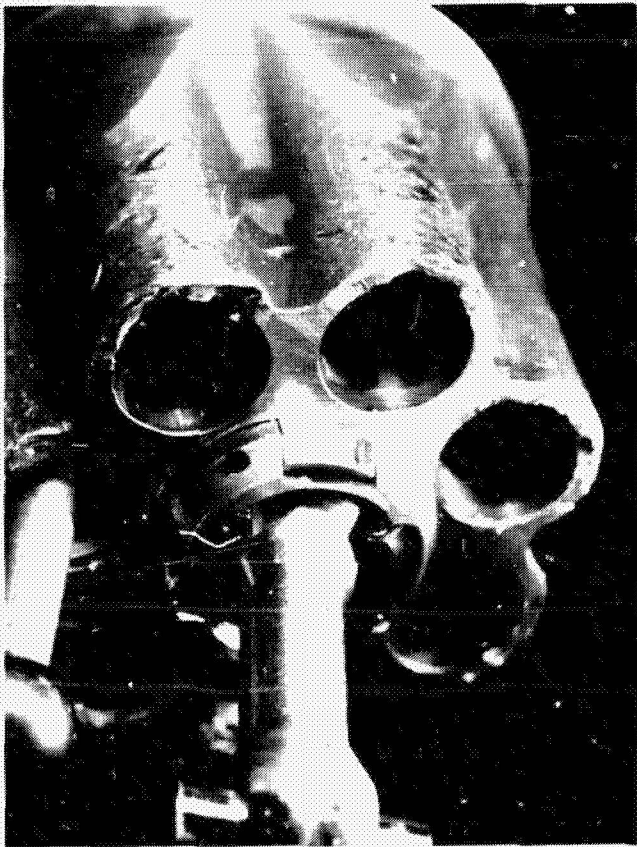


Fig. 1. 64-m antenna drive motor cylinder block

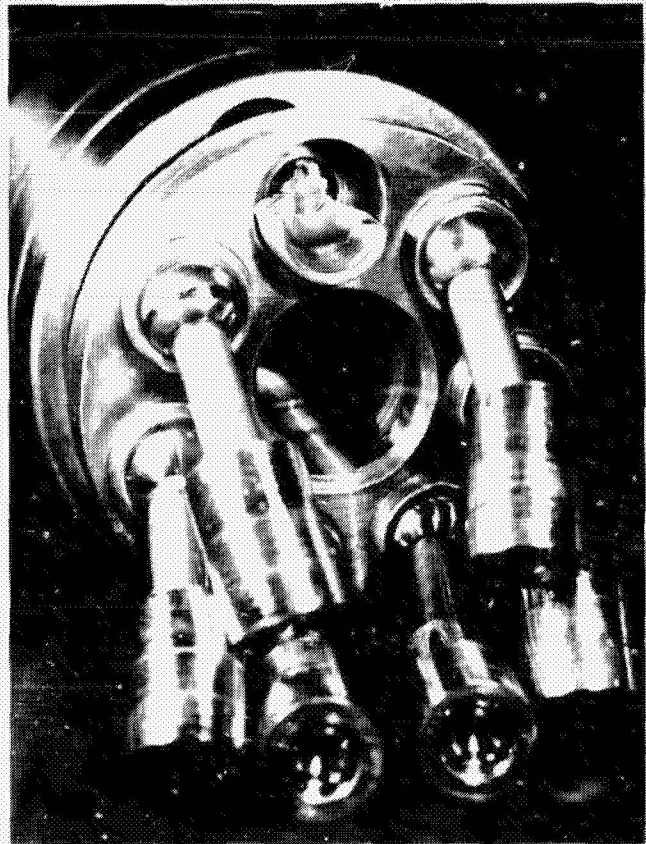


Fig. 2. 64-m antenna drive motor shaft and piston assembly  
(Note separation of piston from bronze shoe.)

# Network Command System Performance Test Report for Mariner Venus/Mercury 1973

B. Falin  
Network Operations Office

*This article presents a description of Network Command System Performance Tests that were executed throughout the DSN in support of the MVM'73 project.*

## I. Introduction

The purpose of this article is to describe the Network Command System Performance Test (SPT) conducted at each DSN station in preparation for the MVM'73 mission, and to report the status of each station at the time of launch. The objectives of the performance tests will be discussed, along with a description of the various sections of the test procedure. Problems uncovered and their solutions will also be discussed. The SPT is contained in Section II of Ref. 1.

## II. Objectives

The overall objective of the Network Command SPT is to verify that the Network Command System can sup-

port MVM'73 operational capabilities. These capabilities are defined in various documents, such as Refs. 2 and 3. A more general statement would be to verify each station's capability to provide the correct modulation mode, phase-shift keyed (PSK) with pseudo-noise (PN) synchronization (sync). More specific objectives are:

- (1) To perform integration testing on telemetry and command processor (TCP) operational software.
- (2) To verify station capabilities after hardware or software changes.
- (3) To verify command capability while processing telemetry in the same TCP computer.
- (4) To train station personnel with TCP operational software.

- (5) To provide the stations with a prepass readiness test.

During the SPT, the telemetry and command data handling subsystem (TCD) operational program DOI-5050-OP Model A, was exclusively used in the TCP.

### III. Test Procedure Format

In this section, the format of the SPT, which will provide a description of the tests that were performed, will be presented. The SPT is divided into four main sections: Countdown, Manual Mode, Automatic Mode, and Reliability. The complete testing can be performed in approximately six hours per TCD.

#### A. Countdown

The Countdown section is used as a prepass readiness test that is performed prior to the data transfer test with Network Operations. Using the appropriate TCP operational software, command capability is verified in the manual and remote mode of operations. The modulation index is adjusted and measured. Monitor interface is verified. Both timed and nontimed commands are transmitted.

#### B. Manual Mode Tests

In this section, the same type of testing is performed as in the Countdown section. Additional tests are performed on Command Modulator Assembly (CMA) configurations and TCP program manipulation. The ability to record and recover command data from an analog tape is performed.

#### C. Automatic Mode Tests

The automatic test uses the digital instrumentation subsystem (DIS) computer to simulate remote command operations. Special test software is used in the DIS to process certain programmed test sequences that can be independently selected by an operator. Each test sequence generates the command data, predicts results and verifies command data from the TCP, by utilizing high-speed data (HSD) interface to the TCP. These test sequences are processed automatically, and the results are output to the operator. All HSD blocks are automatically checked against Ref. 2. The programmed test sequences are:

- (1) CMA mode changes.
- (2) Monitor interface.
- (3) CMA operational alarms and aborts.
  - (a) Symbol rate.
  - (b) Subcarrier frequency.

- (c) Command register and marker bit failure detection.

- (d) PN sync quality.

- (e) Data quality.

- (f) PSK data to PN sync ratio.

- (4) Exciter interface alarms and aborts.

- (5) Time command accuracy.

- (6) Stack warnings.

- (7) PN generator failure detection.

### D. Reliability Tests

In the reliability tests, the capability to command and to process telemetry in the same computer is demonstrated. Continuous commanding is exercised while processing telemetry at bit rates of 33½, 2450, and 117.6 kilobits/s. Commanding consists of priority commands on 26-s centers and timed commands on 30-s centers. The DIS computer is used to generate the command data, to process the command data from the TCP, and to process the telemetry data for errors. This type of testing is performed continuously for four hours per TCD.

An appendix has been added to the reliability section giving the stations the capability to test the PN generators used to generate the PN sync signal. This was developed after detecting bit rate alarms at some stations during the first SPTs. In this peculiar test, the 511-bit PN sequences generated by the CMA are processed as a 511-bit/s telemetry channel. The processed telemetry is checked at the DIS for bit errors in the PN sequence. PN sequences containing bit errors are dumped on a line printer.

### IV. Problems

In the following paragraph, the problems uncovered and the solutions to them will be discussed.

#### A. PSK Data to PN Sync Ratio

The majority of the stations did not have the correct ratio. Analog adjustments within the CMA were made to obtain the correct ratio. The repair depot procedures were changed to reflect the correct ratio adjustments on the CMA analog drawers.

#### B. Subcarrier Frequency Alarms and Aborts

Two stations experienced this problem only during reliability testing while processing 2450-bit/s telemetry.

Engineering change order (ECO) 73-023 was installed in the CMA clock counter interface to eliminate the noise problem on TCP pin/pot lines.

### C. Bit Rate Alarms and Watch Dog Time Failures

DSSs 12, 14, and 42 experienced this problem. This condition was corrected at DSSs 12 and 42 by analog adjustments. However, at Station 14, an emergency ECO was installed as a temporary solution. The final solution for all DSSs is currently being implemented by the Cognizant Operating Engineer (COE). During operations, the bit rate warning limits are narrow to enable detection of bit rate errors caused by PN generator failures.

### D. Exciter Confirmation Phase Detector

Most stations reported excessive dc drifting on the output of the exciter's confirmation phase detector. The drift

was more pronounced at some stations. As a result, command confirmation was changed to use the local confirmation within the CMA. During the investigation, a wrong value capacitor that had been installed at the factory was discovered. Installing a capacitor of the correct value enabled the 26-m DSSs to meet specifications. However, a different problem exists at the 64-m DSS with Programmed Oscillator Control Assembly (POCA) installation. The development section is still working on a solution to this problem.

### V. Status at Launch

DSSs 12, 14, 62, 63, and 71 had successfully completed and passed all command system tests. DSS 42/43 completed and passed approximately 80% of the command system test. DSSs 11 and 51 were not required to perform the tests.

## References

1. *DSIF Standard Test Procedure No. 853-62; 2A-08, Command System Test for MVM'73*, Document No. 853. Jet Propulsion Laboratory, Pasadena, Calif. (JPL internal document in preparation.)
2. *Deep Space Network System Requirements—Detailed Interface Design*, Document No. 820-13. Jet Propulsion Laboratory, Pasadena, Calif., Feb. 1, 1971. (JPL internal document.)
3. *Deep Space Network Support Requirements for MVM'73 Project*, Document No. 615-15-Rev. A. Jet Propulsion Laboratory, Pasadena, Calif., Jan. 15, 1973. (JPL internal document.)

## Bibliography

- Anderson, J. D., *Determination of the Masses of the Moon and Venus and the Astronomical Unit from Radio Tracking Data of the Mariner II Spacecraft*, Technical Report 32-816. Jet Propulsion Laboratory, Pasadena, Calif., July 1, 1967.
- Anderson, J. D., et al., "The Radius of Venus as Determined by Planetary Radar and Mariner V Radio Tracking Data," *J. Atmos. Sci.* pp. 1171-1174 Sept. 25, 1968.
- Anderson, J. D., "Determination of Astrodynamic Constants and a Test of the General Relativistic Time Delay With S-Band Range and Doppler Data From Mariners 6 and 7," *Space Research*, Vol. XI, pp. 105-112, Academic-Verlag, Berlin, 1971.
- Barnum, P. W., et al., *Tracking and Data System Support for the Mariner Mars 1971 Mission: Orbit Insertion Through End of Primary Mission*, Technical Memorandum 33-523, Vol. III. Jet Propulsion Laboratory, Pasadena, Calif., May 15, 1973.
- Bathker, D. A., *Predicted and Measured Errors in the Description of a Large Ground Microwave System*, Technical Memorandum 32-453. Jet Propulsion Laboratory, Pasadena, Calif., Apr. 15, 1971.
- Berman, A. L., *Tracking System Data Analysis Report, Ranger VII Final Report*, Technical Report 32-719. Jet Propulsion Laboratory, Pasadena, Calif., June 1, 1965.
- Butman, S., "Rate Distortion Over Band-Limited Feedback Channels," *IEEE Trans. Inform. Theory*, Vol. IT-17, No. 1, pp. 110-112, Jan. 1971.
- Butman, S., and Timor, U., "Interplex—An Efficient Multichannel PSK-PM Telemetry System," *IEEE Trans. Commun.*, Vol. COM-20, No. 3, pp. 415-419, June 1972.
- Cain, D. L., and Hamilton, T. W., *Determination of Tracking Station Locations by Doppler and Range Measurements to an Earth Satellite*, Technical Report 32-534. Jet Propulsion Laboratory, Pasadena, Calif., Feb. 1, 1964.
- Carey, C. N., and Sjogren, W. L., "Gravitational Inconsistency in the Lunar Theory: Confirmation by Radio Tracking," *Science*, Vol. 160, pp. 875-876, April-June 1968.
- Chadwick, H. D., and Springett, J. C., "The Design of a Low Data Rate MSFK Communication System," *IEEE Trans. Commun. Technol.*, Vol. COM-18, No. 6, pp. 740-750, Dec. 1970.
- Clark, B. G., et al., "High Resolution Observations of Compact Radio Sources at 13 cm," *Astrophys. J.*, Vol. 161, pp. 803-809, Sept. 1970.
- Curkendall, D. W., and Stephenson, R. R., "Earthbased Tracking and Orbit Determination—Backbone of the Planetary Navigation System," *Astronaut. Aeronaut.*, Vol. 7, May 1970.
- Curkendall, D. W., "Planetary Navigation: The New Challenges," *Astronaut. Aeronaut.*, Vol. 7, May 1970.

## Bibliography (contd)

- Downs, G. S., and Reichley, P. E., "Observations of Interstellar Scintillations of Pulsar Signals at 2388 MHz," *Astrophys. J.*, Vol. 163, No. 1, Pt. 2, pp. L11-L16, Jan. 1971.
- Downs, G. S., et al., "Mars Radar Observation, A Preliminary Report," *Science*, Vol. 174, No. 4016, pp. 1324-1327, Dec. 24, 1971.
- Efron, L., and Solloway, C. B., *Proceedings of the Conference on Scientific Applications of Radio and Radar Tracking in the Space Program, Technical Report* 32-1475. Jet Propulsion Laboratory, Pasadena, Calif., July 1970.
- Flanagan, F. M., et al., *Deep Space Network Support of the Manned Space Flight Network for Apollo: 1962-1968*, Technical Memorandum 33-452, Vol. I. Jet Propulsion Laboratory, Pasadena, Calif., July 1970.
- Flanagan, F. M., et al., *Deep Space Network Support of the Manned Space Flight Network for Apollo: 1969-1970*, Technical Memorandum 33-452, Vol. II. Jet Propulsion Laboratory, Pasadena, Calif., May 1, 1971.
- Fjeldbo, G., and Eshleman, V. R., "Radio Occultation Measurements and Interpretations," in *The Atmospheres of Venus and Mars*, p. 225. Gordon and Breach, Science Publishers, Inc., New York, N.Y.
- Georgevic, R. M., *Mathematical Model of the Solar Radiation Force and Torques Acting on the Components of a Spacecraft*, Technical Memorandum 33-494. Jet Propulsion Laboratory, Pasadena, Calif., Oct. 1, 1971.
- Goldstein, R. M., "Radar Time-of-Flight Measurements to Venus," *Astron. J.*, Vol. 73, No. 9, Aug. 1968.
- Goldstein, R. M., "Radar Observations of Mercury," *Astron. J.*, Vol. 76, No. 10, pp. 1152-1154, Dec. 1971.
- Gordon, H. J., et al., *The Mariner 6 and 7 Flight Paths and Their Determination From Tracking Data*, Technical Memorandum 33-469. Jet Propulsion Laboratory, Pasadena, Calif., Dec. 1, 1970.
- Gray, R. M., and Tausworthe, R. C., "Frequency-Counted Measurements, and Phase Locking to Noise Oscillators," *IEEE Trans. Commun. Technol.*, Vol. COM-19, No. 1, pp. 21-30, Feb. 1971.
- Gulkis, S., and Gary, B., "Circular Polarization and Total-Flux Measurements of Jupiter at 13.1 cm Wavelength," *Astron. J.*, Vol. 76, No. 1, pp. 12-16, Feb. 1971.
- Hall, J. R., *Tracking and Data System Support for Lunar Orbiter*, Technical Memorandum 33-450. Jet Propulsion Laboratory, Pasadena, Calif., Apr. 1970.
- Hamilton, T. W., et al., *The Ranger IV Flight Path and Its Determination From Tracking Data*, Technical Report 32-345. Jet Propulsion Laboratory, Pasadena, Calif., Sept. 15, 1962.
- Holmes, J. K., "First Slip Times Versus Static Phase Error Offset for the First and Passive Second-Order Phase-Locked Loop," *IEEE Trans. Commun. Technol.*, Vol. COM-19, No. 2, pp. 234-235, Apr. 1971.
- Holmes, J. K., and Tegnalia, C. R., *Digital Command System Second-Order Sub-carrier Tracking Performance*, Technical Report 32-1540. Jet Propulsion Laboratory, Pasadena, Calif., Oct. 1, 1971.

## Bibliography (contd)

- Holmes, J. K., "Performance of a First Order Transition Sampling Digital Phase-Locked Loop Using Random-Walk Models," *IEEE Trans. Commun.*, Vol. COM-20, No. 2, pp. 119-131, Apr. 1972.
- Kliore, A., "Radio Occultation Measurements of the Atmospheres of Mars and Venus," in *The Atmospheres of Venus and Mars*, by J. C. Brandt and M. E. McElrow, p. 205. Gordon and Breach Science Publishers, Inc., New York, N.Y., 1968.
- Kliore, A. J., et al., "Summary of Mariner 6 and 7 Radio Occultation Results on the Atmosphere of Mars," *Space Research*, Vol. XI, pp. 165-175, Akademie-Verlag, Berlin, 1971.
- Labrum, R. G., et al., *The Surveyor V, VI, and VII Flight Paths and Their Determination from Tracking Data*, Technical Report 32-1302, Jet Propulsion Laboratory, Pasadena, Calif., Dec. 1, 1968.
- Laeser, R. P., et al., *Tracking and Data System Support for the Mariner Mars 1971 Mission: Prelaunch Phase Through First Trajectory Correction Maneuver*, Technical Memorandum 33-523, Vol. I, Jet Propulsion Laboratory, Pasadena, Calif., Mar. 15, 1972.
- Layland, J. W., and Lushbaugh, W. A., "A Flexible High-Speed Sequential Decoder for Deep Space Channels," *IEEE Trans. Commun. Technol.*, Vol. COM-19 No. 5, pp. 813-820, Oct. 1971.
- Leavitt, R. K., *The Least-Squares Process of MEDIA for Computing DRVID Calibration Polynomials*, Technical Memorandum 33-542, Jet Propulsion Laboratory, Pasadena, Calif., May 15, 1972.
- Lieske, J. H., and Null, G. W., "Icarus and the Determination of Astronomical Constants," *Astron. J.*, Vol. 74, No. 2, Mar. 1969.
- Lindsey, W. C., and Simon, M. K., "The Effect of Loop Stress on the Performance of Phase-Coherent Communication Systems," *IEEE Trans. Commun. Technol.*, Vol. COM-18, No. 5, pp. 569-588, Oct. 1970.
- Lindsey, W. C., and Simon, M. K., "Carrier Synchronization and Detection of Polyphase Signals," *IEEE Trans. Commun.*, Vol. COM-20, No. 3, pp. 441-454, June 1972.
- Lorell, J., and Sjogren, W. L., *Lunar Orbiter Data Analysis*, Technical Report 32-1220, Jet Propulsion Laboratory, Pasadena, Calif., Nov. 15, 1967.
- Lorell, J., *Lunar Orbiter Gravity Analysis*, Technical Report 32-1387, Jet Propulsion Laboratory, Pasadena, Calif., June 15, 1969.
- Lorell, J., et al., "Icarus: Celestial Mechanics Experiment for Mariner," *Int. J. Sol. Sys.*, Vol. 12, Jan. 1970.
- Ludwig, A. C., et al., *Gain Calibration of a Horn Antenna Using Pattern Integration*, Technical Report 32-1572, Jet Propulsion Laboratory, Pasadena, Calif., Oct. 1, 1972.
- McNeal, C. E., *Ranger V Tracking Systems Data Analysis Final Report*, Technical Report 32-702, Jet Propulsion Laboratory, Pasadena, Calif., Apr. 15, 1965.

## Bibliography (contd)

- Melbourne, W. G., et al., *Constants and Related Information for Astrodynamical Calculations*, Technical Report 32-1306. Jet Propulsion Laboratory, Pasadena, Calif., July 15, 1968.
- Melbourne, W. G., "Planetary Ephemerides," *Astronaut. Aeronaut.*, Vol. 7, May 1970.
- Miller, L., et al., *The Atlas Centaur VI Flight Path and Its Determination from Tracking Data*, Technical Report 32-911. Jet Propulsion Laboratory, Pasadena, Calif., Apr. 15, 1966.
- Moyer, T. D., *Mathematical Formulation of the Double-Precision Orbit Determination Program (DPODP)*, Technical Report 32-1527. Jet Propulsion Laboratory, Pasadena, Calif., May 17, 1971.
- Mulhall, B. D., et al., *Tracking System Analytic Calibration Activities for the Mariner Mars 1969 Mission*, Technical Report 32-1499. Jet Propulsion Laboratory, Pasadena, Calif., Nov. 15, 1970.
- Mulholland, J. D., and Sjogren, W. L., *Lunar Orbiter Ranging Data*, Technical Report 32-1087. Jet Propulsion Laboratory, Pasadena, Calif., Jan. 6, 1967.
- Mulholland, J. D., *Proceedings of the Symposium on Observation, Analysis, and Space Research Applications of the Lunar Motion*, Technical Report 32-1386. Jet Propulsion Laboratory, Pasadena, Calif., Apr. 1969.
- Muller, P. M., and Sjogren, W. L., *Consistency of Lunar Orbiter Residuals With Trajectory and Local Gravity Effects*, Technical Report 32-1307. Jet Propulsion Laboratory, Pasadena, Calif., Sept. 1, 1968.
- Muller, P. M., and Sjogren, W. L., *Lunar Mass Concentrations*, Technical Report 32-1339. Jet Propulsion Laboratory, Pasadena, Calif., Aug. 16, 1968.
- Null, G. W., et al., *Mariner IV Flight Path and Its Determination From Tracking Data*, Technical Report 32-1108. Jet Propulsion Laboratory, Pasadena, Calif., Aug. 1, 1967.
- O'Neil, W. J., et al., *The Surveyor III and Surveyor IV Flight Paths and Their Determination From Tracking Data*, Technical Report 32-1292. Jet Propulsion Laboratory, Pasadena, Calif., Aug. 15, 1968.
- Otoshi, T. Y., and Stelzried, C. T., "A Precision Compact Rotary Vane Attenuator," *IEEE Trans. Micro. Theor. Technique* Vol. MTT-19, No. 11, pp. 843-854, Nov. 1971.
- Pease, G. E., et al., *The Mariner V Flight Path and Its Determination From Tracking Data*, Technical Report 32-1363. Jet Propulsion Laboratory, Pasadena, Calif., July 1, 1969.
- Renzetti, N. A., *Tracking and Data Acquisition for Ranger Missions I-V*, Technical Memorandum 33-174. Jet Propulsion Laboratory, Pasadena, Calif., July 1, 1964.
- Renzetti, N. A., *Tracking and Data Acquisition for Ranger Missions VI-IX*, Technical Memorandum 33-275. Jet Propulsion Laboratory, Pasadena, Calif., Sept. 15, 1966.



## Bibliography (contd)

- Renzetti, N. A., *Tracking and Data Acquisition Support for the Mariner Venus 1962 Mission*, Technical Memorandum 33-212. Jet Propulsion Laboratory, Pasadena, Calif., July 1, 1965.
- Renzetti, N. A., *Tracking and Data Acquisition Report, Mariner Mars 1964 Mission: Near-Earth Trajectory Phase*, Technical Memorandum 33-239, Vol. I. Jet Propulsion Laboratory, Pasadena, Calif., Jan. 1, 1965.
- Renzetti, N. A., *Tracking and Data Acquisition Report, Mariner Mars 1964 Mission: Cruise to Post-Encounter Phase*, Technical Memorandum 33-239, Vol. II. Jet Propulsion Laboratory, Pasadena, Calif., Oct. 1, 1967.
- Renzetti, N. A., *Tracking and Data Acquisition Report, Mariner Mars 1964 Mission: Extended Mission*, Technical Memorandum 33-239, Vol. III. Jet Propulsion Laboratory, Pasadena, Calif., Dec. 1, 1968.
- Renzetti, N. A., *Tracking and Data System Support for Surveyor: Missions I and II*, Technical Memorandum 33-301, Vol. I. Jet Propulsion Laboratory, Pasadena, Calif., July 15, 1969.
- Renzetti, N. A., *Tracking and Data System Support for Surveyor: Missions III and IV*, Technical Memorandum 33-301, Vol. II. Jet Propulsion Laboratory, Pasadena, Calif., Sept. 1, 1969.
- Renzetti, N. A., *Tracking and Data System Support for Surveyor: Mission V*, Technical Memorandum 33-301, Vol. III. Jet Propulsion Laboratory, Pasadena, Calif., Dec. 1, 1969.
- Renzetti, N. A., *Tracking and Data System Support for Surveyor: Mission VI*, Technical Memorandum 33-301, Vol. IV. Jet Propulsion Laboratory, Pasadena, Calif., Dec. 1, 1969.
- Renzetti, N. A., *Tracking and Data System Support for Surveyor: Mission VII*, Technical Memorandum 33-301, Vol. V. Jet Propulsion Laboratory, Pasadena, Calif., Dec. 1, 1969.
- Renzetti, N. A., *Tracking and Data System Support for the Mariner Venus 67 Mission: Planning Phase Through Midcourse Maneuver*, Technical Memorandum 33-385, Vol. I. Jet Propulsion Laboratory, Pasadena, Calif., Sept. 1, 1969.
- Renzetti, N. A., *Tracking and Data System Support for the Mariner Venus 67 Mission: Midcourse Maneuver Through End of Mission*, Technical Memorandum 33-385, Vol. II. Jet Propulsion Laboratory, Pasadena, Calif., Sept. 1, 1969.
- Renzetti, N. A., *Tracking and Data System Support for the Pioneer Project. Pioneer VI. Prelaunch to End of Nominal Mission*, Technical Memorandum 33-426, Vol. I. Jet Propulsion Laboratory, Pasadena, Calif., Feb. 1, 1970.
- Renzetti, N. A., *Tracking and Data System Support for the Pioneer Project. Pioneer VII. Prelaunch to End of Nominal Mission*, Technical Memorandum 33-426, Vol. II. Jet Propulsion Laboratory, Pasadena, Calif., Apr. 15, 1970.
- Renzetti, N. A., *Tracking and Data System Support for the Pioneer Project. Pioneer VIII. Prelaunch Through May 1968*, Technical Memorandum 33-426, Vol. III. Jet Propulsion Laboratory, Pasadena, Calif., July 15, 1970.

## Bibliography (contd)

- Renzetti, N. A., *Tracking and Data System Support for the Pioneer Project. Pioneer IX. Prelaunch Through June 1969*, Technical Memorandum 33-426, Vol. IV. Jet Propulsion Laboratory, Pasadena, Calif., Nov. 15, 1970.
- Renzetti, N. A., *Tracking and Data System Support for the Pioneer Project. Pioneer VI. Extended Mission: July 1, 1966–July 1, 1969*, Technical Memorandum 33-426, Vol. V. Jet Propulsion Laboratory, Pasadena, Calif., Feb. 1, 1971.
- Renzetti, N. A., *Tracking and Data System Support for the Pioneer Project. Pioneer VII. Extended Mission: February 24, 1967–July 1, 1968*, Technical Memorandum 33-426, Vol. VI. Jet Propulsion Laboratory, Pasadena, Calif., Apr. 15, 1971.
- Renzetti, N. A., *Tracking and Data System Support for the Pioneer Project. Pioneer VII. Extended Mission: July 1, 1968–July 1, 1969*, Technical Memorandum 33-426, Vol. VII. Jet Propulsion Laboratory, Pasadena, Calif., Apr. 15, 1971.
- Renzetti, N. A., *Tracking and Data System Support for the Pioneer Project. Pioneer VIII. Extended Mission: June 1, 1968–July 1, 1969*, Technical Memorandum 33-426, Vol. VIII. Jet Propulsion Laboratory, Pasadena, Calif., May 1, 1971.
- Renzetti, N. A., *Tracking and Data System Support for the Pioneer Project. Pioneers VI–IX. Extended Missions: July 1, 1969–July 1, 1970*, Technical Memorandum 33-426, Vol. IX. Jet Propulsion Laboratory, Pasadena, Calif., Aug. 15, 1971.
- Renzetti, N. A., and Siegmeth, A. J., *Tracking and Data System Support for the Pioneer Project. Pioneers 6–9. Extended Missions: July 1, 1971–July 1, 1972*, Technical Memorandum 33-426, Vol. XI. Jet Propulsion Laboratory, Pasadena, Calif., May 1, 1973.
- Siegmeth, A. J., Purdue, R. E., and Ryan, R. E., *Tracking and Data System Support for the Pioneer Project. Pioneers 6–9. Extended Missions: July 1, 1970–July 1, 1971*, Technical Memorandum 33-426, Vol. X. Jet Propulsion Laboratory, Pasadena, Calif., Aug. 15, 1972.
- Siegmeth, A. J., et al., *Tracking and Data System Support for the Pioneer Project: Pioneer 10–Prelaunch Planning Through Second Trajectory Correction December 4, 1969 to April 1, 1972*, Technical Memorandum 33-584 Vol. I. Jet Propulsion Laboratory, Pasadena, Calif., Apr. 1, 1973.
- Simon, M. K., "Nonlinear Analysis of an Absolute Value Type of an Early-Late Gate Bit Synchronizer," *IEEE Trans. Commun. Technol.*, Vol. COM-18, No. 5, pp. 589–596, Oct. 1970.
- Simon, M. K., and Lindsey, W. C., "Data-Aided Carrier Tracking Loops," *IEEE Trans. Commun. Technol.*, Vol. COM-19, No. 2, pp. 157–168, Apr. 1971.
- Simon, M. K., "On the Selection of an Optimum Design Point for Phase-Coherent Receivers Employing Bandpass Limiters," *IEEE Trans. Commun.*, Vol. COM-20, No. 2, pp. 210–214, Apr. 1972.
- Simon, M. K., "On the Selection of a Sampling Filter Bandwidth for a Digital Data Detector," *IEEE Trans. Commun.*, Vol. COM-20, No. 3, pp. 438–441, June 1972.

## Bibliography (contd)

- Sjogren, W. L., et al., *The Ranger V Flight Path and Its Determination From Tracking Data*, Technical Report 32-562. Jet Propulsion Laboratory, Pasadena, Calif., Dec. 6, 1963.
- Sjogren, W. L., et al., *The Ranger VI Flight Path and Its Determination From Tracking Data*, Technical Report 32-605. Jet Propulsion Laboratory, Pasadena, Calif., Dec. 15, 1964.
- Sjogren, W. L., *The Ranger III Flight Path and Its Determination From Tracking Data*, Technical Report 32-563. Jet Propulsion Laboratory, Pasadena, Calif., Sept. 15, 1965.
- Sjogren, W. L., et al., *Physical Constants as Determined From Radio Tracking of the Ranger Lunar Probes*, Technical Report 32-1057. Jet Propulsion Laboratory, Pasadena, Calif., Dec. 30, 1966.
- Sjogren, W. L., *Proceedings of the JPL Seminar on Uncertainties in the Lunar Ephemeris*, Technical Report 32-1247. Jet Propulsion Laboratory, Pasadena, Calif., May 1, 1968.
- Sjogren, W. L., "Lunar Gravity Estimate: Independent Confirmation," *J. Geophys. Res.*, Vol. 76, No. 29, Oct. 10, 1971.
- Sjogren, W. L., et al., "Lunar Gravity via Apollo 14 Doppler Radio Tracking," *Science*, Vol. 175, No. 4018, pp. 165-168, Jan. 14, 1972.
- Spicer, G. W., *Design and Implementation of Models for the Double Precision Trajectory Program (DPTRAJ)*, Technical Memorandum 33-451. Jet Propulsion Laboratory, Pasadena, Calif., Apr. 15, 1971.
- Springett, J. C., and Simon, M. K., "An Analysis of the Phase Coherent-Incoherent Output of the Bandpass Limiter," *IEEE Trans. Commun. Technol.*, Vol. COM-19, No. 1, pp. 42-49, Feb. 1971.
- Stelzried, C. T., *A Faraday Rotation Measurement of a 13-cm Signal in the Solar Corona*, Technical Report 32-1401. Jet Propulsion Laboratory, Pasadena, Calif., July 15, 1970.
- Stelzried, C. T., et al., "The Quasi-Stationary Coronal Magnetic Field and Electron Density as Determined From a Faraday Rotation Experiment," *Sol. Phys.*, Vol. 14, No. 2, pp. 443-456, Oct. 1970.
- Stelzried, C. T., "Operating Noise-Temperature Calibrations of Low-Noise Receiving Systems," *Microwave J.*, Vol. 14, No. 6, pp. 41-46, 48, June 1971.
- Stelzried, C. T., et al., "Transformation of Received Signal Polarization Angle to the Plane of the Ecliptic," *J. Space. Rock.*, Vol. 9, No. 2, pp. 69-70, Feb. 1972.
- Tausworthe, R. C., "Simplified Formula for Mean-Slip Time of Phase-Locked Loops With Steady-State Phase Error," *IEEE Trans. Commun.*, Vol. COM-20, No. 3, pp. 331-337, June 1972.
- Textor, G. P., Kelly, L. B., and Kelly, M., *Tracking and Data System Support for the Mariner Mars 1971 Mission: First Trajectory Correction Maneuver Through Orbit Insertion*, Technical Memorandum 33-523, Vol. II. Jet Propulsion Laboratory, Pasadena, Calif., June 15, 1972.

## Bibliography (contd)

- Thornton, J. H., Jr., *The Surveyor I and Surveyor II Flight Paths and Their Determination From Tracking Data*, Technical Report 32-1285. Jet Propulsion Laboratory, Pasadena, Calif., Aug. 1, 1968.
- Timor, U., "Equivalence of Time-Multiplexed and Frequency-Multiplexed Signals in Digital Communications," *IEEE Trans. Commun.*, Vol. COM-20, No. 3, pp. 435-438, June 1972.
- Veggs, C. I., et al., *The Ranger IX Flight Path and Its Determination From Tracking Data*, Technical Report 32-767. Jet Propulsion Laboratory, Pasadena, Calif., Nov. 1, 1968.
- Winn, F. B., *Selenographic Location of Surveyor VI, Surveyor VI Mission Report: Part II. Science Results*, Technical Report 32-1262. Jet Propulsion Laboratory, Pasadena, Calif., Jan. 10, 1968.
- Winn, F. B., "Post Landing Tracking Data Analysis," in *Surveyor VII Mission Report: Part II. Science Results*, Technical Report 32-1264. Jet Propulsion Laboratory, Pasadena, Calif., Mar. 15, 1968.
- Winn, F. B., "Post Lunar Touchdown Tracking Data Analysis," in *Surveyor Project Final Report: Part II. Science Results*, Technical Report 32-1265. Jet Propulsion Laboratory, Pasadena, Calif., June 15, 1968.
- Winn, F. B., *Surveyor Posttouchdown Analyses of Tracking Data*, NASA SP-184. National Aeronautics and Space Administration, Washington, D.C., p. 369.
- Wollenhaupt, W. R., et al., *The Ranger VII Flight Path and Its Determination From Tracking Data*, Technical Report 32-694. Jet Propulsion Laboratory, Pasadena, Calif., Dec. 15, 1964.